Optical Metrology Techniques for Dimensional Stability Measurements

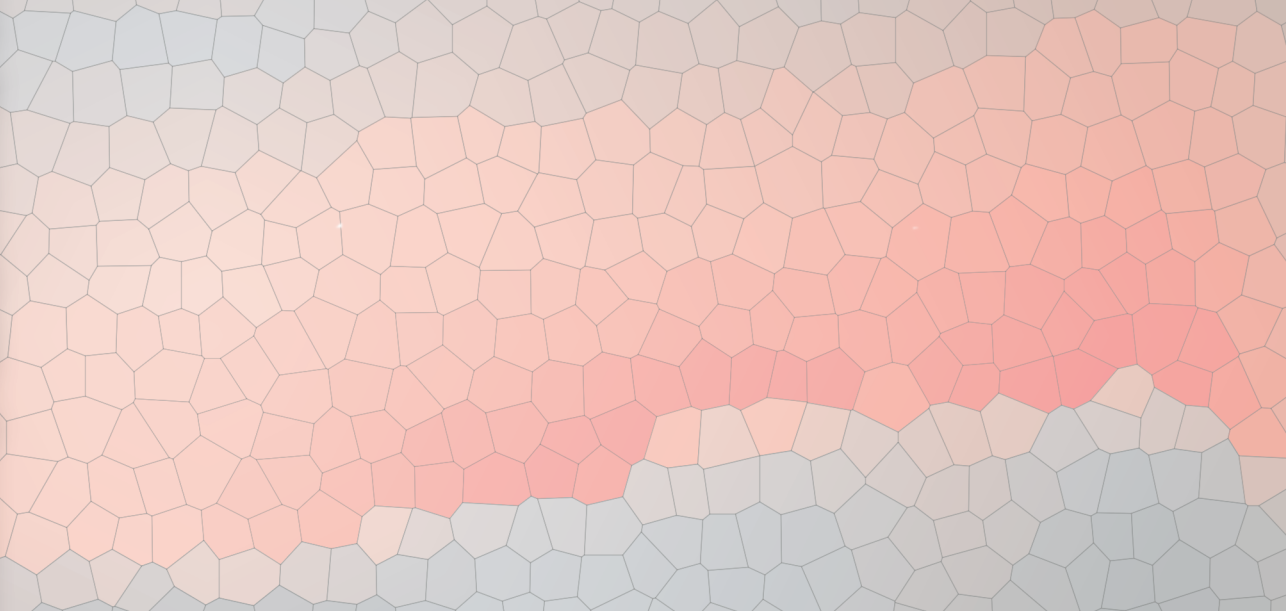

Jonathan D. Ellis

About the cover

Front: Impression of the grain boundary structure within a material. The red color indicates a stress concentration which may lead to a slip along grain boundaries, decreasing the material stability and causing a stability event.

Back: Three photographs of optical setups superimposed over the grain boundary structure. Top: Photograph of the Third Measurement Setup; Middle: Photograph of the custom optics and mounts; Bottom: Photograph of the Fourth Measurement Setup with partial shield for light vacuum measurements.

Optical Metrology Techniques for Dimensional Stability Measurements

Proefschrift

ter verkrijging van de graad van doctor
aan de Technische Universiteit Delft,
op gezag van de Rector Magnificus prof.ir. K.C.A.M. Luyben,
voorzitter van het College voor Promoties,
in het openbaar te verdedigen
op vrijdag 3 december 2010 om 10.00 uur
door

Jonathan David Ellis

Master of Science in Mechanical Engineering,
The University of North Carolina at Charlotte
geboren te Hackensack, New Jersey, Verenigde Staten

Dit proefschrift is goedgekeurd door de promotor:

Prof.ir. R.H. Munnig Schmidt

Samenstelling promotiecommissie:

Rector Magnificus,	voorzitter
Prof.ir. R.H. Munnig Schmidt,	Technische Universiteit Delft, promotor
Ir. J.W. Spronck,	Technische Universiteit Delft, co-promotor
Dr. D. Voigt,	NMI van Swinden Laboratory
Prof.dr. R. Leach,	National Physical Laboratory
Prof.dr.ir. P.P.L. Regtien,	Technische Universiteit Twente
Prof.dr.ir. P.H.J. Schellekens,	Technische Universiteit Eindhoven
Prof.dr. H.P. Urbach,	Technische Universiteit Delft
Prof.dr.ir. J. van Eijk,	Technische Universiteit Delft, reservelid

This research was supported by IOP (project no. IPT06104).

ISBN 978-94-91104-06-0

Printed by Wöhrmann Print Service.

To Kate and Julia,
who mean the world to me,
through and through

Propositions belonging to this thesis

Optical Metrology Techniques for Dimensional Stability Measurements

Jonathan D. Ellis

1. Helium Neon frequency stabilization via the mixed mode is a practical stabilization technique with a higher output power than comparable alternatives with the potential to be a reference standard on par with iodine stabilized lasers.

2. In practice, better measurement results can be obtained using interferometry in air using proper environmental shielding than in vacuum, contrary to popular belief.

3. Even for the short displacements expected in stability measurements, periodic nonlinearity can contribute errors on the nanometer level.

4. Refractive index fluctuations must be corrected at the same bandwidth as the interferometry measurement for ideal correlation, which cannot be performed via environmental parameter measurements.

5. Until we all speak the same language in the precision community, researchers will be looking to buy machines that make measurements with low uncertainty, while metrology equipment manufacturers will be trying to sell very accurate machines.

6. Ph.D. quality work is defined by the contributions to a particular field as a whole and not whether the research satisfies the requirements set forth in a proposal.

7. Most students who do not finish their thesis within four years take jobs in industry as Ph.D. level researchers even though they have not completed their work. Thus, the thesis, and by extension publishing research findings, has little value to industry.

8. The academic financial support system is traveling down a path that cannot sustain itself. The necessity for matching funds from industry, which typically stifles publications and claims all intellectual property, will eventually hamper our ability as researchers to discuss in open forums and build from past generations.

9. Stability measurements are not possible when a colleague is building his or her own interferometer on the opposite side of the same optical bench.

10. Professional sports leagues alienate fans when they fail to recognize that most viewers at home can see with today's technology what they are consistently trying to ignore and refuse to correct.

These propositions are considered opposable and defendable and as such have been approved by the supervisor prof. ir. R.H. Munnig Schmidt.

Contents

Chapter 1

Dimensional Stability

Precision systems currently contain many mechanical, electrical, and/or optical components for achieving a specific purpose. Characterization of a precision system can therefore be extremely difficult as the system complexity and the targeted system performance increases. Additionally, the design and characterization differs depending on the purpose of a particular system. In general, precision systems need a hybrid of structural rigidity, dynamic performance, minimal heat generation, etc. To meet some of these design constraints, lightweight and stiff components are used to increase component resonant frequencies or reduce mass. In these instances, the specific construction technique employed can introduce stability effects at the nanometer and sub-nanometer levels, which may affect the overall system performance.

Stability is a parameter that is often overlooked when designing systems. System instability, often referred to as drift, is the unwanted dimensional changes of the system. Errors in instruments from known drift effects, such as thermal expansion and stress-induced deformation, can be corrected and reduced by applying simple thermo-mechanical models. This requires some in-process correction and environmental parameter measurements, but can generally limit the effect of first order errors. However, as systems become more complex and employ not only mechanical but also electrical and optical components, determining the cause of drift is often difficult.

Increasingly, most systems deal with stability issues in a combination of two different ways: limiting the known first order effects and by a periodic calibration and adjustment. If a linescale is made of a material with a well defined thermal expansion coefficient, placing a small temperature sensor in the read-head could allow for a simple linear correction for thermal fluctuations. This will reduce the errors in the sensor when large temperature changes occur by correcting first order effects. However, this type of sensor should be calibrated by applying a known temperature fluctuation and determining its effect on the measured value. Also, issues such as thermal time constants and thermal gradients should be considered.

A laser beam modulated with an electro-optic crystal is an example of a system combining mechanical, optical, and electrical components. Over time, there may be three causes of drift in this system. Mechanical drift can affect this system by changing the laser pointing and the electro-optic crystal mount alignment. Electronic drift could be

caused by current heating across the electrical connections, changing the resistivity and thus performance, etc. There are also optical drift effects. The polarization state of the beam can change, the crystal may absorb some light causing heating of the crystal, etc. The electronics can also have instability because resistors and capacitors age and oxidize, causing changing voltage levels and phase shifts.

In practice, the following steps are typically taken to reduce instability. Mechanical adjustments are used to reduce pointing instability and thermal expansion issues. Optical coatings reduce absorption and good electrical components are usually made of materials that behave within a certain specification over time. Thus, each instability source is significantly reduced and may be low enough to be considered negligible.

Let us now assume a typical application of this laser beam with an electro-optic crystal example is in a satellite which must be operable under vacuum conditions in orbit around Earth for many years. It is impractical to have many mechanical adjustments to the system because of the added size and mass, which would greatly increase the cost for deployment into space. Plus, those adjustments would require their own motors and control for autonomous maintenance, as well as a feedback system to adjust them over time. This would further increase size and complexity, as well as cost.

Additionally, how is the atmospheric to vacuum transition going to affect the system?

What started as a rather simple example becomes a more difficult problem when particular constraints are applied. That is where the work in this thesis applies. This research is addressing fields where the dimensional stability of a particular object is important to the overall functionality which requires characterization during the design phase. This research focuses on designing and building instrumentation for measuring the dimensional stability of a sample. That sample can be a particular material, formed in a particular manner, or constructed using a particular technique. In order to determine whether a particular material, forming technique, or construction method is stable enough, the measuring instrument must perform these measurements without influence from its own dimensional instability.

The following section describes several measurement artifacts, types, and situations that are of importance in this research. The background and importance of metrology and precision measurements are also presented. Following that, systems used in prior research and their merits and shortfalls are examined. Finally, the research topics for this work and specifications for a stability-measuring instrument are introduced.

1.1 Dimensional Stability

In general, stability is defined as the ability to maintain a specified state, within a certain set of criteria. In the context of mechanical systems, dimensional stability means only intended size changes occur as a function of time. It is widely known, though, that most materials fluctuate in size as a function of time due to temperature fluctuations in that same time span. Additionally, changes in applied forces on a sample can cause elastic deformations which will also change the sample size. These two effects are considered to be known, predictable, and correctable using first order approximations. Samples typically change length linearly on the order of parts per million per kelvin from temperature and a sample will elastically deform based on its material properties and geometry for an applied force.

These assumptions are only valid for small thermal fluctuation ranges and when the applied force is much less than needed for yielding the sample.

These assumptions of small thermal fluctuations and low forces are widely used in precision engineering systems. For example, a temperature fluctuation causes a direct and repeatable error in the instrument's main function. By measuring the temperature, a fluctuation correction could be applied which will reduce that repeatable error in the instrument's main function. This correction is performed in many fields from error mapping axes in precision machines to adaptive mirrors correcting wavefront distortion in lithography systems. This research goes one step further along this methodology by assuming all corrective measures in an instrument will have some inherent drift. Thus, the instrument must be designed to be balanced and have minimal correction correlations. By doing so, the remaining measurement error sources are due to the measured material's properties, which are predictable to a certain extent. The key to determining a sample's dimensional stability is decoupling the known or predictable effects from the material instability and the measuring instrument's instability.

The two biggest known contributors to material instability are thermal fluctuations and load changes. If these effects are precisely monitored and corrected, then further investigation into material instability is possible. This leads to two potential outcomes: 1) determining the sample's inherent stability or 2) knowledge about additional coupled effects which cause much smaller dimensional instability than the instability from temperature and loading effects.

Research in this thesis will allow for an investigation into both cases. While determining a fundamental stability parameter for a particular material can be investigated using the instrumentation developed during this work, it is more likely that more information on forming processes, construction techniques, and measurement environments provide progress towards that target. By understanding the drift process, the component could be designed to mitigate these time-varying effects.

1.2 Stability Measurement Examples

One example the illustrates the fundamental stability against the stability in a particular application is a mirror surface. Optical quality mirror surfaces can be manufactured by diamond turning or a combination of grinding, polishing, and lapping. Once a surface is polished, characterizing the surface relaxation due to the induced stress during the forming process is important in some applications [1]. Also, the material type, such as ceramic or metal materials, may affect the surface relaxation when a particular forming process is used. This is an example of *forming stability measurement*. To test for stability effects, one could assume a piece of material is cut into two pieces of the same size and each piece is formed differently. Then the relative change over time can be measured. By doing this for many materials, a library can be developed that does not necessarily list which is ultimately the most stable process. This library would list "If [material or type of material] is needed in this application with a mirror surface, then [process] provides more stability".

The following is a list of potential stability measurements and what questions could be answered by having the appropriate measurement instrument.

- *Thin Films* – Many systems use thin films as either coatings or connections (adhesives). Using UV-curing adhesives can lead to errors as demonstrated by Schmidtlin, *et al.* [2] where the shrinkage during curing causes unwanted deformations of the assembly. As shown in Figure 1.1a, the interface where the adhesive is applied is a source of additional stress and thermal expansion mismatch, which can cause instability. Recent research by Ressel, *et al.* [3] has shown differences between the stability of hydroxide-catalysis bonding and adhesives, critical for space applications. Also, the alignment of assembled components is generally critical and a non-uniform adhesive layer can cause angular misalignments.

  In addition to adhesives, the stability of thin films on surfaces and the effects of tarnishing or water layer growth on a surface are also important in precision engineering applications. Applying a thin flim on the surface to part of a sample, as shown in Figure 1.1b, while measuring an uncoated surface can give an indication of the thin film stability or dimensional growth on the surface. This, of course, assumes parallelism changes over time are negligible. Special consideration for phase change on reflection is needed [4, 5]. Additional topics to investigate include the surface relaxation or stress while applying a coating and the effect of coating thickness on stability.

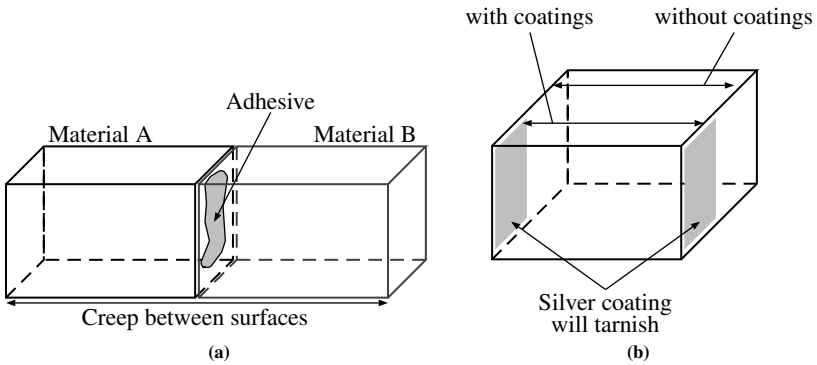

Figure 1.1: *(a) A schematic of two components with different material properties assembled with an adhesive. The materials themselves do contribute some drift but the interface between the two components has changes in stress concentration and thermal properties and is a large drift source. (b) A example of a sample prepared for thin film measurements. Measuring two parts of the same component ensures high symmetry in the measurement, which should reduce errors.*

- *Hollow Constructions* – Precision systems and mirrors are often designed with minimal mass, but high stiffness is required. To accomplish this, some large components are assembled boxes, with large sections of removed materials and some include a thin lid held on with adhesives (e.g. [6–8]). Additionally, there is usually a ribbed structure within the box to provide support and stiffness, as shown in Figure 1.2. The adhesive and box structure produce a component that is over constrained and overstressed in the assembled state with a non-uniform stress distribution.

An example of this type of hollow construction is in adaptive telescope mirrors for wavefront correction. Angel, *et al.* [7] demonstrate a honeycombed mirror with embedded thermal actuators which are used to deform the mirror and correct wavefront errors. These thermal actuators cause a non-uniform stress and thermal loading can cause deformation over time. Additionally, thermal expansion differences and thermal cycling can cause fatigue stress, which may deteriorate the enclosure interface over time.

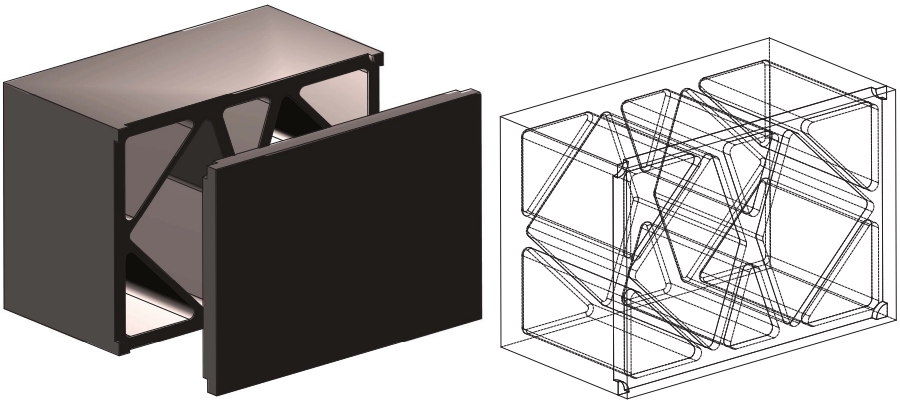

(a) (b)

Figure 1.2: *(a) An exploded view of a box assembly with mass removed to increase resonance frequencies and reduce weight. (b) A wireframe view of the same box shown the matchup of the pockets between the lid and box. These interfaces are typically sealed with an adhesive.*

- *Surface Force Attraction* – Some optical components are currently assembled using optical contacting techniques where the two mating surfaces are virtually atomically flat and when attached, the combined material behaves as a single material. A schematic of this is shown in Figure 1.3a, where two materials are polished and then contacted. The stability of that interface contributes to the overall dimensional stability of the combined materials. Berthold, *et al.* [9] demonstrated that the initial drift rate per optical contacted surface was steep, but appeared to stabilize after 160 days of measurement. More information is needed about this assembly technique as this is a popular technique for assembling optical components.

  Instead of optical contacting, two nominally flat surfaces can be wrung together to assemble components. This is typically performed in gauge block measurements where a series of gauge block are wrung together to create an arbitrary length gauge. At each wrung interface, there is a 'wringing layer' estimated to be between 5 nm and 25 nm thick [4], as shown in Figure 1.3b . This wringing interface and the stress at this interface are seen as a large uncertainty contributors in gauge block interferometers [10, 11].

  Characterizing the fundamental stability of wrung/contacted interfaces can lead to better assembly techniques for space applications where adjustment and realignment

is not possible once a system is deployed. Characterizing the changes in attraction forces after aging is also important. However, in both cases, quantifying these values in short measurements, not lasting months or years is also critical.

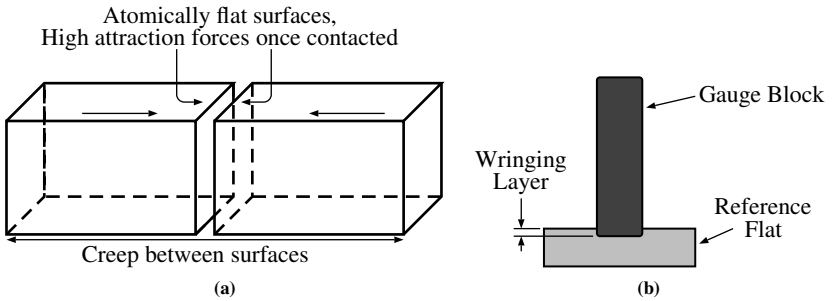

Figure 1.3: *(a) Schematic of two components in the process of being optically contacted. Because both surfaces are atomically flat, the resulting component behaves similar to a single component without an interface. This optical contacting interface has been shown to creep [9]. (b) Schematic of a gauge block wrung to a reference plate with a 'wringing layer' overlap. This wringing layer must be considered when determining the true size of the gauge block.*

- *Vacuum Transitioning* – Many precision systems are used in vacuum environments, including space instrumentation and EUV[1] lithography tools. Components in these systems are manufactured and assembled under atmospheric conditions. When completed, the air is then evacuated from the systems. This globally produces a 101 kPa pressure difference across every surface in the system. This loading change can cause component distortion, misalignment, and, ultimately failure. In space, this is a very expensive problem to fix. For EUV and other vacuum based instruments, correcting component distortion and misalignment means air must be vented back into the system, which could cause contamination. Switching to vacuum removes some problems typically related to instrument performance (i.e. refractive index changes), but can create many other problems. How does the vacuum transition affect a material's stability? Does the change in pressure distort the surface shape? Does outgassing change the size of a material?

- *Kinematic Clamp* – Components are often assembled in a kinematic fashion. This is typically to force the applied load through well defined contacts and to allow components to be designed thermally centric. A typical kinematic clamp is a three V-groove and three sphere combination, which creates six points of Hertzian contact stress between the spheres and planes of the V-grooves, shown in Figure 1.4. The defined loading points also create localized stress concentrations which can cause deformations. These deformations lead to component drift over time, which, if used in conjunction with mirror mounts, for example, will lead to misalignment. How does the distance between the kinematically mounted components change over time, as shown in Figure 1.4c. Also, how well are the two surfaces aligned over time?

[1] For a list of abbreviations throughout this thesis, see Appendix A

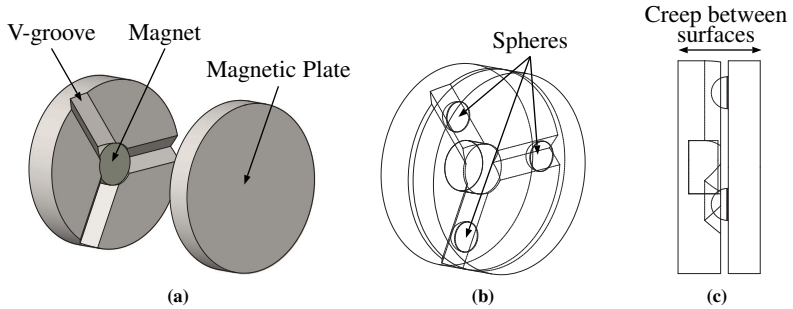

Figure 1.4: *(a) Exploded view of a kinematic coupling with three V-grooves and three spheres (hidden from view). In this case, the plate with the spheres is magnetic and a magnet placed in the V-groove plate provides the holding force. (b) Wireframe view of the unexploded kinematic coupling showing the matching V-grooves and spheres. (c) Side view of the same wireframe view showing the typical dimensions of interest, relative displacement and parallelism the surfaces.*

These six potential measurements are examples of stability measurement types where more research is needed. The research goal in this thesis is to produce an instrument that can perform these stability measurements with minimal measurement uncertainty.

1.3 Research Goals

The goal of this research is to design an instrument capable of measuring material stability and assessing dynamic stability events. To focus on measuring material stability and dynamic events, this work will only focus on displacement measurements as opposed to distance measurements. Currently, there are several instruments capable of distance measurements which means the absolute sample length is determined. This work will differ from previous distance measuring interferometers because it is designed to quantify stability events rather than record the overall length.

There are several prominent reasons for designing for displacement measurements. With a distance measuring interferometer, a sample is typically placed in the instrument, allowed to soak out, and then measured. Afterwards, it is removed and another sample is measured, and so on. While this allows for many different samples and materials to be measured, it provides no information between measurements, only that the sample length has either stayed the same, or changed. Even using some of the best measurement capabilities currently available, the measurement uncertainty for a signal absolute length measurement is still on the order of nanometers. This type of measurement is simulated and shown in Figure 1.5a where there is approximately 0.6 nm of drift in ten measurements over a period of five days. Because the measurement uncertainty for each individual measurement must be considered, the drift is inconclusive compared to the measurement uncertainty.

With a displacement measuring interferometer, the sample effects can be measured dynamically. This gives more information than just one data point every time the sample is measured. Figure 1.5b shows the same simulation from Figure 1.5a but instead of making only ten measurements, the length change is continuously measured at a sampling rate of 20 Hz. In this measurement, stability events are shown ranging from 20 pm in the beginning of the simulation to 5 pm after five days.

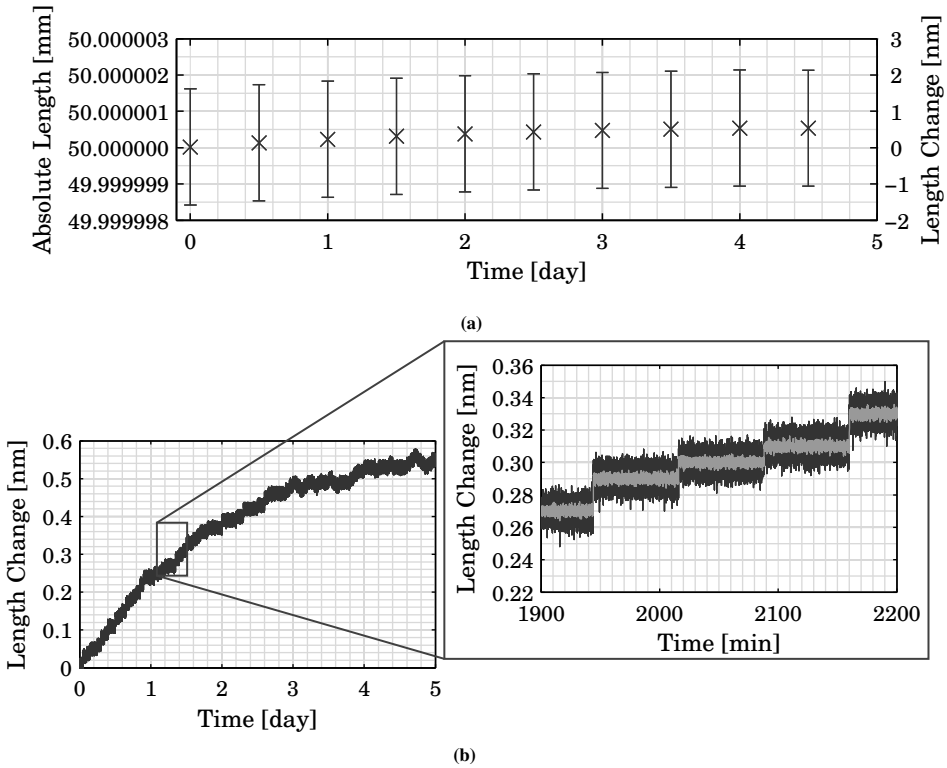

Figure 1.5: *(a) Schematic of a sample measurement using absolute distance techniques. The single shot uncertainty is much higher than the difference between measurement. (b) Same schematic of the sample measurements however this time using displacement interferometry. If the measurement system is stable enough, more short term, dynamic information can be obtained than with the distance measuring system. The red band shows the same simulation with a filter added which would depend on the material properties.*

Distance measuring interferometers only give a few discrete data points and provides no information between data points. However, with the interferometer built during this research, the same overall length change effects can be observed, along with small jumps on the sub-nanometer level, which represent some atomic stick-slick and stress relaxation. With future research and more knowledge about the stability events, estimations can be made about the amount of creep before a material is stable in a given situation. For example, in the simulation shown in Figure 1.5, it may only be necessary to measure the sample for one day to obtain enough information about the drift rate.

Another possible application of short term, initial measurements is to use the initial jump rate and size to quantify the internal stresses present in the material. Once a material has been measured for a long time, some assessment can be made about its stability even after some initial creep. For instance, let us assume the material from the simulations in Figure 1.5 is nominally stable after three months. However, the material still shows some jumps or stability events on the order of 5 pm to 10 pm, while the nominal length remains the same. This 5 pm to 10 pm is then probably the stability limit of the material.

There are two other practical reasons for taking the displacement approach for this research. The first practical reason is there is work ongoing in this area on the absolute stability using distance measuring interferometers. This means researchers already have stability estimates for many materials and there is limited usefulness in starting work in an area with five or more years of research already completed. The second practical reason is there is a finite amount of resources and time available during this work. Implementing absolute distance measuring in an interferometer generally means more complexity and a more expensive laser source. If the research in this thesis is successful, implementing absolute distance measuring capability in addition to displacement measuring is viewed as the next step.

1.3.1 Instrument Measurement Goals

The stability events are estimated to be in range of tens of picometers, thus this research aims to measure stability events as little as 5 pm. Therefore, the target measurement uncertainty for this instrument is 10 pm (k=2) for measurements up to one hour. For longer measurements, the target measurement uncertainty is 100 pm (k=2) for measurements up to four weeks. The interferometer should be designed in such a way to minimize the effect of instrument stability on the measurement.

This interferometer will measure 'gauge block type objects', which are rectangular in shape, with a maximum length of 50 mm (initial measurements). The sample's measurement surfaces (opposing sides) should be nominally flat and parallel with a high reflectivity. The parallelism tolerance should be similar to a Grade K gauge block [12].

1.4 Metrology & International Standards

To determine the appropriate measurement methodology for measuring stability, an understanding of basic metrology techniques and standards is first required. Metrology is the study of measurement and it plays an important role in society in a variety of ways. Metrology examples in society range from how much "stuff" do you get when you buy a "liter" of diesel, to maintaining 230 V and 50 Hz at a wall outlet, or knowing how large an atom is. Metrology is an important part of international standards, which define a level playing field for both manufacturers and consumers alike.

Dimensional metrology is a subset of metrology where the measurement of interest is the size and/or position of an object in either relative or absolute terms. To illustrate this, the typical example used is that of a moving stage relative to some "fixed" reference point. If the stage moves in an assumed linear fashion from point 1 to point 2, there are several questions that are of interest to the user, which point to the need for appropriate dimensional metrology. In most systems, the difference between point 1 and the reference point and the difference between point 2 and the reference point is measured and the difference between those two differences is the displacement. However, the "fixed" reference point can not be infinitely stiff and thus, is moving in time. The user wants to know how that affects the difference between point 1 and point 2. This leads to the question, how does one know that the stage is exactly at point 2? What is the probability of repeating that same motion and ending up exactly at point 2? Additional interesting criteria are the linearity of the traversed path, the true location at each point along the full path, and the consistency of

the sensitivity between the measured signal and the displacement value. These concerns are further compounded if the initial, main reference point changes location while the stage traverses between points 1 and 2.

For a typical system, the method to find the answers to most of these questions can be found in international standards. These range from simple criteria, such as ISO 1 stating that all dimensional measurements shall be performed at 20°C (68°F), to complete calibration procedures, such as ISO 15530/B89.4 defining how a CMM is to be calibrated [13–15]. The international standards are drafted by the scientific community who are interested in a particular industry or research area. Most standards committees comprise industry members, university faculty, and national laboratory researchers, all of which have their own agenda for the standard. However, for stability measurements, there is no current standard on how to perform the measurements. Therefore, the design of this instrument is not bound by a specific measurement methodology set forth in a standard..

The measurements performed by instrument, however, are bound by the definition of the primary measurement units and the number of steps that separate this instrument's measurements from the primary standard. Since this research predominantly focuses length change (relative measurements), the major unit of interest is the meter. However, to measure length accurately, it is essential to know other measurands such as temperature, pressure, humidity, and time. This means the measured drift is always relative to multiple master standard definitions.

When building an instrument, if the employed measurement strategy is removed by a number of steps from the primary standard, the measurement accuracy is likely reduced. This reduction in accuracy is quantified as one part of the measurement uncertainty, which typically increases with each step taken further from the primary standard. The collection of steps (and their known uncertainties) that can be taken from the primary standard to a known reference standard is known as the traceability chain.

An example of the steps from the primary standard to a reference standard is the meter[2]. The meter is the primary length standard and is defined as the distance traveled by light in vacuum $1/c$ seconds where c is the speed of light in vacuum, 299 792 458 $\mathrm{m{\cdot}s^{-1}}$ [17]. While this is the definition, it is currently impossible to measure this quantity directly. Therefore, the practical definition is based on the Helium Neon laser operating with a 632.8 nm wavelength [18]. For example, when a displacement is measured using a conventional capacitance sensor, the capacitance sensor must be calibrated. Because the laser can be linked to the primary length standard, the measurement uncertainty using a capacitance sensor is increased because it must include the laser measurement uncertainty, as well as uncertainties associated with the capacitance sensor measurement. This does not mean accurate, low uncertainty measurement cannot be made with non-primary standard techniques, but this is case dependent and additional design conditions are typically needed.

1.5 Uncertainty & Precision Measurements

For this research, sample length is the specific measurand of interest. More particularly, the length change or a relative measurement is the main focus for this research. This is different

[2]The notation used in this thesis is based on the SI definition as per NIST[16].

than an absolute measurement, where the absolute sample length is measured.

During a measurement, the instrument reports varying values for the sample length change even if the sample length does not change. These fluctuations in the measured value can be attributed to many things, but in general, there is no 'perfect' instrument. If the reported fluctuations are random, the probability distribution for a particular value is Gaussian in nature. When the instrument reports a measurement value, there is an uncertainty in the value, which is related to the shape of the Gaussian distribution. The expected measurement value is the mean value of the Gaussian distribution and the distribution width is related to the standard deviation. As shown in Figure 1.6, a narrower Gaussian distribution means the expected value is closer to the true value, than in the case where the Gaussian distribution is relatively wider. The true value can be anywhere within the full range of the Gaussian distribution, but in practice is unknown.

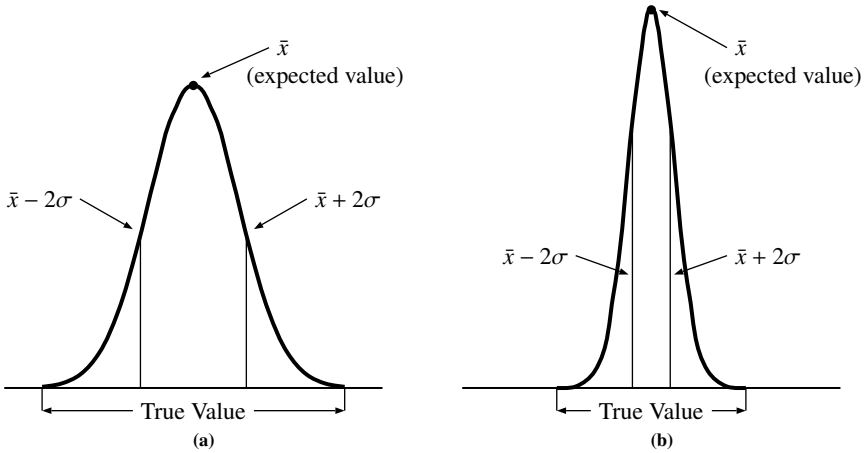

Figure 1.6: *Guassian distributions for a measurement with a wide spread (a) and a narrow spread (b). A measurement instrument with results showing a more narrow distribution give an expected value closer to the true value than an instrument with a wider distribution, although the true value can never be known. Also, the true value can be any value within the complete Gaussian distribution, although it is more likely situated towards the center.*

The "Guide to the Expression of Uncertainty in Measurement" (GUM) [19] has the complete description for the procedures for specifying the measurement uncertainty. In addition to the GUM, there is a shorter version, the so-called "Guide to the GUM" [20] which gives specific examples of how to use the GUM.

A less accurate instrument will have a much wider probability distribution than a more accurate instrument. Because the probability distribution is wider, the uncertainty between the measured value and true value is higher. Since the true value is never known, the mean measured value gives the best estimated true value. The estimated true value should be reported in the form of "X [units] ± Y [units]" which is to say "the estimated value is X [units] with an uncertainty of plus or minus Y [units]". If the uncertainty value contains only 25% of the probable values, then the confidence in the estimated value of X [units] is low. In metrology, the confidence of the measurement is based on the coverage factor, k, typically assuming a Gaussian distribution for a measurement result. In precision measurements,

the uncertainty value is typically stated with confidence of 67%, 95%, or 99%. These confidence values correspond to a measurement with a Gaussian distribution assuming one, two, or three standard deviations, respectively. So if the measured value is reported as "X [units] ± Y [units] (k=1)" with a Gaussian distribution, then it is the same as "the estimated value is X [units] and there is a 67% probability that the true value is between X - Y [units] and X + Y [units]".

When researching literature from the 1980's and earlier, the uncertainty was typically quoted with a k=3 coverage factor or 99% confidence interval. However, in literature from the 1980's until present, the uncertainties quoted typically have a k=2 coverage factor or a 95% confidence interval. It is unclear as to what caused this shift in measurement uncertainty reporting. The uncertainty values in this research have a 95% confidence interval, unless otherwise stated. As an example, the syntax for writing a 20.00 m estimated value with a 0.02 m uncertainty with 95% confidence is

$$x = 20.00 \text{ m } \pm 0.02 \text{ m } (\text{k} = 2) \quad \text{or}$$
$$x = 20.00(2) \text{ m } (\text{k} = 2)\,,$$

where k is the symbol for coverage factor. A confidence interval k of 2 is the same as 2σ (two standard deviations) of a Gaussian distributed measurement.

Typically, in dimensional metrology, a 'precision' measurement has an uncertainty between the measured value and the estimated true value of less than 0.01% of the nominal value (1×10^{-4}) or 1 part in 10^4. In the context of this research, a 10 pm length change uncertainty for a 50 mm sample typically would be considered a precision measurement. However, technically it is not, due to the difference between length uncertainty and length change uncertainty. In order to measure a length change with an uncertainty of 10 pm, the length change must be limited to tens of nanometers, as shown in the following chapters. If the length change uncertainty is 10 pm and the length change is limited to 10 nm, then the fractional uncertainty is only 1×10^{-3}, which is not technically a precision measurement.

However, the goal of this research is to build an instrument to quantify a material stability parameter, which, barring thermal induced expansion, may be on the order of nanometers or picometers for a given material with a specific sample length. Even though a 10 pm length change uncertainty over 10 nm of length change for a 50 mm sample is not technically precise, proving that the material is stable to within nanometers, or even picometers, would be a precise measurement. If the stability uncertainty is 8 nm, for instance, then the fractional uncertainty is 1.6×10^{-7}, which is a precision measurement. Therefore, the instrument to measure length change may not be precise based on the basic definition, but it can be used to examine very precise stability criteria.

1.6 Primary Length Standard

As stated previously, the meter is defined as the length traveled by light in vacuum in $1/c$ seconds. This definition comes directly from the speed of light (299 792 458 m·s^{-1}) [17]. In practice, the meter is realized by a 632.8 nm Helium Neon laser stabilized on the R(127)11-5 hyperfine absorption lines of an $^{127}I_2$ absorption cell [18]. The iodine absorption cell is used with a pressure of 17.4 Pa, which corresponds to a coldfinger temperature of 15°C. There are two typical ways for frequency locking (stabilizing) a laser to an iodine absorption

cell. One method is to use a piezo-driven cavity mirror and the other is to use an electro-optic modulator and phase modulate in a side loop. This will be discussed in more detail in Chapter 5. In either case, the absolute frequency is 473 612 214.705 MHz ± 0.0116 MHz (2σ) with a stability of 5 kHz (1×10^{-11}) when locked to the "i" component with a one second integration time [21]. The laser stabilization fractional frequency uncertainty (1×10^{-11}) is on the limit of the uncertainty required for this research, as will be discussed shortly. The laser is used as the reference for the meter in this research. By maintaining a laser with well-known stability, the measured length can be more accurately determined.

1.7 Established Systems

Before discussing the theory behind optical systems and design considerations for this research, it is necessary to investigate prior research to establish which methods have worked previously and determine their strengths and weaknesses. Generally, stability has not been a property that has been researched exclusively. However, research in the fields of dilatometry (thermal expansion characterization) and high accuracy displacement interferometry apply to stability measurements. The following sections describe several systems that are relevant to this research.

1.7.1 Single Sided Interferometers

Single sided interferometer types have been used for dilatometry experiments in previous research. These interferometers typically measure the sample from one side, making the interferometer compact. Most dilatometry experiments are performed in vacuum and single sided interferometers make it easier to pass beams through a window. Figure 1.7a shows an example of a homodyne interferometer by Bennett [22]. This interferometer has two beamsplitters, a polarizing beam splitter, a quarter wave plate, a mirror, and a retroreflector. The input beam is split into measurement (red) and reference (blue) beams. Two potential

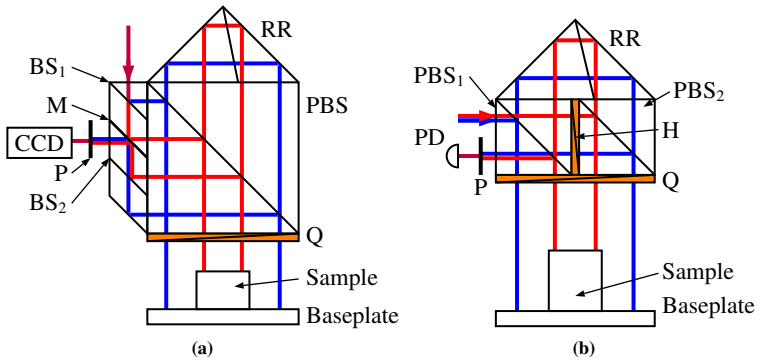

Figure 1.7: *Two single-sided interferometers for dilatometry experiments which measure relative to a reference place. (a) A homodyne interferometer by Bennet [22]. (b) A heterodyne interferometer by Okaji and Imai [23], which was also used by Birch [24].*

measurement signals come from the interferometer, although the top one (shown), which reflects off the mirror, is the more balanced signal. In the more balanced signal, the error

is typically less because the individual interferometer path lengths are largely first order compensated. By measuring the intensity variations of this signal via a photodiode or CCD array, the length change can be determined.

Figure 1.7b shows another single sided interferometer configuration developed by Okaji and Imai [23] and used by Birch [24]. This interferometer uses a heterodyne source with two orthogonally polarized beams (offset in the figure for clarity). The measurement beam (red) has one specific frequency and the reference beam (blue) has a different frequency, with a known offset from the measurement beam frequency. By measuring the relative phase fluctuations between a separate reference signal (not shown) and the measurement signal, the length change can be determined.

These interferometers in Figure 1.7 have several notable features. The retroreflector causes the interferometers to be insensitive to sample tip and tilt. This is an advantage if sample alignment is an issue. However, sample tip and tilt are therefore difficult to measure. These interferometers are compact, meaning they can be easily thermally controlled to limit temperature gradient effects. The beams enter and exit on one side of the complete system, which is why this interferometer is useful as a dilatometry instrument.

The heterodyne system in Figure 1.7b is advantageous because its output signal is easily processed and because it is insensitive to amplitude fluctuations from the laser source. However, the heterodyne source can contribute to frequency mixing, which then makes the signal processing complex and error prone because the phase measurement will have periodic nonlinearity.

The key disadvantage to this type of system is the sample is mounted on a reference plate, meaning the mounting interface is an uncertainty contributor. In a more modern system by Schödel [11], which uses a different one sided configuration with a three color source, one of the largest uncertainty contributors is the sample and reference plate interaction.

1.7.2 Double Sided Interferometers

Wolff and Savedra [25] showed one of the first double sided interferometer types, shown in Figure 1.8. This interferometer was used for vacuum dilatometry experiments where a heater produces radiative heating directed towards the sample. The interferometer measurement then determines the thermal expansion coefficient. This interferometer is actually two interferometers in one. One interferometer (red beams) measures the right side of the sample and reference material, while the other interferometer (blue beams), measures the left side. The two interference signals are measured by the two photodiodes. This interferometer is mostly common path, thus global length changes in the beams are mostly compensated.

However, the interferometer in Figure 1.8 has three aspects that make it unsuitable for stability measurements: non-common sample measurement paths, a reference sample, and multiple passes through a window. While this interferometer is largely common path, it still contains two areas where the reference path and measurement path are different. The non-common path occurs in both the red and blue interferometers where both sample measurement beams reflect off an additional mirror. This path length difference and the additional mirror is a source of instability. Additionally, this interferometer requires a known, perfectly stable reference material. A large assumption of this stability research

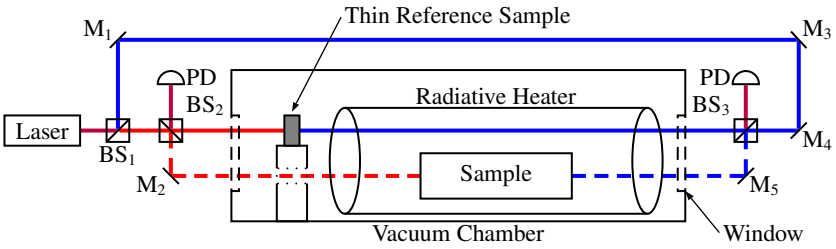

Figure 1.8: *Double sided dilatometer by Wolff and Savedra [25]. A radiative heater is used to change the sample temperature while a reference material is maintained at constant temperature.*

is that there is no known perfectly stable material, this interferometer will not work for this research. Lastly, the vacuum window that the beam passes through has changing birefringence, caused by differential pressure changes. This birefringence in the window causes errors in the measurement, especially because the measurement and reference beams pass through different parts of the window. For this reason, the interferometer design for this research will avoid passing through windows as much as possible.

The double sided interferometer by Suska and Tschirnish [26] uses Fizeau interferometry and two mechanically coupled retroreflectors to measure the sample length change. Figure 1.9 shows a schematic of this interferometer. The input beam reflects from a beamsplitter attached to one retroreflector. Because the incident angle is specifically chosen, only one polarization state reflects from the object. The remaining beam part transmits through the retroreflector. It then passes around the second retroreflector and back to the first where it then exits on the initial beam splitter. Both the reference and measurement signals are then detected using two photodiodes.

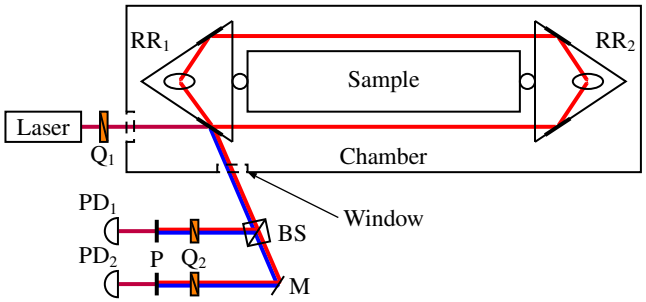

Figure 1.9: *A double sided, 'mechanical' interferometer by Suska and Tschirnish [26]. This interferometer uses two retroreflectors mounted to the sample, where sample length changes cause the retroreflectors to move. This interferometer uses a mechanical coupling to determine length changes in the interferometer.*

This type of interferometer mechanically couples the measurement components to the sample, which is undesirable for stability measurements. Changes in the force between the sample and measurement component will cause Hertzian contact deformation which is difficult to accurately characterize at nanometer levels and below. Additionally, the initial input beam angle must be stable to maintain the Brewster criteria, another source of error in this interferometer.

Kuriyama, *et al.* [10] describe a double sided interferometer for absolute distance, surface

flatness, thermal expansion, and stability measurements. This interferometer, shown in Figure 1.10, uses a triangular shaped layout with three plate beamsplitters producing four beams, and two interferograms, measured by two CCD cameras. The two reference mirrors are driven by PZTs to produce the surface flatness phase maps and absolute distance measurement.

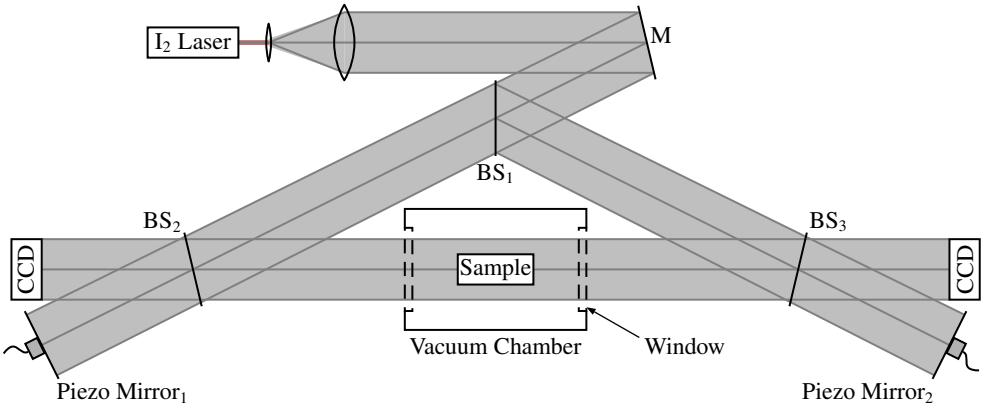

Figure 1.10: *A double sided interferometer by Kuriyama, et al. [10]. Four different paths are measured to create two different interference patterns. Two piezo driven mirrors are used to null the interferometer and determine the absolute length. Additionally, CCD cameras are used which can determine surface deformation of the sample and optics.*

While this configuration is quite complex, it is a balanced system which not only measures the sample but also the interferometer itself. Additionally, it is possible to perform absolute distance measurements, provided the fringe order is known, which means the sample need not be continuously measured. This allows for more sample measurements in the same time period. The main undesirable aspect of this system is the size of the optics, which are susceptible to thermal gradient issues and the power stability of the source because this is a homodyne system. Additionally, this interferometer layout is quite large which is not suitable for certain vacuum applications due to practical implementation limits.

Figure 1.11 show the double sided interferometer by Ren, *et al.* [27], which has a heterodyne, orthogonally polarized source. The input beam passes through a window into a vacuum chamber and reflects off PBS_1. At PBS_1, the coaxial input beam is separated into the reference (red) and measurement (blue) beams, which are also offset by M_1. The reflected reference beam passes through a half wave plate, PBS_2, Q_1, and Q_2, which rotates the polarization state by 90°. After reflecting off M_2, M_3, and M_4, the beam makes a second pass, where the polarization state is rotated a further 90°. When the reference beam comes back to PBS_2, it is transmitted and then reflected from the retroreflector. The beam then makes two more passes in the system, traveling the opposite direction. The reference beam ultimately is transmitted from the PBS_2, where it reflects from M_1 and transmits through PBS_1.

The measurement beam (blue) initially transmits through PBS_1 and reflects off M_1. Then it passes through PBS_1 and Q_1 and reflects off the sample. When the measurement beam then enters PBS_1, it is reflected and travels around to the other side of the sample via M_4,

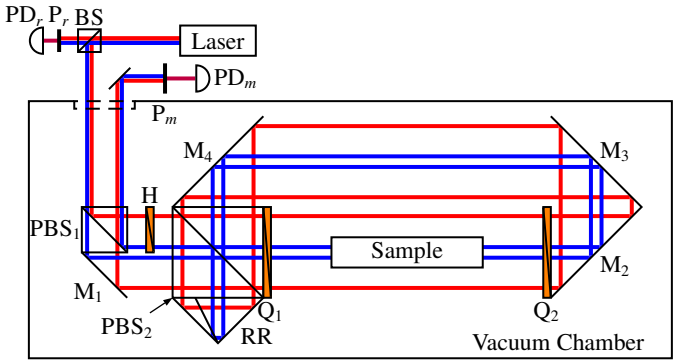

Figure 1.11: *A double pass, double sided interferometer by Ren, et al. [27]. This interferometer has a resolution of λ/4, which is useful for small displacement systems.*

M_3, and M_2 and through Q_2. When the measurement beam reflects off the sample, it passes back around the three mirrors and quarter wave plate, where it transmits through PBS_2 and reflects from the retroreflector. The beam then makes a second trip via the three mirrors and the quarter wave plate to the right side of the sample. After reflecting from the sample and passing back around, it is then reflected by PBS_2 to reflect from the sample's left side a second time. When it travels back to PBS_2, it transmits through, where its polarization state is rotated 90° using the half wave plate and it is the reference beam at PBS_1. The beam then leaves the chamber where it is interfered using a polarizer and is detected.

Since this interferometer was designed for vacuum-based dilatometry applications, it has several advantages. While it is complicated, it is a relatively compact double sided interferometer, which means it can be placed in vacuum. Additionally, the interferometer is designed to be independent of sample length because the mirrors and quarter wave plates can be extended on one side to accommodate larger samples. This interferometer also has high resolution, making it suitable for applications where small displacements (such as drift) are the intended measurements.

While it has advantages, there are also several disadvantages of using this interferometer for drift measurements. The input beam passes through a window, which can rotate the input polarization states due to pressure induced birefringence. Since this beam is an orthogonally polarized, coaxial, two frequency source, this can cause a change in periodic nonlinearity as a function of the pressure induced birefringence because the source frequency mixing will change over time. Since this intended application is just measurement over small ranges a nonlinear signal is difficult to compensate without displacing several fringes over a short time period.

Another disadvantage of this system is the refractive index compensation. This interferometer was designed for a vacuum environment, thus the refractive index is not considered. Because stability measurements are required in air and vacuum, refractive index must be considered and known. One method to measure the refractive index would be to implement a wavelength tracker. But, this is not practical in this interferometer because the reference beams pass by both sides of the sample, meaning a complex vacuum tube is needed.

1.8 Research Topics

All of the interferometers shown in previous research have some disadvantages for stability research. The focus of this research is to design and build an interferometer which mitigates those disadvantages. Several topics must be researched indepth to accomplish this task.

As shown in previous research, double sided interferometers remove a significant uncertainty contributor, the thin film wrung interface with a reference plate [10, 11]. Therefore, this research will focus on designing an instrument capable of measuring a sample from both sides, rather than from a reference plate. A specific aspect to investigate is designing a balanced interferometer which means the reference and measurements arms which interfere to generate the measurement signal nominally pass through the same amount of air and optics. This is particularly important because samples with varying nominal lengths will be measured. Thus, a balanced design for a double sided measurement is needed which is sample length independent.

Materials used in precision systems range from common materials such as aluminum and steel, to exotic materials such as Zerodur, ULE, silicon carbide, and Invar. From previous research, one of the largest measurement errors results from errors in the thermal expansion correction. These errors are due to two sources, knowledge of the thermal expansion and temperature which have their own measurement uncertainties. This uncertainty will add to the overall measurement uncertainty. Additionally, the sample temperature is typically measured using a thermistor attached to the surface. The sample has a finite thermal diffusion rate, which means the surface temperature and core temperature are different due to a time delay. Samples with different sizes and different thermal conductivity will have different diffusion delays. Therefore, a model must be investigated to characterize these effects to better estimate the difference between thermal effects and drift.

Another large uncertainty contributor in interferometry is refractive index of air errors. Using the modified Edlén equation by Birch and Downs, and using typical values of the fluctuations of air temperature, pressure, humidity, and CO_2 concentration, the 2σ fractional uncertainty in the refractive index of air is two parts in 10^8 [28–30]. This uncertainty arises from the empirical data used in the Edlén equation, not from the fluctuations in temperature, pressure, etc. The uncertainty values used in calculating this uncertainty are 0.01 K (temperature), 3.73 Pa (pressure), 1% (relative humidity), and 67 ppm (CO_2 concentration) [31]. Even when these values are known to better than the aforementioned values, the limiting uncertainty is Edlén's equation itself. For 50 mm samples, this is a length change uncertainty of 500 pm. Once again, the instrument in this research must determine stability much smaller than this value, thus, more research is needed for methods that reduce the effect of refractive index uncertainty.

Another consideration for the stability measuring instrument is periodic errors. Periodic errors have been widely reported in literature over the last 15 years. Some of the early work in detecting these errors was performed by Hou and Wilkening [32], and De Freitas and Player [33]. Research has been performed on the sources of periodic errors and measurement techniques [34–42]. These techniques for correcting/removing periodic errors typically require either a constant moving velocity [35, 36, 40] or at least one fringe of motion within a specified measurement period [41]. As stated previously, the dimensional fluctuations from a sample with a relatively high thermal expansion are well below one

fringe of motion in a well controlled environment. Thus, these techniques do not work for stability measurements. These techniques are more intended for motion stages, rather than pure measurement. Therefore, more research is needed on mitigating periodic errors or designing an interferometer without source mixing and periodic errors.

In addition to source mixing, the laser also contributes uncertainty due to wavelength instability. Over short term intervals, commercial sources have wavelength instabilities on the order of parts in 10^9 [43, 44]. Over longer time periods, the instability in these systems can be parts in 10^8 or 10^7, which is not suitable for this research. As with the refractive index, a frequency instability of 10^{-8} contributes 500 pm of length change measurement uncertainty, which higher than the measurement goals of this research. Thus, a source is needed which has a high frequency stability, yet a high enough optical power to be used in practical interferometry applications. For long term measurements, the line shift in the Helium Neon spectrum should be considered, which may decrease long term stability relative to an absolute standard such as an iodine stabilized laser.

1.9 Thesis Focus

This thesis comprises four main sections: the optical layout and characterization; refractive index correction, laser stabilization and heterodyne frequency generation; and periodic error measurement and correction. The following chapters delve into each of these sections plus qualification measurements and improvements for future systems.

Chapter 2 focuses on optical theory and phase measurements. In this chapter, an estimated length change measurement uncertainty is presented based on material properties and system parameters. Chapter 3 introduces and explains periodic errors and their effect on stability measurements and displacement measurements in general. Interferometer designs are presented and experimentally verifiied which mitigate these errors.

Chapter 4 details refractive index measurement and correction techniques. This work includes using a Fabry-Pérot interferometer for refractive index tracking and for wavelength correcting. Additionally, a refractive index tracking technique using heterodyne interferometry is presented. Chapter 5 presents a novel laser stabilization scheme using a mixed mode signal present in a three-mode HeNe laser. This chapter also discusses reference laser design and frequency locking techniques.

Chapter 6 describes the interferometry system for stability measurements, as built through several generations. Preliminary measurements with each generation are presented and recommendations for the next generation system are discussed. Additionally, the overall system design and practical information such as fiber coupling stability and unintended beam leakage is presented. Lastly, Chapter 7 contains a retrospective look at this research, including its shortfalls, potential improvement points, and future measurements.

Chapter 2

Optical Theory

Interferometry involves the interference of two or more electromagnetic waves. The goal of this chapter is to derive the equation of an electromagnetic wave propagating in a medium as a function of time, location, and initial power. Once this equation is known, it can be used to describe light interference which creates a detectable irradiance signal which takes the form of

$$I = A\cos(2\pi f t + \phi) + B, \tag{2.1}$$

where I is the detected irradiance converted (typically to volts), and A, f, ϕ, and B are the amplitude, frequency, phase, and offset of the detected signal, respectively. This derivation will show how the phase change between two interfering optical signals can be used to determine the optical path length change. Once this is shown, an estimated uncertainty budget for the length change is presented assuming an ideal optical system and basic sample properties. Also, a sample thermomechanical model is shown, which is used to determine the short term uncertainty for stability events and prescribes the measurement bandwidth necessary for the detection system. Finally, detection theory and the phase measurement are discussed.

2.1 Wave Equation

2.1.1 Maxwell's Equations

Basic electromagnetic theory states there is a direct relationship between electricity and magnetism. This relationship is shown in the four Maxwell equations, which, in differential form, are

$$\nabla \times \mathbf{E} = -\frac{\partial \mathbf{B}}{\partial t}, \tag{2.2}$$

$$\nabla \times \mathbf{B} = \mu\epsilon\frac{\partial \mathbf{E}}{\partial t}, \tag{2.3}$$

$$\nabla \cdot \mathbf{E} = 0 \quad \text{and} \tag{2.4}$$

$$\nabla \cdot \mathbf{B} = 0. \tag{2.5}$$

where $\mathbf{E}$ and $\mathbf{B}$ are the electric and magnetic field vectors, respectively. Their derivation from first principles is described in detail in Appendix B. These equations will be used to

derive the wave equation of light and then the equations of the interferometric measurement. The complete derivation, include determining the electric field amplitude, was derived from first principles. References used to perform this derivation include work by Born and Wolf [45], Hecht [46], Pedrotti and Pedrotti [47], and Kreyszig [48].

2.1.2 General Form

The second derivatives of Maxwell's Equations are needed to derive the wave equation for an electromagnetic field. To begin, the curl of Equation 2.3 is

$$\nabla \times (\nabla \times \mathbf{B}) = \mu\epsilon \frac{\partial}{\partial t} (\nabla \times \mathbf{E}) . \tag{2.6}$$

If Equation 2.2 is substituted on the right had side and the triple product identity

$$\nabla \times (\nabla \times) = \nabla (\nabla \cdot) - \nabla^2, \tag{2.7}$$

is applied to the left hand side, then

$$\nabla (\nabla \cdot \mathbf{B}) - \nabla^2 \mathbf{B} = -\mu\epsilon \frac{\partial^2 \mathbf{B}}{\partial t^2} \tag{2.8}$$

results. From Equation 2.5, the divergence of a magnetic field is zero, thus

$$\nabla^2 \mathbf{B} = \mu\epsilon \frac{\partial^2 \mathbf{B}}{\partial t^2}, \tag{2.9}$$

where ∇^2 is the Laplacian Operator and is equal to zero. If a similar method is applied to Equation 2.2,

$$\nabla \times (\nabla \times \mathbf{E}) = -\frac{\partial}{\partial t} (\nabla \times \mathbf{B}) , \tag{2.10}$$

then Equation 2.3 can be substituted on the right side and Equation 2.7 can be applied to the left side yielding

$$\nabla^2 \mathbf{E} = \mu\epsilon \frac{\partial^2 \mathbf{E}}{\partial t^2}. \tag{2.11}$$

Equations 2.9 and 2.11 can be expanded out to produce six different scalar wave equations of the form

$$\frac{\partial^2 \psi}{\partial z^2} = \frac{1}{v^2} \frac{\partial^2 \psi}{\partial t^2} \tag{2.12}$$

where ψ is the wave, z is the propagation direction, and v is the wave velocity.

2.1.3 General Solution

Typically in displacement measuring interferometry, a rotated coordinate system is devised such that the propagation direction is chosen to be the Z-direction. The plane orthogonal to the propagation direction is then the X- and Y-directions, with one aligned horizontal and the other vertical. For a electric wave propagating in the Z-direction, it is clear from Equation 2.4 that the gradient in the propagation direction is zero. Therefore, the only

electric fields must be transverse to the propagation direction. Assuming an electric field only in the X-direction, a general solution to Equation 2.12 is

$$\mathbf{E}_x(z,t) = E_x e^{i2\pi f(t-z/v)}\vec{i}, \tag{2.13}$$

where E_x is the electric field amplitude in the X-direction, f is the oscillation frequency, v is the velocity in the propagation direction, and $\vec{i}$ is the unit vector in the X-direction.The second derivatives of Equation 2.13 (in accordance with Equation 2.11) are

$$\frac{\partial^2 \mathbf{E}_x}{\partial t^2} = -(2\pi f E_x)^2 e^{i2\pi f(t-z/v)}\vec{i} \quad \text{and} \tag{2.14}$$

$$\frac{\partial^2 \mathbf{E}_x}{\partial z^2} = -\left(\frac{2\pi f E_x}{v}\right)^2 e^{i2\pi f(t-z/v)}\vec{i}. \tag{2.15}$$

Substituting back into Equation 2.12 yields

$$\left(\frac{2\pi f E_x}{v}\right)^2 e^{i2\pi f(t-z/v)}\vec{i} = \frac{(2\pi f E_x)^2}{v^2} e^{i\pi f(t-z/v)}\vec{i} \tag{2.16}$$

which completes the proof. It should be noted that this proof can also be demonstrated for an electric field aligned in the Y-direction or a combination of electric fields in the X- and Y-directions.

Faraday's Induction Law states that a time-varying magnetic field accompanies any electric field. The magnetic field can be solved for by knowing the electric field direction and the direction of propagation. This can be found by using the $\vec{j}$ part of Equation 2.2

$$-\left(\frac{\partial \mathbf{E}_z}{\partial x} - \frac{\partial \mathbf{E}_x}{\partial z}\right) = -\frac{\partial \mathbf{B}_y}{\partial t}. \tag{2.17}$$

Because $\partial \mathbf{E}_z/\partial x$ is zero, the magnetic field reduces to

$$\mathbf{B}_y = \int \frac{\partial \mathbf{E}_x}{\partial z} dt = \frac{\mathbf{E}_x}{v} e^{i2\pi f(t-z/v)}. \tag{2.18}$$

The electric field and magnetic field magnitudes are proportional to each other based on the speed of propagation

$$vB_y = E_x \tag{2.19}$$

Therefore, a plane (transverse) wave traveling in the Z-direction and with an electric field oriented in the X-direction has a time-varying magnetic field in the Y-direction.

2.1.4 Wave Velocity

From Equations 2.11 and 2.12, the velocity of propagation is

$$v = \frac{1}{\sqrt{\mu\epsilon}} \tag{2.20}$$

where μ and ϵ are the permeability and permittivity of the medium in which the wave travels. Substituting Equations B.10 and B.13 into Equation 2.20, the velocity becomes

$$v = \frac{1}{\sqrt{\mu_r \mu_o \epsilon_r \epsilon_o}}. \tag{2.21}$$

where μ_o is the permeability of free space, μ_r is the relative permeability, ϵ_o is the electric permittivity in a vacuum, and ϵ_r is the dielectric constant or relative electric permittivity to a vacuum.

The refractive index, η, is

$$\eta = \sqrt{\mu_r \epsilon_r} \tag{2.22}$$

and the speed of light in a vacuum is defined as

$$c = \frac{1}{\sqrt{\mu_o \epsilon_o}} = 299\,792\,458 \left[\frac{m}{s}\right]. \tag{2.23}$$

If the wave is not traveling in a vacuum, the speed of the light changes based on the refractive index of the medium. Therefore, the velocity of light propagating in a medium other than vacuum is[1]

$$v = \frac{c}{\eta} = \frac{1}{\sqrt{\mu_r \mu_o \epsilon_r \epsilon_o}}. \tag{2.24}$$

2.1.5 Electric Field Amplitude

The only term in Equation 2.13 that is not yet determined is the amplitude of the electric field. The irradiance must first be defined and will be used in the solution. To determine the irradiance, the rate of energy transfer per unit area transmitted by an electromagnetic wave must be determined. The rate of energy transfer per unit area is

$$S = \frac{P_o}{A}, \tag{2.25}$$

where S is the rate of energy transfer per unit area [$\mathrm{W{\cdot}m^{-2}}$], P_o is the amount of optical power, and A is the cross sectional area of the electromagnetic wave. The energy flowing along a path with velocity, v, has a specified volume of energy, V_u, that will pass through the cross sectional area, A, in a given time interval, Δt. Thus, the energy transferred per unit area is also

$$S = \frac{uv}{V_u}, \tag{2.26}$$

where u is the net energy within the volume. The energy density in an electric field is

$$\frac{u_e}{V_u} = \frac{\epsilon}{2} E_o^2, \tag{2.27}$$

where u_e is the electric field energy and E_o is the magnitude of the electric field. Similarly, the energy density for a magnetic field is

$$\frac{u_m}{V_u} = \frac{B_o^2}{2\mu}, \tag{2.28}$$

where u_m is the magnetic field energy and B_o is the magnitude of the magnetic field. Since the magnitude of the electric field and magnetic field are related by $vB_o = E_o$, Equation 2.28 can be restated as

$$\frac{u_m}{V_u} = \frac{E_o^2}{2v^2\mu}. \tag{2.29}$$

[1] The speed of light and permeability in a vacuum are both *defined* constants and the permittivity is a *derived* constant. Originally, however, both the permeability and the permittivity were determined experimentally and the speed of light was derived from that.

Using Equation 2.20, Equation 2.29 simplifies to

$$\frac{u_m}{V_u} = \frac{\epsilon}{2} E_o^2, \tag{2.30}$$

which is the same as Equation 2.27, thus $u_e = u_m$. The rate of energy transfer per unit area transmitted by an electromagnetic wave is

$$S = \frac{u_{net} v}{V_u} = \frac{(u_e + u_m)\, v}{V_u} = \epsilon v^2 E_o B_o. \tag{2.31}$$

In vector form, the rate of energy transfer per unit area transmitted by an electromagnetic wave is the Poynting vector, **S**, and is in the propagation direction with both the electric field and magnetic field orthogonal to it and mutually orthogonal. The Poynting vector,

$$\mathbf{S} = \epsilon v^2 \mathbf{E} \times \mathbf{B}, \tag{2.32}$$

is used to determine the irradiance of an optical beam. Both **E** and **B** are time varying with the form

$$\mathbf{E}_x\,(z,t) = E_x e^{i2\pi f(t-z/v)} \vec{i} \quad \text{and} \tag{2.33}$$

$$\mathbf{B}_y\,(z,t) = B_y e^{i2\pi f(t-z/v)} \vec{j}, \tag{2.34}$$

which was determined by Equation 2.13 assuming propagation in the Z-direction and the electric and magnetic fields aligned in the X- and Y-directions, respectively. To obtain the real part of these vectors, Euler identities are used. The four Euler identities are

$$\begin{aligned} e^{i\theta} &= \cos\theta + i\sin\theta, \\ e^{-i\theta} &= \cos\theta - i\sin\theta, \\ \cos\theta &= \frac{e^{i\theta} + e^{-i\theta}}{2}, \quad \text{and} \\ \sin\theta &= \frac{e^{i\theta} - e^{-i\theta}}{2i}, \end{aligned}$$

where the first two can be shown to obtain the last two, and vice versa. The real parts of the electric and magnetic fields are needed because only the real part of the electromagnetic wave can be detected. The real parts of the electric and magnetic fields are then

$$\mathrm{Re}\,(\mathbf{E_x}) = \mathbf{E}_x \cos\left(2\pi f\,(t - z/v)\right) \quad \text{and} \tag{2.35}$$

$$\mathrm{Re}\left(\mathbf{B_y}\right) = \mathbf{B}_y \cos\left(2\pi f\,(t - z/v)\right). \tag{2.36}$$

The magnitude of the Poynting vector is

$$|\mathbf{S}| = \epsilon v^2\, |\mathbf{E}_x| \left|\mathbf{B}_y\right| \cos^2\left(2\pi f\,(t - z/v)\right) \sin(\gamma)\,. \tag{2.37}$$

The Poynting vector is the time-varying energy transfer for a given beam diameter at extremely high frequencies ($>10^{14}$ Hz), of which there are no detectors fast enough to measure. Therefore, any detector measures a time average of the magnitude of the Poynting over a certain time period T. The definition of a time average (denoted by the $\langle \cdots \rangle$ brackets) is

$$\left\langle f\,(t) \right\rangle \equiv \frac{1}{T} \int_{t-T/2}^{t+T/2} f\,(t)\, dt. \tag{2.38}$$

Applying this to the Poynting vector magnitude from Equation 2.37 yields the irradiance, I, and is

$$I \equiv \langle |\mathbf{S}| \rangle_T = \epsilon v^2 \left|\mathbf{E}_x\right| \left|\mathbf{B}_y\right| \left\langle \cos^2\left(2\pi f\left(t - z/v\right)\right)\right\rangle_T \sin\left(\gamma\right), \tag{2.39}$$

where γ is the angle between the electric and magnetic field and is always $\pi/2$. When Equation 2.18 is substituted into Equation 2.39, it simplifies to

$$I = \epsilon v \left|\mathbf{E}_x\right|^2 \left\langle \cos^2\left(2\pi f\left(t - z/v\right)\right)\right\rangle. \tag{2.40}$$

Using the definition of a time average from Equation 2.38, it can be shown that

$$\left\langle \cos^2\left(t\right)\right\rangle_T = \frac{1 + \operatorname{sinc}\left(T\right)\cos\left(2t\right)}{2}, \tag{2.41}$$

where $\operatorname{sinc}\left(T\right)$ is $\left(\sin T\right)/T$. As the time average period T tends toward large values (including sampling frequencies on the order of 100 MHz)[2], the *sinc* term tends toward zero. Therefore, the irradiance can be reduced to

$$I = \epsilon v \left\langle \left|\mathbf{E}_o\right|^2 \right\rangle = \frac{\epsilon v}{2} \left|\mathbf{E}_o\right|^2. \tag{2.42}$$

Using Equations 2.25, 2.39, and 2.42 the magnitude of the electric field, E_o, is

$$E_o = \sqrt{\frac{2P_o}{\epsilon v A}}, \tag{2.43}$$

where the electromagnetic wave is generated from a source with a known power output, P_o, and a known cross sectional area, A. If this value is substituted back into the assumed solution from Equation 2.13 and the speed of light is substituted for the wave velocity from Equation 2.24, then the equation for the electric field for a wave propagating in the Z-direction is

$$\mathbf{E} = \sqrt{\frac{2P_o\eta}{\epsilon_r \epsilon_o c A}}\, e^{i2\pi f(t+\eta z/c)} \left(\mathbf{i}\vec{i} + \mathbf{j}\vec{j}\right), \tag{2.44}$$

with optical power P_o, beam area A, relative and absolute permittivities ϵ_r and ϵ_o, refractive index η, speed of light c, electromagnetic frequency of oscillation f, and magnitude vectors $\mathbf{i}$ and $\mathbf{j}$ for the $\vec{i}$ and $\vec{j}$ components. This equation includes the accompanying magnetic field component and for the remainder of this work, the electromagnetic wave will be considered just based on this electric field equation.

2.2 Two Beam Interference

Now that the equation for an electric field propagating in a specific direction has been properly defined (Equation 2.44), the next step is to see how these waves can be used to perform displacement measurements. Displacement interferometers typically use the principle of interference to infer a displacement value from a change in phase of a measured irradiance. Interference occurs when two waves which meet at the same place and time and have electric fields whose polarizations are aligned non-orthogonally. The net electric field at the interference point is the sum of the electric fields of the electromagnetic waves.

[2]This implies ultra-fast detectors in the gigahertz regime must account for the *sinc* term

The non-orthogonality of the electric field polarization states is a requirement as the two waves will not interfere if their electric field polarization states are not aligned orthogonally (proved shortly).

First, we will assume a typical situation where there is interference between two waves, one denoted 'r' for reference wave and the other, 'm' for measurement wave. The electric fields for the measurement and reference beams are, respectively,

$$\mathbf{E}_m = \sqrt{\frac{2P_m\eta_m}{\epsilon_{r,m}\epsilon_o cA}}\, e^{i2\pi f_m(t+\eta_m z_m/c)}\left(\mathbf{i}_m\vec{i} + \mathbf{j}_m\vec{j}\right) \quad \text{and} \tag{2.45}$$

$$\mathbf{E}_r = \sqrt{\frac{2P_r\eta_r}{\epsilon_{r,r}\epsilon_o cA}}\, e^{i2\pi f_r(t+\eta_r z_r/c)}\left(\mathbf{i}_r\vec{i} + \mathbf{j}_r\vec{j}\right), \tag{2.46}$$

and the net electric field is

$$\mathbf{E}_{net} = \mathbf{E}_m + \mathbf{E}_r. \tag{2.47}$$

The total irradiance at the detector is

$$I = \frac{\epsilon c}{\eta}\left\langle |\mathbf{E}_{net}|^2 \right\rangle. \tag{2.48}$$

The square of the magnitude of $\mathbf{E}_{net}$ is the dot product. Thus, substituting the net electric field and expanding yields

$$I = \frac{\epsilon c}{\eta}\left\langle |\mathbf{E}_m + \mathbf{E}_r|^2 \right\rangle = \frac{\epsilon c}{\eta}\left\langle (\mathbf{E}_m + \mathbf{E}_r)\cdot(\mathbf{E}_m + \mathbf{E}_r)\right\rangle, \tag{2.49}$$

which is the same as

$$I = \frac{\epsilon c}{\eta}\left\langle |\mathbf{E}_m|^2 + |\mathbf{E}_r|^2 + 2\mathbf{E}_m\cdot\mathbf{E}_r \right\rangle. \tag{2.50}$$

The $|\mathbf{E}_m|^2$ and $|\mathbf{E}_r|^2$ terms are usually called the DC offset terms and the $2\mathbf{E}_m\cdot\mathbf{E}_r$ term is called the interference term. To simplify the mathematics, the substitutions

$$\omega_m = 2\pi f_m, \tag{2.51}$$

$$\omega_r = 2\pi f_r, \tag{2.52}$$

$$\phi_m = \frac{2\pi f_m \eta_m z_m}{c}, \quad \text{and} \tag{2.53}$$

$$\phi_r = \frac{2\pi f_r \eta_m z_r}{c}, \tag{2.54}$$

are used and then replaced at the end for the complete definition. In Equations 2.52–2.54, ω is the angular frequency, f is the frequency, ϕ is the phase, η is the refractive index through the traveling medium, z is the path length, and c is the speed of light. The subscripts m and r denote measurement and reference waves, respectively. At this point, only the interfering term will be considered by taking the real components and expanding out the dot product resulting in

$$\mathbf{E}_m\cdot\mathbf{E}_r = |\mathbf{E}_m|\cos(\omega_m t + \phi_m)\cdot|\mathbf{E}_r|\cos(\omega_r t + \phi_r). \tag{2.55}$$

This simplifies to

$$\mathbf{E}_m\cdot\mathbf{E}_r = E_m E_r \cos(\omega_m t + \phi_m)\cos(\omega_r t + \phi_r)\cos\alpha, \tag{2.56}$$

where E_m and E_r are the electric field magnitudes and α is the polarization angle between the two interfering waves. If α is zero, then the two waves interfere. However, if α is $\pi/2$, then no interference occurs, although a DC level power is detected. This proves that two waves with orthogonal electric fields do not interfere.

By making use of the trigonometric identity

$$2\cos A\cos B = \cos(A+B) + \cos(A-B), \tag{2.57}$$

it is clear that the resulting interference term will be a cosine wave with two distinct Fourier components, one being the sum and the other, the difference. Since an optical frequency is too fast to detect, then twice an optical frequency will also be too fast to detect. Therefore, only the difference between the two frequencies (also called the beat frequency) is considered. This simplifies the interference term from Equation 2.50 to[3]

$$\langle \mathbf{E}_m \cdot \mathbf{E}_r \rangle = E_m E_r \Big\langle \cos\Big((\omega_m - \omega_r)\, t - (\phi_r - \phi_m) \Big) \Big\rangle. \tag{2.58}$$

The time average of a cosine (or sine) is simply a cosine (or sine), therefore, the time dependence can be removed, resulting in

$$\langle \mathbf{E}_m \cdot \mathbf{E}_r \rangle = E_m E_r \cos\Big((\omega_m - \omega_r)\, t - (\phi_r - \phi_m) \Big). \tag{2.59}$$

If the assumption is made that the electric fields are aligned coincidentally, then the dot product is simply the multiplication of the two electric fields. When the nominal electric field amplitudes from Equations 2.45 and 2.46 are substituted into the interference term, then the resulting interference amplitude is

$$E_m E_r = \sqrt{\frac{2P_m\eta_m}{\epsilon_{r,m}\epsilon_o cA}}\sqrt{\frac{2P_r\eta_r}{\epsilon_{r,r}\epsilon_o cA}}. \tag{2.60}$$

Now, returning to Equation 2.50, there are still the two DC terms to consider. Using the substitutions from Equations 2.45, 2.46, and 2.52 through 2.54, they can be rewritten as

$$I_m = \left\langle |\mathbf{E}_m|^2 \right\rangle = \frac{2P_m\eta_m}{\epsilon_{r,m}\epsilon_o cA} \left\langle \cos^2(\omega_m t + \phi_m) \right\rangle \quad \text{and} \tag{2.61}$$

$$I_r = \left\langle |\mathbf{E}_r|^2 \right\rangle = \frac{2P_r\eta_r}{\epsilon_{r,r}\epsilon_o cA} \left\langle \cos^2(\omega_r t + \phi_r) \right\rangle. \tag{2.62}$$

The time averaged cosine squared terms in Equations 2.61 and 2.62 average out to 1/2, thus the measurement and reference irradiances I_m and I_r can be simplified to

$$I_m = \frac{P_m\eta_m}{\epsilon_{r,m}\epsilon_o cA} \quad \text{and} \tag{2.63}$$

$$I_r = \frac{P_r\eta_r}{\epsilon_{r,r}\epsilon_o cA}. \tag{2.64}$$

[3] Although there is an amplitude dependence in the trigonometric identity, it is ignored for two reasons in this derivation. The first reason shows up when the answer is checked using an ideal case. The added 1/2 multiplier causes a difference between the derived and checked answers. The second reason is the amplitude effect cannot be known because the direct electromagnetic wave cannot be measured. Thus, it may be present but is something that cannot yet be detected and verified.

Equations 2.63 and 2.64 can be used to simplify Equation 2.50 and thus, the interference term (Equation 2.59) reduces to

$$\langle \mathbf{E}_m \cdot \mathbf{E}_r \rangle = \sqrt{I_m I_r} \cos\Big((\omega_m - \omega_r)\, t - (\phi_r - \phi_m) \Big). \tag{2.65}$$

Equations 2.61, 2.62, and 2.65 can be substituted back into 2.50 to yield the standard equation for two beam interference

$$I = I_m + I_r + 2\sqrt{I_m I_r} \cos\Big((\omega_m - \omega_r)\, t - (\phi_r - \phi_m) \Big). \tag{2.66}$$

The equation for two beam interference has the same form as the generic form proposed at the beginning of the chapter in Equation 2.1. If two electromagnetic waves are superimposed and not orthogonally aligned, then the irradiance detected takes the form of Equation 2.1 which is more accurately described by Equation 2.66. If $I_m = I_r$, and there is complete (ideal) interference, then the measured irradiance will be a time varying signal of frequency $f_m - f_r$ with a normalized amplitude ranging from zero to one, as shown in Figure 2.1. If the two waves have some angular difference but are not orthogonal, then the angle α in the cosine term from Equation 2.56 must be considered. Figure 2.1 also shows three other normalized examples where the angle in not zero.

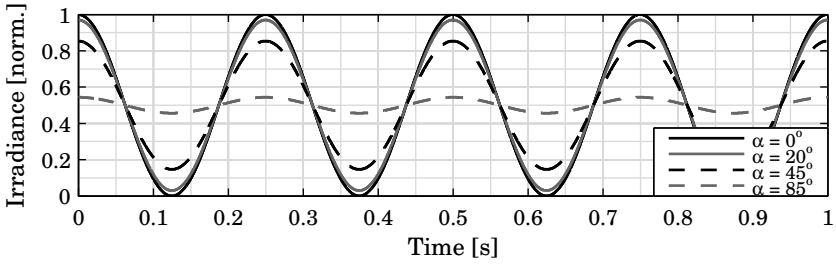

Figure 2.1: *Schematic of an irradiance signal for four difference rotational orientations (polarization angle). When the two electric fields are interfered with the same angular orientation (polarization, α=0°), there is perfect fringe contrast. When the angular orientation is far apart (near orthogonally polarized, α=85°), the fringe contrast is low.*

This combination of AC signal amplitude and offset is used to determine the fringe contrast in the interferometer. The fringe contrast, f_c, is

$$\mathrm{f}_c = \frac{\max(I) - \min(I)}{\max(I) + \min(I)}, \tag{2.67}$$

where the minimum and maximum values are determined from a finite dataset. The fringe contrast ranges from zero to one, with zero being no interference and one being perfect interference. For the examples in Figure 2.67, the values for the misaligned examples are: 0.97 for 20°, 0.83 for 45°, and 0.16 for 85°. This value is mainly used for aligning an optical system and for enhancing the analog to digital conversion going into a data acquisition system, improving signal to noise.

2.3 Phase Measurement

The term $(\phi_r - \phi_m)$ from Equation 2.66 is generally referred to as the time varying phase term. The measured change of this term describes the length change in a displacement measuring interferometer. Accurate measurement of the phase term is the major theme of this research. Before describing a typical phase measurement system, a standard Michelson interferometer will be described to point out several key aspects in interferometry design. Also, this interferometer will be used in subsequent sections where the length change uncertainty is discussed.

2.3.1 Michelson Interferometer

A standard Michelson interferometer configuration is shown in Figure 2.2. The typical laser source for this interferometer is a two frequency heterodyne source with a nominal, constant frequency difference between the two absolute frequencies. This frequency difference is referred to as the split frequency, f_s. The two frequencies, f_1 and f_2, from the source are coaxial and aligned to orthogonal polarzation directions and do not interfere.

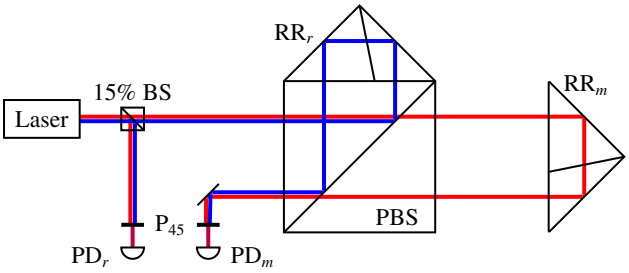

Figure 2.2: *Schematic of a typical retroreflector based heterodyne Michelson interferometer. The detector PD$_r$ measures the reference signal while the detector PD$_m$ measures the difference between the optical path lengths traveling to the reference and measurement retroreflectors.*

A portion of the beam from the laser source is typically split using a partial beamsplitter. The two orthogonal beams are then interfered using a polarizer aligned to 45° and then the reference interference signal is detected using PD$_r$. The remaining main beam traverses to a polarizing beamsplitter where the beams are split via polarization and, in this case, frequency. One beam reflects off a reference retroreflector, typically fixed to the polarizing beamsplitter. The other beam reflects off a measurement retroreflector, fixed to the moving stage or platform. Both beams are then recombined in the polarizing beamsplitter and then interfered using another polarizer, also aligned to 45°. The measured interference signal is also detected using PD$_m$.

There are several key design criteria for this interferometer which will be used in the design of a material stability measuring interferometer. This design is nominally balanced which means the optical path length through the measurement and reference arms is nominally equal. In this case, the path length in the polarizing beamsplitter and in both retroreflectors match, thus, the first order effects from thermal expansion, for instance, are canceled. However, this configuration is susceptible to thermal gradients which will cause

a relative length change due to thermal expansion within the optics which will show up as a false length change. To combat this, interferometer optics are often made of low thermal expansion glass like Fused Silica.

Another key design is the moving target is not sensitive to tip and tilt alignment effects. This is critical for things like moving stages. However, in this research, non-parallelism of the sample is a parameter that should be measured. Thus a stability measuring interferometer should be able to detect this type of dimensional change along with nominal displacements.

The last important aspect to point out is the generation of an optical reference signal for measuring the phase. This is important because change in the split frequency f_s will show up on PD_r and PD_m which will be removed when the relative phase is measured. If this was not the case, then any instability in the split frequency would show up as a false length change.

2.3.2 Signal Attributes

In the interferometer shown in Figure 2.2, the measurement (subscript m) and reference (subscript r) interference signals detected take the form of

$$I_r = A_r \cos(2\pi f_s t + \phi_o) + B_r \quad \text{and} \tag{2.68}$$

$$I_m = A_m \cos\left(2\pi f_s t + \phi_o + \left(\frac{2\pi N \eta \Delta z f}{c}\right)\right) + B_m, \tag{2.69}$$

where I is the measured irradiance, A is the amplitude of the irradiance, B is the offset, f_s is the nominal split frequency of the laser source, ϕ_o is the nominal phase of the laser source, N is the interferometer resolution (two for this configuration), η is the refractive index along the optical path difference, f is the nominal frequency of the laser, c is the speed of light, and Δz is the difference in optical path lengths between the measurement and reference arms.

The offsets B_r and B_m can be removed by a high pass filter and the amplitudes A_r and A_m can be scaled using amplifiers and assuming the nominal optical power for the source and alignment remains the same. Also, the nominal phase of the laser source, ϕ_o, can be canceled because both interference signals are generated from the same laser source and, in most cases, the path length between the reference and measurement is small enough to ignore time of flight issues. Thus, the interference signals can be simplified to

$$I_r \propto \cos(2\pi f_s t) \quad \text{and} \tag{2.70}$$

$$I_m \propto \cos\left(2\pi f_s t + \left(\frac{2\pi N \eta \Delta z f}{c}\right)\right). \tag{2.71}$$

The motion of the moving retroreflector in Figure 2.2 induces a frequency shift known as the Doppler shift, depicted in Figure 2.3. To mitigate measurement errors due to the Doppler effect, the split frequency of the laser source must be chosen with care. The split frequency must be chosen based on the characteristics of the data acquisition system (described shortly) and the dynamics of the system. The split frequency should always satisfy [49]

$$f_s > \frac{|v_m| N \eta f}{c}, \tag{2.72}$$

where $|v_m|$ is the magnitude of the maximum moving stage velocity. This ensures the frequency measured by PD_m never passes through zero, which will cause a directional error.

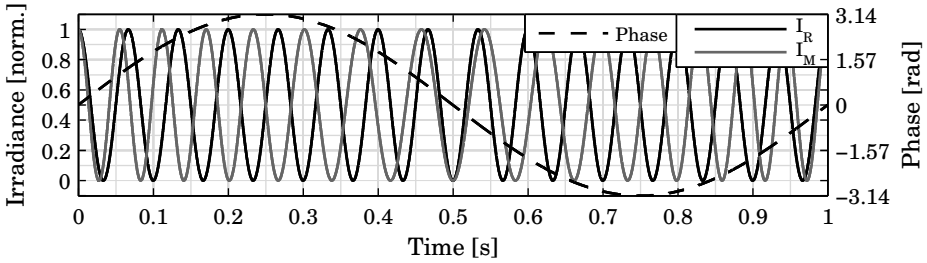

Figure 2.3: *Simulation of a Doppler shift between a reference signal (black) and a measurement signal (red) from a moving stage. The phase difference (blue) ranges between -π and π. The dynamic range of the frequency shift should be considered when choosing a bandpass filter and a split frequency.*

The Doppler effect is also used as a guideline to bandpass filtering. For instance, a 632.8 nm HeNe interferometer with an N of 2 measuring a maximum velocity of 1 mm·s^{-1} experiences a frequency shift of approximately ±3.2 MHz. Thus, the split frequency should be at least 3.2 MHz, to prevent the negative Doppler shifting signal from passing through zero. In this case, assuming a laser source with a split frequency of 10 MHz is used, the frequency range that will be detected is between 6.8 MHz and 13.2 MHz. Thus, a bandpass filter should be selected which has a flat gain and minimal phase lag between 6.8 MHz and 13.2 MHz, which will remove the offsets (B_r and B_m), provide anti-aliasing, and help prevent unwanted harmonics in the measurement band.

2.3.3 Lock-In Detection

The bandpass filtering described in the previous section is typically applied on the input to a lock-in amplifier [50] which is used to measure the phase difference between the reference interference signal and the measurement interference signal. Figure 2.4 shows a schematic of a typical lock-in amplifier used to measure the phase between two signals.

Both the measurement (M) and reference (R) signals are bandpass filtered to remove their nominal offset, eliminate the sensitivity to optical power fluctuations, and provide anti-aliasing filtering. The reference signal is then sent to a phase locked loop. In most digitial systems, the phase locked loop consists of a phase detector, filter, and a voltage controlled oscillator [51]. In most digital systems, the voltage controlled oscillator has a nominal phase offset option. Thus, the output from the filter in the phase locked loop is sent to two voltage controlled oscillators with a 90° phase difference between them, generating a sine and a cosine signal phase locked to the input signal.

The two outputs from the phase locked loop, R_c and R_s are then sent to two multipliers along with the measurement signal to generate two signals, the In-Phase (I) and Quadrature

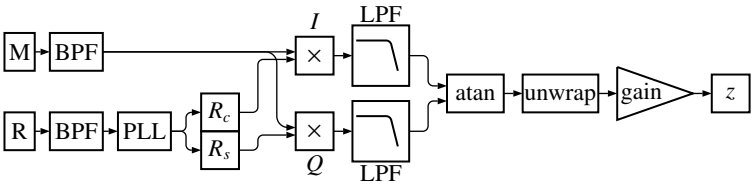

Figure 2.4: *Schematic of a lock-in amplifier for phase measurements. Two signals are detected and initially filtered. The reference signal, R, is sent to a phase-locked loop to generate matched sine and cosine signals. Those are then multiplied with the filtered measurement signal, M, to produce in-phase (I) and quadrature (Q) outputs. Those are then low-pass filtered and sent to an arctangent function. The phase is then unwrapped and a gain is applied to determine displacement from unwrapped phase.*

(Q) signals. The In-Phase and Quadrature signals are

$$I = R_c M = \cos(2\pi f_s t)\cos(2\pi f_s t + \phi_z) \quad \text{and} \tag{2.73}$$

$$Q = R_s M = \cos(2\pi f_s t + \pi/2)\cos(2\pi f_s t + \phi_z)\,, \tag{2.74}$$

where ϕ_z is the phase change as a function of displacement. Applying Equation 2.57 yields

$$I = \frac{1}{2}\cos(4\pi f_s t + \phi_z) + \frac{1}{2}\cos(\phi_z) \quad \text{and} \tag{2.75}$$

$$Q = \frac{1}{2}\cos(4\pi f_s t + \pi/2 + \phi_z) + \frac{1}{2}\cos(\pi/2 + \phi_z)\,. \tag{2.76}$$

If a low pass filter is used after both multipliers to provide sufficient attenuation to the signal at a frequency of $2f_s$, then the remaining signals are

$$I = \frac{1}{2}\cos(\phi_z) \quad \text{and} \tag{2.77}$$

$$Q = \frac{1}{2}\cos(\pi/2 + \phi_z) = \frac{1}{2}\sin(\phi_z)\,. \tag{2.78}$$

The phase is then determined by

$$\phi_z = \arctan\left(\frac{Q}{I}\right), \tag{2.79}$$

and ensuring the sign of the input values is taken into consideration to place the angle in the proper quadrant. The last step needed is an unwrapping function which properly adds or subtracts 2π across successive 2π phase jumps. The phase can then be scaled to the displacement value by knowing the refractive index, interferometer constant and the nominal laser frequency.

There are several other methods for measuring the phase in an interferometer signal, including other techniques called time interval analysis. Work by Oka, *et al.* [52], Oldham, *et al.* [53], Demarest [49], Holmes [54], Pollack [55], and Shaddock, *et al.* [56] have all demonstrated phasemeters with various capabilities.

2.4 Uncertainty Estimates

For heterodyne displacement systems, the measurement signal is always measured with respect to a reference signal in the interferometer. In the full process, displacement

is inferred from phase changes which are derived from relative deviations between two time-varying irradiance signals. The two time-varying irradiance signals are converted to electrical signals using photodiodes and then the electrical signals are processed to determine a phase change, which is then used to determine displacement.

Thus, there are two major sources of uncertainty in displacement interferometry systems. The first is determining whether the interferometer detects only the desired displacement changes and all other changes in the system are otherwise compensated. The second uncertainty source is from the phase measurement and determining whether it converts only the desired phase shift into a measurement signal. There is a subtle, yet important difference between these two uncertainty sources. The former pertains to the interferometer design and direct compensation or cancellation by balancing the system whereas the latter deals more with the laser system employed, measurement environment, phase-to-displacement conversion, and sample properties.

In subsequent sections, the phase measurement uncertainty will be derived for a generic sample with unspecified measurement environment conditions. This derivation assumes the interferometer contributes no measurement uncertainty, the ideal case. Additionally, the derivation assumes the interferometer is designed to eliminate periodic errors, which cause additional measurement uncertainty at the nanometer and sub-nanometer levels. This inherently establishes two design criteria for the interferometer: having a completely balanced system and eliminating any chance for periodic errors. These particular design points are discussed in later chapters.

After describing the phase uncertainty derivation, practical values are assumed to establish a baseline measurement limit. Additionally, each source is examined to either push the uncertainty contribution to 1 pm or lower, or the best possible measurement will be inserted for the sake of comparison. Finally, a table of best-case measurement uncertainty values for several materials used in typical precision engineering systems is presented.

2.4.1 Phase Uncertainty Derivation

As shown in Equations 2.70 and 2.71, the phase difference between two interfering signals contains the optical path length difference. Thus, the optical path difference in an interferometer, z, can be defined as the difference between the total reference path length, z_r, minus the total measurement path length, z_m. If the optical path difference is only the sample which is being measured, the measured phase from the interference signal is

$$\phi = \frac{2\pi N z \eta f}{c}, \tag{2.80}$$

where N is the interferometer constant, η is the refractive index, f is the laser frequency, and c is the speed of light [299 792 458 m·s^{-1}]. Since this research is concerned with displacement interferometry (not distance), the absolute phase of the measurement is unknown. Only deviations from the starting phase value can be determined. Therefore, only length changes are determined, not absolute length. The time derivative of the phase is needed to determine the measured length change. The variables z, f, and η can all change as functions of time, thus the time derivative of phase is

$$\frac{d\phi}{dt} = \frac{2\pi N}{c}\left(\eta f \frac{dz}{dt} + z\eta \frac{df}{dt} + zf\frac{d\eta}{dt}\right). \tag{2.81}$$

For discrete, constant time intervals, the dt variable can be set equal to one and the differentiated terms can be swapped with discrete differences from two consecutive time intervals. After this substitution and some rearranging, the length change, Δz, is

$$\Delta z = \frac{c\Delta\phi}{2\pi N\eta f} - \frac{z\Delta f}{f} - \frac{z\Delta\eta}{\eta}. \tag{2.82}$$

This shows that when length change is measured from phase changes, the nominal frequency and refractive index as well as changes in frequency and refractive index result in length changes. By knowing the nominal frequency, nominal refractive index, frequency changes, refractive index changes, and the phase resolution, the minimum measurable length change can be determined. Since this derivation assumes the phase change is caused by a sample length change, there are two different types of length changes, correctable and uncorrectable. The total length change is then

$$\Delta z = \Delta z_c + \Delta z_u, \tag{2.83}$$

where Δz_c are the correctable length changes and Δz_u are the uncorrectable length changes (drift, the desired measurement). The correctable length changes are dominated by thermal and pressure effects,

$$\Delta z_c = \alpha z\Delta T - \frac{z\Delta P}{K} \tag{2.84}$$

where α is the material's thermal expansion coefficient, z is the nominal sample length, ΔT is the temperature change, ΔP is the pressure change, and K is the material's bulk modulus. Length change due to pressure change is a volumetric effect, thus the bulk modulus is used. The bulk modulus is related to the elastic modulus by

$$K = \frac{E}{3\,(1-2\nu)}, \tag{2.85}$$

where E is the elastic modulus and ν is Poisson's ratio for the material. When Equations 2.83, 2.84, and 2.85 are substituted into Equation 2.82, the uncorrectable length change is

$$\Delta z_u = \frac{c\Delta\phi}{2\pi N\eta f} - \frac{z\Delta f}{f} - \frac{z\Delta\eta}{\eta} - \alpha z\Delta T + \frac{3z\,(1-2\nu)\,\Delta P}{E}. \tag{2.86}$$

Equation 2.86 is the measured length change from phase after correcting for known first order environmental effects on the sample. When the assumption is made that the uncertainty sources are uncorrelated [19], the first order uncertainty expansion, $U_Y^2 = \sum_{i=1}^{n}\left(\frac{\partial Y}{\partial y_i}\right)^2 U_{y_i}^2$, is used to determine the measured length change uncertainty where U_Y is the uncertainty, Y is the function for which the uncertainty is desired, y_i are the uncertainty parameters in the function, and U_{y_i} is the uncertainty of each specific parameter. The phase uncertainty sources are assumed to be uncorrelated because the expected temperature and pressure fluctuations are minimal. Thus, effects like a temperature dependence on the material thermal expansion coefficient are not applicable in this instance. Applying the first

order uncertainty expansion to Equation 2.86, the expanded length change uncertainty is

$$\begin{aligned} U_{\Delta z}^2 = \quad & \left(\frac{-\Delta\eta}{\eta} - \frac{\Delta f}{f} - \alpha\Delta T + \frac{3\,(1-2\nu)\,\Delta P}{E}\right)^2 U_z^2 + \left(\frac{-z}{f}\right)^2 U_{\Delta f}^2 + \\ & \left(\frac{-z}{\eta}\right)^2 U_{\Delta\eta}^2 + \left(\frac{z\Delta\eta}{\eta^2} - \frac{c\Delta\phi}{2\pi N\eta^2 f}\right)^2 U_\eta^2 + \left(\frac{z\Delta f}{f^2} - \frac{c\Delta\phi}{2\pi N\eta f^2}\right)^2 U_f^2 + \\ & \left(\frac{c}{2\pi N\eta f}\right)^2 U_{\Delta\phi}^2 + (-z\Delta T)^2\, U_\alpha^2 + (-\alpha z)^2\, U_{\Delta T}^2 + \left(\frac{-6z\Delta P}{E}\right)^2 U_\nu^2 + \\ & \left(\frac{-3z\,(1-2\nu)\,\Delta P}{E^2}\right)^2 U_E^2 + \left(\frac{3z\,(1-2\nu)}{E}\right)^2 U_{\Delta P}^2. \end{aligned} \tag{2.87}$$

The following section illustrates the length change uncertainty from Equation 2.87 for a normal material under normal measurement conditions using an aluminum sample. Table 2.1 summarizes the nominal parameters and their associated uncertainties. The fractional uncertainty (1σ) is defined as a fractional value of the nominal value. The absolute uncertainty refers to a uncertainty value (1σ) irrespective of the nominal value unless otherwise indicated.

Equation 2.87 can be broken down into eleven separate equations where each uncertainty contributor can be analyzed individually. The uncertainties resulting from each individual components are

$$U_{\Delta z}\,(U_z) = \left(\tfrac{-\Delta\eta}{\eta} - \tfrac{\Delta f}{f} - \alpha\Delta T + \tfrac{3(1-2\nu)\Delta P}{E}\right) U_z \quad \cong 0 \text{ pm} \tag{2.88}$$

$$U_{\Delta z}\left(U_{\Delta f}\right) = \left(\tfrac{-z}{f}\right) U_{\Delta f} \quad \cong 500 \text{ pm} \tag{2.89}$$

$$U_{\Delta z}\left(U_{\Delta\eta}\right) = \left(\tfrac{-z}{\eta}\right) U_{\Delta\eta} \quad \cong 500 \text{ pm} \tag{2.90}$$

$$U_{\Delta z}\left(U_\eta\right) = \left(\tfrac{z\Delta\eta}{\eta^2} - \tfrac{c\Delta\phi}{2\pi N\eta^2 f}\right) U_\eta \quad \cong 0 \text{ pm} \tag{2.91}$$

$$U_{\Delta z}\left(U_f\right) = \left(\tfrac{z\Delta f}{f^2} - \tfrac{c\Delta\phi}{2\pi N\eta f^2}\right) U_f \quad \cong 0 \text{ pm} \tag{2.92}$$

$$U_{\Delta z}\left(U_{\Delta\phi}\right) = \left(\tfrac{c}{2\pi N\eta f}\right) U_{\Delta\phi} \quad \cong 0.2 \text{ pm} \tag{2.93}$$

$$U_{\Delta z}\,(U_\alpha) = (-z\Delta T)\, U_\alpha \quad \cong 57.5 \text{ pm} \tag{2.94}$$

$$U_{\Delta z}\,(U_{\Delta T}) = (-\alpha z)\, U_{\Delta T} \quad \cong 575 \text{ pm} \tag{2.95}$$

$$U_{\Delta z}\,(U_\nu) = \left(\tfrac{-6z\Delta P}{E}\right) U_\nu \quad \cong 0 \text{ pm} \tag{2.96}$$

$$U_{\Delta z}\,(U_E) = \left(\tfrac{3z(1-2\nu)\Delta P}{E^2}\right) U_E \quad \cong 0.1 \text{ pm} \tag{2.97}$$

$$U_{\Delta z}\,(U_{\Delta P}) = \left(\tfrac{3z(1-2\nu)}{E}\right) U_{\Delta P} \quad \cong 1.7 \text{ pm} \tag{2.98}$$

The syntax for Equations 2.88–2.98 is the uncertainty contribution to length change, $U_{\Delta z}$, due to the uncertainty in each component, U_i. The estimated uncertainties in Equations 2.88–2.98 are the absolute values.

As shown, the uncertainties due to frequency change, refractive index change, thermal expansion coefficient, temperature change, and, to a lesser extent, pressure change are all above the desired limit. To reach a 1 pm threshold, all of these uncertainties must be reduced. For instance, both the frequency change and refractive index change uncertainties must be better than 2 parts in 10^{11}. Additionally, the thermal expansion coefficient

Table 2.1: *Parameters for the uncertainty of an aluminum sample length change.*

Parameter	Nominal Value	Fractional Uncertainty	Absolute Uncertainty
Speed of light (c)	299792458 m·s^{-1}	-	-
Constant (N)	2	-	-
Phase Change ($\Delta\phi$)	3.5 µrad	-	3.5 µrad
Refractive Index (η)	1.00029	1×10^{-8}	-
RI Change ($\Delta\eta$)	1×10^{-8}	1×10^{-8}	-
Frequency (f)	473.7555 THz	1×10^{-8}	-
Frequency Change (Δf)	200 Hz	-	200+U_f Hz
Nominal Length (z)	50 mm	-	100 nm
CTE (α)	23 ppm·K^{-1}	1%	-
Temperature Change (ΔT)	5 mK	-	0.5 mK
Pressure Change (ΔP)	10 Pa	-	2 Pa
Modulus (E)	72 GPa	1%	-
Poisson's Ratio (ν)	0.3	10%	-

uncertainty must be limited to 0.02% of the nominal value and the temperature change uncertainty must be below 1 µk. Lastly, the pressure change uncertainty must be limited to 1 Pa.

However, if the same value and relative uncertainties are used for steel, for instance, the numbers come out quite differently. Because the thermal expansion coefficient is lower and the modulus is higher, the pressure change uncertainty is below the 1 pm threshold and the uncertainties due to the thermal expansion coefficient uncertainty and temperature change uncertainty are 28 pm and 275 pm, respectively. The frequency change uncertainty and refractive index change uncertainty still have the same effect, thus they are independent of sample properties.

The temperature and thermal expansion effects are further decreased by a factor of two when ceramics are considered. Typically, the thermal expansion coefficient of a ceramic is half the thermal expansion coefficient of steel, which is a large source of uncertainty.

2.4.2 Frequency Uncertainty

The laser frequency change and refractive index change uncertainties depend only on sample length, not material type. To meet the uncertainty goals, these values must be decreased. The frequency change uncertainty is

$$U_{\Delta f} = \Delta f + U_f \cong U_f \tag{2.99}$$

because the nominal frequency must include the instantaneous Doppler frequency shift, Δf. Since the Doppler frequency for stability measurements is low, the frequency change uncertainty, $U_{\Delta f}$ is the frequency uncertainty, U_f. Also, the sample expansion rate should be relatively slow (when compared to moving stages), thus the Doppler shift due to thermal expansion will also not affect frequency change uncertainty.

The nominal laser frequency uncertainty must be better 2 parts in 10^{11} to reduce its effect on the length change measurement uncertainty. An iodine stabilized, helium neon laser

has the frequency uncertainty to achieve this value [21]. However, this laser source has low power output, which limits its applicability to calibration and frequency comparisons, rather than a potential heterodyne source.

An iodine stabilized laser can, however, be used for two things: as a laser source for stabilizing a higher power laser source or as a continuous frequency standard for comparison. The former idea is not practical because an iodine stabilized laser is expensive and not available for this research on a continuous basis. The latter is not recommended for determining 'stability events', which are described in the next section because too much averaging is needed for an accurate measurement.

In this research, a novel three mode laser which uses an intrinsic mixed mode signal to stabilize the absolute frequency was developed instead of using an iodine stabilized laser. Using this technique, a frequency stability on the order of parts in 10^{11} has been achieved over short timeframes. Chapter 5 discusses the laser system, including the design, operating principle, establishing heterodyne frequencies, and calibration. Thus, using this laser and stabilization technique, the source requirements including output power and frequency stability can be met.

2.4.3 Refractive Index Uncertainty

The refractive index change uncertainty is a more difficult error to overcome. This is in large part due to the systematic uncertainty in the equations used to calculate the refractive index. Even with ideal environmental parameter measurements, there still is an uncertainty due to the equations used and the empirical data from which they are based. From Birch and Downs [29, 30], the typical calculation for refractive index is the modified Edlén equation [28]

$$\eta_{TP} - 1 = \frac{P\,(\eta - 1)_\lambda}{96095.43} \frac{1 + 10^{-8}\,(0.601 - 0.00972TP)}{1 + 0.003661T} \tag{2.100}$$

$$(\eta - 1)_\lambda \times 10^{-8} = 8343.05 + \frac{2406294}{130 - \lambda^2} + \frac{15999}{38.9 - \lambda^2}, \tag{2.101}$$

where the refractive index, η_{TP}, is for dry air, which is a function of wavelength, λ, in micrometers, temperature, T, in degrees Celsius and pressure, P, in pascals. The refractive index for non-dry air, $\eta_{TP\upsilon}$, is calculated by

$$\eta_{TP\upsilon} - \eta_{TP} = -\upsilon\left(3.7345 - 0.0401\lambda^2\right) \times 10^{-10}, \tag{2.102}$$

where the vapor pressure, υ, is in pascals and λ is in micrometers. The dispersion of air still requires an additional correction factor due to the presence of CO_2 because standard dry air has 300 ppm. Research by Bönsch and Potulski [57] produced an updated Edlén equation including compensation for CO_2 concentration.

Using Equations 2.100, 2.101, and 2.102, the calculated refractive index can be known to 1 part in 10^8 [31], which is three orders of magnitude worse than what is needed to measure with 1 pm uncertainty. To fix this problem, the next logical step is to then devise a measurement where the refractive index change can be measured with a low uncertainty. However, problems arise when correlating the measured refractive index change to the actual change. Chapter 4 discusses this problem, along with wavelength corrected interferometry and interferometry with an internal refractometer.

2.4.4 Phase Uncertainty Summary

Table 2.2 contains a summary of the constant uncertainty sources used when determining the estimated phase uncertainty for all materials. As described previously, this estimate assumes the interferometer does not contribute any significant uncertainty. However, if it does, it must be added in a root-sum-square (RSS) fashion to determine the total measurement uncertainty.

The frequency change and refractive index uncertainties are both assumed to be 1 part in 10^8 because this value is readily available from commercial lasers and environmental parameter measurements. The temperature and pressure fluctuations are assumed to be 5 mK and 10 Pa, respectively, which are the specifications of a sealed chamber used in this research. The material property uncertainties: thermal expansion coefficient, elastic modulus, and Poisson's ratio, are assumed to be a percentage of the nominal values and are 1%, 1%, and 10%, respectively.

Table 2.2: *Constant parameters for the phase uncertainty analysis based on different materials.*

Parameter	Nominal Value	Fractional Uncertainty	Absolute Uncertainty
Nominal Length (z)	50 mm	-	100 nm
Refractive Index (η)	1.00028	1×10^{-8}	-
RI Change ($\Delta\eta$)	1×10^{-8}	1×10^{-8}	-
Frequency (f)	473.7555 THz	1×10^{-8}	-
Frequency Change (Δf)	200 Hz	-	200+U_f Hz
Phase Change ($\Delta\phi$)	3.5 µrad	-	3.5 µrad
Temperature Change (ΔT)	5 mK	-	0.5 mK
Pressure Change (ΔP)	10 Pa	-	2 Pa
CTE (α)	-	1%	-
Modulus (E)	-	1%	-
Poisson's Ratio (ν)	-	10%	-

Several different material types are typically used in precision systems. Commonly used metals are aluminum 7075-T6, Invar, 18-8 stainless steel, and titanium (Grade 5). Aluminum 7075-T6 is a stress relieved, aircraft grade material used for its high strength-to-weight ratio combined with its relatively low cost and ease of machining. Additionally, this type of aluminum is a good conductor, although not as good as pure aluminum. Invar is an iron-nickel alloy which is used for its low thermal expansion properties. 18-8 stainless steel is a common stainless steel which has high stiffness and moderate thermal properties. Titanium (Grade 5) is the most commonly used titanium alloy with an extremely high strength-to-weight ratio, relatively high specific stiffness, and high resistance to thermal fluctuations.

Commonly used ceramics include aluminum oxide, borosilicate glass, fused silica, reaction bonded silicon carbide, and Zerodur®. Aluminum oxide (Al_2O_3), commonly referred to as alumina, is a hard ceramic with a high specific stiffness and moderate thermal properties. Borosilicate glass, commonly referred to as BK7, is a common, low-cost optical glass used in many optical systems. Fused silica is a low thermal expansion glass with lower

temperature-induced birefringence than BK7 and is typically found in high-end optical systems. Reaction bonded silicon carbide (SiC) is a hard ceramic with a very high specific stiffness and moderate thermal conductivity, making it resistant to thermal gradients while having a low thermal expansion coefficient. Zerodur® is a glass with moderate optical properties and a near zero thermal expansion coefficient at 20°.

Each of these materials has applications in precision systems. Thus, drift of components manufactured from these materials is important to this research. Table 2.3 shows a comparison of the estimated length change uncertainty based on the differing material properties. Additionally, the table contains the total estimated measurement uncertainty (Total RSS column) including information from Table 2.2.

Table 2.3: *Length change uncertainty by uncertainty source in picometers. The uncertainty contribution from the nominal length, nominal refractive index, nominal frequency, elastic modulus, and Poisson ratio uncertainties are all much less than 1 pm. The total RSS uncertainty includes contributions from the following: 500 pm from refractive index change uncertainty, 500 pm from frequency change uncertainty, and 1 pm from phase change uncertainty.*

Material	$U_{\Delta z}(U_\alpha)$	$U_{\Delta z}(U_{\Delta T})$	$U_{\Delta z}(U_{\Delta P})$	Material-Based RSS $U_{\Delta z}$	Total RSS $U_{\Delta z}$ (1σ)
Al_2O_3	21	210	0.4	211	738
Al7075-T6	58.8	588	1.4	590	922
BK7	11.2	113	2.8	113	716
Fused silica	1.4	13.8	2.8	14	707
Invar	2.6	26.3	1.2	27	708
SiC	11	110	0.4	110	716
18-8 stainless steel	41.5	415	0.6	417	821
Titanium (Grade 5)	22.5	225	0.8	226	742
Zerodur®	2.5	1.8	1.7	3.5	707

It is clear the combination of the thermal expansion coefficient uncertainty and the temperature change uncertainty are the largest uncertainty contributors due to material properties. This a particular issue for high thermal expansion materials such as aluminum and stainless steel. Alumina and titanium are not affected as much, but their estimated uncertainty is much higher than the other ceramics and Invar, which have extremely low thermal expansion coefficients.

Although the estimated measurement uncertainty establishes a lower limit on measurable length changes, another model is needed to distinguish thermal expansion effects from stability effects. One possible model to account for this is presented in the next section.

2.5 Thermomechanical Sample Model

2.5.1 Model Description

A thermomechanical model is needed to distinguish temperature induced effects from material instability. Figures 2.5, 2.6, and 2.7 illustrate graphically why this is needed. In all

of the figures, it is assumed the temperature and pressure fluctuations are kept between constant, known bounds. In the first scenario, shown in Figure 2.5, the sample length fluctuations have a lower and upper bound, largely induced by temperature and pressure variations. If the measured length change slowly drifts outside of those bounds, then this could be an indication of material instability. This assumes the interferometer used for this measurement does not contribute to these bounds. The nominal measurement value has some noise value, typically much less than the expected length change bounding width.

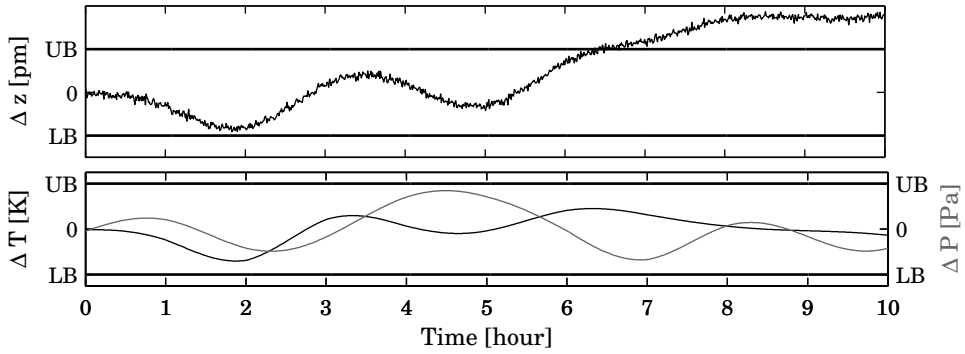

Figure 2.5: *Schematic with the sample drifting outside the maximum expansion bounds. The upper bounds (UB) and lower bounds (LB) are largely estimated by the thermal fluctuations, thermal expansion coefficient, bulk modulus, and pressure fluctuations. Based on this, the measured value drifts outside of its typical bounds.*

In most measurements, however, it is more likely that the sample never exceeds the temperature and pressure bounds. Additionally, the measured displacement is typically filtered to reduce the noise level, which may cause drift effects to appear similar to thermal effects. This scenario is shown in Figure 2.6. In this case, it is impossible to determine whether the sample is drifting or if the measurement just shows filtered thermal effects.

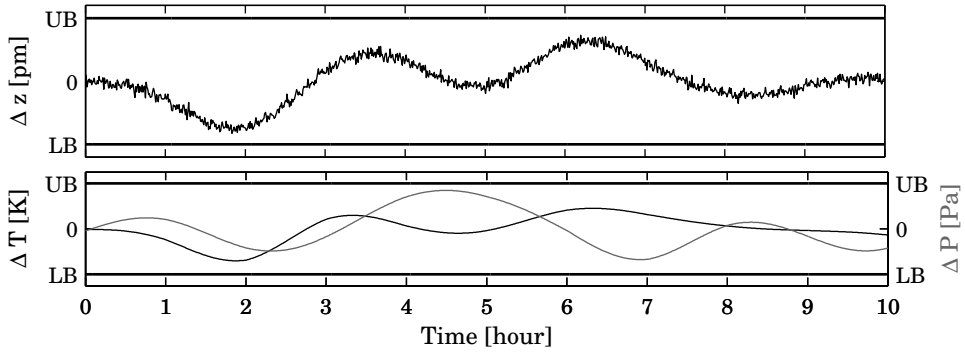

Figure 2.6: *Schematic of a measurement where the sample length change never exceeds the bounds prescribed by the environmental and known electrical effects. In this case, drift effects are typically interpreted as thermal effects and a stability criteria can not be determined.*

The signal to noise ratio must be very high with a high bandwidth to determine the

drift in these situations. The ideal case is to observe 'cracks' or 'jumps' in the data. This would give an indication that a 'stability event' occurred. A schematic of this is shown in Figure 2.7, which indicates a large jump in the data which is unexplained by temperature or pressure fluctuations. This jump could occur due to stress relaxation, which causes some atomic stick-slip criteria to be overcome resulting in a large and fast sample displacement. This means the measurement bandwidth must be high enough to ensure these effects are not filtered out from the data.

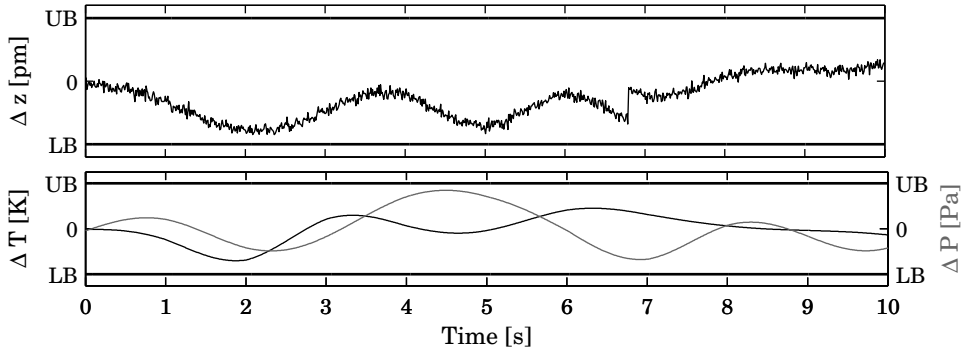

Figure 2.7: *Schematic of a measurement where the bandwidth is sufficiently high that a jump in the data can be measured (6.8 s). If the environmental conditions remain within their bounds, then this jump is an indication of instability in the measured material. Note, the time scale is different from Figures 2.5 and 2.6.*

A simple thermomechanical model using the material's thermal conductance and resistance is one method to determine whether a stability event could occur. This model is based on a resistance-capacitance low pass filter from electronics. This is because the sample has a resistance to heat flow and a capacitance for holding heat. This model will be used to determine the measurement parameters needed to measure a stability event. A stability event would occur if the measured displacement is faster than the sample's thermal time constant, meaning the measured displacement is unexplainable by thermal expansion. For the interferometer to measure this, it must have a high enough bandwidth and a low enough noise level. The model shown here will determine the required bandwidth and noise level.

2.5.2 Gauge Block *RC* Model

The instrument designed in this thesis is intended to measure gauge blocks typically sized 9 mm by 30 mm by L mm, where L can be up to 50 mm. Since the gauge block width is more than three times thinner than its height, the fastest heat transfer will occur across the width to the core of the sample. For gauge blocks with a length smaller than the width, the smaller of the two dimensions should be used. While this model assumes heat transfer in a single dimension, it gives an indication of the measurement bandwidth needed to distinguish stability events from filtered thermal expansion effects.

The thermal capacitance, C_{th}, of the sample is

$$C_{th} = C_p \rho V, \quad [\mathrm{J \cdot K^{-1}}] \tag{2.103}$$

where C_p is the specific heat [J·kg^{-1}·K^{-1}], ρ is the density [kg·m^{-3}], and V is the volume [m^3]. The thermal resistance, R_{th}, is

$$R_{th} = \frac{L}{kA}, \quad [\mathrm{K} \cdot \mathrm{W}^{-1}] \tag{2.104}$$

where L is the traveled heat path length, k is the thermal conductance, and A is conducting area. The heat path length is half the smallest side in a sample and the conducting area is twice the surface area in the direction normal to the heat path. The modeled system behaves similarly to a voltage-based RC-circuit except the input is an instantaneous temperature, T_i, change at the surface of the sample. The thermal response can, therefore, be characterized by

$$T_o = T_i\left(1 - e^{-t/\tau}\right), \tag{2.105}$$

where T_o is the ouput temperature response of the sample, t is the time, and τ is thermal time constant and is equal to $R_{th}C_{th}$. The rate of the sample temperature response is determined by taking the derivative,

$$\frac{dT_o}{dt} = \frac{T_i e^{-t/\tau}}{\tau}, \tag{2.106}$$

which is at its maximum when t is zero. Thus, the maximum sample expansion velocity due to thermal fluctuations is

$$\dot{z}_{CTE} = \frac{z\alpha T_i}{\tau} = \psi\frac{\alpha k}{C_p\rho}, \tag{2.107}$$

where ψ is $\frac{zT_iA}{LV}$, a constant for the gauge blocks in this research.

This model is assumed to be a worst case scenario because the temperature fluctuation at the surface will always change much slower due to the interaction with the air. Additionally, the sample may absorb some heat from the laser beams which are used to measure the length change. The heat absorbed from the laser will match the heat conducted through the mount and the air after a nominal transient period and thus, can be ignored.

This model also establishes two different measurement criteria. First, the measurement bandwidth must be higher than the thermal time constant of the sample. Otherwise, stability effects will look like a gradual thermal fluctuation. Second, if the measured sample expansion velocity is greater than the value from Equation 2.107, then a measured stability event may have occurred. Table 2.4 shows the material properties used in the following sections to determine the thermal time constant for a gauge block 9 mm by 30 mm by 50 mm.

2.5.3 Thermomechanical Model Summary

The summary of the thermomechanical modeling of temperature induced material expansion is shown in Table 2.5. The materials properties used in this model are shown in Appendix C. There are two observations from this data. The first is aluminum and silicon carbide have nearly the same thermal bandwidth, which is the highest of the selected materials. Their maximum expansion rates differ because their respective thermal expansion coefficients have a difference of five times. The second observation is that even for samples smaller than 50 mm, a modest measurement bandwidth of 1 Hz to 10 Hz is needed to keep up with thermal expansion. This means sampling at frequencies higher than this bandwidth (easily achievable) can help reduce noise while still allowing for stability events to appear.

Table 2.4: *Nominal sample properties from the thermomechanical model which are consistent between the various material estimates. These are used to establish a Gauge Block Constant to cross compare differing materials for thermal bandwidth and thermal expansion rate.*

Property	Symbol	Nominal Value
Sample Length	z	0.05 m
Volume	V	1.35×10^{-5}m^3
Heat Path	L	0.0045 m
Conducting Area	A	0.003 m^2
Temperature Input	T_i	0.005 K
Gauge Block Constant	ψ	12.346 K·m^{-1}

Table 2.5: *Results from a thermomechanical RC model for various materials used in precision instruments. Aluminum and SiC had the highest thermal bandwidth while the aluminum had the fastest thermal expansion rate at 15 nm·s^{-1}. This translates to a maximum Doppler shift of 0.05 Hz.*

Material	Thermal TC τ [s]	Thermal BW f_T [Hz]	Expansion Rate $\dot{z}_{CTE}$ [nm·s^{-1}]
Al_2O_3	1.99	0.08	1.0
Al7075-T6	0.39	0.41	15.1
BK7	38.1	0.004	0.03
Fused silica	30.3	0.005	0.006
Invar	3.2	0.05	0.075
SiC	0.34	0.47	3.2
18-8 stainless steel	4.9	0.03	0.85
Titanium (Grade 5)	7.1	0.022	0.32
Zerodur®	28.1	0.006	0.0004

2.6 Data Acquisition Requirements

From Table 2.5 and Equation 2.72, the fastest expansion induced Doppler shift is approximately 0.05 Hz (15.1 nm·s^{-1}). To measure stability events, the data acquisition system must be capable of measuring drift rates at least 100 times faster, ±5 Hz, which is the same as measuring velocities of 1.5 µm·s^{-1}. While this may not be fast enough to measure the direct characteristics of the stability event, it will be enough to distinguish stability events from thermal drift.

The lock-in amplifier from Figure 2.4 will be used for the data acquisition system. Simulations were performed in Matlab to estimate the filtering and signal to noise level requirements. Since the maximum estimated Doppler shift is ±5 Hz, the laser source split frequency should be at least 5 Hz, although higher is preferable to allow for averaging.

The actual lock-in amplifier will be compiled in Simulink and the phase will be measured using a dSPACE data acquisition system with a sampling frequency below 100 kHz. Thus, a laser split frequency is needed which can be tuned between 1 kHz and 10 kHz. This will allow, at worst, ten data points per cycle, which can then allow for more averaging. The bandpass filter cutoff frequencies were simulated to be ±40 Hz from the split frequency.

In these simulations, the split frequency was modeled at 1 kHz, 5 kHz, and 10 kHz with little variability in the results. This wider filter prevents excessive gain changes and phase errors in the ±5 Hz+f_s measurement band. Figure 2.8 shows a Bode plot of the bandpass filter gain and phase error. The low pass filter cutoff of I and Q was 10 Hz. This was also chosen wider than the estimated maximum Doppler shift to prevent excessive gain roll off and phase lag.

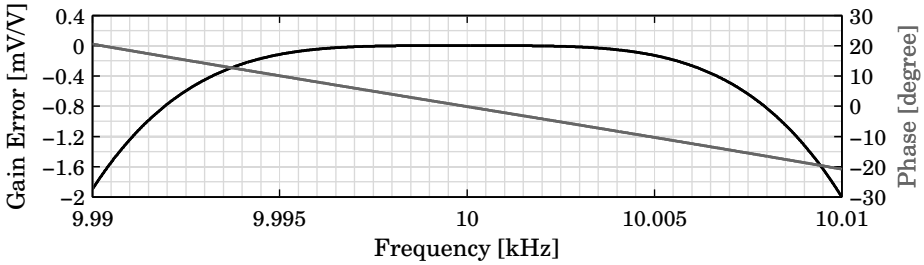

Figure 2.8: *Bode plot of the initial BPF on the input to the data acquisition system. A tight window, ±40 Hz, around a 10 kHz split frequency allows for high spurious signal rejection with minimal gain error and phase lag in the ±5 Hz+f_s measurement band.*

The simulated displacement is a triangular wave with a 1.5 µm peak-to-peak (pk-pk) value and a period of two seconds. This simulates a signal rapidly changing from 1.5 µm·s^{-1} to -1.5 µm·s^{-1}, which is the assumed worst case. Figure 2.9 shows the simulated ideal displacement and velocity over ten seconds.

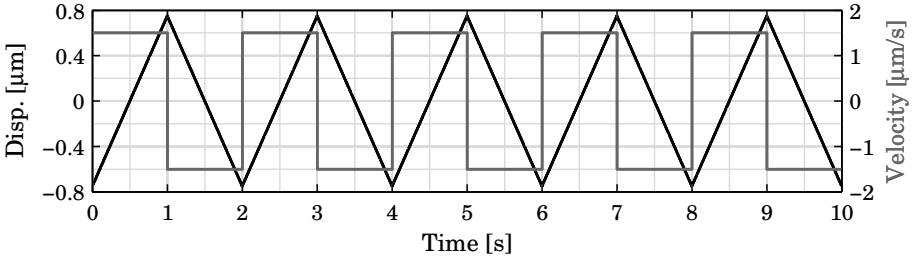

Figure 2.9: *Simulated displacement (red, left Y-axis) and velocity (blue, right Y-axis). The highest thermal expansion rate is 15 nm·s^{-1} and to distinguish stability events from thermal effects, the interferometer must be capable of measuring velocities about 100 times faster than this. This means a maximum velocity of 1.5 µm·s^{-1}, which is a Doppler shift of 5 Hz.*

There is, of course, always some lag between the ideal displacement signal and the simulated measurement signal. In this research, this effect is not important because the signals are used for measurement, not control. But, an error source that does have a direct effect on the measurement is the noise on the detected signal. Low fringe contrast, low optical power, and poor pre-amplification can all affect the signal fidelity prior to

the measurement system. Figure 2.10 shows the difference from the ideally simulated measurement signal (no noise) with three different noise levels (2σ) at the detector: 0.1 V, 0.05 V, and 0.01 V, all with a 18 V pk-pk nominal signal.

These three irradiance noise levels contribute the following displacement error: 13 pm for 0.1 V, 6 pm for 0.05 V, and 1.2 pm for 0.01 V. As previously described in Section 2.4.1, the purpose of this derivation was to determine how to reduce each uncertainty contribution to either the best attainable or to the 1 pm level. Thus, the laser power stability, fringe contrast, and optical power at the detector should be high enough to obtain 18 V of signal range (with pre-amplification) with a noise level of 0.01 V which is 5.5 parts in 10^4 (2σ) or better than 12 bits of signal quality. The dSPACE system has analog to digital converters with 16 bit resolution with approximately 1 bit of noise, thus it is possible to achieve this noise level with this data acquisition system. If this noise level can be achieved, then it is possible to measure displacements as low at 1.2 pm (2σ) with a bandwidth lower than 5 Hz. The qualification of the data acquisition and electronics is discussed further in Chapter 6.

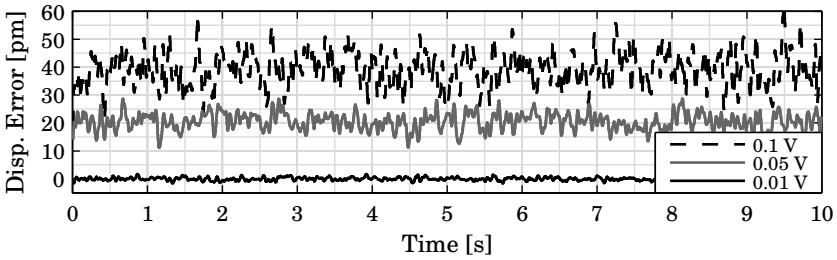

Figure 2.10: *Simulated displacement error from the ideal measurement assuming noise levels of 0.1 V, 0.05 V, and 0.01 V (Gaussian, 2σ) with an 18 V pk-pk nominal signal value. These irradiance noise values lead to displacement errors of 13 pm, 6 pm, and 1.2 pm (2σ), respectively.The data is offset for clarity.*

2.7 Conclusions

The uncertainty estimate shown in this chapter helps establish some design criteria for the measurement methodology and the interferometer. The major measurement uncertainty sources will come from the refractive index stability, laser frequency stability, periodic nonlinearity in the measurement, and the stability of the interferometer itself. When these four criteria are limited by using compensation techniques or some other method, then the limiting measurement uncertainty should be based on the sample material properties. This is largely dominated by the temperature change uncertainty and the thermal expansion coefficient of the material. While the measurement uncertainty will remain the same, having an estimate of the thermal bandwidth and thermal expansion rate can help distinguish the difference between slow thermal expansion and stability events.

Based on this approximate, 1D *RC* model, the measurement bandwidth should be in the range of DC to 5 Hz or higher. If the bandwidth is much higher, the measured results can be averaged to increase the signal to noise ratio while still maintaining the possibility of

measuring stability events. The phase measurement was simulated using a lock-in amplifier technique. The simulated measurement and reference signals each had a tight bandpass filter on the input to have high noise rejection. The noise level on the measurement signal must be better than 5.5 parts in 10^4 (2σ) to measure with a noise level of 1.2 pm. This will be used during the interferometer design to establish criteria on the laser amplitude noise, power at the detector, and fringe contrast.

Chapter 3

Eliminating Periodic Errors

Since the Doppler frequency shift measurement technology using a two-frequency source was invented in the 1970's, heterodyne laser interferometry has been widely used as an accurate positioning sensor to measure displacements of precision stages [31]. The combination of increasing the optical resolution and the rapid development of electronic phase measuring technology made it possible to measure subnanometer displacements. When a helium neon laser (λ = 632.8 nm) is used as an optical source, a commercial displacement interferometer with retroreflectors, which has the optical resolution of $\lambda/2$ (316.4 nm), can achieve displacement measurements with a $\lambda/2048$ (0.31 nm) resolution from fringe interpolation [49]. However, improper phase interpolation introduces measurement errors because the measured phase shift is not always linear with respect to the Doppler frequency shift from the moving component. This measurement error takes the form of periodic nonlinearity caused by impurity of the interference signals [58]. Figure 3.3 shows a schematic of a linear traverse with periodic errors.

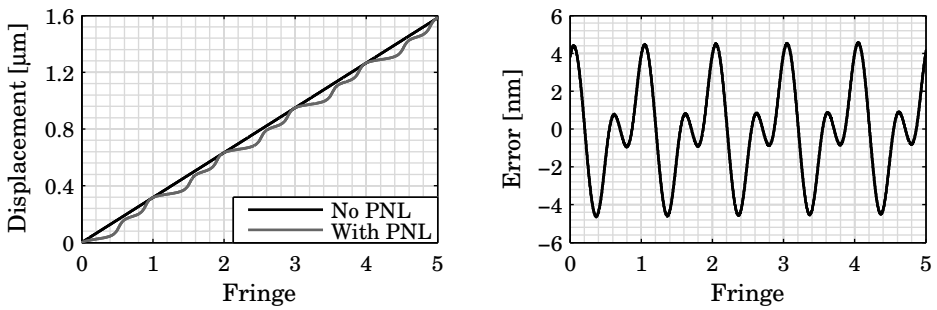

(a) (b)

Figure 3.1: *(a) Comparison between a linear signal and a signal with periodic nonlinearity, highly exaggerated for illustrative purposes. (b) Linear displacement with 5 nm of periodic errors with the nominal slope removed. The periodic errors typically have a first order component with one cycle per fringe and a second order component with two cycles per fringe. Higher orders may appear from additional ghost reflections or stray signals.*

From previous research [32, 59, 60], it is clear the periodic nonlinearity originates from a mixed heterodyne source and imperfect polarizing optics. In the typical heterodyne displacement interferometer, a two frequency, orthogonally polarized source is used, which has polarization orthogonality errors and slightly elliptical beams which contribute errors. These combined with imperfect polarizing optics, polarization alignment between the source and optics, ghost reflections, and electronic nonlinearity all create additional nonlinearity errors [58]. Small leakage components from these invoke an unexpected phase change between reference and measurement signals. In an ideal environment, the periodic nonlinearity is the fundamental error source limiting the implementation of subnanometer displacement measurements when the geometrical errors are minimized. This assumes the measurement is performed in an ideal environment, such as in vacuum, or when the measurement length is minimized so the refractive index effects are minimal. In this research, the measured optical path difference can be up to 50 mm long, which means refractive index effects cannot be ignored. This is discussed further in Chapter 4.

Reducing errors from periodic nonlinearity has been the subject of much research, which can be categorized as either algorithm methods [35, 36, 41, 61, 62] or two spatially separated beam interferometer configurations [63–68]. The reduction method algorithms typically ensure a periodic nonlinearity below 1 nm without changes to the interferometer configuration; however, they require calibration and additional calculation time. Appendix D discusses periodic error algorithms and modeling for displacement interferometry. Alternatively, real time reductions can be implemented with modified interferometer setups using two spatially separated beams. The only limitation of these interferometer configurations is their special and often complicated configurations that limit their applicability in industrial and scientific fields.

3.1 Periodic Error Effect for Stability Measurements

The nominal measurement interference signal without periodic errors is

$$I = A\cos\left(2\pi f_s t + \phi_z\right), \tag{3.1}$$

where

$$\phi_z = \frac{2\pi z N f}{c}, \tag{3.2}$$

and f_s is the split frequency, f is the nominal laser frequency, z is the optical path length difference, N is the interferometer resolution, and c is the speed of light. The measurement interference signal with periodic errors is

$$M = \Gamma_0\cos\left(2\pi f_s t + \phi_z\right) + \Gamma_1\cos\left(2\pi f_s t\right) + \Gamma_2\cos\left(2\pi f_s t - \phi_z\right), \tag{3.3}$$

where Γ_0 is the nominal signal amplitude, Γ_1 is the first order periodic error coefficient, Γ_2 is the second order periodic error coefficient [35, 64]. When Γ_1 and Γ_2 are zero, Equation 3.3 reverts back to the form of Equation 3.1.

The periodic errors from a ideally linear motion depicted in Figure 3.1b have a more subtle effect when it comes to stability measurements. In this research, the target resolution is small and thus, the environment conditions must be well controlled and

buffered from outside effects. A 50 mm aluminum sample in a ±0.01 K temperature controlled environment will have an ±11.8 nm temperature induced length change during a measurement. Initially, however, the sample must be mounted and the surrounding environment will not be as stable as during the measurement. Thus, there will be thermal soak-out induced drift which means the starting point for the periodic nonlinearity cannot be known. The effect of not knowing the starting point is shown in Figure 3.2.

The sample's length then fluctuates slowly as a function of temperature over a range of approximately 20 nm. Since the starting point on the periodic nonlinearity curve is unknown, this 20 nm range could be in regions with either high or low errors from the periodic nonlinearity. Figure 3.2a shows an example of the periodic nonlinearity and five different 20 nm sections, all exhibiting different error characteristics. Those five 20 nm traces are then shown in Figure 3.2b, where they are offset to coincide with zero as will be the case in a measurement.

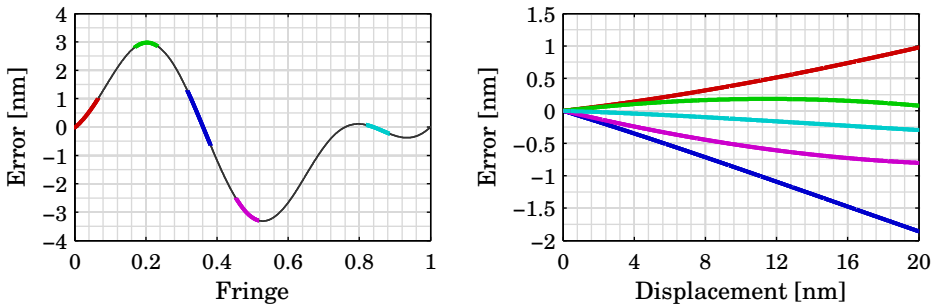

(a) (b)

Figure 3.2: *(a) Five different 20 nm sections for an interferometer with ±3 nm of periodic error. Because the starting phase the system is unknown, the exact place on the periodic nonlinearity curve is unknown and uncorrectable. (b) Simulated measurement error due to periodic nonlinearity over a 20 nm length change depending on the starting phase of the measurement.*

Figures 3.3a–3.3f show three different simulated periodic error values and 50 different, random 20 nm traces for each periodic error value. The 50 random traces are used to determine the maximum error for a given periodic error.

From Figures 3.3a and 3.3b, the pk-pk periodic error of 6 nm can contribute up to 1.75 nm of error (29%). Figures 3.3c and 3.3d show a 3.4 nm periodic nonlinearity error contributing up to 1.1 nm of error (32%). Figures 3.3e and 3.3f show a 1.5 nm periodic nonlinearity error contributing up to 0.45 nm of error (30%). From these three simulations, the maximum error for a 20 nm displacement appears to be about 30% of the pk-pk periodic error value.

Most measurement and corrective techniques for periodic nonlinearity are designed for stages which displace more than one fringe and typically operate under constant velocity conditions. Because of this, most periodic nonlinearity correction algorithms need at least one fringe of motion or a constant velocity sweep to properly correct the motion [35, 36, 41, 61, 62, 69]. Even when the majority of the nonlinearity is corrected, errors occur with

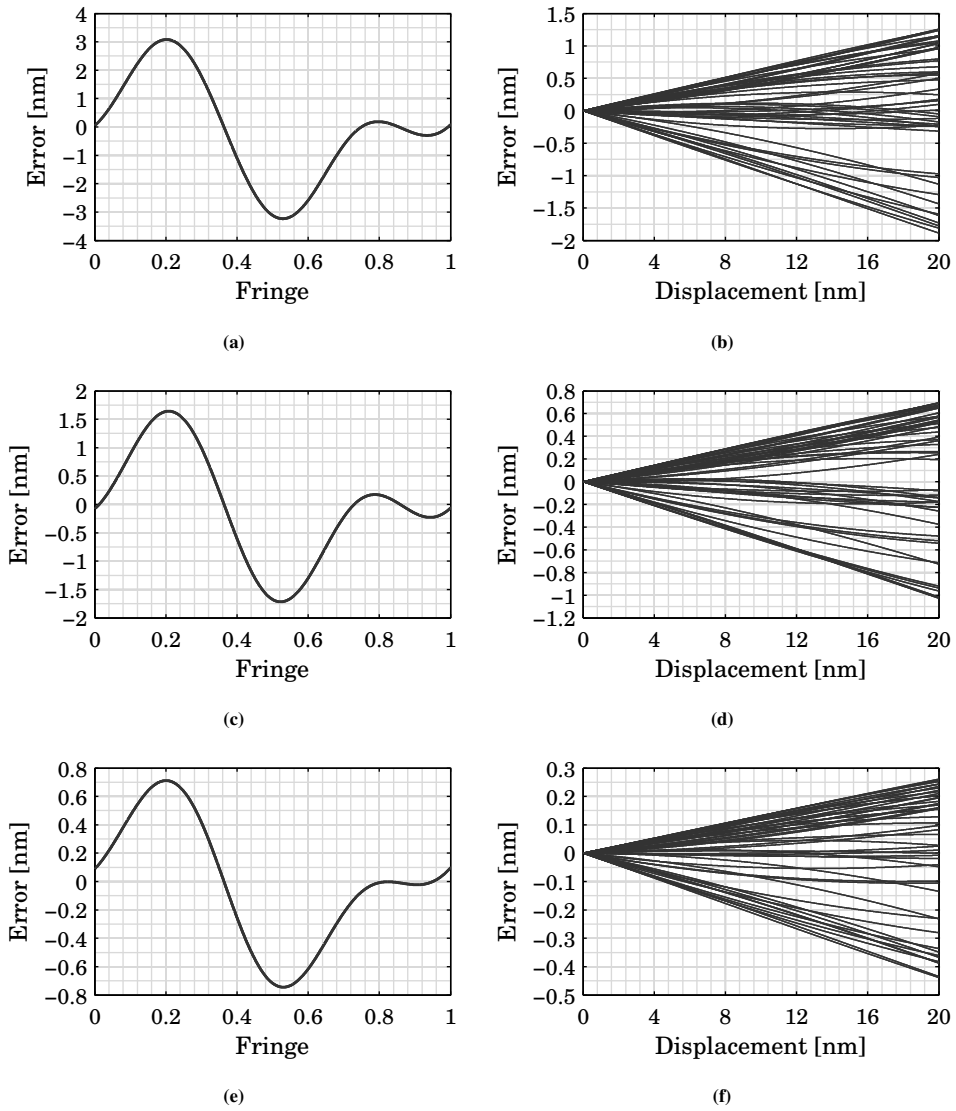

Figure 3.3: *(a,c,e) The periodic error during a signal fringe of motion for three different periodic error values. (b,d,f) Corresponding error for 50 different, random traces to simulate the error because of an unknown starting phase. Based on these simulations, the maximum error from periodic nonlinearity for a motion during a stability measurement (<20 nm) is about 30% of the pk-pk nonlinearity error.*

these algorithms when the motion is nonlinear and noise can be added to the measurement that was not originally present [70]. Appendix D discusses this in more detail with respect to high speed motion stages.

For stability measurements, the measured motion will most likely be less than one fringe. The typical correction algorithms will not work due to the lack of displacement and/or

velocity. Thus, an interferometer is needed which does not have periodic errors, rather than using measurement and correction algorithms. The following sections discuss periodic error free interferometer designs for displacement measurements. The focus of this part of the research was to, not only understand the designs of periodic error free interferometers, but develop and characterize new designs for displacement interferometry. The knowledge learned during this part of the research was then used for designing the stability measuring interferometer.

3.2 Spatially Separated Source

The common feature of most periodic error free heterodyne interferometers is that the two input beams are spatially separated instead of being coaxial and orthogonally polarized. Spatially separating the input beams limits the chances for frequency mixing between the beams. Then, by using clever interferometer designs, it is possible to mitigate unwanted mixed beams, beam overlap, and ghost reflections which reduce or eliminate periodic errors. In the following sections, a common heterodyne source for generating spatially separated beams is presented. Also, two of the more common interferometer designs cited in literature are described in more detail. Lastly, interferometer configurations designed during concurrent research to this work are discussed. This includes confirming measurements of periodic error free interferometry.

The common technique for generating spatially separated beams from a single frequency stabilized laser source is shown in Figure 3.4 [63]. Typically, a stabilized, single frequency laser is used in the type of setup. The beam then passes through an optical isolator to prevent feedback destabilization in the laser cavity (if needed). Then, a half wave plate is used to orient the initial polarization state of the beam. A 50% beamsplitter is used to separate the source into its spatially separated components. Finally, each beam is transmitted through an acousto-optic modulator to introduce a frequency shift proportional to the modulation frequency. For most displacement interferometry applications, a frequency shifting acousto-optic modulator is preferred instead of an amplitude modulating type. This maintains the nominal wavelength of the light used with a slight adjustment, instead of introducing a synthetic wavelength.

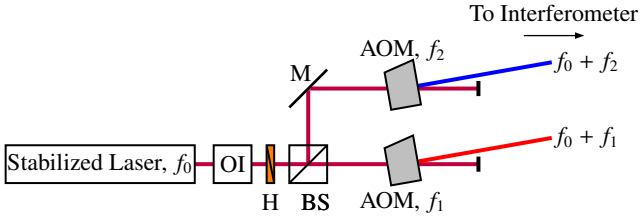

Figure 3.4: *Typical heterodyne laser source for generating spatially separated beams. A stabilized laser is split into two beams and two acousto-optic modulators are used to generate two beams with slightly differing frequencies.*

The light transmitting through the acousto-optic modulator is diffracted into multiple orders (positive and negative). The frequency of the output beams is $f_o + m f_i$, where f_o is the stabilized frequency value, m is the integer fraction order, and f_i is the input frequency to the

acousto-optic modulator[1]. The beam separation between consecutive orders is a function of the nominal laser wavelength, acousto-optic modulator crystal type, and modulation frequency.

By aligning the acousto-optic modulator to the Bragg angle, the output beams are largely limited to the 0^{th} and 1^{st} order beams, which increases the efficiency of the 1^{st} order beam. Figure 3.5 shows a schematic of an acousto-optic modulator with the input beam orthogonally aligned and with the input aligned to the Bragg angle.

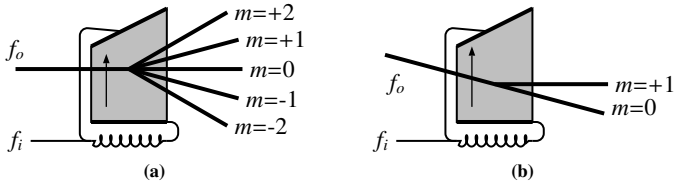

Figure 3.5: *Diffraction from an acousto-optic modulator with (a) normal input and (b) input at the Bragg angle. The output beams are modulated based on the driver input frequency f_i.*

Typically, the 1^{st} order beam is isolated from the other beams using a pinhole. Then, the beams are launched into fibers or steered into the interferometer using a series of mirrors. The key component to this type of heterodyne source is the drive frequencies of the acousto-optic modulators. Theacousto-optic modulators are usually driven with slightly different frequencies, which means the difference between the two drive frequencies is the detected heterodyne frequency. If the wavelength is 632.8 nm, for instance, and one acousto-optic modulator is driven at 80 MHz and the other acousto-optic modulator is driven at 80.1 MHz, the detectable interference frequencies are at 0.1 MHz and 160.1 MHz. By applying a modest cutoff filter, the lower frequency can be isolated and further processed to determine the phase.

The cutoff filter can serve two different purposes. The first purpose is to eliminate harmonics at the modulation frequencies. While it is possible to drive one acousto-optic modulator at 40 MHz and another at 80 MHz, this would cause the main heterodyne signal to coincide with the modulation frequency which can cause errors. Another reason this is done is to reduce the heterodyne frequency to a much lower frequency because a particular measurement is not dominated by the need for a high heterodyne frequency. This means typical laboratory equipment can be used instead of dedicated detectors, phasemeters, amplifiers, and filters, which are designed for the 50+ MHz regime. Some of the interferometers in the following sections use this type of spatially separated source.

3.3 Wu-type Interferometers

One of the first interferometer configurations specifically designed to limit periodic errors is the layout by Wu, *et al.* [64]. This interferometer uses the heterodyne splitting scheme

[1]Some acousto-optic modulators produce an optical frequency shift which is an integer multiple of the acousto-optic modulator drive frequency. During this research, acousto-optic modulators with a frequency shift equal to the acousto-optic modulator drive frequency were used. However, newer, more efficient acousto-optic modulators were purchased towards the end of the project, which had an output frequency of twice the modulation frequency.

shown in the previous section. Once the two spatially separated beams with an offset frequency are obtained, each beam is launched into polarization maintaining fiber. The two fibers are then delivered to the interferometer as shown in Figure 3.6.

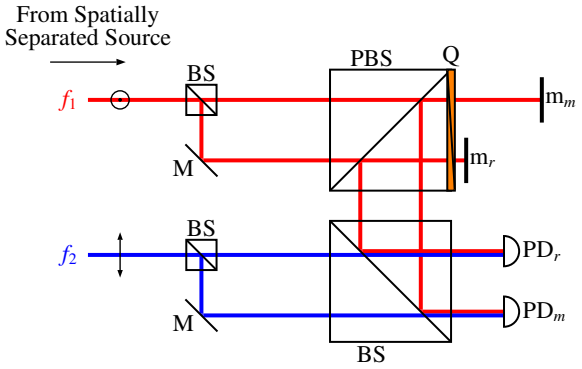

Figure 3.6: *Schematic of the Wu interferometer. This interferometer configuration uses the spatially separated source from Section 3.2.*

One input beam is vertically polarized while the other beam is horizontally polarized. One beam is split into two parallel beams using a beamsplitter and mirror. Then, the two beams transmit through a polarizing beamsplitter and a quarter wave plate, where one beam reflects off the measurement mirror and the other beam reflects off the reference mirror. After passing though the quarter wave plate for a second time, the polarization state is rotated 90° and now the beams reflect. They then traverse to a 50% beamsplitter which is where the main interference occurs.

The second input beam is also split into two parallel beams using a beamsplitter and a mirror. These beams then interfere with their respective measurement and reference beams in the 50% beamsplitter. Two interference signals can then be detected, and thus, the relative displacement between the two mirrors can be determined.

The interferometer by Wu, *et al.* demonstrated periodic errors below 50 pm. However, there was some noticable drift in their periodic error over time, which may be caused by either ghost reflections or birefringence changes in the input polarization maintaining fibers.

This interferometer configuration has been adapted to several different applications including space metrology, surface metrology, and dilatometry systems [71–74]. Additionally, this interferometer is tilt sensitive, which makes it suitable as a three degree-of-freedom interferometer, particularly with differential wavefront sensing (DWS) techniques [75, 76].

A lack of symmetry between measurement and reference beams can cause measurement errors while using this interferometer. To minimize the optical path difference by the initial 50% beamsplitters and mirrors for the two input beams, cube beamsplitters rotated at 45° have been used [71, 72]. This minimizes the optical path difference, although a special coating is needed on the beamsplitter surface to ensure the output beams have equal power. Additionally, adapting this interferometer to measure a sample from both sides while maintaining symmetry and balance is difficult. This must be addressed for measuring the dimensional stability of materials.

3.4 Lawall and Kessler Interferometer

Another interferometer configuration often cited in literature is a system designed by Lawall and Kessler [65]. In this interferometer, shown in Figure 3.7, the acousto-optic modulators are essentially used as beamsplitters and isolators to prevent unwanted stray beams. This interferometer uses a different heterodyne source than the one presented in previous sections because of the combined acousto-optic modulator functions.

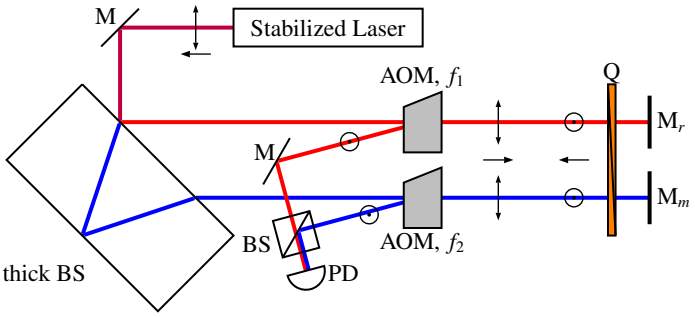

Figure 3.7: *Schematic of the Lawall and Kessler interfeormeter. In this interferometer, the acousto-optic modulators are polarization sensitive.*

A stabilized laser is used as the input into the system [77]. Two parallel beams are then obtained by using a thick plate beamsplitter. The two input beams pass orthogonally through separate, polarization sensitive acousto-optic modulators, each driven at a slightly different frequency. The beams then pass through quarter wave plate and reflect off two mirrors, one as the measurement mirror and the other as the reference mirror. After passing back through quarter wave plate and the acousto-optic modulators, the polarization state is rotated 90°. These beams are then diffracted and frequency shifted by the acousto-optic modulators due to the change in polarization state. A mirror and beamsplitter combination is then used to interfere the measurement and reference beams. After this, the interference signal at the difference frequency between the two acousto-optic modulators can be detected. The reference signal for this system is typically generated from the acousto-optic modulator drivers, using a frequency mixer and low pass filter.

This interferometer demonstrated errors below 10 pm, which is in the target regime for this research. However, this interferometer has two optical path imbalances, which may cause measurement errors. One imbalance occurs in the initial thick plate beamsplitter where the measurement arm passes through more material than the reference arm. The second imbalance occurs with the combining beamsplitter and mirror combination. As shown in Figure 3.7, the reference beam reflects off one extra mirror prior to the combining beamsplitter.

These two imbalances can cause measurement errors, especially if stability is needed. Additionally, this interferometer configuration is not easily adaptable to measuring an object from both sides. This is further compounded by the size constraint from the acousto-optic modulators which need a large spatial separation due to the size of the components and to properly isolate the first order diffracted beam from the other orders.

3.5 Joo-type Interferometers

A third architecture for linear displacement interferometry without periodic errors was developed by Joo[2] and colleagues [67, 68, 78, 79]. One large problem with the previous periodic error free interferometers is their limited applicability for industrial systems. The focus of this research was to design and develop a periodic error free interferometer specifically for industrial applications.

3.5.1 Retroreflector Target Interferometer

Schematics of the Joo-retroreflector (Joo RR) based interferometer are shown in Figure 3.8. This interferometer uses the heterodyne laser source from Section 3.2 to generate the two spatially separated beams. Each beam is split by a 50% beamsplitter. The reflected beams travel to a right angle prism to generate the reference arms in the interferometers. When the reference beams travel back to the initial beamsplitter, they are offset from the input beams to avoid overlap.

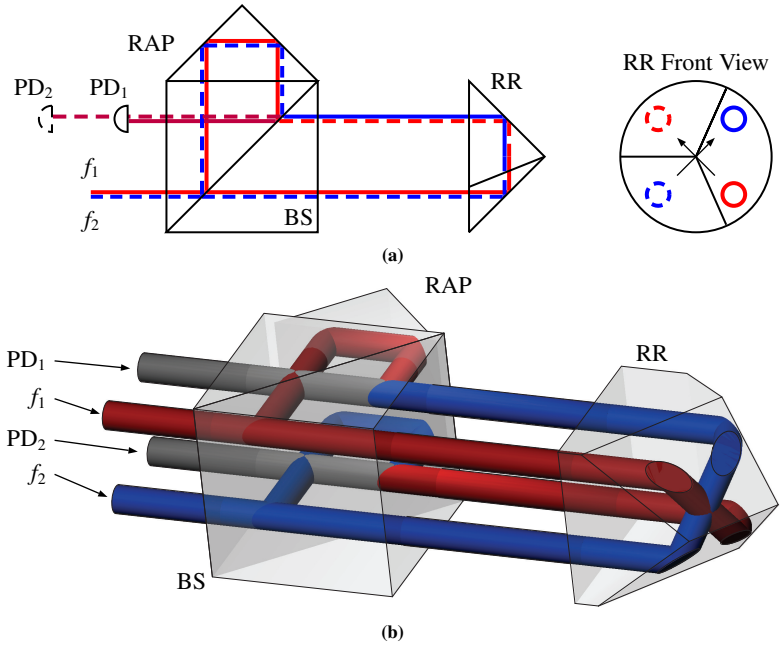

Figure 3.8: *(a) Schematic of the retroreflector-based Joo interferometer. The beams are offset for clarity and the dashed beams are below (into the page) the solid beams. (b) Three dimensional model of the retroreflector-based Joo interferometer.*

The two beams that pass through the beamsplitter travel to a retroreflector attached to the moving stage. When the two beams come back from the moving retroreflector, they are reflected diagonally from their initial input position across the retroreflector. This ensures

[2]Dr. Ki-Nam Joo worked as a postdoctoral researcher at TU Delft in a partner IOP project on subnanometer interferometry. This section contains more detail than the previous two sections because of my involvement in this research. My contributions were in building, testing, characterizing, and reporting this research.

a reference arm containing a beam with frequency f_1 overlaps with a measurement arm containing a beam with frequency f_2. This occurs for the other interference signal, which has a reference arm of f_2 and a measurement arm of f_1. Two photodiodes (PD_1 and PD_2) are used to detect the interfering beams. After assuming f_1-f_2=f_s and simplifying, the two interference signals are

$$I_1 = cos\left(2\pi f_s t + \frac{2\pi N\eta\Delta z}{\lambda}\right) \quad \text{and} \tag{3.4}$$

$$I_2 = cos\left(2\pi f_s t - \frac{2\pi N\eta\Delta z}{\lambda}\right), \tag{3.5}$$

where N is the interferometer resolution, Δz is the stage displacement, and λ is the laser wavelength. The measured phase difference between I_1 and I_2 is $\frac{8\pi\eta\Delta z}{\lambda}$. The Doppler frequency shift is the same direction for both beams but the nominal frequency is different. This causes the interference frequency to be different. Thus, the Doppler frequency value is the same but the measured frequency shift from the nominal heterodyne frequency is in opposite directions. When the phase difference is measurement between the two interference signals, the effective resolution is increased by a factor of two. This effect is because there is not a separate reference signal, rather two measurement signals that are both phase shifted in equal and opposite directions. This technique is useful for increasing the measurement sensitivity without many changes to the electronics and signal processing.

Measurement Setup

A linear displacement over many fringes is a simple and effective method to measure the periodic nonlinearity. This is assuming the displacement is nominally linear and the stage errors do not occur at the same frequency as the periodic nonlinearity. To determine the amplitude of the periodic nonlinearity after a linear displacement over many fringes, typically a linear fit is removed from the data, leaving the residual error. Then, a Fourier analysis is performed on the residual error, but instead of assuming a constant sampling frequency, a constant displacement step (in fringes) is used, determining the fringe order. When the single-sided Fourier amplitude spectrum is plotted with respect to the fringe order, peaks appear at the first and second fringe order if there are periodic errors present. Also, sometimes, peaks can appear at the half fringe order or third fringe order, which are typically from ghost reflections.

The problem with using this technique is that it assumes the stage errors do not occur at the same fringe order as the periodic errors. The typical method to determine whether the stage is causing the errors or if it is indeed attributed to periodic nonlinearity in the phase measurement is to perform several linear displacements at different velocities. If the periodic error as a function of displaced fringes changes in the Fourier domain, then this can be attributed to the stage. If the periodic error as a function of displaced fringes remains constant, then this is the periodic error in the interferometer. In these experiments, the stage was displaced with several different velocities to separate stage vibrations from periodic nonlinearity.

The periodic nonlinearity of the Joo RR interferometer was assessed by performing 10 μm linear traces with a piezo stage [80]. The measurement retroreflector was mounted to the piezo stage and the stage was driven and controlled from its internal capacitance sensor,

as shown in Figure 3.9. The stage was commanded to displace 10 μm in 20 nm steps, which was the smallest step possible. The phase was measured using a commercial lock-in amplifier [81].

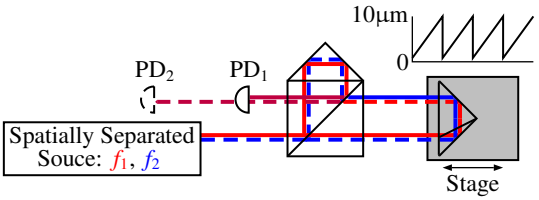

Figure 3.9: *Schematic of the test setup for determining the periodic nonlinearity of the Joo-retroreflector target interferometer. A piezo stage was linearly displaced 10 μm to determine the periodic errors.*

Signal Processing

Since the stage will displace 20 nm per step and the periodic errors are in the nanometer or sub-nanometer range, some selective filtering was needed. First, the linear trend from the displacement data was removed. In the next step, a Fourier analysis was performed to see where the data had high frequency components. In particular, the 20 nm steps show up as a high frequency noise at a fringe order of 7.91. To remove those steps and the low frequency components, the data below 0.4 fringe order and above 4.5 fringe order was set to zero in the Fourier domain. An inverse Fourier transform was then applied to this filtered Fourier data. Figure 3.10a shows the residual error after a linear fit and Fourier filtering. Another Fourier analysis was applied to the filtered data, this time with respect to the displacement in fringes. The results from this analysis are used to determine the periodic nonlinearity, as shown in Figure 3.10.

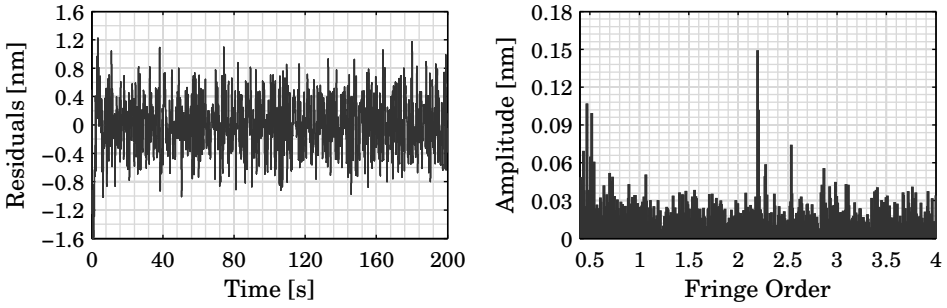

Figure 3.10: *(a) Residual error from a linear fit after filtering frequency components below 0.4 fringe order and 4.5 fringe order. (b) Results from a Fourier analysis on the data in (a) for determining the amplitude of the periodic nonlinearity. The peaks at 2.2 and 2.55 fringe orders are due to stage vibrations.*

Results & Discussion

The residual error after removing a linear fit and after filtering on a single linear trace of 10 μm is shown in Figure 3.10a. The residual error clearly shows nanometer level performance from the Joo retroreflector interferometer. The Fourier analysis, shown in Figure 3.10b, showed peaks at fringe orders of 2.2 and 2.55, which correspond to stage vibrations. These were verified as stage displacements by displacing the stage with a faster velocity which caused these peaks to shift in the frequency domain. The peaks around a fringe order of 0.5 are likely due to errors in driving the stage from its internal capacitance sensor and errors from linear fitting. At the first and second fringe orders, the peaks appear to be in the 30 pm to 40 pm range, which is essentially the noise floor in the Fourier domain, signifying no detectable periodic nonlinearity.

This analysis was performed for eight linear sweeps, each with the same stage speed and data acquisition parameters. This was performed to evaluate the consistency of the periodic errors. Figure 3.11 shows the averaged residual error in the Fourier domain (converted to fringe order). The red peaks correspond to the averaged value plus one standard deviation of the eight measurement values. These results show the periodic nonlinearity was consistently near 50 pm except for stage vibrations (2.2, 2.55, 2.8) and low frequency variations (<0.7). None of the peaks measured correspond to the typical periodic error values at the first or second order.

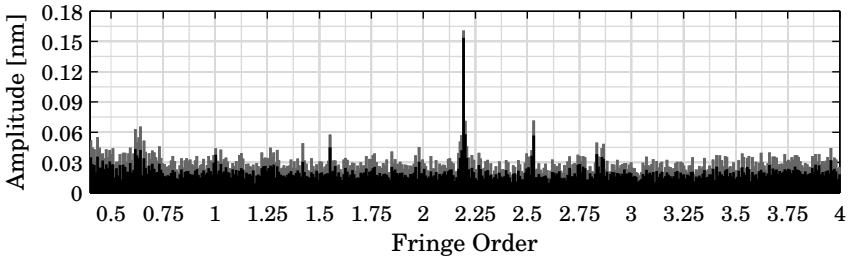

Figure 3.11: *Results from the Fourier analysis after detrending and filtering eight linear sweeps with the Joo retroreflector interferometer. The red signifies the mean periodic error amplitude plus one standard deviation of the eight measurements. The periodic error amplitude is below 50 pm. The three peaks (fringe order 2.2, 2.55, 2.8) are due to vibrations from the stage motion.*

In this interferometer configuration, there are only three critical components to align, and none require a rotational alignment about the azmuthal angle. This means the interferometer is insensitive to polarization effects. The three critical alignments are the parallelism between the initial input beams, matching the lateral offset in the right angle prism, retroreflector, and input beams, and the right angle prism tilt alignment. However, the tilt alignment in the right angle prism can be minimized by the manufacturing tolerance of the beamsplitter and right angle prism. This leaves the input beam and the target alignment as the only two aspects to align when in industrial systems, which is the same as all retroreflector-based interferometers.

3.5.2 Plane Mirror Target Interferometer

The interferometer concept to separate the two beams and use a right angle prism can also be adapted for plane mirror targets, as shown in Figures 3.12a and 3.12b, which are commonly used in multi-degree of freedom systems. This interferometer also has minimal (no) periodic errors. The Joo plane mirror interferometer configuration consists of a beamsplitter, a polarizing beamsplitter, a right angle prism, a retroreflector, a quarter wave plate, and a mirror.

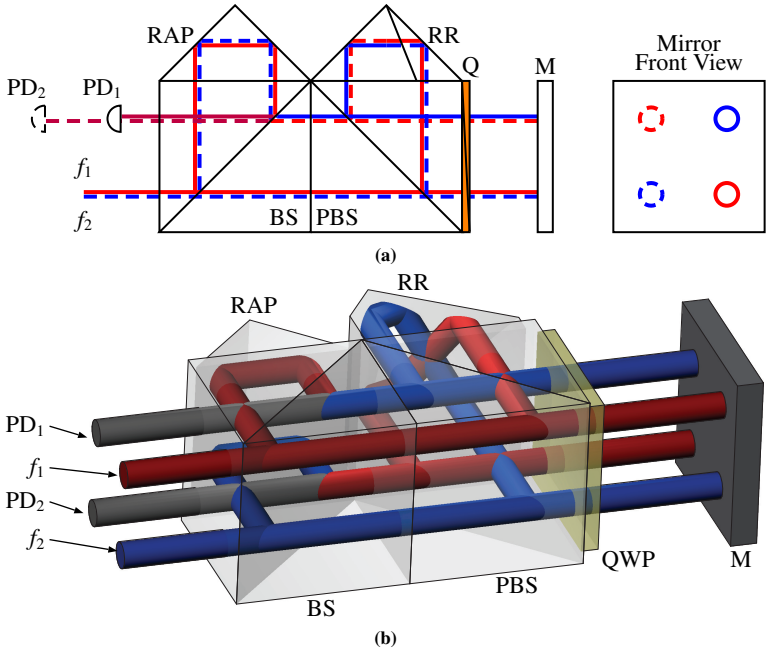

Figure 3.12: *(a) Schematic of the Joo interferometer adapted for a plane mirror target. The beams are offset for clarity and the dashed beams are lower than the solid beams in the plane. (b) Three dimensional model of the plane mirror Joo interferometer.*

In this interferometer, the optical resolution is $\lambda/8$ (79.1 nm) because of the double path interferometer setup. The reference and measurement beams are completely separated until they are combined by the beamsplitter, which eliminates the chances for frequency or polarization mixing. With the exception of ghost reflections, there is also no beam leakage present, thus it is theoretically free from periodic errors. The drawback of this plane mirror interferometer is the unbalanced configuration between the reference and measurement paths. The polarizing beamsplitter and quarter wave plate add a significantly longer glass path for the measurement beams, thus thermal gradients will contribute large errors.

The Joo plane mirror interferometer (Joo PMI) was assessed using the same method presented for the Joo RR interferometer. The spatially separated source from Section 3.2 and the Joo RR interferometer was used for the Joo PMI. These experiments were compared simultaneously to a traditional plane mirror Michelson interferometer, as shown in Figure 3.13.

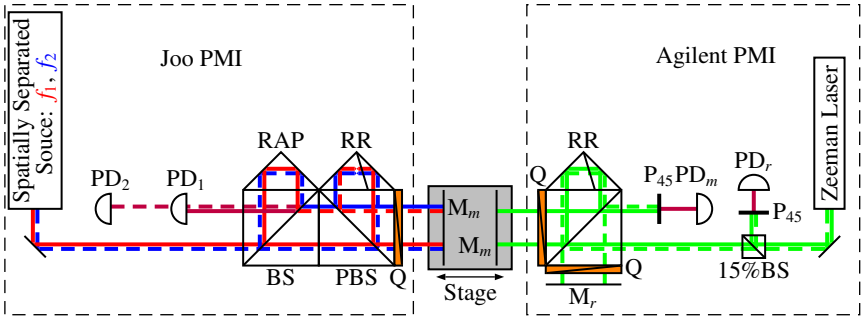

Figure 3.13: *Schematic of the setup for measuring the periodic nonlinearity of the Joo PMI and a commercial Agilent PMI. Both systems were measured simultaneously to assess stage vibrations and to compare the Joo PMI to a commercial alternative.*

The Michelson interferometer consisted of an Agilent Zeeman laser and an Agilent plane mirror interferometer [43, 82]. The Zeeman laser (described in more detail in Chapter 5) is a frequency stabilized laser with two coaxial, orthogonally polarized beams with a nominal frequency difference of 3.5 MHz. Part of the beams from the Zeeman laser are split using a 15% beamsplitter for a reference. A polarizer at 45° and PD$_r$ are used to measure the reference frequency. The remaining beam travels to a polarizing beamsplitter where the two beams are split via polarization state.

The reference arm (dashed line) gets reflected off the polarizing beamsplitter, passes through a quarter wave plate, and reflects off M$_r$. This beam passes back through the polarizing beamsplitter, reflects off the retroreflector, and reflects off M$_r$ a second time. The beam then passes back through the quarter wave plate and now reflects off the polarizing beamsplitter. The measurement arm (solid line) passes through the polarizing beamsplitter and quarter wave plate and reflects off a mirror mounted to the piezo stage. The beam now reflects off the polarizing beamsplitter, the retroreflector, and the polarizing beamsplitter a second time where it then travels to the measurement mirror a second time. This time, the beam passes back through the polarizing beamsplitter where it is interfered with the reference arm with a polarizer at 45° and is detected with PD$_m$.

The same piezo stage with the same 10 µm displacements was used for the linear traces. After detrending and filtering higher fringe orders, the residual motions measured by the two interferometers have similar noise levels, as shown in Figure 3.14a. The Fourier analysis of the two measurements is shown in Figure 3.14, where the Agilent PMI has a first and second order periodic nonlinearity amplitudes of 250 pm and 100 pm, respectively. The Joo PMI showed no appreciable periodic nonlinearity amplitudes above 50 pm.

However, there are two peaks which have the same nominal amplitude, 150 pm, but occur at a fringe order of 2.2 for the Agilent PMI and at 1.1 for the Joo PMI. This is the same stage vibration that was measured with the Joo RR interferometer since the stage was commanded with the same velocity for both measurements. The vibration amplitude was approximately 150 pm for all three interferometers. Additionally, both the Agilent PMI and the Joo RR interferometer have an optical resolution of $\lambda/4$ (158.2 nm), which is why the vibration occurs at the same fringe order (2.2). The Joo PMI has double the resolution as the other two, $\lambda/8$ (79.1 nm), which is why the vibration occurs at half the fringe order (1.1).

Eight linear traverses were made with the piezo stage to assess the periodic nonlinearity,

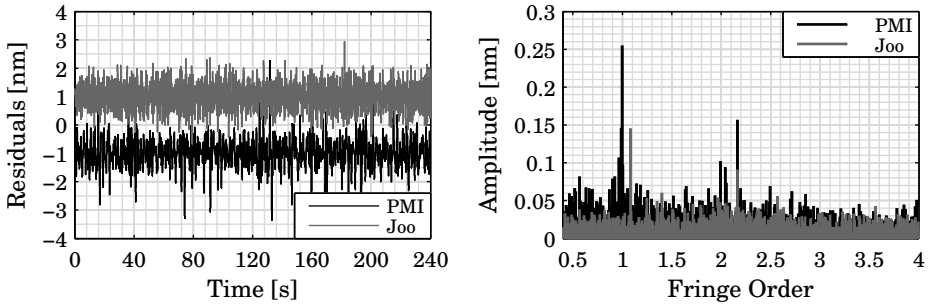

(a) (b)

Figure 3.14: *(a) Residual error from the linear displacement after filtering. Both measurements had similar noise levels and the data is offset for clarity. (b) Results from the Fourier analysis (converted to fringe order). The Agilent PMI shows first and second order peaks at 250 pm and 100 pm, respectively, whereas the Joo PMI has no appreciable periodic nonlinearity. The peaks at fringe orders 1.1 and 2.2 with the same 150 pm amplitude are due to stage vibrations. The slight difference in amplitude is possible due to measurement mirror mounting effects.*

same as the Joo RR interferometer. The data was detrended and filtered in the Fourier domain before being transferred back to the time domain. The data was then analyzed in the Fourier domain with respect to the displaced fringes. Figures 3.15a and 3.15b show the average periodic error amplitude for the Joo PMI and Agilent PMI over eight measurements with the same measurement parameters. The red data in the Fourier domain shows the mean plus one standard deviation of the eight measurements to show the variability in the periodic nonlinearity and vibrations.

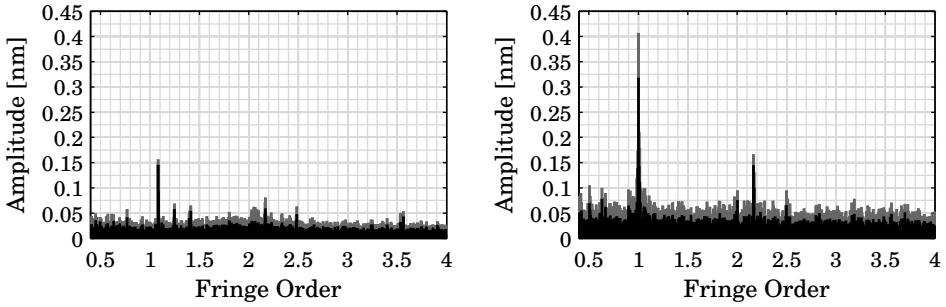

(a) (b)

Figure 3.15: *Average of eight measurement amplitudes of the residuals after filtering in the Fourier domain with the Joo PMI (a) and the Agilent PMI (b). The data in red is the average value plus one standard deviation of the eight values to show the amount of variability in the results. The Joo PMI shows no appreciable periodic nonlinearity wheres the Agilent PMI has first and second order periodic nonlinearity.*

The Joo PMI showed little variability in periodic nonlinearity and vibrations and the

amplitudes were below 50 pm. The Agilent PMI showed a higher variability in the results, particularly for the first and second order periodic nonlinearity. For the Agilent PMI, the average first order error amplitude was 315 pm with a standard deviation of 90 pm. The average second order error amplitude was 75 pm with a standard deviation of 25 pm. This means the periodic nonlinearity is a time varying effect, which has been demonstrated previously by Hou and Zhao [83].

3.5.3 Generalized Interferometer

The Joo PMI can be more generalized as shown in Figure 3.16. Instead of using a right angle prism and a retroreflector to ensure the proper overlapping between measurement and reference arms in the interferometer, a large retroreflector and two smaller retroreflectors can be used instead. This contributes two significant aspects. The first is the alignment tolerance on the right angle prism is removed because retroreflectors are insensitive to tilt. The second contribution is the beams traveling to the mirror are not diagonal from each other, but side-by-side. This is significant because a reflective coating can be placed on the quarter wave plate surface to generate the reference signal.

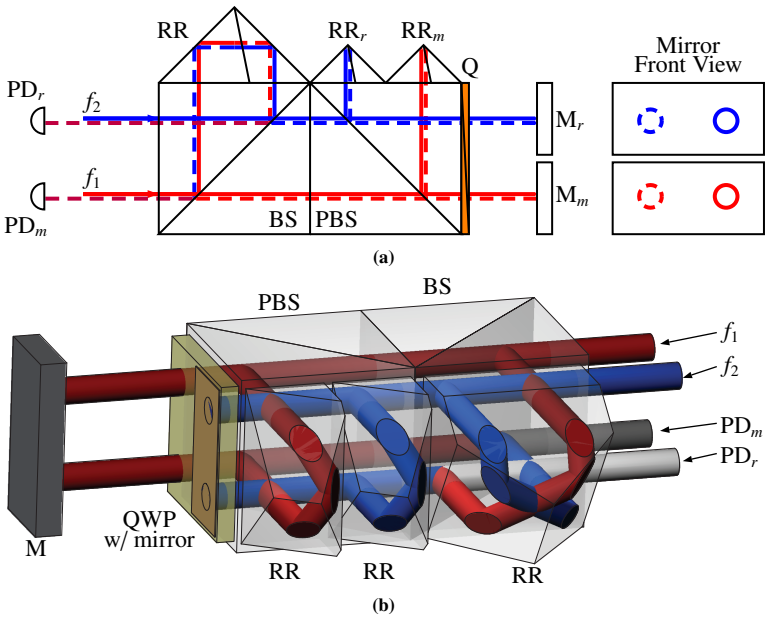

Figure 3.16: *(a) Schematic of the generalized Joo PMI. This interferometer uses three retroreflectors to limit the measurement mirror tilt sensitivity and initial component alignment sensitivity. (b) Three dimensional model of the generalized Joo PMI. This model uses a thin coating on the quarter wave plate as a reference mirror.*

The addition of the reference mirror removes the interferometer resolution doubling from the system, but it allows for multi-axis system implementation. While this configuration also has an optical path imbalance, it does have a well defined thermal datum for system design aspects. The thermal datum is the reference reflective coating on the quarter wave

plate surface. Alternatively, if a separate optical reference signal is generated, the two sets of measurement beams can be used to measure two different mirrors as in a differential interferometer.

Another adaptation of the interferometer is for three axis measurements along the Z-, θ_Z-, and θ_Y-axes. This is done by stacking two generalized interferometers (Figure 3.16a) and applying some initial beam splitting and steering components. This interferometer is shown in Figure 3.17.

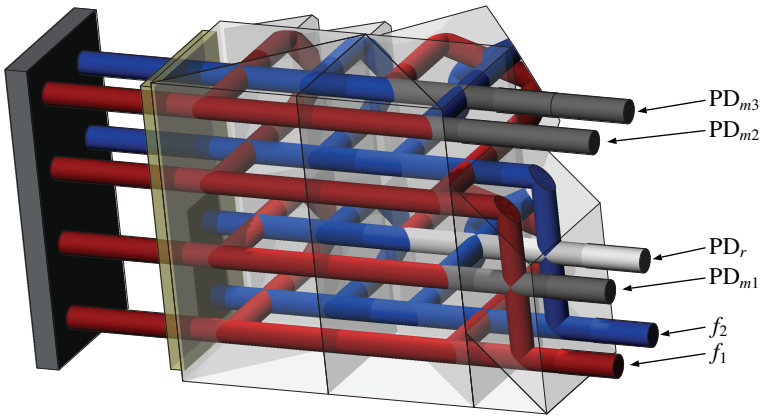

Figure 3.17: *Model of the generalized Joo interferometer adapted for three measurement axes. This interferometer can measure one linear and two rotational degrees of freedom.*

By knowing the beam spacing between the different measurement axes, the difference between two measurements dividing by the beam separation measures the rotational dimension. This can be further expanded into a five-axis system by adding a third tier to the three-axis system and adding a 45° mirror to the target with an additional reference mirror, as shown in Figure 3.18. This allows for measurements along the Z-, X-, θ_X- , θ_Y-, and θ_Z-axes. This configuration also provides many redundant measurement axes, allowing for self calibration in some specialized systems.

An added benefit of all of these configurations is the input beam alignment. Some specialized systems require input and detection beams to occur inline with the main measurement axis. However, if space is an issue, it is often desirable to align the beams orthogonal to the interferometer. The Joo-type interferometers allow for multiple combinations of input and output beams to suit the intended application without adding additional components. This means more optical components are not needed to adjust the orientation, reducing cost and increasing alignment stability.

3.5.4 Joo-type Interferometer Summary

The Joo RR interferometer and the Joo PMI were both demonstrated to have periodic nonlinearity less than 50 pm. Both interferometers also showed the capability to measure subnanometer vibrations due to the stage stepping motion. The motion was determined to be from stage vibrations by verifying it with a commercial interferometer and by changing the stage velocity to shift the peak in the frequency domain. The commercial interferometer

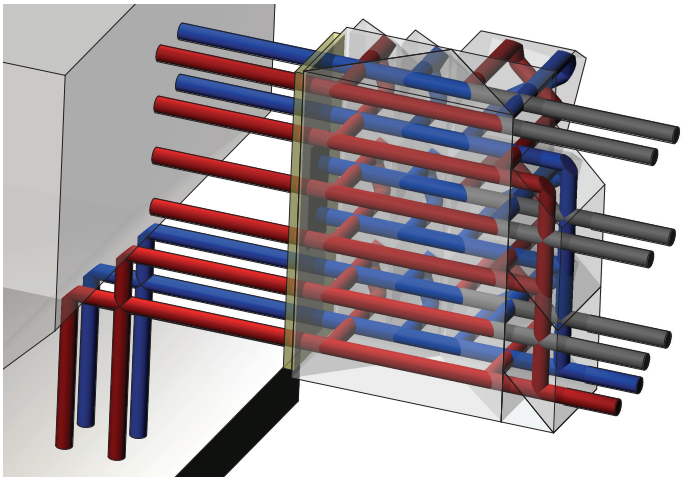

Figure 3.18: *Model of the generalized Joo interferometer adapted for five measurement axes. This interferometer can measure two linear and three rotational degrees of freedom. This interferometer requires a target mirror with a 45° mirror attached and an additional reference mirror.*

results exhibited the same vibration amplitude at the frequency expected from the Joo interferometer measurements.

The Joo-type interferometer can also be modified into a generalized form where a reference beam can be integrated into the interferometer. This generalized form will also allow for multi-axis interferometry with either three axes or five axes, depending on the desired configuration.

The generalized Joo interferometer has a disadvantage over other conventional displacement interferometers because it needs a separate reference signal per interferometer block. Traditional interferometers only need one reference signal per system, which means more data acquisition channels are necessary with the Joo interferometer. However, as interferometry systems move more toward fiber-based systems, each conventional interferometer block will inherently need its own reference signal because unwanted frequency and phase shifts will occur in the fibers. Also, the data acquisition system is simpler and more robust than systems requiring periodic nonlinearity correction which will ultimately save on the data acquisition system's cost.

3.6 Conclusions on Eliminating Periodic Errors

All three periodic error free interferometers shown here have demonstrated 50 pm of periodic error or less [64, 65, 67, 68]. This limit is likely due to the algorithm used to assess the periodic errors, the repeatability of the stage, and the consistency of the measurement environment, rather than the actual detection of periodic error. Also, each interferometer utilizes spatially separated beams to eliminate periodic errors.

A common design theme for periodic error free interferometry is to spatially separate the beams to avoid any source mixing. Also, minimizing the number of polarization rotations reduces the chance for periodic error. For sample stability measurements, the

main disadvantage for periodic error free interferometers is their often complex architecture with long beam paths. Thus, designing a balanced interferometer with a minimal optical path length is difficult.

For stability tests, the measured displacement is likely slow and nonlinear. This presents a problem for using algorithm techniques for correcting periodic errors and for designing a system to eliminate source mixing and beam overlap. In non-stability measurements, when the displacement is more than one fringe and linear, the algorithms can effectively detect the presence of periodic errors. This is particularly the case when using a Fourier analysis. As discussed in Appendix D, the continuous elliptical compensation algorithm is very effective correcting periodic errors in linear displacements but has errors when correcting for nonlinear displacements.

The slow and nonlinear motion of a stability measurement is an issue for designing a periodic error free interferometer because assessing the periodic error will be difficult. Because the expected measured displacement is less than 20 nm during a stability measurement and the starting point of the periodic errors is unknown, the results can still have errors at nanometer level. The maximum error from periodic nonlinearity during any 20 nm displacement is approximately 30% of the peak-to-peak periodic error value. Thus, 0.5 nm periodic error can still contribute up to 150 pm of error.

An interferometer designed to measure material stability at picometer levels should meet the following criteria. First, the input beams should be spatially separated to eliminate source mixing. Additionally, the beam paths in the interferometer should avoid coaxial beams with orthogonal polarization states. This eliminates another potential beam mixing source. If this cannot be avoided, then the necessary alignment techniques should be considered during the design phase to reduce stray reflections and ghost reflections at the detector.

Second, a frequency sweep or scan should be implemented to assess the periodic errors in the system if necessary. This will keep the balance in the interferometer but allow for a variable optical path difference greater than one fringe. This will allow for short, linear displacements to be recorded to assess the periodic errors in the interferometer. By implementing a known linear scan, it will also be possible to use periodic error correction techniques to remove any residual periodic error from stray and ghost reflections.

Third, the data acquisition system should accommodate a periodic error correction technique if necessary. Since these measurements do not need to be performed in real-time (as in feedback control systems), the computation time is not an issue. From Appendix D, the continuous elliptical compensation technique [40] showed the greatest periodic error reduction for nonlinear displacements. Thus, a continuous linear sweep correctly timed with this periodic error correction technique can be used to reduce the remaining periodic errors.

Chapter 4

Refractive Index Correction

After periodic errors are removed, the next limiting factor in most precision displacement interferometry applications is the environmental conditions of the surrounding air. A difference in the air pressure, temperature, humidity, and CO_2 concentration between measurement and reference beams, along with optical path length differences creates a situation where localized air refractive index differences occur along a beam path. These differences change the instantaneous wavelength of the light which ultimately causes measurement uncertainty because the assumed wavelength is slightly different than the actual wavelength.

Fundamentally, the phase change ($\Delta\phi$) detected from an interference signal is dependent on a length difference between two arms (L), a length change (ΔL), a refractive index of the medium (η), and a refractive index change ($\Delta\eta$) in the form of ($L\Delta\eta + \eta\Delta L$). This means the length measurement uncertainty is proportional to the total measured length which is why optical interferometry with subnanometer uncertainty is difficult to obtain, while subnanometer resolution is readily achievable [58]. Typically, refractive index changes are compensated by correcting measurements using well-known empirical equations, which were derived from theoretical models and environmental parameter measurements [28–30, 84]. In well-controlled environments with minimal air fluctuations and temperature gradients, these equations contribute a relative uncertainty of 2×10^{-8} [84], when not limited by the uncertainty of temperature, pressure, humidity and CO_2 concentration measurements.

In practice, each of these parameters must be continuously measured with low uncertainty and with the same bandwidth as the interference signal for proper in-process correction. However, this procedure is time consuming due to the necessary integration time for low uncertainty measurements for some of the environmental parameters, limiting the measurement bandwidth. Furthermore, this method has limited applicability even with minimized air turbulence because of local variations of refractive index in the beam path.

There are three different methods to measure the refractive index. The first method is an absolute refractometer where the measurement and reference paths in a balanced interferometer both start in vacuum [85–87]. Air is then slowly bled into one path to measure the absolute air refractive index. The second method is a refractometer which only detects refractive index changes by measuring balanced measurement and reference paths

where the reference path passes through a vacuum environment [88]. If absolute distance interferometry is applied to this method, the absolute refractive index can be determined. The last method uses a fixed external cavity as a reference to measure refractive index fluctuations [89–92]. These systems are typically called wavelength trackers because they can only track the refractive index changes and a separate system is needed to determine the absolute refractive index value.

An absolute refractometer typically uses optical techniques to measure the absolute air refractive index relative a vacuum where η is defined as one. Conversely, a wavelength tracker detects the refractive index changes using a cavity with a known length. Wavelength trackers typically can only detect refractive index changes; the absolute air refractive index must be initially determined from equations. Either of these techniques are suitable for stability measurements because the environment is nominally stable with minimal air turbulance and flow.

For dynamic applications, two-color interferometry[1] has been proposed and successfully demonstrated to compensate the local refractive index variations [93]. Typically, beams with 532 nm and 1064 nm wavelengths from a Nd:YAG laser or a Nd:VYO_4 laser pass through the same path as the main interference beams, so the fluctuations caused by refractive index changes affect all beams simultaneously. The refractive index can then be determined using the dispersion relationship equation, assuming dry air [94]. However, the measurement uncertainty is consequently limited by the validity of the equation and the assumed the dry air conditions. Additionally, acoustic waves have been used to measure the refractive index in some displacement interferometry applications [95]. This method has demonstrated similar measurement uncertainty to the typical equation-based methods. In either of these alternative techniques, the limiting factor is the equations governing the relationship between the measurement value and the refractive index value.

A refractive index measurement or correction technique which limits refractive index change measurement uncertainty to better than 1 part in 10^{11} is needed for stability measurements. This is three orders of magnitude better than the best available equation-based techniques. For this research, two different wavelength tracking techniques were investigated. The first technique, wavelength correcting interferometry, uses a fixed cavity Fabry-Pérot interferometer as wavelength tracker. The laser wavelength is then stabilized to the Fabry-Pérot cavity, which changes the laser frequency to correct for refractive index changes in real time. The second technique is a wavelength tracker based on a vacuum tube reference using standard heterodyne interferometry. Both topics are discussed in this chapter, including designs, results, and uncertainty analyses.

4.1 Measurement Systems

The following sections describe four different measurement systems: an absolute refractometer, a refractometer using a reference vacuum tube, a wavelength tracker based on a

[1] The term ‘two-color’ generally refers to two different laser wavelengths with a large difference between their values. Technically, all heterodyne systems are ‘two-color’ systems. However, a 20 MHz split frequency is a wavelength difference of 0.03 pm at a 633 nm wavelength. This is contrasted by red laser light (633 nm, for instance) versus green laser light (532 nm, for instance) which is a wavelength difference of 99 nm. The former is typically referred to as heterodyne interferometry, whereas the latter can be described as two-color interferometry.

fixed cavity using a heterodyne interferometer, and a wavelength tracker based on a fixed cavity using a Fabry-Pérot interferometer.

4.1.1 Absolute Refractometer

An example of an absolute refractometer by Schellekens, *et al.* [85] is shown in Figure 4.1. This refractometer uses two cavities, one with a fixed vacuum tube and one with tube which can be filled with air or evacuated to match the fixed vacuum tube. By starting both tubes in vacuum and slowly bleeding the air into one tube, the absolute refractive index can be determined.

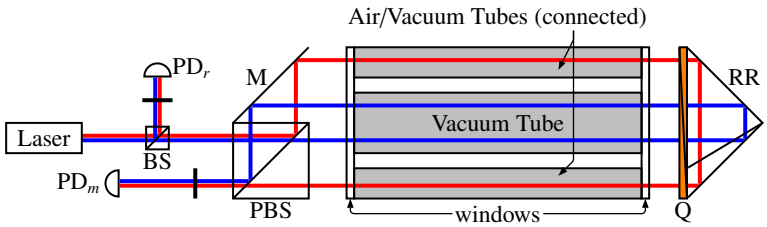

Figure 4.1: *An absolute refractometer using commercially available optical components by Schellekens, et al. [85]. A heterodyne laser with coaxial, orthogonally polarized was used in a differential setup to measure refractive index fluctuations. The two outer tubes, which are connected via piping, can be evacuated or filled with air to determine the absolute refractive index value.*

The laser source for this refractometer is a commercial source with two coaxial, orthogonally polarized beams with an offset frequency between them. A part of the output beam is split using a beamsplitter to generate a reference signal. The two orthogonal beams are interfered using a polarizer aligned to 45° about the azimuthal angle. This is then detected using PD$_r$, generating the reference signal. The remaining beam travels to the polarizing beamsplitter where it is split into measurement and reference arms. The reference arm is transmitted through the polarizing beamsplitter and passes through the vacuum tube. The beam then passes through a quarter wave plate and reflects off a retroreflector. The beam is then offset and passes back through the quarter wave plate and vacuum tube for a second time. The beam then reflects off a mirror and the polarizing beamsplitter where it is interfered with the measurement beam.

The measurement beam reflects off the polarizing beamsplitter and mirror. The beam then passes through a window into another tube which can be evacuated or filled with air. The beam then passes through the quarter wave plate, reflects off the retroreflector, and then passes back through the quarter wave plate. The measurement beam then passes through the fillable tube for a second time. The beam then transmits through the polarizing beamsplitter where it interferes with the measurement beam at the 45° polarizer.

This refractometer configuration by Schellekens, *et al.* has several advantages. The sensing principle is heterodyne interferometry which has a high signal to noise ratio. The alignment is not susceptible to tilt fluctuations because a retroreflector is used instead of a mirror. However, it does require a larger vacuum tube and optical components, increasing the overall size. Additionally, by starting with two evacuated tubes (inner and outer), the

outer tube can be exposed to the air to determine the absolute refractive index value. Thus, this system is good for both tracking applications and absolute refractometry.

4.1.2 Vacuum Reference Cavity

Figure 4.2 shows a simple refractometer by Terrien [88] which can be used for wavelength tracking. The input beam is split into measurement and reference arms using a plate beamsplitter. The reference beam transmits through the beamsplitter and reflects off a mirror. It then passes through a window into a vacuum tube. The reference beam then exits the vacuum tube and reflects off another mirror before passing through the vacuum tube for a second time. The beam the reflects back off the mirror and beamsplitter where it interferes with the measurement beam. The measurement arm follows a similar path expect it initially reflects off the beamsplitter and does not travel through the vacuum tube, although is still passes through both windows.

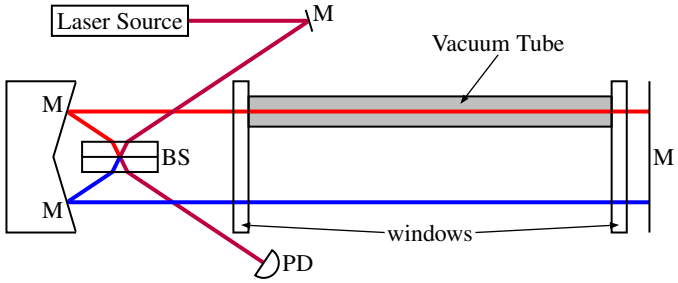

Figure 4.2: *Schematic of a refractometer demonstrated by Terrien [88]. An input beam is split where one arm passes through a vacuum tube twice while the other arm follows a balanced path in air.*

The interference signal detected by the photodiode is used to detect optical path length changes between the measurement and reference arms. The nominal path length of the measurement and reference arms are balanced and both beams pass through the same number of components. The difference between the two signals is caused by the vacuum tube. The refractive index in a vacuum is one whereas the refractive index of air is approximately 1.00027, at standard temperature and pressure, and is a function of temperature, pressure, humidity, and CO_2 concentration. Even though the physical length is nominally the same between both arms, changes in the environmental parameters will appear as a length change and is detected by the photodiode.

This type of refractometer relies on homodyne interferometry and is not direction sensitive. Additionally, the interference signal is sensitive to optical power changes, which is a particular problem because the intensity of the measurement arm may changed due to scattering and absorption.

Using a vacuum tube can cause some issues when designing an interferometer to measure refractive index changes. Systems without a fixed vacuum tube must account for piping to evacuate the vacuum tube. Also, the window deformation from pressure changes must be considered in the design and mounting. Also, the windows should be compensated in the other arm of the interferometer, which can lead to more complex designs.

4.1.3 Low Expansion Reference Cavity

An alternative method to measure refractive index changes uses a fixed reference cavity with a known nominal length. Figure 4.3 shows an example of a commercial refractometer [89]. As with the refractometer by Schellekens, *et al.*, this refractometer uses a standard commercial heterodyne laser source.

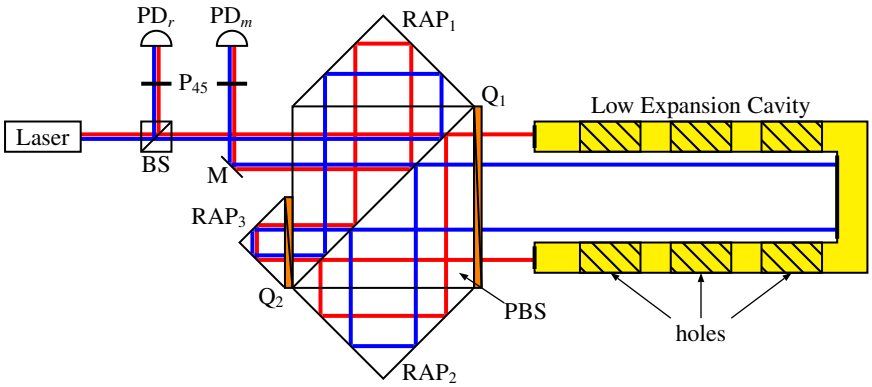

Figure 4.3: *Schematic of a commercial wavelength tracker by Agilent, Inc. [89]. Rather than using a vacuum tube, this refractometer uses a stable, low thermal expansion reference cavity to measure refractive index changes.*

A part from both beams is split from the laser source using a beamsplitter. A polarizer aligned to 45° is used to interfere the two beams and PD$_r$ is used to measure the reference signal. The remaining part from the laser source is sent to a polarizing beamsplitter where it is split into measurement (blue) and reference arms (red).

The reference beam transmits through the polarizing beamsplitter where it reflects off the front of the low expansion cavity after passing through Q$_1$. The reference beam passes back through the Q$_1$ where it is rotated 90° from its original polarization state. The beam then reflects off the polarizing beamsplitter where it is sent to RAP$_2$. RAP$_2$ displaces the reference beam and send it back to the polarizing beamsplitter where it reflects again. The beam then passes through Q$_1$ where it reflects off the low expansion cavity a second time. When it passes back through Q$_1$, its polarization state is rotated back to its original form, which means it will transmit through the polarizing beamsplitter. The reference beam then passes through Q$_2$ and is offset by RAP$_3$. The beam then reflects off the polarizing beamsplitter after passing through Q$_2$. The beam is then sent to RAP$_1$ on top of the polarizing beamsplitter where it reflects again and is eventually steered to a polarizer and PD$_m$.

The measurement beam (blue) reflects off, in this order, the polarizing beamsplitter, RAP$_1$, and the polarizing beamsplitter again, before it passes through Q$_2$. It reflects off RAP$_3$ and passes through Q$_2$ a second time, where it now transmits through the polarizing beamsplitter. The measurement beam then passes through Q$_1$ and enters into the cavity where it reflects off the back surface. Upon reflection, the beam then exits the cavity, passes through Q$_1$, where it reflects off the polarizing beamsplitter, RAP$_2$, and the polarizing beamsplitter again. It passes through Q$_1$ and enters the cavity a second time. After

reflecting off the back surface a second time, the measurement beam then passes through Q_1, polarizing beamsplitter, and interferes with the reference beam at a polarizer aligned to 45°. The measurement signal is then detected with PD_m.

The measured phase change from this interference signal is a function of path length changes, frequency changes, and refractive index changes. If the cavity remains nominally stable and the laser frequency is stable, then the change in the phase difference between PD_r and PD_m is only due to refractive index fluctuations. This assumes the material used for the cavity is stable and has a low thermal expansion coefficient because fluctuations in cavity length will be measured in the phase difference. Also, the mirrored surfaces should either be machined directly onto the cavity or be mounted in a thermally neutral position. This can increase the cost of the reference cavity or introduce stresses from the mirror mounts which make reduce cavity stability over time.

4.1.4 Fabry-Pérot Reference Cavity

Another type of refractometer uses a Fabry-Pérot cavity. A Fabry-Pérot cavity consists of two highly reflecting surfaces, typically one flat and one concave mirror, which help create multiple interferences. The input light passes through the first mirror and reflects off the second mirror and travels back to the first mirror. When the light hits the first mirror, a part is transmitted but the majority is reflected. The reflected part passes back through the cavity and reflects off the second mirror again. This is repeated until the light finally exits the cavity.

If a continuous laser source is used, then light will be added to the cavity continuously and multiple interferences occur prior to exiting. Figure 4.4 shows a schematic of a Fabry-Pérot cavity with short pulse input and the power decaying (denoted by the line width) after multiple passes. If the cavity length matches the frequency of the input light, then the multiple interferences create constructive interference. Conversely, if the cavity length does not match the frequency of the light, destructive interference occurs.

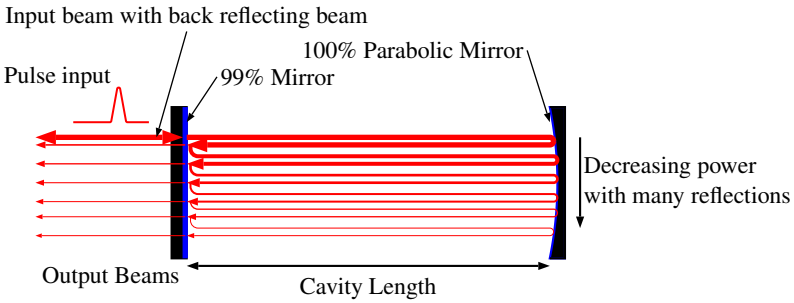

Figure 4.4: *Example of a Fabry-Pérot cavity with multiple reflections. The line width is representative of the optical power. As the number of passes increases, the output power drops. The beams are non-overlapping for clarity. In practice, all beams are coaxial if the windows are aligned properly.*

The multiple passes in a Fabry-Pérot cavity make it highly sensitive to laser frequency changes, refractive index changes, and cavity length changes. When a fixed reference cavity with thermally neutral mirrors is used and a frequency stabilized laser is used as the input,

the change in refractive index can be measured with high sensitivity, provided the laser frequency matches the cavity. Conversely, a tunable laser can be locked to the Fabry-Pérot resonance peak and the measured frequency shift relative to the frequency stabilized laser can be used to determine the length change of the cavity when a mirror is moved [96–99]. However, if the cavity length is fixed and a tunable laser is locked to the resonance peak, refractive index changes in the cavity can then be measured using the frequency shift relative to a reference laser.

This principle was used to measure refractive index changes and implement wavelength corrected interferometry during this research. The principles of traceable Fabry-Pérot interferometry and the design of a wavelength corrected interferometer, along with experimental setups and results are presented in the following sections.

4.2 Wavelength Corrected Interferometry

One way to correct for refractive index fluctuations in real time is to use wavelength corrected interferometry. In wavelength corrected interferometry, the refractive index changes are compensated by changing the laser frequency of the optical source used for the interferometer. In this research, wavelength corrected interferometry was applied to traditional displacement interferometry to compare its effectiveness to equation-based methods.

The optical frequency of the interferometry source was locked to the resonance peak of an open Fabry-Pérot cavity. When the cavity is dimensionally stable, refractive index changes measured in the cavity are appropriately corrected by changing the optical frequency, directly linking the refractive index changes to frequency changes. This method can compensate the interferometer wavelength for refractive index changes in real time, eliminating the bandwidth issues of equation-based corrections. A part of the optical source used to do this wavelength corrections and the remaining part is sent to a heterodyne laser interferometer which then measures the displacement independent of the refractive index fluctuations.

Compared to other wavelength tracking methods [85–92, 100, 101], this method does not need any post calculation procedure to compensate the refractive index because the refractive index change is automatically linked to the optical frequency and compensated with the relationship of phase and measurement errors. Figure 4.5 shows the optical configuration for a generic wavelength corrected heterodyne laser interferometer. The optical frequency of a single mode HeNe laser is locked to the resonance peak of an open Fabry-Pérot cavity with the Pound-Drever-Hall (PDH) method [102], which is based on the phase modulation from an electro-optic modulator and demodulation with a lock-in amplifier. After locking, the refractive index fluctuations are directly converted to optical frequency fluctuations using a thin-film heater to control the HeNe laser tube length.

The main part of the beam from the single mode HeNe laser is then converted to heterodyne signals using frequency or continuous phase modulation. The heterodyne signals are then sent to the interferometer where the measurement target is located near the Fabry-Pérot cavity to ensure high correlation between refractive index fluctuations. Because the source frequency is locked to the resonance peak of the open Fabry-Pérot cavity and affected by refractive index changes, the errors originating from refractive index changes

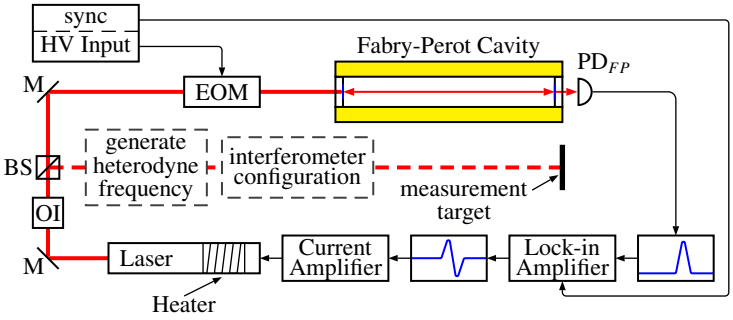

Figure 4.5: *The optical configuration for a wavelength correcting heterodyne laser interferometer. The optical frequency of the source is locked to Fabry-Pérot cavity which compensates for refractive index fluctuations in the heterodyne interferometer.*

are automatically cancelled in the interferometer.

When the optical frequency of the source is locked to the resonance peak of an open Fabry-Pérot cavity in air, the frequency fluctuation (Δf) can be expressed with the cavity length change (Δl) and the refractive index change of air ($\Delta\eta$) by

$$\frac{\Delta f}{f} = -\frac{\Delta l}{l} - \frac{\Delta \eta}{\eta} \tag{4.1}$$

where f is the nominal optical frequency of the source, l is the cavity length, and η is the air refractive index [98]. As shown in Equation 4.1, linking the refractive index changes to the source frequency changes is desirable if the cavity length changes can be ignored. To minimize this effect, the cavity can be constructed using thermally stable material such as Zerodur®, which has a thermal expansion coefficient of approximately 0.05 $\mu m \cdot m^{-1} \cdot K^{-1}$ at room temperature. Then, measuring Δf allows for tracking the refractive index changes without any other sensors. Moreover, the frequency measurement improves the measurement sensitivity and accuracy when a highly stable reference frequency is used. In most of cases, however, the reference laser, typically an iodine stabilized HeNe laser, is needed to determine the optical frequency in this type of wavelength tracker, and this limits the applicability and adds complexity and cost.

Since refractive index changes and frequency changes are couple through the cavity, length changes in the cavity will cause a displacement measurement error. The phase, θ, of an interference signal obtained from a displacement interferometer is related to the geometrical path length, x, and air refractive index by

$$\theta = \frac{2\pi N \eta f x}{c} \tag{4.2}$$

where c is the speed of light in vacuum, N is an integer pertaining to the optical resolution. The displacement of the target (Δx) is derived from Equation 4.2 as

$$\Delta x = \frac{c\Delta\theta}{2\pi N} - \left(\frac{\Delta f}{f} + \frac{\Delta \eta}{\eta}\right) x \tag{4.3}$$

where the Δ's represent the change in a nominal value during a measurement period. Apart from the displacements from the phase information, the additional terms caused by Δf and

$\Delta\eta$ lead to the measurement errors as shown in Equation 4.3. To reduce these errors, a frequency stabilized source and refractive index compensation using equations are typically used. In this investigation, a wavelength tracking technique to remove the additional terms in the displacement is used. When the optical frequency of the source in the interferometer is locked to the open Fabry-Pérot cavity, Δx can be rewritten as

$$\Delta x = \frac{c\Delta\theta}{2\pi N} - \left(-\frac{\Delta\eta}{\eta} - \frac{\Delta L}{L} + \frac{\Delta\eta}{\eta}\right)x = \frac{c\Delta\theta}{2\pi N} + \frac{\Delta L}{L}x \tag{4.4}$$

by substituting Equation 4.1 into Equation 4.3. When a thermally stable cavity with thermally neutral mirrors are used, $^{\Delta Lx}/_{L}$ can largely be ignored. The residual cavity length change is an uncertainty source and must be considered in the full analysis. This will be explained later in Section 4.2.4. Consequently, the error caused by refractive index fluctuations is cancelled by changing the source frequency and thus, the real displacement can be measured independent of refractive index fluctuations. This assumes the refractive index in the Fabry-Pérot cavity is the same in the displacement interferometer measurement and reference arms.

4.2.1 Transmission Fabry-Pérot Interferometer

A transmission Fabry-Pérot interferometer was used in this research for wavelength tracking and correcting. Figure 4.6 shows a schematic of the transmission Fabry-Pérot interferometer. A beam from a tunable HeNe laser tube is isolated using a free space optical isolator. A part is then split and mixed with a beam from a frequency stabilized laser. The interference is then detected using an avalanche photodiode and a frequency counter is used to measure the frequency difference.

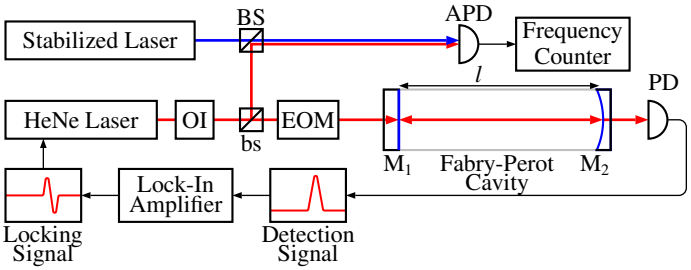

Figure 4.6: *Optical configuration of a transmission Fabry-Pérot interferometer and wavelength tracker. The output beam from the cavity exits on the opposite side from the input, eliminating the high power back-beam.*

The beam not sent to interfere with the reference laser passes through an electro-optic modulator, which continuously and linearly changes the phase. The beam then enters the Fabry-Pérot cavity where multiple reflections and interferences occur. A part is transmitted through the opposite side of the cavity where the DC optical power is detected. This signal is then sent to a lock in amplifier, which is used to tune the laser frequency to maintain a resonance peak in the Fabry-Pérot cavity. A transmission Fabry-Pérot cavity is only one type of Fabry-Pérot cavity that can be used. Appendix E describes other cavity designs investigated during this research.

The signal exiting the Fabry-Pérot cavity is [103]

$$(FP_T) = t_1 t_2 \mathrm{e}^{ikl} + t_1 t_2 r_1 r_2 \mathrm{e}^{3ikl} + t_1 t_2 r_1^2 r_2^2 \mathrm{e}^{5ikl} + t_1 t_2 r_1^3 r_2^3 \mathrm{e}^{7ikl} + \cdots \quad (4.5)$$

$$= t_1 t_2 \mathrm{e}^{ikL} \sum_{p=0}^{\infty} (r_1 r_2)^p \, \mathrm{e}^{2pikl}, \quad (4.6)$$

where k is the wavenumber ($2\pi/\lambda$), $t_{1,2}$ and $r_{1,2}$ are the electric field transmission and reflectivity coefficients for M_1 and M_2, respectively. Equation 4.6 is a geometric series of the form

$$y = a + ax + ax^2 + ax^3 + \cdots \quad (4.7)$$

$$= \sum_{p=0}^{\infty} ax^p, \quad (4.8)$$

whose sum converges to a solution, providing x is less than one. The sum of Equation 4.8 is

$$y_\Sigma = \frac{a}{1-x}. \quad (4.9)$$

Applying Equation 4.9 to Equation 4.6 yields

$$(FP_T)_\Sigma = \frac{t_1 t_2 \mathrm{e}^{ikL}}{1 - r_1 r_2 \mathrm{e}^{2ikl}}. \quad (4.10)$$

The total irradiance of the light exiting the Fabry-Pérot, $I_{FP,T}$ is $(FP_T)^*_\Sigma (FP_T)_\Sigma$. Using this, the gain is

$$\frac{I_{FP,T}}{I_i} = \frac{t_1^2 t_2^2}{\left(1 + r_1^2 r_2^2\right) - 2 r_1 r_2 \cos(2kl)}, \quad (4.11)$$

where I_i is the input irradiance from the laser source. The gain can be simplified by

$$\frac{I_{FP,T}}{I_i} = \frac{T_1 T_2}{(1 + R_1 R_2) - 2\sqrt{R_1 R_2}\cos(2kl)}, \quad (4.12)$$

where $T_{1,2}$ is the irradiance transmission coefficient ($T_i = t_i^2$) and $R_{1,2}$ is the reflectance coefficient ($R_i = r_i^2$) for $M_{1,2}$, respectively. But, in the complete system shown in Figure 4.6, there are more components which affect the measured intensity from the Fabry-Pérot. Thus,the irradiance of the complete transmission Fabry-Pérot detected by the photodiode is

$$\frac{I_{sys,T}}{I_i} = \frac{T_1 T_2 T_{OI} T_{bs} T_{EOM}}{(1 + R_1 R_2) - 2\sqrt{R_1 R_2}\cos(2kL)}, \quad (4.13)$$

where T_{OI} is the optical isolator irradiance transmission coefficient, T_{bs} is the beam sampler irradiance transmission coefficient, T_{EOM} is the electro-optic modulator irradiance transmission coefficient. If an ideal case is assumed, then T_{OI} is 90 %, T_{bs} is 96 %, T_{EOM} is 90 %. Additionally, both M_1 and M_2 must be partially transmissive, thus, $R_{1,2}$ was assumed to be 99 % reflective. Figure 4.7 shows the Fabry-Pérot gain and system gain as a function of cavity displacement, where $R_{1,2}$ is 1-$T_{1,2}$.

The maximum efficiency of the Fabry-Pérot cavity is approximately 100 % at resonance and drops approximately 18 % when the initial components in the complete system are

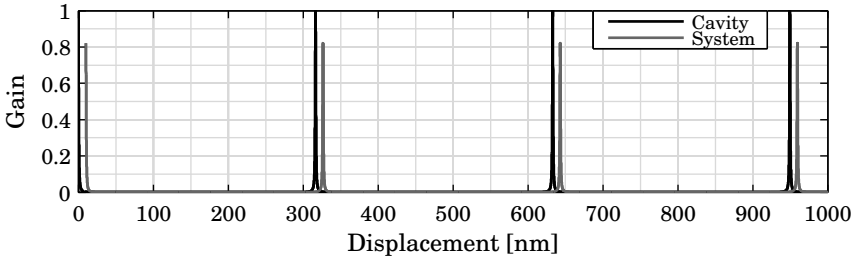

Figure 4.7: *Ideal gain of the transmission Fabry-Pérot cavity and system as a function of cavity displacement. The system includes modest losses in components before the Fabry-Pérot cavity. The system plot is offset in the X-axis for clarity.*

considered. The difference between the ideal cavity gain and the complete system can be mitigated by using high quality components with a low absorption. Figure 4.8 shows the transmission peak for both the cavity and system with different mirror coefficients, assuming $R_1 = R_2$.

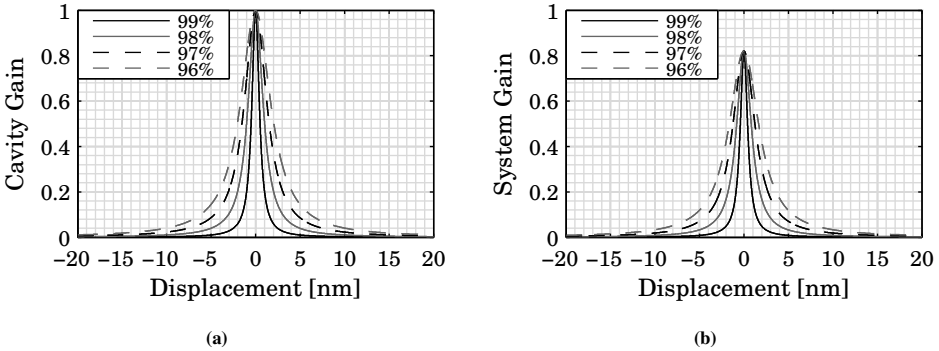

Figure 4.8: *Close-up of a single resonance peak of the (a) cavity and (b) system in the transmission Fabry-Pérot interferometer. These values are from a numerical simulation where M_1 and M_2 both had the reflection value labeled in the figure.*

The mirror inefficiencies do not limit the peak intensity. Instead of decreasing in value, the mirror inefficiency causes the peak to be broader. This is called an increased linewidth which is a critical component for determining the locking stability. More will be discussed on this topic when discussing the Fabry-Pérot locking uncertainty.

4.2.2 Refractive Index Tracking

Figure 4.9 show a photograph of the experimental setup of the wavelength tracker in this research. A single mode HeNe laser [104] with an attached flexible heat film was used as the optical source and was mounted in an aluminum block. The optical isolator was used to prevent destabilization from the Fabry-Pérot reflected back-beam and a half wave plate was used to rotate the polarization state. The light was phase modulated after passing through an electro-optic modulator [105] and incident to the open Fabry-Pérot cavity. Then,

the transmitted light from the cavity was detected with a photodiode and converted to an electronic signal used for the PDH locking method. The demodulated signal from the commercial lock-in amplifier [106] was amplified and used for feedback to operate a current amplifier and a thin film resistive heater which controlled the laser tube length.

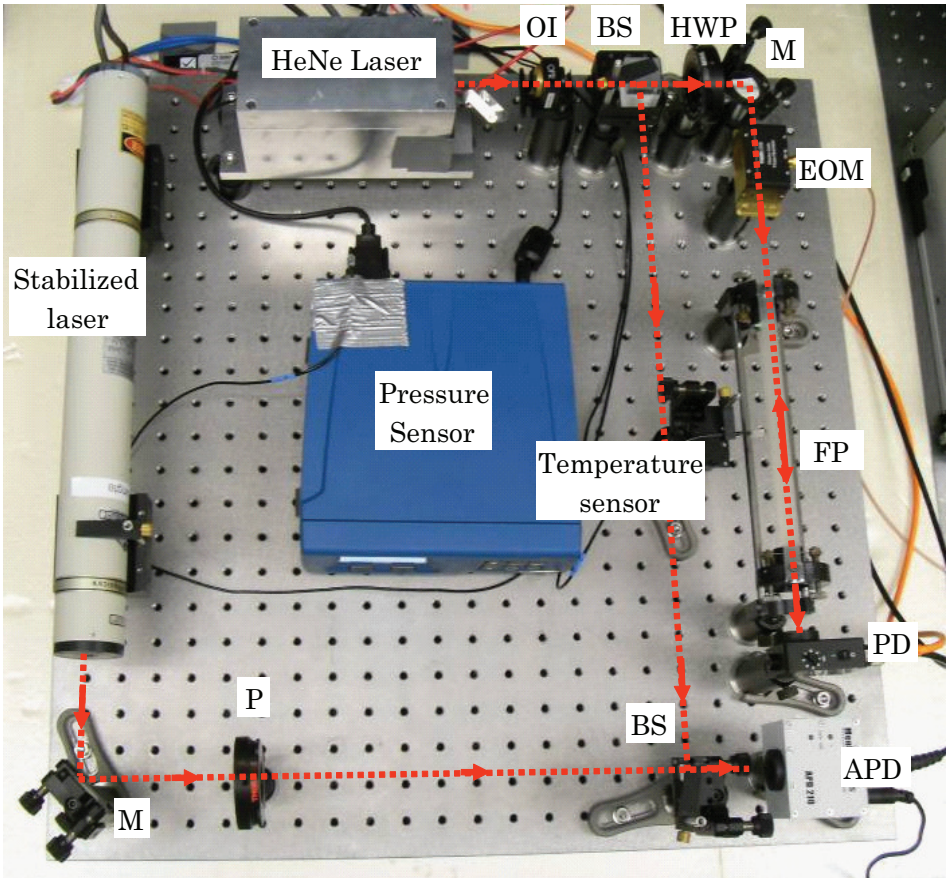

Figure 4.9: *Photo of the wavelength tracker setup.*

The open Fabry-Pérot cavity was 175 mm long and consisted of two parabolic mirrors, kinematic mirror mounts, and two 200 mm long Zerodur® rods to minimize the thermal expansion. The optical frequency shift was measured using a commercial frequency stabilized HeNe laser [107] with a fractional frequency stability of 2×10^{-10} (10 s).

The performance of the wavelength tracker was evaluated by measuring the environmental parameters concurrently with the frequency shift due to refractive index changes in the Fabry-Pérot cavity. During approximately two hours (7000 s), the relative refractive index slightly increased by 3.26×10^{-7} with slow oscillations caused by temperature and pressure changes in the laboratory as shown in Figure 4.10. The frequency shift measured from the avalanche photodiode was converted to the refractive index values using Equation 4.1 to compare with the calculated value from the Edlén formula [28]. The experimental results show the frequency tracked the refractive index fluctuations well and the standard deviation

of the difference was 4.93×10^{-8}.

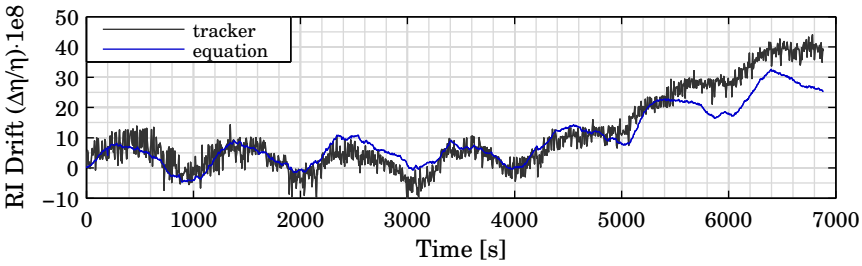

Figure 4.10: *Experimental results of the wavelength tracker compared to the results by calculated by the Edlén equation. The standard deviation of the difference was 4.93×10^{-8}.*

4.2.3 Wavelength Corrected DMI

The single mode HeNe laser whose frequency was locked to the open cavity, was directly used as an optical source for the wavelength corrected heterodyne laser interferometer. As previously mentioned, the system consists of two main parts: a wavelength tracker and a heterodyne laser interferometer. The optical schematic is shown in Figure 4.11 and a photograph of the setup is shown in Figure 4.12.

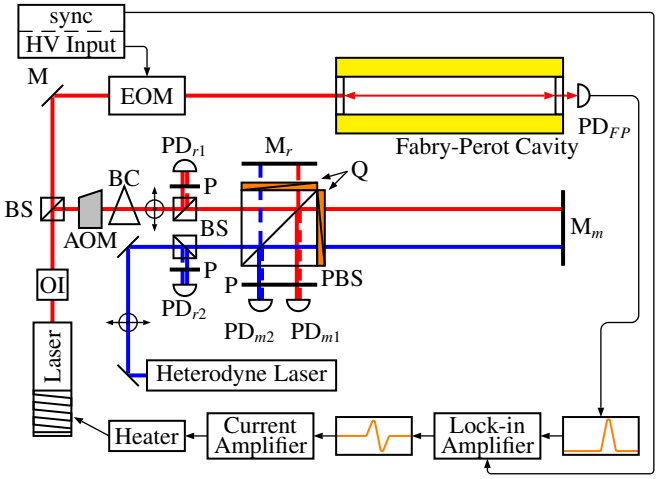

Figure 4.11: *Optical schematic of the wavelength tracking interferometer and commercial heterodyne laser interferometer measurement. The wavelength tracking interferometer is corrected for refractive index fluctuations in real-time while the commercial system is corrected using equations.*

The optical frequency of a single mode HeNe laser is locked to the resonance peak of the open Fabry-Pérot cavity using the PDH method. After locking, the refractive index fluctuations are directly converted to optical frequency fluctuations using a thin-film heater

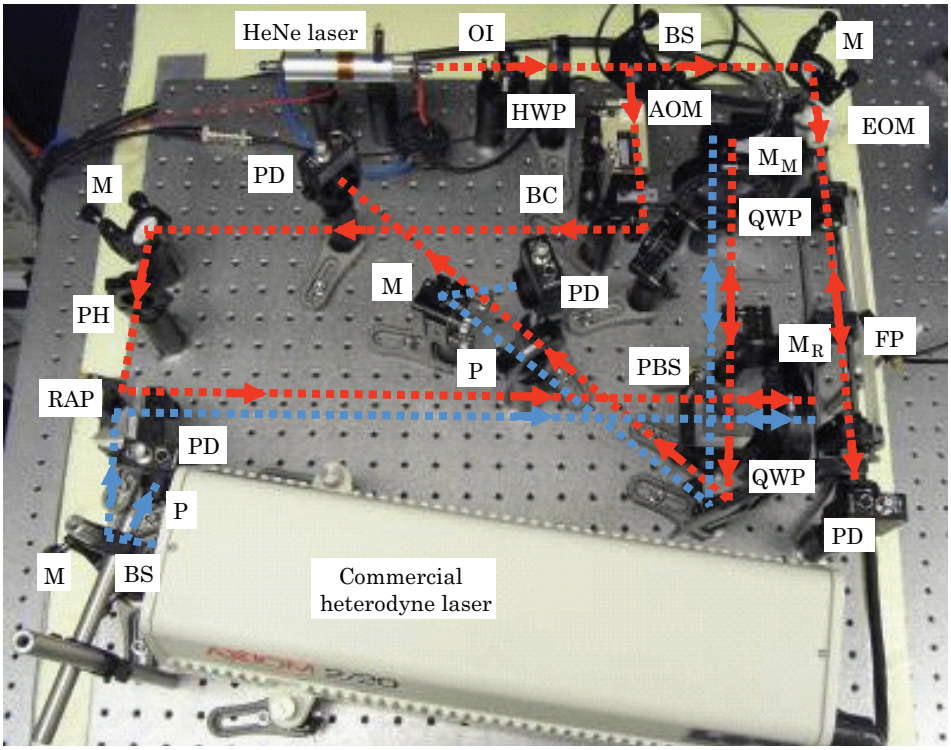

Figure 4.12: *Photo of the optical setup for wavelength tracking.*

to control the HeNe laser tube length. The main part of the light from the single mode HeNe laser, now with the corrected wavelength, passes through an acousto-optic modulator to generate the split frequency for the heterodyne laser interferometer. The original beam and the frequency-shifted beam from the acousto-optic modulator are coaxially overlapped using a birefringent crystal. While not completely coaxial, the spatial separation is small because the distance between the acousto-optic modulator and the birefringent crystal is kept to a minimum [108]. The 'coaxial', orthogonally polarized beams are then used in a single pass, polarizing Michelson interferometer to measure the displacement difference between the reference mirror M_r and the measurement mirror M_m.

For comparison, a commercial heterodyne laser interferometer [109] was used to measure displacement of the target in addition to this wavelength correcting system. Because both interferometers pass through the same optical components and the same nominal air path, refractive index fluctuations and interferometer motions affect both interferometers simultaneously. The measurement paths of both interferometers are close to the Fabry-Pérot cavity to minimize the environmental difference from spatially separated measurements. The reference and measurement mirrors are fixed and only move by the thermal expansion of the base plate. The wavelength corrected interferometer is the red beams and the conventional interferometer is the blue beams in Figures 4.11 and 4.12.

Figure 4.13 shows the measurement results of the wavelength correcting interferometer compared to the traditional Michelson interferometer. In the wavelength correcting interferometer, the displacement difference between measurement and reference path,

caused by the thermal expansion, was approximately 100 nm during 10 minutes while the displacement by the normal interferometer was less than the 100 nm due to refractive index fluctuations. The temperature and pressure was also measured and used to compensate the displacement of the traditional interferometer using the Edlén equation [28]. The difference between the equation-corrected and wavelength corrected measurements is also shown in Figure 4.13. The standard deviation of the difference between the equation-corrected measurements and the in-process wavelength correcting interferometer is 2 nm.

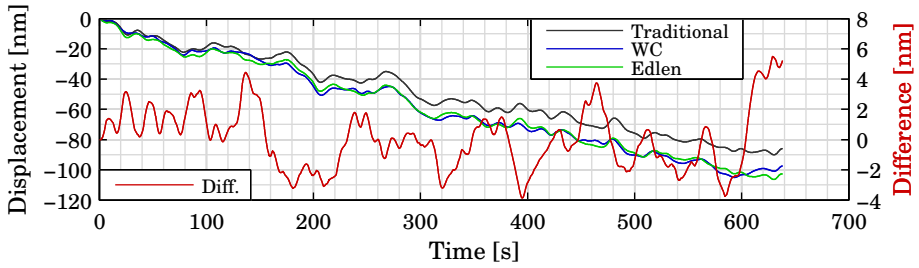

Figure 4.13: *Experimental results comparing the traditional interferometer measurement, the traditional interferometer measurement corrected using the Edlén equation, and the wavelength correcting (WC) interferometer. The difference between the equation-corrected and the wavelength-corrected measurements (Diff.) had a standard deviation is 2.02 nm.*

4.2.4 Uncertainty analysis

Although the experimental results of the wavelength correcting interferometer compared favorably to conventional measurements (compensated by well-established equations), the measurement uncertainty based on the theoretical model and practical measurements should be evaluated in order to validate the system performance. The main uncertainty sources are the locking stability, the cavity length stability, and environmental difference between two regions, summarized in Table 4.1.

Table 4.1: *Uncertainty analysis results for correction of the displacements caused by the refractive index fluctuation in the interferometer. The Fabry-Pérot temperature change is ΔT and the displacement of the measurement target is Δx*

	Locking Stability Δf	Length Stability $\Delta l/l$
Value	1.46 MHz	–
Relative Uncertainty	3.1×10^{-9}	$-0.89\times10^{-6}\Delta T$
Uncertainy	$3.1\times10^{-9}\Delta L$	$-0.89\times10^{-6}\Delta T\Delta L$

The frequency locking stability is determined by the transmission peak linewidth and the free spectral range (FSR) of the cavity. The transmission peak linewidth ($\Delta\nu$) was

previously determined based on an estimate of 98.8 % reflectance of both M_1 and M_2. In these experiments, $\Delta\nu$ was 3.29 MHz and the FSR range was 857.1 MHz. The peak signal from the detector was 0.330 V and the minimum voltage signal in the locking region was 0.183 V. From this data, the frequency locking range, regarded as the locking stability in this investigation, was 1.46 MHz and the relative stability was 3.1×10^{-9} [97].

In the wavelength correcting interferometer, the most important parameter is the cavity length stability because the cavity length should be fixed during the measurement to effectively correct the refractive index fluctuations as expressed in Equations 4.1 and 4.4. Thermal effects are typically the main cause for cavity instability, thus stable materials are needed for the cavity. As shown in Figure 4.14, the cavity consists of two Zerodur® rods to minimize thermal expansion and has two aluminum kinematic mirror mounts with steel thumbscrews for mirror adjustments.

Figure 4.14: *Photo of the Fabry-Pérot cavity with the Zerodur® supports, aluminum adjustable mirror mounts, and steel thumbscrews. The thermal expansion in the cavity is dominated by the steel thumbscrews based on the mirror positions relative to the supports*

From one fixed point to the other, the rod length is 190 mm and the actual cavity length is approximately 175 mm when the mirrors are on the mounts. Based on the position of the thumbscrews and the location of the mirrors in the mounts, the thermal expansion of the mirror mount is largely driven by the expansion of the thumbscrews. The thermal expansion length change of the cavity (Δl) according to the temperature change (ΔT) is

$$\frac{\Delta l}{l} = \frac{(0.19\alpha_z - 0.015\alpha_s)}{0.175} = -0.89\ \mu\text{m}\cdot\text{m}^{-1}\cdot\Delta T \tag{4.14}$$

where α_z (=0.05 $\mu\text{m}\cdot\text{m}^{-1}\cdot\text{K}^{-1}$) and α_s (=11 $\mu\text{m}\cdot\text{m}^{-1}\cdot\text{K}^{-1}$) are the thermal expansion coefficients of Zerodur® and steel, respectively.

In these measurement, the environmental conditions between the Fabry-Pérot optical path, the temperature sensors, pressure sensor, and the interferometer's measurement path are assumed identical. The system was shielded from air flow and the length change was slow which eliminates dynamic refractive index changes due to stage motions. This is critical for satisfying Equation 4.4.

In practical situations, however, it is not possible to have the exact environmental conditions and measure the differences for all parameters in both regions. To avoid the errors from the environmental difference, the cavity should be located near the interferometer's measurement path with a minimal gap.

Moreover, this type of interferometric system is difficult in applications where dynamic motion, such as high speed stages, causes localized transient pressure changes which are not

correlated in the cavity locking measurement. In static applications, where the environment is well controlled, the refractive index fluctuations can be successfully corrected without any environmental sensors and time delay using this method.

4.2.5 Wavelength Correction Conclusions

As shown in Table 4.1, the dominant uncertainty source of the experimental setup in this investigation is the effective thermal expansion coefficient of the cavity (-0.89 $\mu m \cdot m^{-1} \cdot K^{-1}$), which is slightly lower than the temperature sensitivity of the refractive index ($1 \times 10^{-6} \cdot K^{-1}$). The kinematic mirror mounts, which were used for precise mirror alignment, led to a worsening of the cavity stability. One consideration is the thermal capacitance of the aluminum and steel, which effectively creates a buffer to temperature changes, which contributes some stability. However, the Fabry-Pérot cavity should be redesigned to minimize the thermal effects, for example, by directly fixing the mirrors to a low expansion support or by using another low expansion material for the kinematic mounts. Also, designing thermally neutral mirror mounts can minimize the thermal expansion effect. This enhancement can reduce the effective thermal expansion coefficient by at least an order of magnitude and thus the uncertainty will be less than in the current system.

Another important issue is the laser locking stability, which determines the short term noise level in the system. The locking stability is affected by the cavity linewidth, control electronics, and actuator bandwidth to change the source laser frequency. Among these three, the actuator performance is critical for a high bandwidth. A resistive thin-film heater was attached to the glass surface of a HeNe laser and used to control the length via thermal expansion in this investigation. Because of the HeNe laser construction and the thin-film heater response time, the heat was slow in transferring to the laser cavity and this caused a time delay in the control loop. As the result, the locking stability was 1.46 MHz, which is low for this kind of system.

For better stability, the thin-film heater should be replaced with a faster actuator such as a piezo-electric transducer. In this case, the locking stability is expected to be better than 1 MHz but careful attention is needed to avoid the alignment problems or PZT hysteresis. A more efficient way is to use a tunable diode laser with current-controlled feedback. This will increase the cost and nominal laser linewidth for the heterodyne system, but the response bandwidth is extremely high and the wider gain bandwidth allows for a smaller cavity.

As previously discussed, this wavelength corrected heterodyne interferometer has several advantages when applied to static measurement applications. Numerous simultaneous environmental parameter measurements are not necessary to correct for refractive index fluctuations. After the initial wavelength is determined, the wavelength in air can be automatically tracked with the Fabry-Pérot which can be used for a stabilized frequency reference and refractive index sensing during a measurement. In addition, there is no time delay for environmental measurements which typically have long integration times relative to the desired measurement bandwidth. The only limit here is the locking stability, and, in turn, bandwidth of the actuator controlling the laser tube length. In principle, this can be orders of magnitude higher than precise temperature and pressure measurements, potentially with the same measurement bandwidth as the desired measurement system. This allows for real time refractive index measurement and correction.

4.3 Heterodyne Phase Tracking

While Fabry-Pérot interferometry is an effective method for measuring refractive index fluctuations, it requires a completely different setup than a traditional displacement interferometer, which must be calibrated and characterized. This adds to the overall system complexity because a free space cavity and a vacuum cavity is needed, along with the corresponding optical components.

More importantly, there is an unknown correlation between the refractometer and the sample-measuring interferometer. Determining this correlation can be difficult, specifically when considering the systematic effects. Therefore, it is beneficial to implement a refractometer within the sample measuring interferometer rather than having a completely separate system. The refractive index change can be measured in a directly correlating system which leaves only the length difference correlation between the sample and vacuum tube. This type of interferometer is described in the following section, including example interferometers and uncertainty estimates.

4.3.1 Example Interferometer System

An interferometer with an internal wavelength tracker assumes there are essentially two interferometers in the sample measuring interferometer, one to measure the sample fluctuations and one to measure the refractive index changes. This also means interferometer instability is largely common to both systems. Thus, the instability would be reduced when the difference between the two systems is taken.

An example of a sample measuring interferometer with an internal refractometer is shown in Figure 4.15. As shown in Chapter 3, spatially separating the input beams is an effective method to limit periodic errors. This interferometer uses a source similar to the source presented in Section 3.2. One beam is directed to the left side of the interferometer where the beam's polarization is aligned to pass through PBS_1. This beam, with frequency f_1, is then split equally and aligned to have a spatial offset using a BS_1 and M_1. This separation is the main splitting between sample measuring (solid line) and refractive index measuring (dashed line) interferometers.

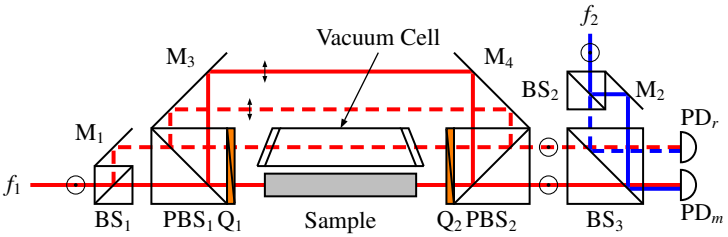

Figure 4.15: *Schematic of a dual interferometer with one interferometer measuring sample displacements while the other measures refractive index fluctuations. While this interferometer is not balanced, it is an example system used for performing an uncertainty analysis.*

The sample measurement beam passes through PBS_1 and Q_1 (aligned to 45°). This beam then reflects off the sample, passes back through Q_1 where the polarization is rotated 90°.

Now the beam reflects off PBS_1, M_3, and M_4, where it then reflects off PBS_2 and passes through Q_2. The beam then reflects of the sample's right side, and passes back through Q_2 and PBS_2. Finally, the beam passes to BS_3 where it interferes with a reference beam with frequency f_2 and is detected by PD_m.

The refractive index measuring interferometer follows a slightly different path. After being initially split, this beam passes through PBS_1 and Q_1, where it then passes through the vacuum cell. Upon exiting, the beam passes through Q_2. Since both quarter wave plates have the same orientation, the net effect is that of a half wave plate with a 45° orientation. The polarization state of the beam is rotated 90°, where it reflects off PBS_2. After reflecting off M_4, M_3, and PBS_1, the beam then passes through Q_1, the vacuum cell, and Q_2 for a second time. Now, the beam's polarization state is rotated back to 0°, where it passes through PBS_2. The beam then interferes with a reference f_2 beam and is detected by PD_r.

The signal detected by PD_r will have phase changes from refractive index fluctuations and interferometer vibrations. The signal detected by PD_m will have phase changes from refractive index fluctuations, interferometer vibrations, and sample length changes. Thus, both signals can be used to cancel refractive index fluctuations and interferometer vibrations.

This interferometer has several advantages. First, it is a double-sided interferometer, which is desired based on the design constraints. Second, this interferometer has a refractive index measuring interferometer co-located, which means a separate refractometer is not needed. Third, the input beams are spatially separated and barring any ghost reflections, periodic errors should be minimized.

In addition to these advantages, this system has several disadvantages for stability measurements. First, there are optical imbalances between the beam inputs and their separation into sample and refractometer beams. Additionally, there are large differences between the reference arms and their respective measurement arms. If the quarter wave plates are not aligned properly, there is a leakage beam in the refractometer measurement arm, which may contribute periodic error.

Assuming the optics are made of a thermally stable materials (fused silica, for instance) and their mounts are relatively stable, this interferometer could be used to measure material stability. Ideally, an external optical reference would be established near the heterodyne splitting source, which is the reference signal for both interferometers. Then, PD_m would measure the material stability, refractive index changes, and interferometer fluctuations while PD_r would measure refractive index changes and interferometer fluctuations. Although this interferometer is not balanced, it can be used as an example to investigate the potential measurement uncertainty if the optical path differences can be corrected. The next section described an uncertainty analysis for this type of interferometer, assuming the interferometer is balanced.

4.3.2 Refractive Index Uncertainty Estimate

In Section 2.4, the measurement uncertainty for a double-sided interferometer was presented. In that estimation, the interferometer was assumed to be completely balanced between measurement and reference arms, except for the path difference created by the sample. In this uncertainty estimate for the refractive index measurement, the same

assumption is made, except the sample will be replaced with a vacuum cell. The vacuum cell is assumed to be a tube of length L which has windows to pass the beam through. Assuming this is the only difference between measurement and reference arms in this interferometer, the phase measured is

$$\phi = \frac{2\pi NL\,(\eta - 1)\,f}{c}, \tag{4.15}$$

where L is the vacuum tube length. Once again, the phase changes as a function of time and the length, frequency, and refractive index all can change as a function of time as well. The time derivative of the phase is

$$\frac{d\phi}{dt} = \frac{2\pi N}{c}\left[(\eta - 1)\,f\frac{dL}{dt} + L\,(\eta - 1)\,\frac{df}{dt} + Lf\frac{d\eta}{dt}\right]. \tag{4.16}$$

Equation 4.16 needs to be rearranged to solve for refractive index changes after canceling the time derivatives and switching to discrete time intervals. Additionally, the vacuum tube length will also change as a function of temperature and pressure similarly to Equation 2.84 where

$$\Delta L = \alpha L\Delta T - \frac{3L\,(1 - 2\nu)\,\Delta P}{E}. \tag{4.17}$$

After rearranging Equation 4.16 and substituting Equation 4.17, the measured refractive index change is

$$\Delta\eta = \frac{c\Delta\phi}{2\pi NLf} - (\eta - 1)\left(\alpha\Delta T - \frac{3\,(1 - 2\nu)\,\Delta P}{E}\right) - \frac{(\eta - 1)\,\Delta f}{f}. \tag{4.18}$$

In this derviation, the environment is assumed to be nominally stable, thus the uncertainty sources are assumed uncorrelated. After performing the first order combined uncertainty expansion, the refractive index change uncertainty is

$$\begin{aligned} U_{\Delta\eta}^2 = \quad & \left(\frac{c}{2\pi NLf}\right)^2 U_{\Delta\phi}^2 + \left(\frac{-c\Delta\phi}{2\pi NL^2 f}\right)^2 U_L^2 + \left(\frac{-c\Delta\phi}{2\pi NLf^2} + \frac{\eta\Delta f}{f^2} - \frac{\Delta f}{f^2}\right)^2 U_f^2 \\ & \left(-\alpha\Delta T + \frac{3\,(1 - 2\nu)\,\Delta P}{E} - \frac{\Delta f}{f}\right)^2 U_\eta^2 + (-\eta\Delta T + \Delta T)^2\,U_\alpha^2 + (-\eta\alpha + \alpha)^2\,U_{\Delta T}^2 \\ & \left(\frac{3\,(n - 1)\,(1 - 2\nu)}{E}\right)^2 U_{\Delta P}^2 + \left(\frac{3\Delta P\,(1 - 2\nu)\,(1 - \eta)}{E^2}\right)^2 U_E^2 + \\ & \left(\frac{1 - \eta}{f}\right)^2 U_{\Delta f}^2 + \left(\frac{6\Delta P\,(\eta - 1)}{E}\right)^2 U_\nu^2. \end{aligned} \tag{4.19}$$

To estimate the uncertainty of the measured refractive index, the parameters in Table 4.2 were used. Investigation of the uncertainty sources individually reveals that there are several contributors at the 10^{-12} level.

Table 4.2: *Parameters for the uncertainty of a BK7 vacuum tube refractive index reference.*

Parameter	Nominal Value	Fractional Uncertainty $\frac{U_{q_i}}{q_i}$	Absolute Uncertainty
Speed of light (c)	299792458 m·s^{-1}	-	-
Interferometer Constant (N)	2	-	-
Phase Change ($\Delta\phi$)	3.5×10^{-6} rad	-	3.5×10^{-6} rad
Refractive Index (η)	1.00029	1×10^{-8}	-
Frequency (f)	473.7555 THz	1×10^{-8}	-
Frequency Change (Δf)	200 Hz	-	200+U_f Hz
Nominal Length (x)	100 mm	-	100 nm
CTE (α)	8 µm·m^{-1}·K^{-1}	1 %	-
Temperature Change (ΔT)	5 mK	-	0.5 mK
Pressure Change (ΔP)	10 Pa	-	2 Pa
Modulus (E)	67 GPa	1 %	-
Poisson's Ratio (ν)	0.17	10 %	-

$$U_{\Delta\eta}\left(U_{\Delta\phi}\right) = \frac{c}{2\pi NLf}U_{\Delta\phi} \cong 1.8\times10^{-12} \tag{4.20}$$

$$U_{\Delta\eta}\left(U_L\right) = \frac{-c\Delta\phi}{2\pi NL^2 f}U_L \cong 0 \tag{4.21}$$

$$U_{\Delta\eta}\left(U_f\right) = \left(\frac{-c\Delta\phi}{2\pi NLf^2} + \frac{\eta\Delta f}{f^2} - \frac{\Delta f}{f^2}\right)U_f \cong 0 \tag{4.22}$$

$$U_{\Delta\eta}\left(U_\eta\right) = \left(-\alpha\Delta T + \frac{3(1-2\nu)\Delta P}{E} - \frac{\Delta f}{f}\right)U_\eta \cong 0 \tag{4.23}$$

$$U_{\Delta\eta}\left(U_\alpha\right) = \left(-\eta\Delta T + \Delta T\right)U_\alpha \cong 1.6\times10^{-13} \tag{4.24}$$

$$U_{\Delta\eta}\left(U_{\Delta T}\right) = \left(-\eta\alpha + \alpha\right)U_{\Delta T} \cong 1.6\times10^{-12} \tag{4.25}$$

$$U_{\Delta\eta}\left(U_{\Delta P}\right) = \frac{3(n-1)(1-2\nu)}{E}U_{\Delta P} \cong 8.6\times10^{-14} \tag{4.26}$$

$$U_{\Delta\eta}\left(U_E\right) = \frac{3\Delta P(1-2\nu)(1-\eta)}{E^2}U_E \cong 2.5\times10^{-12} \tag{4.27}$$

$$U_{\Delta\eta}\left(U_{\Delta f}\right) = \left(\frac{1-\eta}{f}\right)U_{\Delta f} \cong 2.9\times10^{-12} \tag{4.28}$$

$$U_{\Delta\eta}\left(U_\nu\right) = \left(\frac{6\Delta P(\eta-1)}{E}\right)U_\nu \cong 0 \tag{4.29}$$

The estimated combined uncertainty (RSS) is 4.4×10^{-12}. The largest uncertainty contributions come from the phase measurement uncertainty and the temperature uncertainty. However, these are still one order of magnitude better than the desired contribution for this investigation. Therefore, if the refractive index is uniform between the two interferometers in the system, then this technique can be used to compensate the refractive index. For stability measurements, the environment surrounding the interferometer should be kept relatively constant and controlled. Only minor gradients should be present in the system, which means the uniform refractive index is a sound assumption.

4.3.3 In-process Refractive Index Correction

The interferometer shown in Figure 4.15 also allows for overall system instability correction. An example of this is shown in Figure 4.16. In Figure 4.16, the configuration is similar to the wavelength correcting interferometry from Section 4.2. But,instead of measuring and correcting for refractive index fluctuations during post processing, it is possible to use the signal from PD$_r$ as the feedback from a control loop which controls the laser frequency. In

this configuration, refractive index fluctuations and small interferometer perturbations can be corrected by updating the instantaneous laser frequency.

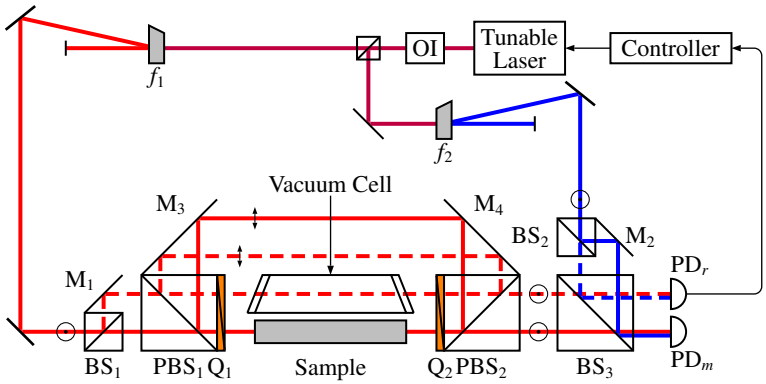

Figure 4.16: *Schematic of a dual interferometer with one interferometer measuring sample displacements while the other measures refractive index fluctuations. This interferometer uses the signal from PD_r to control the laser wavelength in a wavelength correcting interferometer.*

The signal measured by PD_m would then also be corrected for these effects. The sample measurement would then only need to be corrected for thermal effects and pressure-induced changes on the sample length. One disadvantage of this system is this requires a tunable laser with a bandwidth of at least 10 Hz or higher.

For practical reasons, it may be better to use a stabilized laser instead of a tunable laser as the source for the system. If this is the case, then it is still possible to control the refractive index to a set value. An example of this system is shown in Figure 4.17. Instead of changing the laser wavelength to correct for refractive index fluctuations and small interferometer perturbations, a phase modulator can be used to maintain a constant signal from PD_r. Since the electro-optic modulator is placed before the split between both reference beams, this will effect both the sample measuring interferometer and the refractive index measuring interferometer.

The phase of the reference signal can then be adjusted using a feedback controller to maintain a constant signal from PD_r. When the refractive index changes, then the signal from PD_r will also change. That change can be fed into a controller to adjust the electro-optic modulator to maintain a constant value from PD_r. Thus, the electro-optic modulator will also change the sample measurement reference arm, which will correct the sample measurement signal (PD_m) by the appropriate amount to cancel refractive index fluctuations and interferometer perturbations.

A distinct advantage of this type of system, a sample measuring interferometer with an internal refractometer, is that the measurement values should be closely correlated because the same interferometer components are used for both measurements. The internal refractometer does not need to be separately characterized because the instability should be common between both measurements. Also, the measurement method for the refractive index is the same as the sample measurement (heterodyne interferometry). This is

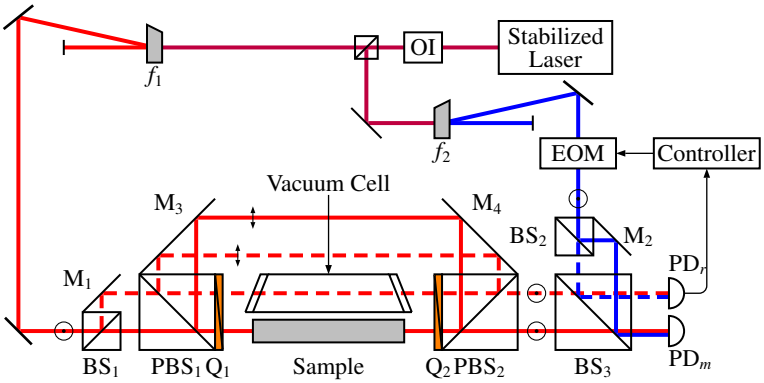

Figure 4.17: *Schematic of a dual interferometer with one interferometer measuring sample displacements while the other measures refractive index fluctuations. This interferometer uses the signal from PD_r to control an electro-optic modulator to maintain a constant phase on the refractometer photodiode.*

contrasted by Fabry-Pérot interferometry as an alternative which is a different measurement principle.

4.4 Refractive Index Correction Summary

A transmission Fabry-Pérot cavity was used for both refractive index tracking and wavelength correcting interferometry. The refractive index tracking was measured to be within 4.9×10^{-8} which is nearly the limit achievable with Edlén equations. In the wavelength correcting experiments, the difference between the empirical equation-based methods and the wavelength corrected DMI was approximately 2 nm over a 100 nm range.

While a Fabry-Pérot wavelength tracker could be used to correct for refractive index fluctuations, it requires a stable cavity made of thermally stable materials. Additionally, the Fabry-Pérot mirrors must be highly efficient and must be mounted in a thermally neutral plane. This increases the complexity and cost of the cavity design and more optical components are needed to utilize this system in conjunction with a sample measuring interferometer. Since this type of system employs a completely different measurement principle to measure and correct the refractive index, an alternative method should be used to correct the refractive index fluctuations.

An alternative method presented in this work is to develop a dual interferometer. One interferometer measures the sample fluctuations and the other measures refractive index fluctuations. If the refractive index fluctuations are nominally uniform throughout the interferometer, then this configuration could be suitable for measuring refractive index fluctuations. A detailed uncertainty analysis was presented and the two largest uncertainty contributors are the phase measurement itself and the temperature change uncertainty.

For the research in this thesis, a dual interferometer was chosen because the measurement and reference beams from both interferometers would pass through the same components, adding more balance into the system. Additionally, the sample measurement and refractive index measurement would both be performed with heterodyne interferometry. Building a dual system with additional channels for measurements which have the same measurement

principles is easier to achieve than two completely different measurement principles. This system also has the potential for wavelength correcting interferometry, where source frequency is changed to cancel the refractive index fluctuations. This interferometer is discussed in detail in Chapter 6

Chapter 5

Laser Stabilization

Chapter 2 discussed three main error sources in most heterodyne interferometers. While the frequency change uncertainty and the refractive index change uncertainty are both solely dependent on the optical path difference, Chapter 4 showed how it difficult it was to potentially achieve the desired uncertainty level of 1 part in 10^{11}. Achieving this level of uncertainty for the frequency stability is much more readily available as most calibration lasers have an uncertainty of 2 parts in 10^{12}. These metrology lasers, however, are often complex and not practical for many interferometry applications, which will be discussed for two such systems in Section 5.1

In Chapter 3, methods were discussed to minimize optical mixing, which lead to periodic errors in the phase measurement. These methods included minimizing beam overlap in the optics and employing a spatially separated heterodyne laser source. This type of source is not the standard configuration for commercial displacement interferometry systems. Most commercial laser systems consist of a stabilized laser with orthogonally polarized, coaxial beams with a split frequency between the two polarization states. Two examples of common heterodyne interferometry sources are presented in the following sections.

Separating the coaxial beams of a commercial laser system into spatially separated beams will contribute to frequency mixing due to imperfect optics. Also, the added components will contribute to losses in the system, decreasing the optical power available for detection. A more ideal solution to eliminate the frequency mixing is to use a stabilized laser with a high power while achieving the desired frequency stability of 1 part in 10^{11}. The high power is needed because the heterodyne frequency will be generated after the stabilized laser and the higher output power should mitigate the losses in the heterodyne frequency generation system.

Section 5.3 discusses a novel three-mode laser stabilization technique developed for this research. Using an intrinsic mixed mode signal, the central mode of a three mode laser was stabilized, providing more than 2 mW of power output with a fractional frequency stability of 5 parts in 10^{10} relative to an iodine stabilized laser. After tuning the controller and adding environmental isolation, the estimated laser frequency stabilization was better than 2 parts in 10^{11} with a one second integration time. This estimation assumes the calibration coefficients relative to the iodine stabilized laser remained constant and there is no Helium Neon line shift. Thus, this frequency stability value is only for short measurement periods.

5.1 Reference Laser Systems

The two reference laser systems described in this section are the iodine stabilized laser and the frequency comb laser system. Both laser systems can be used for stabilizing a 632.8 nm wavelength laser. These sections give general overviews of the two systems but do not discuss some of the more detailed aspects behind the designs. Also, several variations of both laser systems have been demonstrated; these presented here are for illustrative purposes only.

5.1.1 Iodine Stabilized Laser

The iodine stabilized laser is the practical standard for determining the meter [18]. This system, shown in Figure 5.1, comprises a HeNe laser which is stabilized on the R(127)11-5 hyperfine absorption lines of an $^{127}I_2$ absorption cell [110–112]. The iodine absorption cell is used with a pressure of 17.4 Pa, which corresponds to a coldfinger temperature of 15°C. The frequency dependence of the iodine lines are -11.5 kHz·Pa^{-1}. Using a sealed iodine absoprtion cell, the pressure to temperature relation is 1.35 Pa·K^{-1}, thus temperature control of the iodine cell coldfiner better than 0.2 K is needed[1]. There are two typical ways for frequency locking (stabilizing) a laser to an iodine absorption cell. One method is to use a piezo-driven cavity mirror (depicted in the figure) and the other is to use an electro-optic modulator and phase modulate in a side loop [113]. In most cases, the hyperfine absorption peaks are difficult to view due to intensity fluctuations and multiple derivatives of the gain profile are needed to successfully stabilize the laser [21, 111, 114].

Using this hyperfine absorption technique, the absolute frequency is 473 672 214.705 MHz ± 0.012 MHz (2σ) with a stability of 5 kHz (1×10^{-11}) when locked to the 'i' component with a one second integration time [21]. Since this system is an absolute reference, the absolute wavelength uncertainty and the wavelength stability uncertainty are the same value[2]. Over long periods of time, however, the leakage in the absorption cell will cause some absolute frequency drift [115, 116].

The iodine stabilized laser consists of three major components. The laser tube (on the right side in Figure 5.1) has one highly reflective internal mirror which is fixed to the tube. This side is near the output beam. The other side of the laser tube consists of a window with anti-reflection coatings. The beam then exits the laser tube and passes through an iodine absorption cell, which is the second major component. The iodine absorption cell is kept at 15°C by controlling the coldfinger temperature. After passing through the absorption cell, the beam reflects off the other laser mirror which is mounted on a piezo stage, which is the third major component. Most of the light is reflected from this surface but some transmits, which is detected using a photodiode.

In the system shown in Figure 5.1, the components are shielded using passive, low expansion materials. Additionally, the laser cavity is sometimes temperature controlled to ease the amount of correction needed by the piezo stage. The laser is typically 150 mm

[1] This information comes from a private communication with Professor P.H.J. Schellekens.

[2] A laser system which is not an absolute reference typically has two different values for the absolute wavelength uncertainty and the wavelength stability uncertainty. The absolute wavelength uncertainty is the degree to which the vacuum wavelength of a particular laser is known. The wavelength stability uncertainty relates to the amount of deviation from the absolute vacuum wavelength value during operation

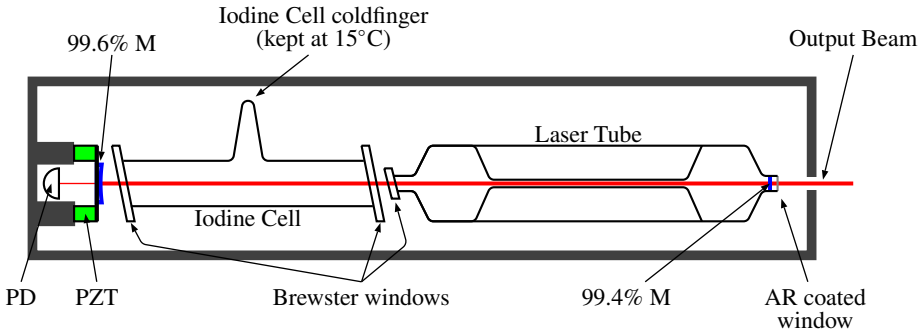

Figure 5.1: *Schematic of an iodine stabilized laser. This laser contains a HeNe laser tube with Brewster windows, an iodine cell kept at 15°, and a mirror mounted on a piezo stage. The back beam is detected and used for wavelength stabilization.*

long and contains two Brewster windows which ensure only one polarization state is emitted from the laser. The iodine cell is typically 100 mm long and the overall resonance cavity is approximately 260 mm. The FSR of this cavity is 575 MHz and when the iodine cell is removed, this laser would typically have either two or three modes. However, when the iodine cell is present, the overall gain is lowered and only one mode is present.

The iodine vapor in the absorption cell has a broad absorption curve, which is why only one mode is present. In addition to the broad absorption curve, there are 14 hyperfine absorption peaks labeled 'a' through 'n'. When the laser frequency matches one of these absorption peaks, the output gain drops slightly. By repeatedly scanning across a certain peak, the resonance can be detected at a multiple harmonic of the modulation frequency [21, 111, 114]. This essentially sharpens the gain drop. The output gain drop is detected by PD and fed into a controller, which adjusts the DC level sent to the piezo stage to change the cavity length. The piezo stage is also modulated with an AC signal, typically on the order of 1 kHz and corresponds to a laser frequency modulation of approximately 6 MHz. This provides the repeated scanning of the peak to ultimately control the laser frequency.

The scanning from the piezo mounted mirror results in an output beam which is modulated. The output beam of the iodine stabilized laser has a frequency of approximately 473 THz but it is modulated ±6 MHz at frequency of approximately 1 kHz. This output beam also has a low power, around 100 μW, which is not suitable for most interferometry applications. This output beam can be mixed with a beam sampled from another tunable laser and the difference in frequency can be measured and used to control the tunable laser. Once the tunable laser system is locked relative to the iodine stabilized laser, the main output of the tunable laser can be used for interferometry applications with high frequency stability.

5.1.2 Frequency Comb Laser System

Since redefining the meter in 1993, the iodine laser has been the practical standard calibration laser for most national metrology laboratories and calibration institutes [18]. While the iodine laser is compact and a relatively simple system, it has one major drawback which is the iodine absorption cell leaks slowly over time [115, 116]. Thus, the location of the hyperfine peaks shift slightly over time, which decreases the stability. Also, in addition to the iodine cell contamination, the definition of the meter is based on the distance light traveled in $1/c$ seconds in vacuum. Therefore, in the definition of the meter, the primary unit

of length is dependent on another primary unit, which is the second.

The second is defined the time interval of 9 192 631 770 radiation cycles corresponding to the transition between two energy levels of the caesium-133 atom [117]. The uncertainty in the measured value of the second using atomic clocks is approximately 1 part in 10^{15} [118]. Since the advent of the frequency comb, optical clocks have shown stabilities better than parts in 10^{17} [119]. This leads to a future redefinition of the practical standard of the meter, which can be determined with a much lower uncertaitny.

A major breakthrough in this research occured a decade ago when the radio frequency (RF) standards, which are derived from atomic clocks, and the optical frequency standards, which are derived from lasers, were linked using frequency comb lasers. Figure 5.2 shows a simplified schematic of a frequency comb laser comprising a femtosecond (fs) laser locked to an atomic clock that is then used as a reference to stabilize a tunable HeNe laser. This figure does not ecompass all of the minute details needed for employing such a system but it gives a general scope of main components. This figure has been adapted from several sources and more detail can be found in their respective works [120–127].

Figure 5.2 is split into four different sections denoted by the gray dashed boxes. Additionally, there are some external components such as the microstructured fiber and clock which are crucial for having a stable system and a central reference. The top box in the figure shows a schematic of a fs-laser system. The central elements are the titanium doped sapphire (Ti:S) crystal which has light directed through it from a pump laser. The pulse train generated is typically 80 MHz to 90 MHz with a pulse width as short at 10 fs using a Kerr locking technique. The central output wavelength is around 830 nm with a width of ±35 nm. The pulse train resonates in an optical cavity comprising a tilt controlled mirror and a translation controlled mirror. Two dispersion prisms are inserted into the optical cavity ultimately to account for the variations in group velocity which will be discussed shortly.

After a part is transmitted through a translation mirror, a small amount is split from the main beam and detected. This signal is fed to a phase locked loop system with respect to an atomic clock. The output drives the translation mirror of the cavity and synchronizes the pump laser to maintain the constant repetition rate and pulse width. At this point, the fs-laser can still shift in wavelength while maintaining the same pulse width and repetition rate. Also, the group velocity of the pulse can change due to atmospheric effects, which means the spacing between optical frequencies is not consistent. Mode matching [120] or 'f–2f' referencing [127] can be used to correct both of these effects, which are both shown in Figure 5.2 .

Prior to the mode matching or 'f–2f' referencing section, the output of the fs-laser is passed through a microstructured fiber which broadens the initial pulse from 70 nm to nearly 600 nm. Also, because of the wavelengths encompassed by the broadened pulse, more than an octave is available at 1064 nm.

One method for stabilizing the group velocity is to use mode matching. In this method, the broadened pulse train is mixed with both the output of a Nd:YAG laser at 1064 nm and its second harmonic at 532 nm, which is generated using a frequency doubling crystal. Because the output of the Nd:YAG laser is well known using absorption spectroscopy, this can be used to stabilize the group velocity and lock the absolute wavelength in the fs-laser. The triaxial beam is dispersed using a grating and the interference between the 532 nm

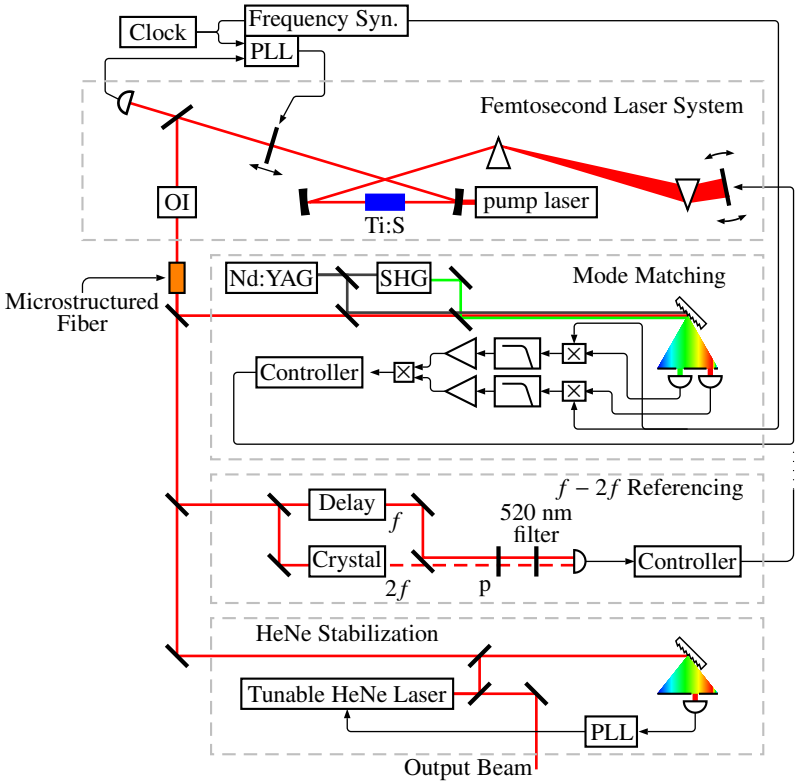

Figure 5.2: *Schematic of a frequency comb laser metrology system. The top box contains the fs-laser with a translation mirror and a rotational mirror. The translation mirror stabilizes the pulse rate and width in conjunction with the titanium doped sapphire crystal and pump laser. Either the second or third box is needed to stabilize the group velocity by tuning the rotational mirror in the fs-laser which stabilizes the wavelength. The last box contains a schematic for locking a tunable HeNe laser to the frequency comb and generating an output beam.*

beam and the fs-laser and the interference between the 1064 nm beam and the fs-laser are detected separately using avalanche photodiodes.

The output signals are relatively weak and at a high frequency. They are then mixed with a frequency synthesized signal from the atomic clock, filtered, and finally amplified. Those signals are then mixed and sent to a controller which controls the tilt angle of the mirror in the fs-laser. This stabilizes the group velocity of the pulse train and the absolute wavelength of the fs-laser.

An alternative method for generating this stabilization signal is to use a 'f–$2f$' referencing scheme. The output of the microstructured fiber is split using a dichroic beamsplitter where the visible part is sent to an optical delay, typically generated using an acousto-optic modulator or a Babinet-Soleil compensator. The near infrared part is sent through a frequency doubling crystal (typically β-barium-borate or periodically poled lithium niobate). Both beams are combined on another beamsplitter and passed through a 10 nm optical filter centered around 520 nm. The resulting optical signal is detected and sent to a controller which stabilizes the tilt mirror in the fs-laser.

Once the output of the frequency comb laser has a stable wavelength, group velocity, repetition rate, and pulse width, the output signal can be mixed with a sample signal from a tunable HeNe laser. The signal is then dispersed using a grating and the interference between the fs-laser and tunable laser is detected using an avalanche photodiode. The output is sent to a phase locked loop or other controller which is used to tune the HeNe laser output. Once this system is locked to the frequency comb laser, the output beam can be used for heterodyne interferometry, wavelength sweeping interferometry, and/or absolute displacement interferometry.

Ye, *et al.* [125] and Cundiff, *et al.* [122] present excellent reviews of frequency comb laser and optical metrology techniques. Additionally, they present a collection of wavelengths which have shown uncertainties from 10^{-12} to 10^{-15}, depending on optical frequency. Therefore, frequency comb lasers can be used for precision optical frequency stabilization which is certainly adequate for this research.

5.2 Heterodyne Interferometry Lasers

While metrology lasers have high frequency stability, they are generally limited to frequency stabilization and wavelength references rather than practical interferometry applications. The output power of the iodine stabilized laser is low and unsuitable for many applications. Additionally, it usually contains a modulation frequency superimposed on the optical frequency which adds complexity to interference detection. For metrology, this output beam is instead usually mixed with a beam from a single mode HeNe laser tube. The HeNe laser tube is then controlled relative to this mixed signal. However, the output is still 1 mW or less which may not be suitable for some interferometry applications. The mode-locked lasers present even higher frequency stability but they are also costly and require many components and control loops to work effectively. For practical optical systems, a bench-top system is generally desired where the wavelength stability is still adequate and the cost of a system is relatively low. The following sections show two typical stabilized laser systems used for many displacement interferometry applications.

5.2.1 Zeeman Laser

Figure 5.3 shows a schematic of a Zeeman laser system [128]. Typically, a single mode laser is placed inside an annular axial magnet. The axial magnetic field creates the Zeeman effect where the HeNe gain curve is split into two different refractive indices, creating two different polarization states. This is shown on the left side of the figure. When the laser mode is near the side of the curve, the difference frequency f_z can be detected. This is generally detected using the leakage beam shown on the left side of the laser tube. A polarizer is needed to interfere the left circular and right circular polarization states. Because of frequency pulling effects, when the mode is near the side of the gain curve, the signal f_z can be detected and used to control the cavity length which stabilizes the laser. Depending on the strength of the applied magnetic field, f_z typically ranges from 1 MHz to 4 MHz.

This frequency difference is also used as the heterodyne frequency in interferometry applications. The laser output must pass through a quarter wave plate to change orientations from circular polarization states to linear polarization states. The beam is then collimated using a series of lenses and sent to the desired interferometer.

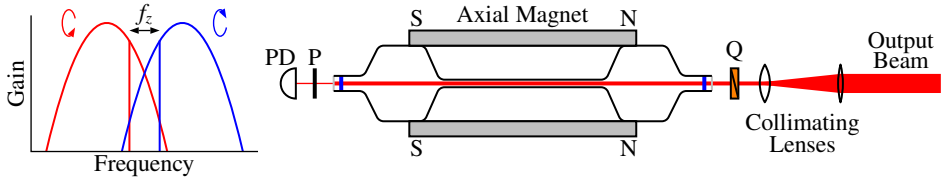

Figure 5.3: *Schematic of a Zeeman laser which is used to stabilize the wavelength and generate a heterodyne source. An annular axial magnet around the laser tube splits the HeNe gain curve into two parts, left circular polarization and right circular polarization as shown in the left part of the figure. When the frequency is near the side of the gain curve, the difference f_z can be detected and used to stabilize the wavelength. The output beam is shifted to two orthogonal, linearly polarized beams using a quarter wave plate.*

This system requires a tight tolerance on the quarter wave plate to ensure linear polarization states. Additionally, changes in the magnetic field due to temperature or other stray fields can cause destabilization or mode hopping. The output power of this system is typically low, around 500 μW, although it already contains the heterodyne frequency generation. This is a benefit, because this system is compact, but it is also a disadvantage because there will inherently be frequency mixing between the heterodyne beams due to manufacturing tolerances. Zeeman lasers have shown a frequency stability as high as 10^{-10}, but their susceptibility to stray magnetic fields and temperature dependence of the magnetic field limits this value to 10^{-8} for most practical systems [43].

5.2.2 Two-Mode Intensity Balanced Laser

Another stabilization scheme uses two-mode intensity balancing in the laser [129]. A schematic of the system, including heterodyne frequency generation is shown in Figure 5.4. This laser does not have Brewster windows and the cavity length must be large enough to have two modes. When this occurs, successive modes have alternating linear polarization states, which are used for frequency stabilization. The back beam is once again used for the stabilization scheme. The back beam is split using a polarizing beamsplitter and the DC intensity of each polarization state is detected.

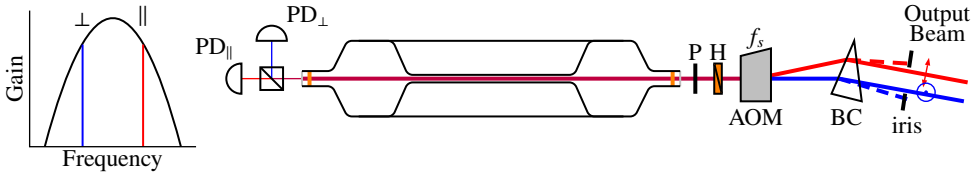

Figure 5.4: *Schematic of the two-mode intensity balancing frequency stabilization technique and heterodyne frequency generation using a birefringent crystal. The two orthogonal modes of the back beam are split by polarization and the DC level intensity is recorded. By balancing the difference, the laser can be stabilized. The output beam has one polarization state blocked and then it is rotated to 45°. An acousto-optic modulator splits the beam based on polarization and a birefringent crystal is used to combine the orthogonal, heterodyne beams.*

When the two modes in the laser are nominally symmetric with respect to the gain curve, as shown in the left in the figure, the output intensity of each mode is nominally the same.

This can be detected from the split back beam and used to stabilize the cavity length, which stabilizes the laser frequency. If a sufficiently long laser cavity is used, the laser will operate with either two or three modes. However, a longer cavity generally generates more optical power and if the cavity is selected with nearly four modes, the two outermost modes will not have sufficient power to properly lase. The two central modes will then have higher power; output power around 1.3 mW is achievable per mode [44]. The output of the laser is a coaxial beam with two orthogonally polarized states with a split frequency around 650 MHz. This split frequency is generally perceived as difficult to work with for practical interferometry applications, so an alternative means is typically used to generate a more manageable heterodyne frequency.

One mode can be blocked using a polarizer and a half wave plate is then used to rotate the polarization state to 45°. The beam is then passed through an acousto-optic modulator and a matched birefringent crystal, generating almost coaxial, orthogonally polarized beams with a frequency difference determined by the acousto-optic modulator drive frequency [108, 130]. The output heterodyne frequency is typically 20 MHz for this type of system.

Aside from the higher power in this system compared to the Zeeman laser, the two-mode intensity balanced system also decouples the frequency stabilization from the heterodyne frequency generation. This is useful when smaller split frequencies are desired. Thus, a heterodyne frequency generation system described in Section 3.2 can be used instead. Additionally, the polarizing beamsplitter used prior to the two photodiodes for the stabilization system can suffer from manufacturing tolerances and there will be some leakage from both polarization states onto both detectors. This can limit the sensitivity of the system. However, most commercial systems have a frequency stability around 10^{-8} [44, 109].

5.3 Three-Mode Laser Stabilization

The motivation for this work was to develop a frequency stabilized HeNe laser with a usable output power greater than 2 mW. Although the two mode intensity balanced laser does have a high power output (>1 mW), it is rather inefficient because the central part of the HeNe gain curve is not used. In this research, the interferometer will be placed in an environmental chamber, which means fiber coupling is likely. Losses up to 25% are common when fiber coupling into polarization maintaining fiber. Coupling in and out of the chamber will mean a maximum efficiency of about 56% with 75% coupling efficiency. For a 1 mW source, that leaves about 560 μW of power available for the rest of the system (not including losses in the optics and coatings).

This research began by trying to duplicate research that used the so-called ‘secondary beat’ of a three mode 633 nm HeNe laser to stabilize the absolute frequency [131–133]. This technique has been shown to have a fractional frequency stability better than 10^{-10} and higher output power than traditional stabilization methods. The initial hypothesis was that a strong transverse magnetic field could be used to force a particular polarization output and increase the HeNe gain profile to obtain more output power. The findings from this research [134], showed there was a discrepancy between the results found in literature. The research then focused on determining the real causes of the observed ‘secondary beat’ rather than continuing with the magnetic field effects.

The secondary beat stabilization in a three mode laser was investigated assuming a semiclassical model of the three mode laser [135–137]. In practice, the assumed secondary beat is not the beat signal between two interference signals but rather it is an intrinsic mixed mode signal. The intrinsic mixed mode signal is directly correlated to the absolute frequency because of nonlinear interactions between adjacent modes. This allows for laser frequency stabilization with a single mode output and high optical power. This research contradicts previous research [131–133] because the secondary beat frequency, which is akin to the mixed mode signal, cannot be measured without direct measurement of the intermode beat frequencies and subsequent mixing. This is explained theoretically and verified experimentally.

5.3.1 Three Mode Laser Model

In previous research, the secondary beat signal, ν_b was assumed to be the optical interference between the first and second modes, ν_{12}, and the second and third modes, ν_{23}, which can be seen in Figure 5.5 [131–133]. The stabilization signal was generated by placing a polarizer at 45° to interfere the three modes, creating the secondary beat signal, where this signal is detected by a slow speed detector and used for stabilization feedback. This was assumed to create a detectable interference signal ν_{23}-ν_{12}=ν_b. The secondary beat frequency, ν_b, is on the order of hundreds of kilohertz, which means direct measurement of the laser's mode frequency spacing should not be needed.

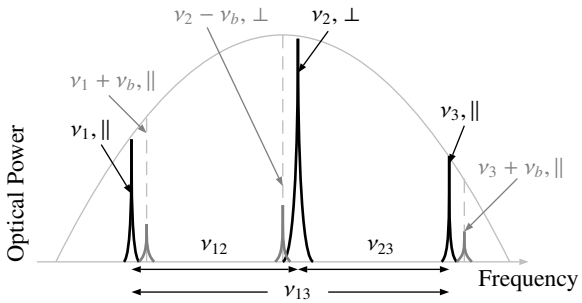

Figure 5.5: *A schematic of the three laser modes including three additional mixed modes. These modes arise from nonlinear optical interaction between ν_1, ν_2, and ν_3.*

However, Lamb [135] showed that in addition to the normal main frequencies, i.e., those frequencies whose source is the linear part of the polarization of the active laser medium, there are the so-called combination frequencies whose source is the third-order nonlinear harmonics. The magnitude of the frequency difference between them depends in detail on the exact cavity tuning and the state of excitation of the active medium. Compared to the second-order nonlinear harmonics, it can always be generated without any symmetry restrictions of the medium at the condition of the high intensity such as the HeNe gas inside the laser cavity. Specifically in three mode operation, three additional frequencies, $(2\nu_2 - \nu_3)$, $(\nu_1 + \nu_3 - \nu_2)$, and $(2\nu_2 - \nu_1)$, are generated near the main frequencies, ν_1, ν_2 and ν_3, respectively. It is noted that besides these three combination frequencies, there are more frequencies which do not produce appreciable effects due to the gain bandwidth and threshold of the medium. In this case, each of the three main modes are oscillated by the

interaction with the adjacent modes, which can be seen in Figure 5.5.

These time dependent main frequencies are [137]

$$\nu_1 + \dot{\varphi_1} = \Omega_1 + \sigma_1 + \rho_1 E_1^2 + \tau_{12} E_2^2 + \tau_{13} E_3^2 - (\eta_{23} \sin\psi - \xi_{23} \cos\psi)\, E_2^2 E_3 E_1^{-1}, \quad (5.1)$$

$$\nu_2 + \dot{\varphi_2} = \Omega_2 + \sigma_2 + \tau_{21} E_1^2 + \rho_2 E_2^2 + \tau_{23} E_3^2 + (\eta_{13} \sin\psi - \xi_{13} \cos\psi)\, E_1 E_3, \quad (5.2)$$

$$\nu_3 + \dot{\varphi_3} = \Omega_3 + \sigma_3 + \tau_{31} E_1^2 + \tau_{32} E_2^2 + \rho_3 E_3^2 - (\eta_{21} \sin\psi - \xi_{21} \cos\psi)\, E_2^2 E_1 E_3^{-1}, \quad (5.3)$$

where

$$\psi \;=\; (2\nu_2 - \nu_1 - \nu_3)\, t + (2\varphi_2 - \varphi_1 - \varphi_3) \;=\; \nu_b t + \varphi_b \quad (5.4)$$

and all parameters refer to Lamb's corrected paper [136]. As shown in Equations 5.1, 5.2, and 5.3, the main frequencies are time varying with a frequency of ν_b, the same frequency as the secondary beat.

Using the complete model, six different modes are assumed in the three mode laser, which can be seen in Figure 5.5. These include the three main modes (M_i), which are, in the frequency domain,

$$M_1 = \nu_1 + \dot{\varphi_1} \quad (5.5)$$

$$M_2 = \nu_2 + \dot{\varphi_2} \quad (5.6)$$

$$M_3 = \nu_3 + \dot{\varphi_3}, \quad (5.7)$$

which are found by removing the time-varying phase function from the adjacent mode and simplifying Equations 5.1, 5.2, and 5.3. The three mixed mode frequencies, which arise from interaction with the adjacent modes, are

$$M_{1,m} = \nu_1 + \nu_b + \dot{\varphi_b} \quad (5.8)$$

$$M_{2,m} = \nu_2 - \nu_b - \dot{\varphi_b} \quad (5.9)$$

$$M_{3,m} = \nu_3 + \nu_b + \dot{\varphi_b}, \quad (5.10)$$

in the absolute frequency domain, where $M_{i,m}$ is the i^{th} mode from lowest to highest frequency and the m idicates a mixed mode. Each mixed mode has the same polarization state as the adjacent main model. This was verified by using a Glan–Thompson polarizer aligned to block the central mode and an optical spectrum analyzer. If the polarization state of the adjacent mixed mode $M_{2,m}$ was different than, M_2, it would be detected by the optical spectrum analyzer, which was not the case. Additionally, when the outer modes, M_1 and M_3, were blocked, their respective adjacent mixed modes were blocked as well.

5.3.2 Experimental Verification

To verify the presence of the mixed modes, the experimental setup in Figure 5.6 was used. This setup has a common polarizer for all three different detectors, a low speed photodiode (DC to 500 kHz), a high speed avalanche photodiode (1 MHz to 1.5 GHz), and an optical spectrum analyzer. The low speed detector was used to compare with previous laser stabilization experiments [131–133]. The avalanche photodiode was used to compare with the previous superheterodyning experiment [138]. The optical spectrum analyzer was used to verify the presence of each particular mode during an experiment.

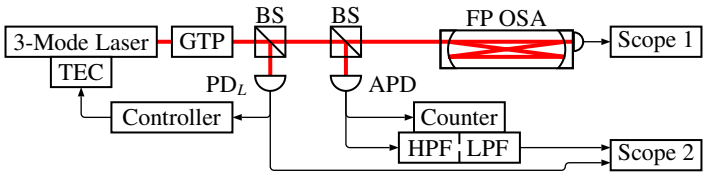

Figure 5.6: *Optical schematic for characterizing the three mode laser behavior. A common polarizer is used between the three different detectors and the high pass filter-low pass filter combination behaves like a self mixing circuit.*

For these experiments, the polarizer was rotated in increments of 15°, starting at 0°, where the central mode (M_2) was only visible on the optical spectrum analyzer. From previous experiments with the three mode laser (25-LHR-121, Melles Griot), the frequency of the intrinsic signal was known to be between 200 kHz and 400 kHz. When a signal in that frequency range was detected on Scope 1, the peak-to-peak value of PD$_L$ and APD was recorded, as shown in Figure 5.7. It should be noted that the bandpass filter from the high pass filter and low pass filter behaves similarly to a self mixing circuit, which was used in research by Yokoyama, *et al.* [138].

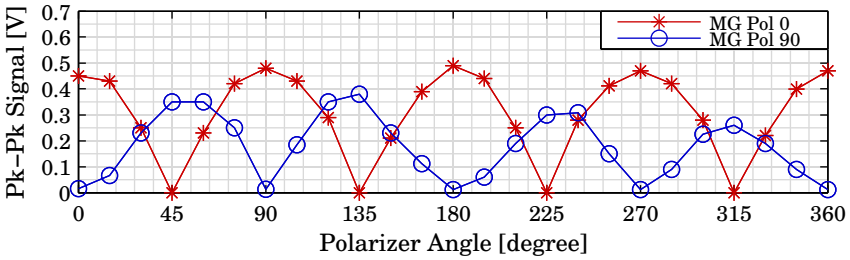

Figure 5.7: *Measured frequency from both detectors as a function of polarization rotation. The signals are 45° out of phase, which was unexpected.*

From these measurements, it is clear the signals from the separate detectors are 180° out of phase (45° based on polarizer angle) meaning the two detectors do not measure the same thing, which was not expected. Additionally, these measurements directly counter previous research [131–133] where a 45° polarizer angle was used to create the secondary beat signal without direct measurement of the intermode beat frequencies. To fully explain these results from these experiments and why they contradict previous research, the three additional mixed modes in the semiclassical three mode laser model must be used.

5.3.3 Theory of Operation

At a polarizer angle of 0°, the four outer modes, M_1, $M_{1,m}$, M_3, and $M_{3,m}$, are all blocked leaving M_2 and $M_{2,m}$. This is clearly visible on the optical spectrum analyzer, however, the resolution is not fine enough to see the mixed mode adjacent to M_2. The two central modes M_2 and $M_{2,m}$ interfere creating the detectable time domain signal

$$I_{pd}^{0} = \cos\left(2\pi\nu_b t + 3\varphi_2 - \varphi_1 - \varphi_3\right), \tag{5.11}$$

where I is the irradiance, the superscript indicates the polarizer angle, and the subscript indicates the signal is within the detectable bandwidth for a specific detector. The frequency of ν_b is within the detectable bandwidth of the photodiode but not within the bandwidth of the avalanche photodiode, thus, the photodiode only measures the mixed modal frequency.

When the polarizer is at 90°, the opposite effect occurs. The two central modes are blocked; the four outer modes interfere and are detected. The time domain signals

$$I_{pd}^{90} = \cos(2\pi\nu_b t + 2\varphi_2 - 2\varphi_1 - \varphi_3) + \cos(2\pi\nu_b t + 2\varphi_2 - \varphi_1 - 2\varphi_3) \quad \text{and} \tag{5.12}$$

$$I_{apd}^{90} = \cos(2\pi\nu_{13} t + \varphi_3 - \varphi_1), \tag{5.13}$$

are detected, where ν_{13} is the frequency between the two outer modes. If $\varphi_1 = \varphi_3 = \varphi_{13}$, then Equations 5.12 and 5.13 become

$$I_{pd}^{90} = \cos(2\pi\nu_b t + 2\varphi_2 - 3\varphi_{13}) \quad \text{and} \tag{5.14}$$

$$I_{apd}^{90} = \cos(2\pi\nu_{13} t). \tag{5.15}$$

Additionally, the mixed interference modes, $M_{1,m}$ with M_3 and $M_{3,m}$ with M_1 are assumed to be much lower in signal power than the interference between M_1 and M_3, and thus are negligible. Once again, the photodiode detects the mixed modal frequency, whereas the avalanche photodiode detects only the difference frequency between the two outer modes.

With the polarizer at 45°, all six modes interfere to produce numerous interference signals. The detected interference signals are

$$I_{pd}^{45} = \cos(2\pi\nu_b t + 2\varphi_2 - 3\varphi_{13}) + \cos(2\pi\nu_b + 3\varphi_2 - 2\varphi_{13}) \quad \text{and} \tag{5.16}$$

$$I_{apd}^{45} = \cos(2\pi\nu_{12} t + \varphi_2 - \varphi_{13}) + \cos(2\pi\nu_{23} t + \varphi_{13} - \varphi_2) + \cos(2\pi\nu_{13} t) \tag{5.17}$$

where ν_{12} is $\nu_2 - \nu_1$ and ν_{23} is $\nu_3 - \nu_2$. Once again, the high frequency mixed interference modes are assumed negligible in signal strength compared to the main modal beat frequencies ν_{12}, ν_{23}, and ν_{13}. The avalanche photodiode does detect the secondary beat frequency while the photodiode does not at this polarizer angle.

If the avalanche photodiode signal is examined first, ν_{12} differs slightly from ν_{23} (Figure 5.5) due to frequency pulling effects [135]. However, both optical signals are detected, which means there are corresponding electrical signals, which get mixed in the transimpedance amplifier. Once the signals are bandpass filtered and amplified, the frequency difference between them can then be detected; this is the true secondary beat signal ν_b.

The signal from the photodiode is the sum of I_{pd}^{0} and I_{pd}^{90}, which produces no signal. This means the mixed modal frequency from I_{pd}^{0} and the secondary beat frequency from I_{pd}^{90} must be 180° out of phase, causing destructive interference. Since it was already assumed $\varphi_1 = \varphi_3 = \varphi_{13}$, then this only occurs if $\varphi_2 + \varphi_{13} = 180°$.

The optical setup shown in Figure 5.8a was used to verify this claim. In this schematic, the signal from the laser is split equally and two separate Glan-Thompson polarizers are aligned to the central and outer modes, respectively. This was confirmed using the optical spectrum analyzer. While the laser is in three mode operation, the signals from PD_0 and PD_{90} are indeed 180° out of phase, which can be seen in Figure 5.8b. To ensure this was

not an anomaly with the laser, a different three mode laser (Model 098-2, JDSU) was used in the same setup. When this laser was in three mode operation, the same 180° difference was observed between PD_0 and PD_{90}, which can also be see in Figure 5.8b.

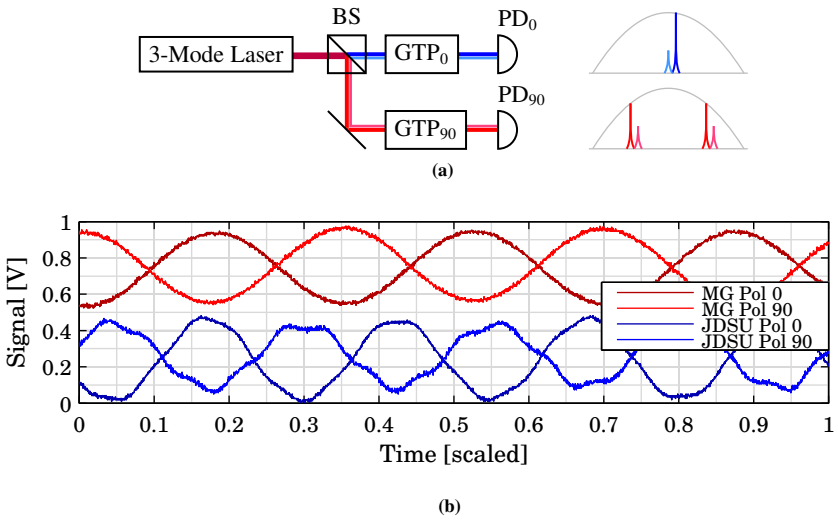

Figure 5.8: *(a) Optical schematic for verifying the phase between I^0_{pd} and I^{90}_{pd}. Two Glan-Thompson polarizers were used to isolate the inner and outer modes, which was verified using an optical spectrum analyzer. (b) Comparison of I^0_{pd} and I^{90}_{pd} for two different three mode lasers. The mixed modal beat frequencies are 180° out of phase which shows a low speed detector cannot detect the secondary beat frequency.*

5.3.4 Frequency Calibration

The mixed modal signal from the center mode, I^0_{pd}, was used to stabilize the three mode laser. The length of the laser tube, and thus frequency, was controlled via a thermo-electric cooler which was driven by frequency fluctuations in I^0_{pd}. The optical setup for calibrating the laser with respect to an iodine stabilized laser is shown in Figure 5.9.

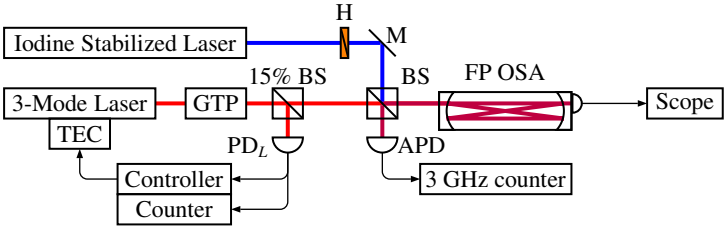

Figure 5.9: *Schematic of the calibration setup for determining the effectiveness of the intrinsic mixed mode stabilizations compared to an iodine stabilized laser. The 3 GHz counter measures the difference between the two lasers, which a normal counter measures the mixed mode signals. Correlated fluctuations can be determined and removed to estimate the frequency stability. The optical spectrum analyzer is used to view the modes of the two lasers.*

The frequency difference between the three-mode laser and the iodine laser, measured by the high speed counter is, shown in Figure 5.10a. Additionally, the measured intrinsic mode signal corrected with a linear fit to correlate it to frequency fluctuations is also shown in the figure. The difference between the measured and fitted values is shown in Figure 5.10b. The intrinsic mode signal has a sensitivity of 593.6 $^{Hz}/_{Hz}$ relative to the iodine stabilized laser. Using this signal and the thermo-electric cooler, and after correcting for known frequency fluctuations, the laser frequency from ν_2 was stabilized to better than 5.2×10^{-10} compared to the iodine stabilized laser.

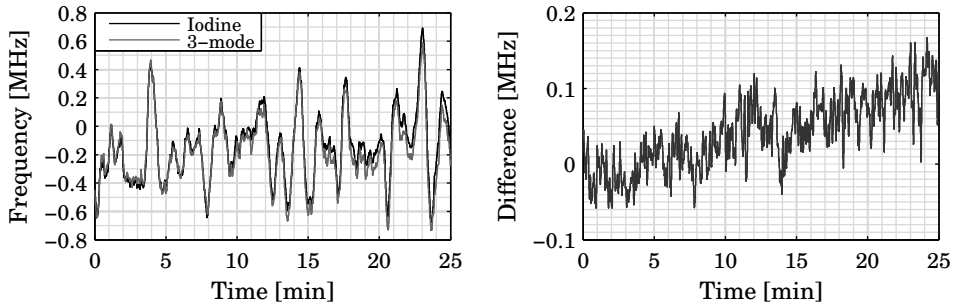

(a) (b)

Figure 5.10: *(a) Comparison between the measured difference and the corrected fluctuations of the mixed mode signal with a sensitivity of 593.6 $^{Hz}/_{Hz}$. (b) Difference between the measured fluctuations and corrected mixed mode signal. The source of the linear drift is assumed to come from thermal fluctuations in the plasma tube.*

The fractional frequency stability Allan deviation and amplitude spectrum are shown in Figure 5.11. The fractional frequency amplitude spectrum, shown in Figure 5.11b has one minor peak at 10^{-2} Hz which is likely to be caused by the time constant of the thermal mass in the system. A larger than desired thermal mass was used to buffer the laser from external disturbances which also limited the locking point stability due to long term environmental changes. Since the controller is based on a thermal actuator, changes in the environment from the original testing environment change the transfer function of the controller. Originally, the controller was tuned for an environment with high temperature changes, which meant a tight lock could not be established. When it was compared to the iodine stabilized laser, the controller was not tuned for the new environment and thus a tight lock was still not achieved.

The long term stability (many months) was not assessed due to the limited availability of the reference laser. Instead the laser system was moved to the test facility at TNO Science & Industry into a temperature controlled environment with better than 1°C temperature stability. Additionally, the controller was rebuilt on a single PCB board which reduced noise. The thermal mass of the system was also reduced and shielded with an aluminum cover to keep the temperature uniform in the surrounding environment. The controller was tuned with new gains because the changes to the thermal environment caused the original controller to become unstable. A DC voltage output from the controller proportional to the frequency input was used to determine the value of the intrinsic mixed mode signal. This

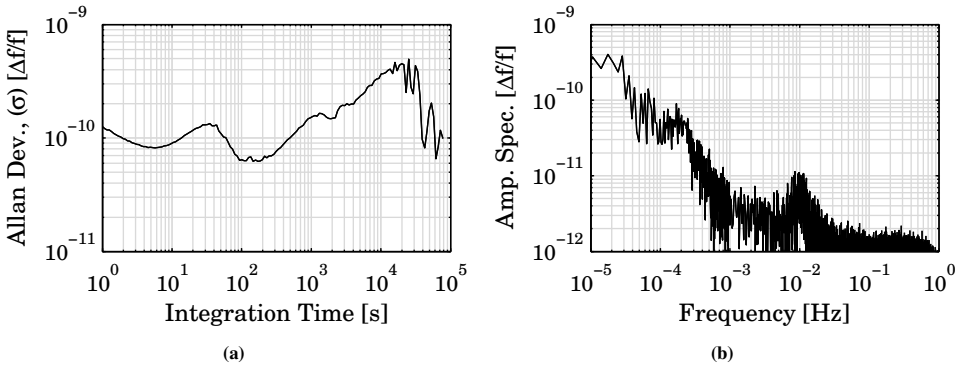

Figure 5.11: *Fractional frequency stability Allan deviation (a) and fractional amplitude spectrum (b) of the center mode, ν_2, when compared with an iodine stabilized laser using the signal generated from I^0_{pd}. This data was corrected for the known frequency fluctuations of the mixed mode signal. (The power spectral density and cumulative power spectrum is shown in Figure G.1a).*

correlation, shown in Figure 5.12a, has a frequency resolution of 10 Hz, limited by the number of bits in the controller. However, once the system is stabilized, the intrinsic mixed mode frequency was stable to 50 Hz, which is minimum frequency step achievable in the controller. This is shown in Figure 5.12b.

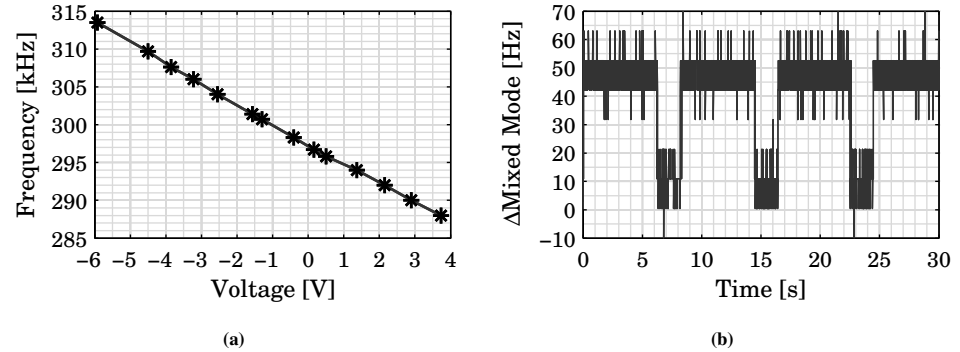

Figure 5.12: *(a) Linear sensitivity of the voltage output from the controller as a function of frequency input. (b) Stabilized mixed mode signal fluctuations after removing thermal mass, shielding the laser, and updating the controller. The locking point has a resolution of 50 Hz, which is the stability limit and the frequency output has a resolution of 10 Hz.*

The estimated fractional frequency stability using the updated controller and shielded environment is better than 2 parts in 10^{11} over one second, as shown in Figure 5.13a. During this measurement period, the peak to peak fractional frequency amplitude spectrum was better than 2 parts in 10^{12}, as shown in Figure 5.13b. This assumes a constant sensitivity coefficient (593.6 $^{\text{Hz}}/_{\text{Hz}}$) between the frequency to voltage converter and absolute frequency stability to mixed mode frequency. The amplitude spectral density shows some peaks around 0.1 Hz, which is the closed loop bandwidth of the system with the updated controller

parameters in a shielded, more stable environment and with thermal mass removed.

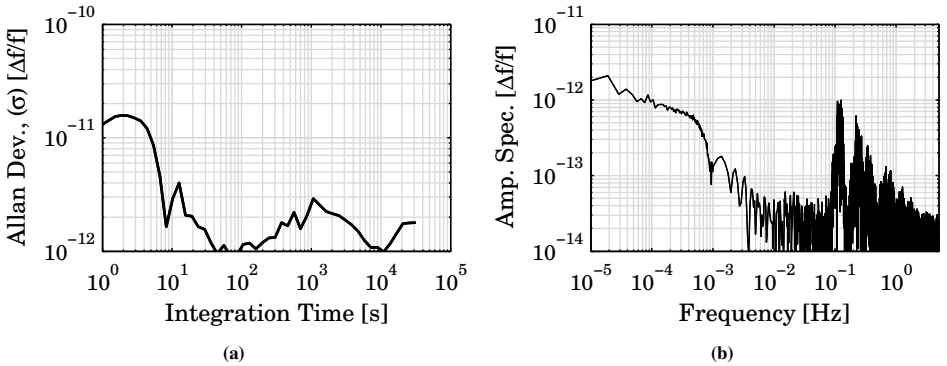

Figure 5.13: *Fractional frequency stability Allan deviation (a) and fractional amplitude spectrum (b) of the center mode center mode ν_2 assuming a sensitivity of 593.6 $^{Hz}/_{Hz}$. This data was corrected for the known frequency fluctuations of the mixed mode signal. Long term stability relative to the iodine laser could not be assessed due to its limited availability. (The power spectral density and cumulative power spectrum is shown in Figure G.1b)*

Because the laser controller has a stability of 50 Hz on the mixed mode signal (Figure 5.12b), the subsequent peaks behave similarly to the frequency response of a square wave. Two steps can be taken to improve this system: remove more thermal mass or replace the thermal actuator with a mechanical actuator. These are discussed in more detail in Chapter 7.

An additional benefit of using this three mode laser stabilization system is the central mode has a power greater than 2 mW, which is suitable for interferometry applications which need a higher power source. Two acousto-optic modulators can then be used, similar to the system described in Section 3.2, to generate the heterodyne frequency. This frequency, in general, should be chosen far away from the intrinsic mixed mode signal at 300 kHz to prevent frequency mixing or spurious signals.

5.3.5 Conclusions

This research shows there is a detectable, intrinsic signal in a three mode HeNe gas laser which can be used for feedback stabilization. This mixed mode signal is different from the secondary beat frequency because direct measurement of the intermode frequencies is unnecessary. Additionally, the outer and outer-mixed mode signals are 180° from the central and central-mixed mode signal, causing destructive interference for detecting the secondary beat frequency. The current system has demonstrated a short term stability of 2×10^{-11}, contributing an uncertainty of 1 pm for a 50 mm sample, which is suitable for this research.

Replacing the TEC-based actuator with a non-thermal method of controlling the cavity length would remove the unwanted thermal effects in the system and increase the locking point stability. A possible solution is to use a sealed cavity laser with anti-reflectance coatings on one side of the laser tube and an externally located, piezo controlled laser mirror.

A piezo-controlled mirror would increase bandwidth and remove most heat generation but alignment and the overall system concept need to be considered.

A long-term assessment is still needed to verify the frequency stability compared to a metrology laser system. Additionally, the intrinsic mixed mode may depend on the temperature and pressure of the plasma tube. Previous research by White [139] showed changes to the HeNe mixture, purity, discharge current, and pressure within the plasma tube can cause the whole gain profile to shift in the frequency domain up to 10's of megahertz. Bloom and Wright [140] demonstrate a 40 MHz line shift over plasma pressures of 2.5 torr to 4 torr, which translates to a line shift sensitivity of ~200 kHz·Pa^{-1}. In that research, the focus was on single mode lasers, which differs from the three mode lasers used in the research in this thesis.

More research is needed to quantify this for 3-mode HeNe lasers and determine its effect on the instrinsic mixed mode signal. By stabilizing the system without using a thermal actuator, potentially more stability can be gained from the system because the cavity length and tube temperature can then be controlled independently. If the HeNe mixture is known and the cavity length, temperature, and discharge current are kept constant, then it may be possible to stabilize the whole gain profile in the frequency domain, which would help increase the stability of the laser.

Chapter 6

Interferometry Systems

The previous four chapters outlined the research necessary to develop an interferometer suitable for measuring material stability with a low measurement uncertainty. A detailed error budget was put forth in Chapter 2, which set criteria for the uncertainty contributions from periodic nonlinearity, refractive index, and optical frequency. The research discussed in Chapter 3 proved the most effective way for limiting periodic nonlinearity is to spatially separate the two input beams and have no prior mixed states. Chapter 4 showed the refractive index can be measured using a variety of methods. Of the methods shown, the heterodyne phase tracking method showed the most promise because it is performed using similar measurement principles and optical components as the sample measuring interferometer. This eliminates the need for an additional setup and cross-correlation measurements.

Chapter 5 presented research from a novel frequency stabilization technique using an intrinsic mixed mode signal in a three-mode laser. This laser nearly satisfies the frequency stability requirements and has suitable power and contributes no discernible frequency mixing in the systems evaluated during this research[1]. An example of a double-sided interferometer for measuring material stability that incorporated each of these techniques was presented in Chapter 4. This interferometer, shown again in Figure 6.1, has spatially separated beams generated from a stabilized source. Internally, it has a vacuum cell for measuring refractive index changes by phase tracking. In principle, if the optical path imbalance can be reduced or removed, this design has the potential to measure material stability.

The largest optical path imbalance occurs because the reference beams do not pass through the same components as the measurement beams. Additionally, the sample measurement arm (red, solid) has a slightly shorter path length than the refractometer measurement arm (red, dashed). This can be mitigated by having the same optical path difference between the sample reference arm and the refractometer reference arm. Correcting the optical imbalance was the focus of two design iterations, shown here. In the preliminary optical concept, the reference arms for both interferometer channels were

[1]The stabilized laser presented in Chapter 5 was used as the source for the Joo-type interferometers discussed in Section 3.5. In those configurations, the noise level was approximately 50 pm, which is the limit of the periodic errors as no discernible peaks were detected.

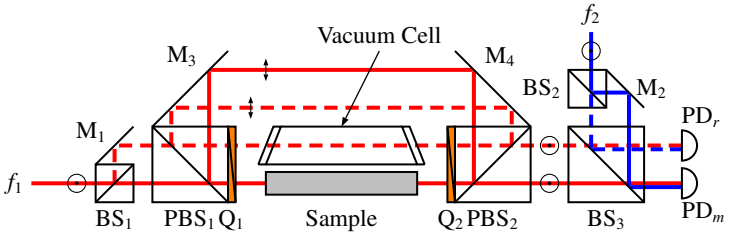

Figure 6.1: *Schematic of a dual interferometer with one interferometer measuring sample displacements while the other measures refractive index fluctuations.*

moved into the same location as the measurement arms. This interferometer was used only a basic, commercially available source and optics to establish a baseline measurement of the system. The second iteration corrected a slight optical path imbalance in the first iteration. Also, high-end, commercially available optics were used to perform experiments with the interferometer. After those experiments were completed, custom optics, that minimized the number of optical mounts and alignment axes, were used for further measurements.

The following section introduces the preliminary optical concept. Details and preliminary measurements are discussed in Appendix F. Following that, the generalized interferometer concept is discussed in detail, including the concept and optical modeling. Then, three different setup versions are discussed, particularly noting the detailed differences between setup versions, measurement results, and preliminary conclusions.

6.1 Preliminary Optical System Concept

The preliminary optical system concept is shown in Figure 6.2. This optical system contains two interferometers. The optical path length difference in one interferometer (dashed lines) measures sample length changes multiplied by refractive index changes. An accurate measurement for the refractive index in the surrounding environment is needed to decouple refractive index changes from sample length changes. The second interferometer (solid lines) in the optical system measures refractive index changes relative to a vacuum tube. The refractive index change can then be determined using Equation 4.18 and then Equation 2.86 can be used to determine the measured sample drift. For details on this interferometer description, see Appendix F

This optical system was extensively modeled using Zemax, an optical modeling software package. Because a lateral displacement beamsplitter was used as the main interfering element, the sample measurement arm (SM) and the refractometer reference arm (RR) both pass through an additional 10 mm portion of optical path length compared to their respective interfering beams. Another imbalance in the system is the difference between the (f) beam and the $(f + \delta f)$ beam. The (f) beam enters the initial beamsplitter closer to the splitting surface, which means it is split sooner than the $(f + \delta f)$ beam, which enters further from the splitting surface. This creates an additional optical path length difference which should be corrected in the next design iteration.

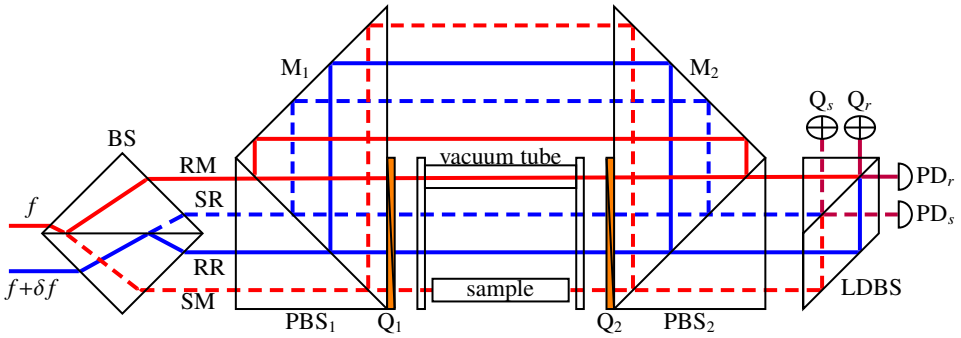

Figure 6.2: *Preliminary optical system concept containing two interferometers. One interferometer measures sample length changes times refractive index changes whereas the other measures refractive index changes. (RM, refractometer-measurement arm; SR, sample-reference arm; RR, refractometer-refreference arm; SM, sample-measurement arm)*

6.2 Main Optical System Concept

6.2.1 Interferometer Description

One of the more practical ways to alter the preliminary concept from Figure 6.2 was to move the reference and measurement beams out of plane from each other. This also allows the input beams to enter the first beamsplitter on the same side, rather than opposite sides, which eliminates another optical path imbalance. The interferometer without beams is shown in Figure 6.3a with both top and front views to show the beams moved out of plane. Two spatially separated, parallel beams with a known split frequency are still used as the source for this interferometer. The beams then enter a beamsplitter rotated 45° from a traditional configuration, where they are split into four beams; two for the sample measurement and two for the refractometer measurement. Then, two polarizing beamsplitters and quarter wave plates similar to the preliminary concept are used. Finally, a lateral displacement beamsplitter is used to interfere the beams into measurement and refractometer signals.

In the ideal configuration, this interferometer will be made of three separate, custom optics. The first optic will be the initial beamsplitter with anit-reflection coatings designed for 45° input beams and a 50% beamsplitting surface designed for equal splitting at a non-45° input. The second optic will consist of a polarizing beamsplitter (PBS_1), right angle prism acting like a mirror, and a quarter wave plate (Q_1). The polarizing beamsplitter and the mirror will ideally be manufactured from only two pieces of fused silica and Q_1 will be optically contacted to the surface where needed. The third optic will consist of the same components as the second optic, plus an additional lateral displacement beamsplitter for combining the reference and measurement arms. Aside from anti-reflection coating the necessary surfaces, the mirrors connected to the polarizing beamsplitters should be extended by a spacer for additional room for the vacuum tube. A schematic of this three optic setup is shown in Figure 6.3b having a minimum number of optical components to reduce alignment errors between individual components.

Both reference arms for the sample and refractometer measurements come from the same input beam, which is linearly polarized and oriented to pass through PBS_1. Referring to Figure 6.4, the top input beam is split equally at the beamsplitter. This results in the *refractometer-reference* and the *sample-measurement* beams, labeled RR and SR,

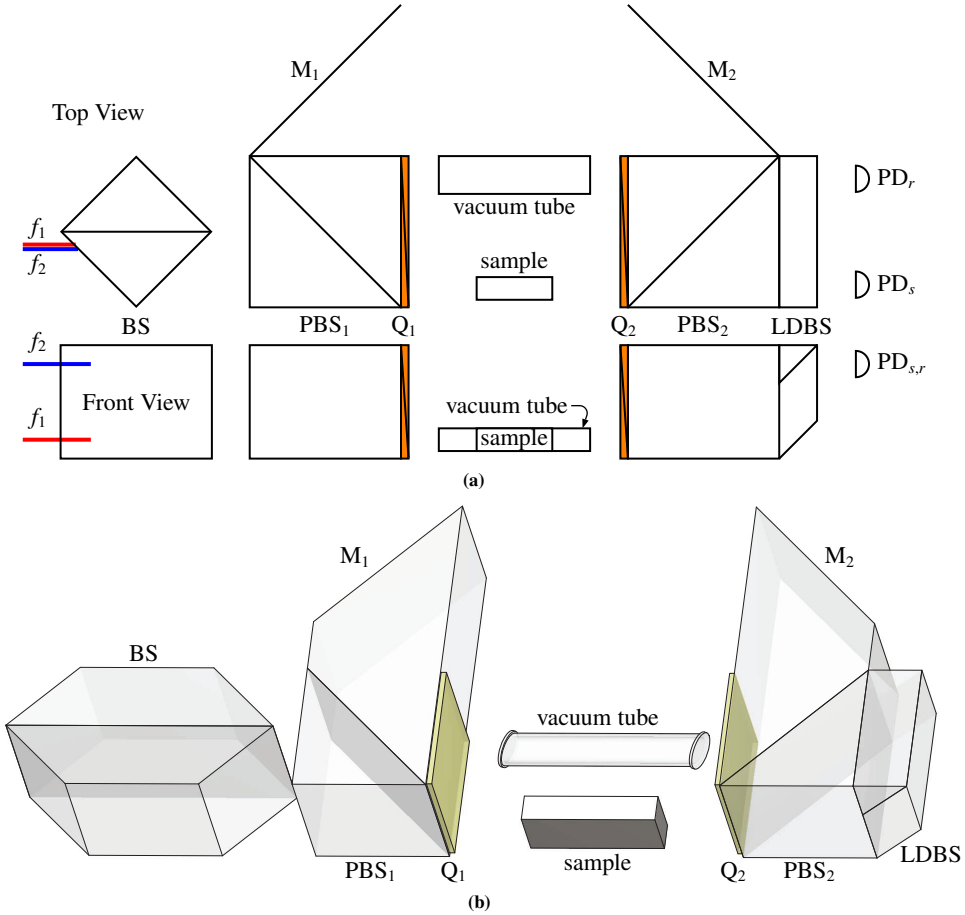

Figure 6.3: *(a) Schematic of the main optical system for this research. This system is a dual interferometer with one interferometer measuring the sample and the other measuring a vacuum tube for characterizing refractive index changes. With respect to the preliminary concept, the reference input beam was moved out of plane to reduce the optical path imbalance. (b) Model of the main optical system comprising three main optical blocks.*

respectively. The input polarization is oriented to transmit the majority of the light through PBS_1. Both beams pass through Q_1 where they are rotated 45°. When they pass through Q_2, they are rotated a further 45°, which makes them reflect off PBS_2. They then reflect off M_2 and M_1 and enter PBS_1 from the top. Due to their 90° rotated polarization state from their initial state, the beams reflect off PBS_1. They then pass through Q_1 and Q_2 a second time, where the polarization state is rotated from 90° back to 0°. This causes the beams to pass through PBS_2 and into the LDBS. There, they travel to a 50% beamsplitting surface which transmits and reflects equal parts. This is also the interfering surface with the two respective measurement beams.

The two measurement beams come from the bottom input beam, as shown in Figure 6.4 There, they are split into the *sample-measurement* and the *refractometer-measurement* (SM and RM, respectively) beams. As with the reference input beam, the initial input polarization state is oriented to transmit most of the light through PBS_1.

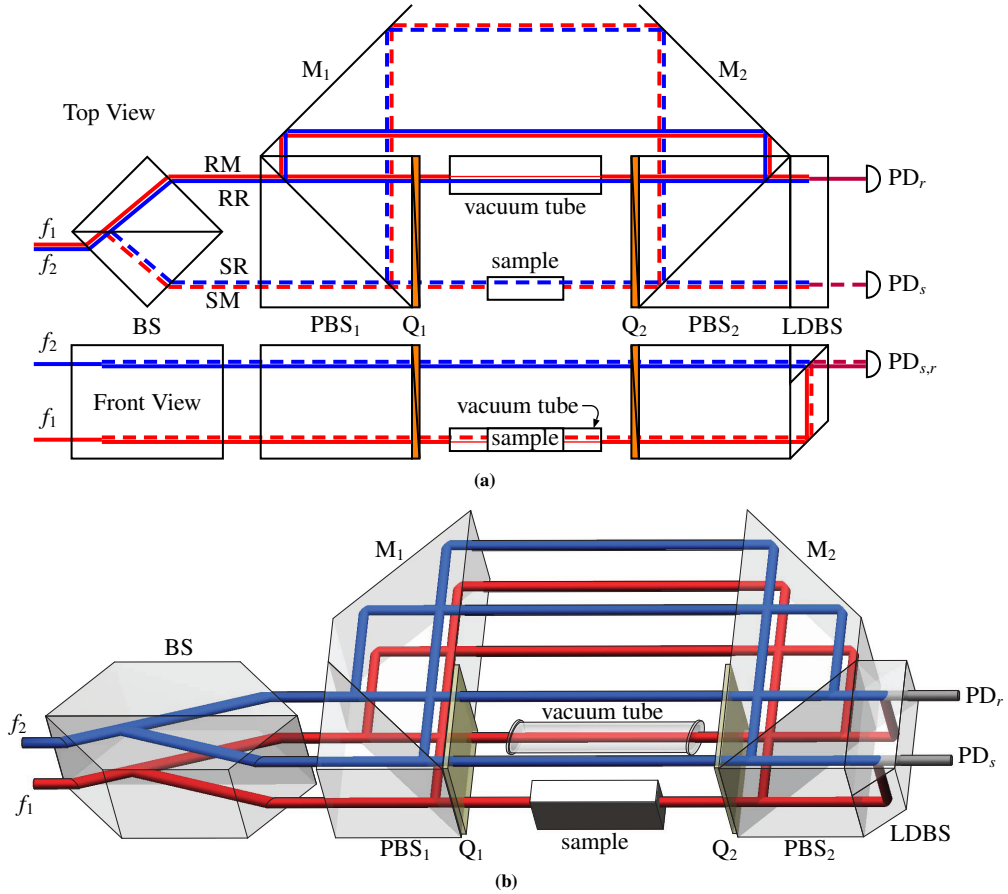

Figure 6.4: *(a) Top view and front view of the complete optical schematic of the main interferometer concept in this research. (b) Model of the optical system. This system is a dual interferometer for double sided measurements on a sample with its own internal refractometer for refractive index tracking. Two additional interference beams exit from the top of the lateral displacement beamsplitter, although they are not initially used in this system.*

The RM beam follows a path similar to that of the RR and SR beams with the same initial polarization state. After being split by the initial beamsplitter, the beam passes through PBS_1 and Q_1 where the polarization state is rotated 45°. The beam then passes through a vacuum tube which has the air removed to provide a refractive index of unity. After passing through the vacuum tube, the beam transmits through Q_2 where the polarization state is rotated a further 45°. Now, the polarization state has been rotated 90° and it reflects off PBS_2. It then reflects off two more mirrors and PBS_1. The beam then passes through Q_1, the vacuum tube, and Q_2 for a second time. Now the polarization state is oriented back to 0°, where it transmits through PBS_2. The RM beam is then reflected vertically by the lateral displacement beamsplitter where it interferes with the RR beam. This produces two measurement signals from the lateral displacement beamsplitter, one exiting horizontally and one exiting vertically (not shown in the figure). One of these signals is then used to measure the refractive index fluctuations.

The SM beam follows a different path than the RM, RR, and SR beams. After passing through PBS_1 and Q_1, the polarization state is rotated 45°. The beam then reflects off the sample and passes back through Q_1. The polarization state is then oriented to 90° where the beam reflects off PBS_1. After reflecting off two mirrors and PBS_2, the beam passes through Q_2, where the polarization state is rotated back to 45°. After reflecting off the sample a second time, it passes back through Q_2, where the polarization state is oriented back to 0°, where it transmits through PBS_2. The SM beam then reflects vertically in the lateral displacement beamsplitter where it interferes with the SR beam at the beamsplitting surface. Two interference signals are created, one exiting vertically (not shown) and the other exiting horizontally from the lateral displacement beamsplitter. The complete interferometer with all beams is shown in Figure 6.4a.

The two measured, time-varying irradiance signals detected from PD_s and PD_r, respectively, are

$$I_s \propto \cos(2\pi\Delta f_s t + \phi_s) \quad \text{and} \tag{6.1}$$

$$I_r \propto \cos(2\pi\Delta f_s t + \phi_r), \tag{6.2}$$

where I_s and I_r are the sample and refractometer irradiances, respectively, Δf_s is the laser split frequency, and ϕ_s and ϕ_r are the sample and refractometer phases, respectively. The measured phases are

$$\phi_s = \frac{2\pi N x \eta f}{c} \quad \text{and} \tag{6.3}$$

$$\phi_r = \frac{2\pi N L(\eta - 1) f}{c}, \tag{6.4}$$

where N, the interferometer constant, is two, x is the sample length, L is the vacuum tube length, η is the refractive index, f is the absolute laser frequency, and c is the speed of light. Using these equations, combined with the material properties, the measured drift can be determined as described in Section 2.4

6.2.2 Optical Modeling

This interferometer was modeled using Zemax to determine sensitivity coefficients for alignment and stability. The optical setup was assumed to be made of three optics and four fiber couplers, two for inputs and two for output, as was shown in Figure 6.5a. Once the sensitivity coefficients for the components and the alignment were determined, a Monte-Carlo simulation was performed, assuming the optics were mounted on aluminum mounts. The worse-case temperature gradient was assumed to be the largest source of component motions. The results from the Monte-Carlo simulation are shown in Figure 6.5b.

The results showed a Gaussian distribution with a $\pm 2\sigma$ error of 180 pm. Thus, assuming the phase, refractive index changes, frequency fluctuations, and all other errors are minimal, the resulting drift should be about 180 pm.

Table 6.1 shows the six highest sensitivity coefficients and their estimated error. The physical description of each error is shown in Figure 6.6. Minimal data was available from the manufacturer about the fiber couplers [141]. However, other researchers[2] have shown

[2]Personal communication with Dr. Jerald Overcash, University of North Carolina at Charlotte

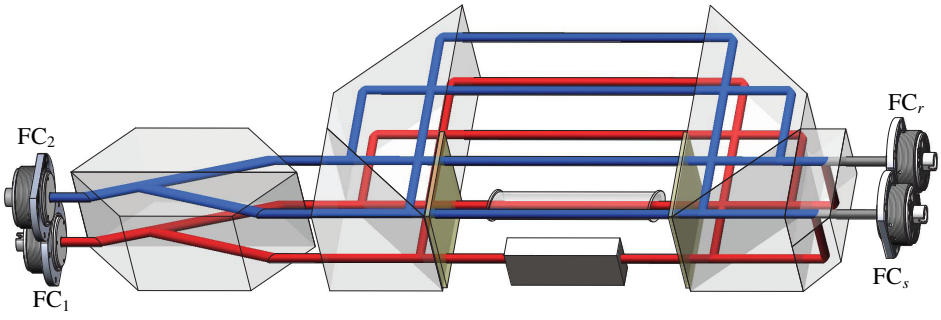

(a)

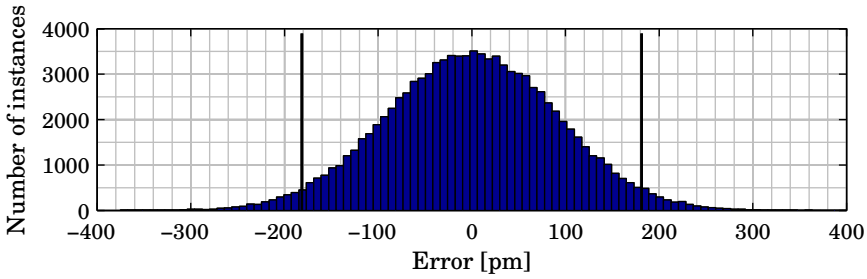

(b)

Figure 6.5: *(a) Model of the optical system comprising three optical blocks, sample, vacuum tube, and four fiber couplers, $FC_{1,2,r,s}$, for beam launching and detection. (b) Results from a Monte-Carlo simulation where the sensitivity coefficients were determined from a Zemax simulation and the randomized variable is component motions due to thermal effects. Based on this estimation, the $\pm 2\sigma$ noise level in the system should be 180 nm.*

very good stability with these couplers, an estimated 50 nrad, during non-related research. The PBS_1+M_1 optic stability for X-rotation was a highly sensitive error source. This is due to the sample measurement arm traveling a different path than the sample reference arm or the two refractometer beams. As with the difference in the optical path propagation, the sample non-parallelism causes a similar error.

Table 6.1: *The seven highest sensitivity coefficients in the interferometer assuming three optic block are used. The fiber coupler error was estimated by talking to other researchers which have used these couplers. The other errors are due to the maximum thermal gradient.*

Component	Motion	Sensitivity [nm·μrad^{-1}]	Error [μrad]	Value [pm]
Top Fiber Coupler	X-rotation	1.26	0.05	63
	Y-rotation	0.88	0.05	44
Bottom Fiber Coupler	X-rotation	1.35	0.05	68
	Y-rotation	0.88	0.05	44
PBS_1+M_1	X-rotation	2.33	0.005	11
Sample	non-parallelism	2.38	0.004	10

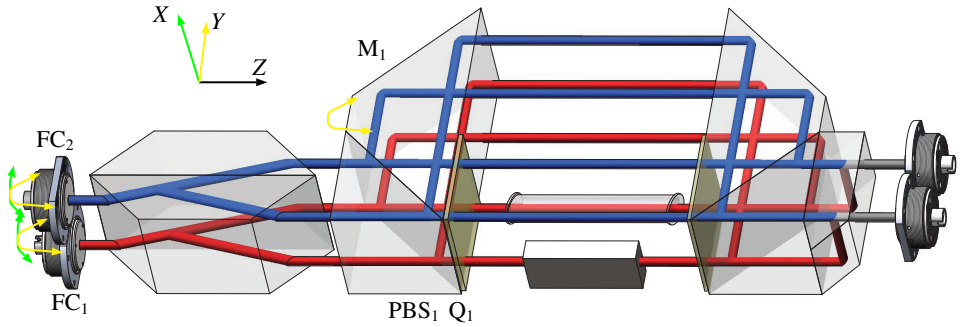

Figure 6.6: *Model of the optical system highlighting the major error contributors and their directional sensitivity. The input beam alignment in both axes was estimated to be the highest potential error contributor. The X-direction is more sensitive because it creates a longer cosine error for the measurement paths than the reference paths.*

6.2.3 Optical Path Imbalance

This interferometer configuration has some optical imbalance in three areas: the refractometer windows, the difference between the vacuum tube length and the sample length, and the lateral displacement beamsplitter prior to interference. The imbalance from the vacuum tube can be corrected by placing compensation windows in the other three paths which should mitigate this effect. This system was modeled with the compensation windows and without. Based on the optical modeling, the compensation windows contribute to an additional error source because the vacuum tube motions may not be correlated to the compensation windows. Therefore, these windows were omitted, but they can be added later if needed.

The difference between the vacuum tube length and sample length means the refractive index changes measured by the refractometer will not be directly matched in the sample interferometer measurement. For instance, if the sample is x and the vacuum tube is L, then the refractive index measured should be scaled by L/x.

The last optical path imbalance can be corrected by placing an equal lateral displacement beamsplitter after the laser source and prior to the acousto-optic modulators. Figure 6.7 shows the main optical system concept including the laser source and heterodyne generation parts. In this system, the optical path imbalance is also corrected for the added optical heterodyne reference. This, however, is only practical when the system is not fiber-fed (free space system) or if the acousto-optic modulators are placed in a vacuum vessel. This also means the beam steering optics that would replace the fiber coupling inputs as modeled in the previous section must provide the same pointing stability.

6.2.4 Measurement Systems

The following sections describe several measurement systems during the overall progression of the work in this thesis. Each section presenting a particular system, labeled 1st Measurement System, 2nd Measurement System, and so on, contains a detailed description of the practical implementation, changes from the previous system, measurements with that system, and conclusions. Overall conclusions from all of the different measurement systems are presented at the end of this chapter.

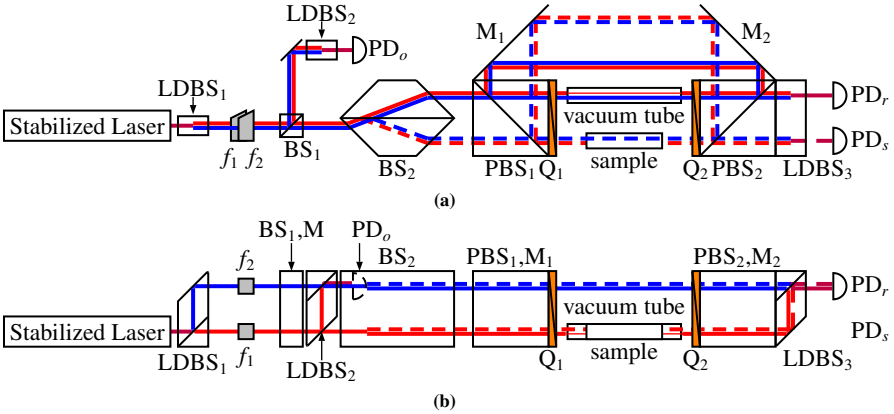

Figure 6.7: *Top view (a) and front view (b) of the optical setup correcting for the optical path imbalance in $LDBS_3$ by splitting the reference and measurement beams via an equal and opposite $LDBS_1$. The optical reference detected via PD_o corrects for the imbalance created with $LDBS_1$ by combining with $LDBS_2$. (The acousto-optic modulators generating f_1 and f_2 are offset in the top view for clarity.)*

6.3 1st Measurement System

The 1st Measurement System was built at TU Delft as a proof of concept with a interferometer stability target of 20 nm. This was chosen to establish baseline measurements, which could be improved upon over subsequent measurement system iterations. A photo of the setup during the initial setup procedure is shown in Figure 6.8.

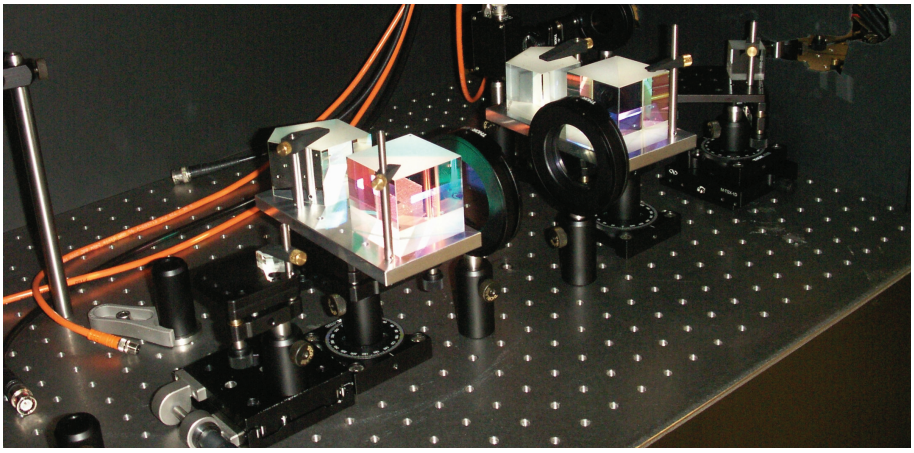

Figure 6.8: *Photo of the 1st Measurement System during the initial alignment*

6.3.1 Practical Implementation

The periodic nonlinearity research from Chapter 3 was performed concurrently with this phase of the research. The laser source with two acousto-optic modulators was not available, thus a single acousto-optic modulator was used with a 20 MHz split frequency. While this

will mean some frequency mixing will occur, the error foreseen from periodic nonlinearity was assumed to be minimal. Figure 6.9 shows a schematic of the three parts of the optical system: the laser source, the interferometer configuration, and the data acquisition.

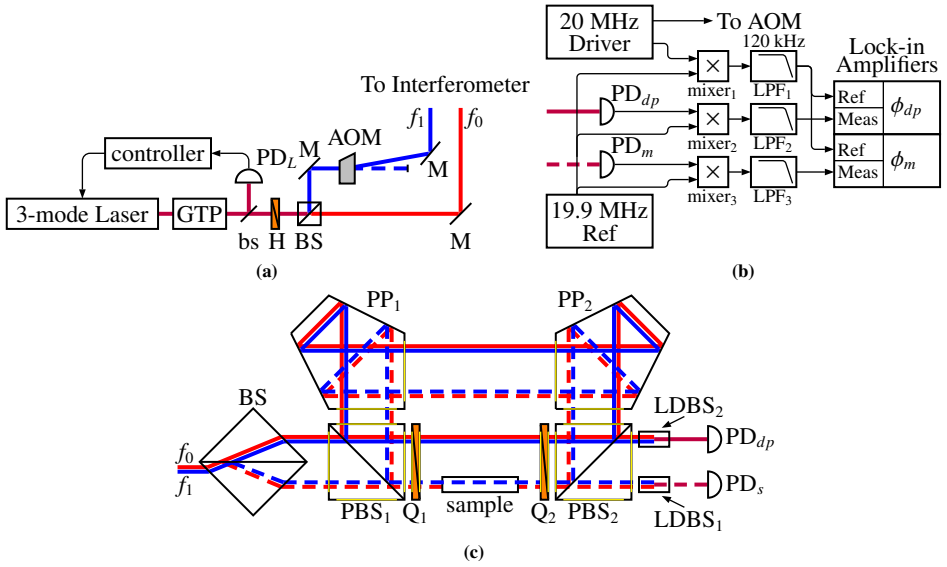

Figure 6.9: *Laser system and heterodyne frequency generation (a), data acquisiton system (b) and interferometer components (c) for the 1st measurement system. The stabilized laser was the custom laser from Chapter 5. The optical and electrical reference signals are mixed with a common 19.9 MHz oscillator and filter prior to measuring the phase using two lock-in amplifiers. The interferometer is slightly modified from Figure 6.4, using two penta prisms to simplifiy alignment.*

The laser source was the custom three-mode stabilized laser system described in Section 5. This laser source has high frequency stability and has a high output power, around 2 mW. The output beam from the three-mode laser first passes through a Glan-Thompson polarizer to block the two outer modes. A beam sampler is used to detect the intrinsic mixed mode signal, which is then sent to the laser controller, current amplifier, and Peltier heater controlling the laser tube length. The main beam is then split using a 50% beamsplitter and the transmitted beam passes through an acousto-optic modulator driven at 20 MHz.

Since a low laser power and a lack of anti-reflection coatings contributed to questionable data in the preliminary concept (see Appendix F), the increased power from this custom laser source means more optical power will be available at the detector. Also, the interferometer components were switched to tighter tolerance, off the shelf counterparts with better splitting coatings and anti-reflection coatings that the air-glass transitions to reduce power loss in the interferometer. Two larger polarizing beamsplitters were used (50 mm-edged cubes) to reduce the edge effects. Also, two penta-prisms with a 5 arcsec tolerance used to remove an alignment error in one tilt axis from M_1 and M_2. Each surface with an anti-reflection coating better than 0.25% is shownby a yellow line. Having a higher powered source and anti-reflection coatings on each of these surfaces meant much higher

power was detected, around 20 μW per signal, with the photodetectors.

Unlike the preliminary concept, the direct interference signal at 20 MHz from the photodetectors was directly visible on an oscilloscope. The interference signal was clearly visible without any assistance from amplifiers, mixers, or filters because a higher optical power was available at the detector. Once on the scope, the signals were optimized by adjusting the alignment to maximize the interference fringe contrast. After finely adjusting the optical components to improve the fringe contrast, the phase was measured by mixing the 20 MHz detection signals with a local oscillator at 19.9 MHz. The 100 kHz difference frequency was filtered using a Butterworth low pass filter, where the signal was then amplified. Both signals were sent to two lock-in amplifiers [81] with a 0.01° phase resolution. The wrapped phase was acquired by a National Instrument data acquisition card and the phase was then unwrapped using a program in Matlab.

The temperature and pressure of the surrounding environment was also measured. Two temperature probes, mounted near the sample, were used to measure the air temperature and another probe was used to measure the sample's surface temperature. Each of these sensors were calibrated with a 7 mk uncertainty at the VSL Dutch Metrology Institute. Additionally, the VSL Dutch Metrology Institute provided a pressure monitoring station. Each of these was measured using a Matlab program, along with the measured phase.

6.3.2 Double Deadpath Measurement

The first measurement with this interferometer was a double deadpath measurement. Neither the sample, nor the vacuum tube was included in this measurement. Thus, the two signals globally should have minimal drift, only a small temperature induced value from the slight optical path difference between the measurement and reference arms. When the difference is taken, the result should be zero for an ideal case. Any difference between the two measured signals should be taken as the baseline minimal noise and drift level of the system.

Figure 6.10 shows the measured double deadpath and the air temperature and pressure over 14 hours. Both measured signals show a drift of nearly 500 nm with approximately 250 Pa of pressure change and 0.25 K temperature change. The temperature showed a continuous ripple of approximately 25 mk every 15 minutes superimposed over a general decrease in temperature. The ripple every 15 minute is consistent with fluctuations in the measured interference signals. Because of the high symmetry in the system, there is a strong correlation between the two interference signals, as shown in Figure 6.10a.

The length change in the interferometers had a noise level of approximately 50 nm, pk-pk, which was unexpected. The reason for this noise is likely to be due to the optical mounts and vibrations in the system. The optical components were mounted on standard tip-tilt mounts that are known to have some drift at the micrometer level. This drift is highly correlated between the two signals because when the difference is taken, as shown in Figure 6.11, the results are quite unexpected.

The difference between the measured length change between the two interferometer, the drift, was less than 1 nm over 13 hours with a 14 nm (pk-pk) noise level. During that same time, the temperature fluctuations were greater than 250 mk and the pressure change was over 250 Pa. Thus, even in a relatively unstable environment (for this type of measurement)

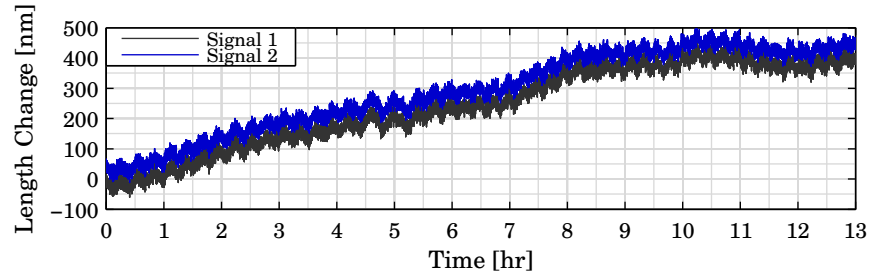

(a)

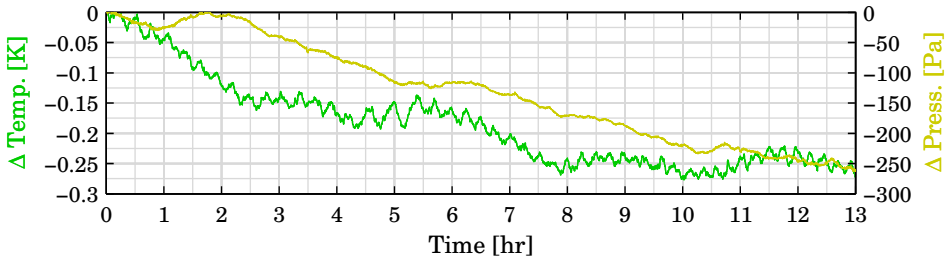

(b)

Figure 6.10: *(a) Measured length change of the two interferometers, offset for clarity, and (b) environmental changes from the double deadpath interferometer. The length change showed a strong correlation to the temperature fluctuations.*

using standard optical components and mounts, this interferometer has low drift.

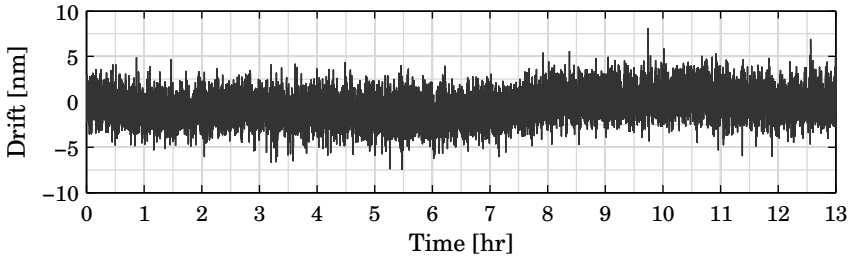

Figure 6.11: *Difference between the two deadpath signals in the interferometer. The drift appeared to be below 1 nm with a 14 nm (pk-pk) noise level. The noise level was still higher than expected but significantly lower than the 50 nm noise level in the individual interferometer measurements.*

6.3.3 30 mm Gauge Block Measurement

After assessing the double deadpath, a 30 mm steel gauge block was measured using this interferometer. The vacuum cell was still not available for refractive index compensation. However, measuring the temperature and pressure and correcting with the Edlén equation

permitted assessment of the drift at nanometer levels. The measured results from almost ten hours of testing are shown in Figure 6.12.

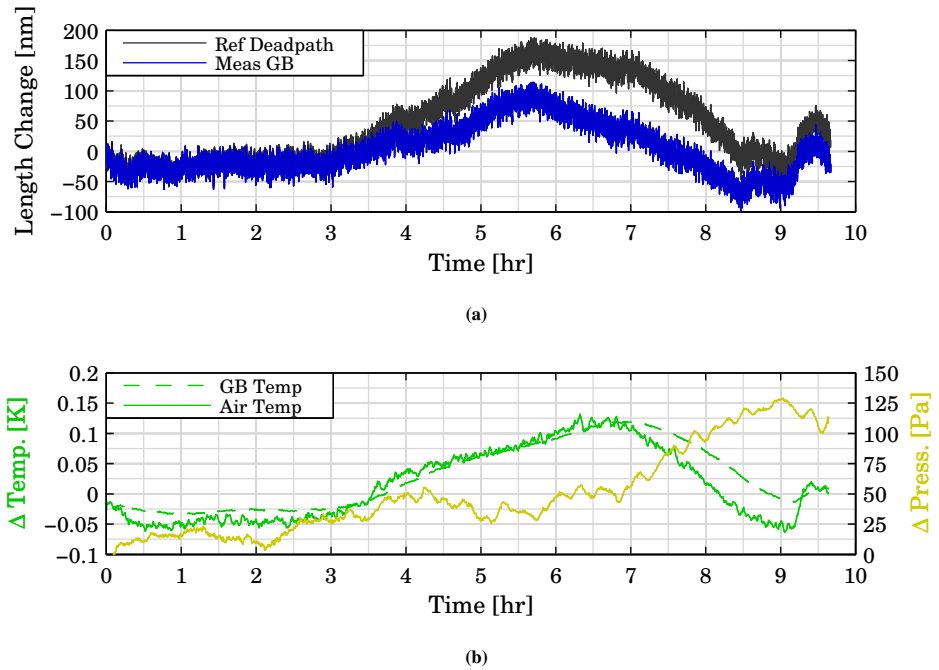

Figure 6.12: *(a) Measured optical path length change of the reference deadpath and the sample arm in the interferometer. (b) Air and sample surface temperature changes and pressure change during the measurement. The measured length change showed a strong correlation to temperature changes.*

The measured deadpath, which was the reference, increased 200 nm before decreasing back down to the starting value. The gauge block signal only changed 100 nm, before decreasing back down to near the starting value. This artifact in the measurement is clearly temperature driven as shown in Figure 6.12b. The temperature change was less than in the double deadpath measurements and the peak length change in both the reference and gauge block signals coincide with the peak temperature difference. Also, the air temperature changed faster than the gauge block temperature due to a higher thermal mass and slower time constant with the sample. This is important to note the difference because the air temperature is used for refractive index correction and the sample temperature is used for thermal expansion correction.

The noise level for each interferometer was approximately 50 nm, which was similar to the double deadpath measurements. While the optical mounts will contribute some noise, the more important issue is the potential effect when using the vacuum tube. This is explained in more detail in the following section.

The drift in the system was assessed by removing the fluctuations from known effects such as temperature and pressure changes. The difference between the deadpath and the sample measuring signal was 100 nm. When converting to a length change value, this was

divided by two because this interferometer has an interferometer resolution of two. The measured length change is determined from

$$\Delta L_\phi = \frac{\lambda}{2\pi N}\left(\phi_r - \phi_s\right), \tag{6.5}$$

where ΔL_ϕ is the measured length change from phase fluctuations, λ is the nominal wavelength, N is the interferometer resolution, and ϕ_r and ϕ_s are the measured and unwrapped phase values for the reference and sample measuring signals.

The measurement was corrected for known frequency fluctuations using

$$\Delta L_{freq} = -\frac{\Delta f}{f} L_o, \tag{6.6}$$

where ΔL_{freq} is the length change due to frequency fluctuations, $\Delta f/f$ is the fractional change in laser frequency, and L_o is the nominal gauge block length (30 mm).

Correcting for refractive index and thermal expansion fluctuations was more difficult because the phase measurements and the environmental parameter measurements occurred at two different sampling rates. The phase and frequency fluctuations were measured at 4 Hz, whereas the temperature and pressure was measured at 0.1 Hz. The temperature and pressure signals were digitally upsampled to 1 Hz using a linear interpolation. The phase fluctuations were low-pass filtered using a digitial Butterworth filter with a cutoff frequency of 1 Hz. The filtered phase signals were then downsampled four times to have a sampling rate of 1 Hz. The digital downsampling and upsampling of the signals and additionally filtering may slightly alter the measured values but it should give an indication of whether the data is suitably corrected for refractive index fluctuations and thermal expansion effects.

Rather than using the complete Edlén formula to correct for refractive index fluctuations, estimated correction values based on a sensitivity function were used. From Estler [31], a $1{\times}10^{-8}$ relative refractive index change is caused by changes of -0.01°C, 3.73 Pa, and 1% RH. This correction is suitable for cases where the environmental parameters have minimal fluctuation around standard temperature, pressure, and humidity (20°C, 101 kPa, and 40% RH). The relative humidity was assumed constant for these experiments. The length change due to refractive index fluctuations is

$$\Delta L_{RI} = -\left(\frac{\Delta P}{3.73} - \frac{\Delta T_a}{0.01}\right) \times 10^{-8} L_o, \tag{6.7}$$

where ΔP is the air pressure change and ΔT_a is the air temperature change. The sample was corrected for thermal expansion effects by

$$\Delta L_{CTE} = -\alpha_s L_o \Delta T_s, \tag{6.8}$$

where α_s is the thermal expansion coefficient of steel (11.8 $\mu m{\cdot}m^{-1}{\cdot}K^{-1}$) and ΔT_s is the sample temperature change. The last correction needed was for the pressure fluctuations. This was corrected by

$$\Delta L_P = \frac{3L_o\left(1 - 2\nu_s\right)\Delta P}{E_s}, \tag{6.9}$$

where ν_s is the Poisson ratio for steel (0.3) and E_s is the elastic modulus of steel (190 GPa). The total corrected length change is

$$\Delta L = \Delta L_\phi + \Delta L_{freq} + \Delta L_{RI} + \Delta L_{CTE} + \Delta L_P. \tag{6.10}$$

Figure 6.13a shows the measured sample length change and the correction components. The sample displaced a maximum of 50 nm which was largely due to thermal expansion induced fluctuations. The refractive index change had the next highest impact at about 10 nm. The refractive index was largely driven by pressure fluctuations which changed as much as 125 Pa. The laser frequency-induced and pressure driven length change was minimal, as expected.

The total sample length change after compensating for known effects is shown in Figure 6.13b. This measured drift has a noise band of 5 nm pk-pk, which was still higher than anticipated, but lower than the deadpath measurement. The measured length change showed no appreciable drift, except between 5 and 7 hours. This is likely due to an improper temperature correlation. As stated previously, the temperature sensor was placed on the sample surface which has a slightly different value than the sample core temperature. This could lead to an improper thermal expansion correction. If the surface temperature was different from the core temperature by 2.8 mk, this is conceivable (1 nm$\cdot\alpha_s^{-1}\cdot L_o^{-1}$). However, the mean value of this disturbance was about 1 nm, which was four times less than the total noise band. Thus, it can not be decisively stated that this drift is noise or due to a temperature measurement error.

6.3.4 Interpreting Drift Data

There are several methods for interpreting drift data. An Allan deviation is typically used to find an optimal data averaging point. Also, the Allan deviation typically has an upswing at high integration times which means averaging more data points does not improve the measurement because drift has occurred. A single sided amplitude spectrum from a Fourier analysis gives an indication where a resonance occurs at a specific frequency. Also, the Fourier analysis shows where $1/f$ noise begins. A power spectral density plot shows the amount of power in a signal at a specific frequency. A cumulative power spectrum plot sums the power spectral density signal and is useful in determining the total error contribution in a signal and the specific frequency at which an error occurs. These four analyses were performed on the double deadpath drift data and the 30 mm gauge block drift data. The results from the Allan deviation and single sided amplitude spectrum are shown in Figure 6.14. The power spectral density and cumulative power spectrum are shown in Appendix G

Figure 6.14a shows the Allan deviations of the deadpath and gauge block drift measurements. The deadpath measurement had a higher noise level (7 nm pk-pk) compared to the gauge block noise (5 nm pk-pk) and the Allan deviation data reflects this over short integration times. The two Allan deviations have their lowest point at just after 10^3 seconds, which corresponds to high stability over 20 min. Afterwards, an upswing occurs in both Allan deviations, signifying drift. The Fourier analysis, shown in Figure 6.14b, shows most of the spectrum at frequencies higher than 10^{-4} Hz are below 100 pm. Also, there are no distinct peaks in the Fourier domain, only a ver broad section between 10^{-3} Hz and 10^{-1} Hz.

6.3.5 Vibration Cancellation

The 50 nm noise superimposed over long term fluctuations was mostly canceled between the two interferometers because the noise was mostly common between both interferometers.

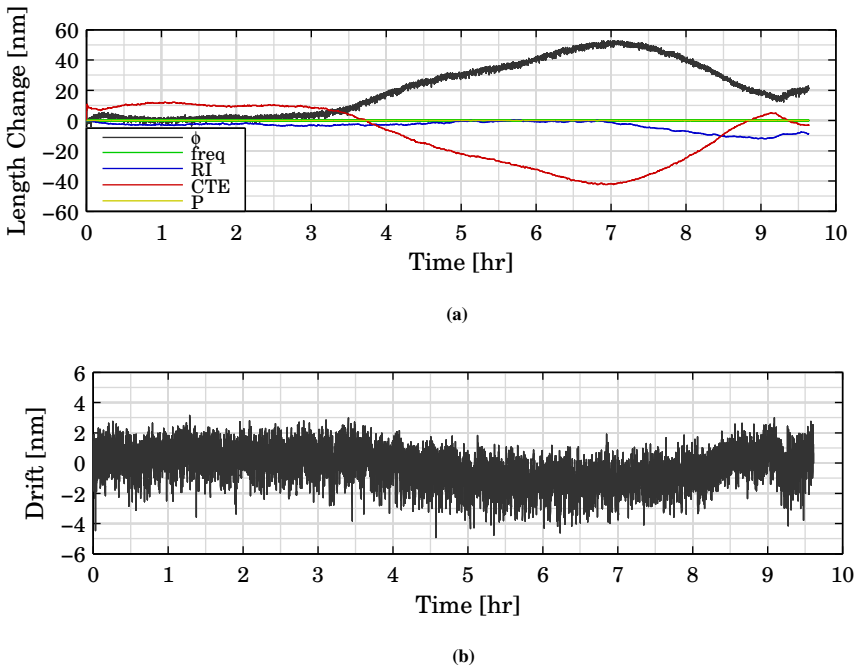

Figure 6.13: *(a) Measured sample length change (ϕ) and the four correction components: frequency fluctuations (freq), refractive index changes (RI), thermal expansion effects (CTE), and pressure changes (P). The thermal expansion effects and refractive index changes showed the strongest correlations to the sample length changes. (b) Measured drift of the 30 mm gauge block after correcting for frequency fluctuations, refractive index changes, thermal expansion effects, and pressure changes. The slight drift between 5 and 7 hours is likely caused from a difference in the sample's surface and core temperatures and would be caused by only a 2.8 mk difference.*

This noise is likely attributed to the many optical mounts used and different vibration modes causing slight optical path changes in the measurements. This vibration error was not taken into account during the analysis in Chapter 2 for determining sample drift and the analysis in Chapter 4 for correcting refractive index fluctuations. In the presence of vibrations, the interferometer may behave differently.

Since this interferometer is used with and without the vacuum tube, three different phase assessments are needed: one for the sample measurement, one for the vacuum tube measurement, and one for the deadpath measurement. When vibrations are present, displacement, x_v, is induced in the reference arm of all three potential interferometers. The common vibrations in the respective measurement arms should cancel, thus, this is only for the uncommon vibrations. The measured phases when this displacement is considered are

$$\phi_s = \frac{2\pi N\,(x - x_v)\,\eta f}{c}, \tag{6.11}$$

$$\phi_r = \frac{2\pi N\Big(L\,(\eta - 1) - x_v\eta\Big) f}{c}, \quad \text{and} \tag{6.12}$$

$$\phi_{dp} = \frac{-2\pi N x_v \eta f}{c}, \tag{6.13}$$

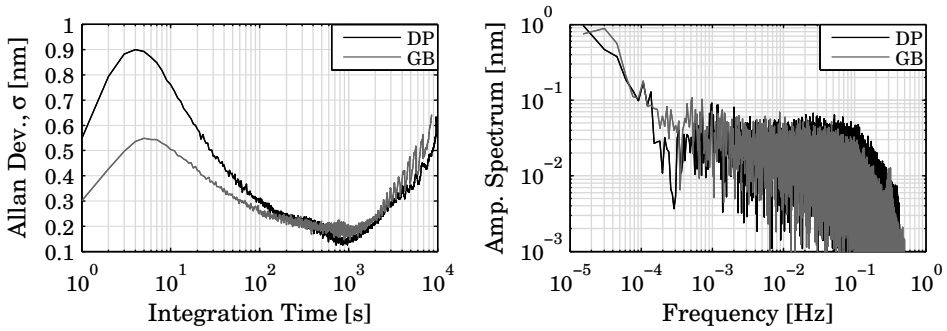

Figure 6.14: *Allan deviation (a) and single sided amplitude spectrum (b) of the double deadpath and 30 mm gauge block measurements. The Allan deviations show a slight increase up to ~7 seconds before decreasing to the lowest point at just after 10^3 seconds. After an integration time of 10^3 seconds, the typical upswing signifying drift occurs. The amplitude spectrum showed significant noise in the 10^{-3} Hz and 10^{-1} Hz frequency band which is presumably due to refractive index fluctuations. (The power spectral densities and cumulative amplitude spectra are shown in Figure G.2.)*

where ϕ_s, ϕ_r, and ϕ_{dp} are the measured phase values for the sample, refractometer, and deadpath, respectively, x is the sample length, η is the refractive index, f is the laser frequency, c is the speed of light, N is the interferometer constant, L is the vacuum tube length, and x_v is the vibration induced displacement. The time varying variables are ϕ_s, ϕ_r, ϕ_{dp}, x, η, f, L, and x_v. Thus, for constant sampling intervals, the measured phase change for the three interferometers is

$$\Delta\phi_s = \frac{2\pi N}{c}\Big(\eta f\Delta x - \eta f\Delta x_v + (x - x_v)\, f\Delta n + (x - x_v)\,\eta\Delta f\Big), \tag{6.14}$$

$$\Delta\phi_r = \frac{2\pi N}{c}\Big[\,(\eta - 1)\, f\Delta L - \eta f\Delta x_v + (L - x_v)\, f\eta_n + \big(L\,(\eta - 1) - x_v\eta\big)\Big], \text{ and} \tag{6.15}$$

$$\Delta\phi_{dp} = \frac{-2\pi N}{c}\Big(\eta f\Delta x_v + x_v\eta\Delta f + x_v f\Delta n\Big), \tag{6.16}$$

where the Δs represent changes from the starting value. The desired measurement value is the sample length change, Δx, which is

$$\Delta x = \frac{\Delta\phi_s c}{2\pi N\eta f} + \Delta x_v - (x - x_v)\,\frac{\Delta\eta}{\eta} - (x - x_v)\,\frac{\Delta f}{f}, \tag{6.17}$$

after rearranging Equation 6.14. Equation 6.17 has three variables, x_v, Δx_v and $\Delta\eta$ which must be known to determine the sample length change. The other variables are either known at the start of a measurement (x, f, N, η, c), measured ($\Delta\phi_s$), or are sufficiently reduced by other means (Δf). When the deadpath interferometer is used as the reference interferometer, the refractive index change must be determined using another method. However, the deadpath interferometer can be used to correct for vibration induced length changes, as shown here. Rearranging Equation 6.16 yields

$$\Delta x_v = \frac{-\Delta\phi_{dp} c}{2\pi N\eta f} - x_v\frac{\Delta f}{f} - x_v\frac{\Delta\eta}{\eta}. \tag{6.18}$$

Substituting Equation 6.18 into Equation 6.17 results in

$$\Delta x = \frac{\Delta\phi_s c}{2\pi N\eta f} - (x - x_v)\frac{\Delta\eta}{\eta} - (x - x_v)\frac{\Delta f}{f} - \frac{\Delta\phi_{dp} c}{2\pi N\eta f} - x_v\frac{\Delta f}{f} - x_v\frac{\Delta\eta}{\eta} \tag{6.19}$$

which simplifies to

$$\Delta x = \frac{\left(\Delta\phi_s - \Delta\phi_{dp}\right)c}{2\pi N\eta f} - x\frac{\Delta f}{f} - x\frac{\Delta\eta}{\eta}, \tag{6.20}$$

canceling the vibration induced length changes. Therefore, the deadpath interferometer can be used to correct for vibrations in the interferometer. But, a frequency stabilized laser and another method for refractive index characterization is still needed to maintain a low measurement uncertainty of Δx.

When the vacuum tube is used, the internal refractometer is needed to cancel refractive index changes. The refractive index change, including vibration induced length changes, is

$$\Delta\eta = \frac{\Delta\phi_r c}{2\pi N f\,(L - x_v)} - \frac{(\eta - 1)\,\Delta L}{(L - v)} - \frac{\eta\Delta x_v}{(L - x_v)} - \frac{\left(L\,(\eta - 1) - x_v\eta\right)\Delta f}{f\,(L - x_v)} \tag{6.21}$$

which is determined by rearranging Equation 6.15. Equation 6.21 can be substituted into Equation 6.17 to cancel refractive index changes. Assuming the sample length is the same length as the vacuum tube ($x = L$), the sample length change after rearranging is

$$\Delta x = \frac{(\Delta\phi_s - \Delta\phi_r)\,c}{2\pi N\eta f} - x\frac{\Delta f}{f} + \frac{(\eta - 1)}{\eta}\Delta L + \frac{(\eta - 1)}{\eta}\frac{L\Delta f}{f}. \tag{6.22}$$

Equation 6.22 contains four separate terms which determine the resolution of the sample length change. The first term is driven by the phase resolution of the two interferometers. The second term is driven by the laser frequency stability and sample size, which is expected. The laser frequency stability, Δf, is assumed to be small enough to have a minimal affect on Δx. The third term is driven by the vacuum tube length stability. Assuming the vacuum tube length does not change more than 10 nm due to temperature or drift (after correcting for thermal expansion), then the contribution to the measured sample length change is minimal because $(\eta - 1)/\eta$ is $2.6{\times}10^{-4}$. Because the last term contains $\Delta f/f$, it has a minimal affect on the length change. Thus, the sample length change is largely driven by the phase resolution of both interferometers and is nominally

$$\Delta x \cong \frac{(\Delta\phi_s - \Delta\phi_r)\,c}{2\pi N\eta f}. \tag{6.23}$$

This is not valid when the sample and vacuum tube are different lengths ($x \neq L$) because an added multiplier is needed when substituting the refractive index from Equation 6.21 into Equation 6.17. If κ is L/x, then the sample length change becomes

$$\begin{aligned}\Delta x \;=\; & \frac{\Delta\phi_s c}{2\pi N\eta f} + \Delta x_v - (x - x_v)\frac{\Delta f}{f} - \\ & \frac{(x - x_v)}{\eta}\kappa\left[\frac{\Delta\phi_r c}{2\pi N f\,(L - x_v)} - \frac{(\eta - 1)\,\Delta L}{(L - v)} - \frac{\eta\Delta x_v}{(L - x_v)} - \frac{\left(L\,(\eta - 1) - x_v\eta\right)\Delta f}{f\,(L - x_v)}\right].\end{aligned} \tag{6.24}$$

When the vibration amplitudes are small (<100 nm), then $\frac{\kappa(x-x_v)}{(L-x_v)} \cong 1$. Then, Equation 6.24 simplifies to

$$\Delta x \cong \frac{(\Delta\phi_s - \kappa\Delta\phi_r)\,c}{2\pi N\eta f} - x\frac{\Delta f}{f} + \frac{(\eta-1)}{\eta}\Delta L + \frac{(\eta-1)}{\eta}\frac{L\Delta f}{f}. \tag{6.25}$$

Similar to the previous case where the vacuum tube length changes are minimized and the laser frequency is stable, the sample length change is determined by

$$\Delta x \cong \frac{(\Delta\phi_s - \kappa\Delta\phi_r)\,c}{2\pi N\eta f}. \tag{6.26}$$

When the sample length change must be corrected for thermal expansion and pressure induces fluctuations, Equations 6.22 and 6.25 should be used for the correction in the appropriate case.

6.3.6 1st Measurement System Summary & Conclusions

A double deadpath measurement of the 1st Measurement System showed minimal drift, less than 0.4 nm (2σ) over any 20 min measurement period. Over the full 13 hour measurement, the pk-pk noise level was better than 14 nm. The noise level and drift of each individual interferometer was relatively high, 50 nm and 500 nm, respectively. However, double deadpath measurements showed this was largely common to both interferometers when the difference was taken. The individual interferometer's large length change is likely due to thermal effects in the optics due to a strong correlation and a sensitivity of approximately 1700 nm·K^{-1}. The source of the 50 nm noise level is assumed to be the optical mounts, which were commercial kinematic mounts with varying natural frequencies.

A 30 mm steel gauge block was measured to establish a baseline measurement. The deadpath signal was used as the reference, which changed a maximum of 200 nm, in an environment changing ~0.2 K and 125 Pa. The sample measurement signal fluctuated only 100 nm and was strongly correlated with temperature fluctuations. The difference between the two measurements was taken and converted to a total sample length change of about 50 nm. This also had a strong correlation with thermal fluctuations and a weak correlation with refractive index changes. The measured length change was corrected for thermal expansion effects and refractive index changes using the Edlén equation. The measured drift was less than 0.5 nm (2σ) over 20 min and combined with the 0.4 nm drift from the interferometer, the sample induces less than 0.1 nm (2σ) instability. In the long term, both Allan deviations showed the characteristic upswing signifying drift, which should be reduced and pushed to higher integration times for future systems.

A Fourier analysis was performed on both drift signals which showed no distinct peaks and less than 100 pm amplitudes on all frequencies below 10^{-4} Hz. The difference between the two systems, with the double deadpath measurement having slightly more error, is probably due to slight alignment changes when implementing the sample and a lower temperature and pressure change during the course of the measurement.

The 1st Measurement System used the high powered stabilized laser from Chapter 5 and anti-reflection coated optics, including two penta-prisms instead of mirrors which improved optical power and alignment stability. More optical power was available for detection as a result. Thus, the fringe contrast could be used as feedback for the alignment to enhance the interference.

6.4 2nd Measurement System

The purpose of the 2nd Measurement System was to improve the 1st Measurement System in three areas: stabilizing the optical alignment and mounts, shielding and stabilizing the environment, and limiting source mixing. These target improvements were chosen because the 1st Measurement System showed a high common-mode noise rejection but the base noise level for each individual signal was almost 50 nm. If the noise level could be reduced to the 1 nm to 5 nm range and the same common-mode noise rejection ratio was still valid, the measurement results could be improved by a factor of ten or more. Also, placing the interferometer in a pressure sealed environment would also limit refractive index changes and improve temperature stability, provided limited heat sources were in the sealed chamber. Lastly, the source from the 1st Measurement System still had the potential for frequency mixing with the main f_0 beam and a δf_0 component in the f_1 beam. Correcting this potential for a mixed state will limit the chances for periodic error in the measurement.

6.4.1 Custom Optics & Mounts

Custom fused silica optics were manufactured by TNO Science & Industry, shown in Figure 6.15. Fused silica was chosen as the material because of its low thermal expansion coefficient, low birefringence, and low refractive index change as a function of temperature (compared to BK7, another typical optical material). The optics consisted of a beamsplitter for generating two spatially separated beams with minimal optical path difference[3] between the two output beams after the splitting surface. Next there are two optics consisting of two polarizing beamsplitters with built-in right angle prisms and attached quarter wave plates. The final optic also had a lateral displacement beamsplitter attached at the output to combine and interfere the beams in the interferometer.

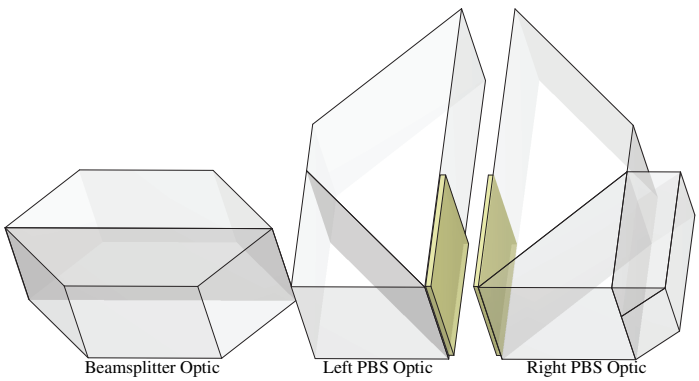

Figure 6.15: *Model of the three component custom optics manufactured by TNO Science & Industry. The initial beamsplitting optic has custom anti-reflection coatings on the input and output surfaces and a custom 50% beamsplitting coating in the middle. The left PBS optic consists of a polarizing beamsplitter, quarter wave plate and right angle prism. The right PBS optic consist of a polarizing beamsplitter, quarter wave plate, right angle prism, and lateral displacement beamsplitter.*

[3] The maximum optical path difference is driven by the dimensional tolerance of 0.1 mm in the manufacturing process.

The beamsplitting optic has anti-reflection coatings specifically designed for a 632.8 nm wavelength laser beam entering and exiting the optic at 45°. Because the beam enters at 45°, the refracted beam hits the beamsplitting surface at 74°. The power splitting ratio was specified to be better than 55%/45%. This was verified using a power stabilized laser and a power meter, with the beamsplitter having an output ratio of 52%/48% with less than 2% lost from the input.

The left polarizing beamsplitter optic was designed to transmit nearly all of one polarization state and reflect the other polarization state (where it would exit the interferometer and not be used). Figure 6.16 shows a comparison between the left polarizing beamsplitter splitting efficiency and the efficiency of a high tolerance, commercial polarizing beamsplitter [142]. This efficiency was measured using a Glan-Thompson polarizer placed in the beam path prior to the polarizing beamsplitter. The transmitted and reflected intensities were measured using DC-level photodetectors. As the Glan-Thompson polarizer was rotated, the transmitted and reflected beams both increase until the polarization is nominally aligned with the polarizing beamsplitter transmission axis. Here, the transmitted polarization is at its peak, whereas the reflected beam is reduced in power. After normalizing to the maximum power, the commerical polarizing beamsplitter still have 10% leakage, whereas the custom TNO optics had 1.2% leakage.

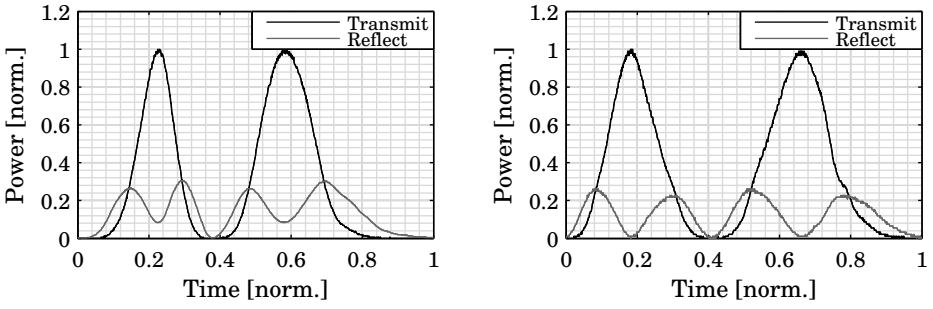

Figure 6.16: *Comparison between a high quality commercial PBS (a) and the custom TNO PBS (b). As the Glan-Thompson polarizer (placed before the polarizing beamsplitter) is rotated through 360°, two transmission peaks appear where the Glan-Thompson polarizer is aligned to the polarizing beamsplitter axis. The reflected beam should be minimal at this point. The commercial and TNO polarizing beamsplitters had leakages of 10% and 1.2%, respectively.*

The polarizing beamsplitter coating for the left PBS optic has a high splitting ratio which should also limit leakage paths in the interferometer. The right angle prism was built into the polarizing beamsplitter to improve stability (only two glass pieces are used) and to use manufacturing tolerances to provide alignment tolerances. This simplified the number of mechanical mounts for optics in the overall system. The quarter wave plate was purchased from a commercial supplier [143], which was subsequently cut, mounted, and aligned to the polarizing beamsplitter optic.

The right PBS optic was designed as a mirror opposite of the left PBS optic. The

optic also contained a 30 mm lateral displacement beamsplitter attached on the output side. The 30 mm lateral displacement beamsplitter allows for a grid spacing of 30 mm between beams, both directions, prior to interference. All optical surfaces were polished with a $\lambda/10$ specification over any 5 mm area, although the permitted flatness of the whole surface was larger. Anti-reflection coatings, less than 0.25%, were added to all optical surfaces with air-glass transitions.

The custom optics were designed to use manufacturing tolerances to establish a nominal system alignment. Custom mounts would then be used for the final alignment, as shown in Figure 6.17. In addition to three mounts for the optics, a fourth large mount was manufactured for the input fiber coupling. The detection fiber coupling was attached to the right PBS optic mount to also limit the number of mounts and alignment axes. Also, mounts and alignment mechanisms were designed for the vacuum tube and sample.

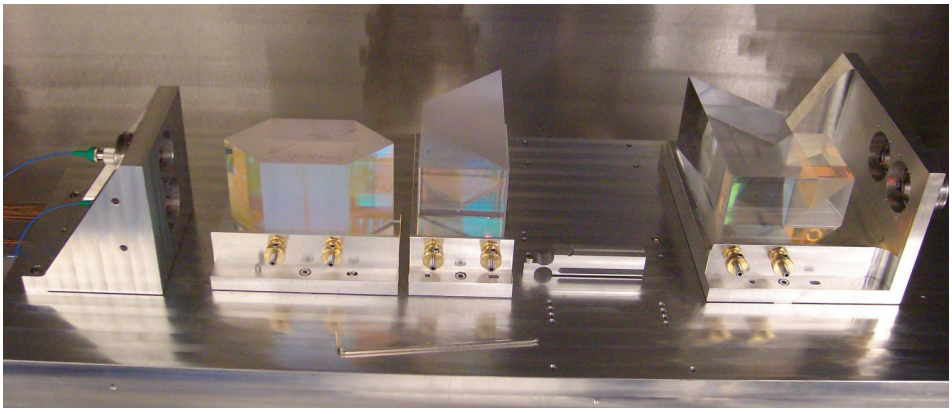

Figure 6.17: *Photo of the custom optics and mounts manufacturing by TNO, housed in the vacuum vessel. The light enters from fibers couplers mounted on the left aluminum block. The right block holding the right PBS optic also includes mounts for the detection fiber couplers.*

Each mount was designed to hold the optics in a kinematic arrangement with minimal applied force. To accomplish this, a Y-shaped, V-groove channel was machined into each mounting surface and three 2 mm spheres were placed in each V-groove, providing three well defined contact points for the optic. Because each of the three optics were large, the weight of the optic was estimated to be sufficient as a mounting force. Thus, no external force or mechanism was applied to the optic, which may cause stress. The three spheres on the bottom flat of the optic provided one linear and two rotational constraints. Models and photographs of the mounts are shown in Figure 6.18.

Two more degrees of freedom (DOFs), one linear and the last rotation, were constrained using two fine-pitch screws with balled ends attached to the mount. The two balled ends provided two well defined contact points while the fine-pitch screws would be used for lateral adjustments. The last linear DOF was not constrained because this DOF was in-line with the main optical axis and the measurement system was insensitive in this direction.

Figure 6.19 shows the fiber coupling input mount (which holds two commercial 5-DOF collimators), the sample mount, and the vacuum tube mount. The sides of the mounting

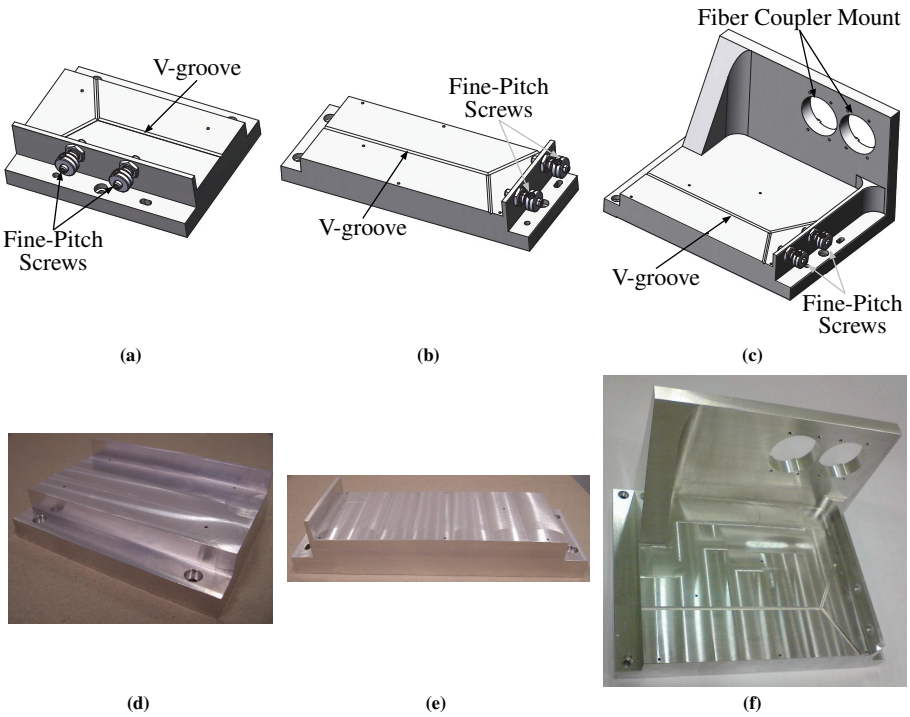

Figure 6.18: *Models and photos of the three optic mounts. (a),(d) Initial beamsplitter mount. (b),(e) Left PBS optic mount. (c),(f) Right PBS optic mount. The right PBS optic mount also includes mounts for the detection fiber couplers. The mounts where manufacturing from stress relieved aluminum to limit gradients. The mounts used V-gooves with 3 spheres per mount (not shown) to constrain the optics in 3-DOFs. Two other DOFs are constrained using the ball-ended fine pitch screws.*

block and mounting wall were designed to be thick to achieve a high natural frequency.

The sample mount was a hinge flexure with a cantilever arm as shown in Figures 6.19b and 6.19e. A leaf spring was also machined into the mount and a ball-ended, fine-pitch screw was used to align the rotation about the Y-axis. The alignment about the X-axis was done using an external push bar and fine pitch screws which can be retracted once the sample is aligned. Lastly, the mount also contained a V-groove with for placing three 2 mm spheres to kinematically mount the sample.

The vacuum tube mount was similar to the sample mount. Instead of using a single axis hinge, a two axis hinge was machined into the vacuum tube mount to provide rotational alignment about the X- and Y-axes. The alignment was also done with two fine pitched screws. One screw pushes on the side of the mount while the other screw pushes from below. The vacuum tube will also rest on four spheres, to constrain four DOFs of the cylinder.

The manufacturing tolerances for the mounts and the placement of the mounts were also used to establish a nominal alignment for the system. As shown in Figure 6.20, each mount for the fiber coupling and optics had a slip-fit 3 mm dowel hole and a 3.1 mm wide slot which were used to align the mounts to a common baseplate. The mating dowel pins were press-

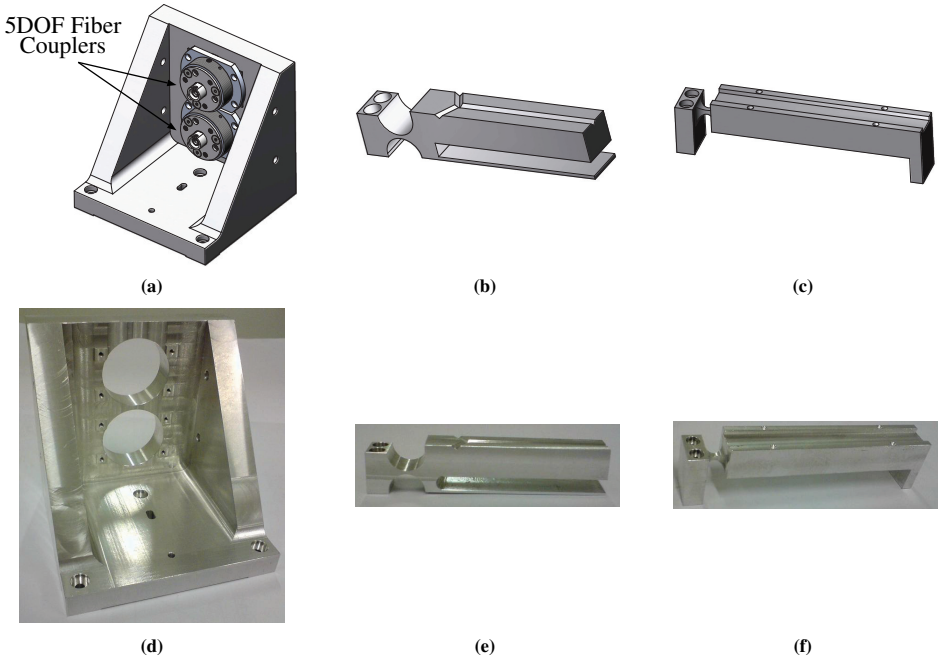

Figure 6.19: *Model and photo of the input fiber coupling mount (a)(d), sample mount (b)(e), and vacuum tube mount (c)(f). The input fiber coupling mount was designed to be stiff to limit mechanical vibrations. The sample mount and vacuum tube mount both used flexures and fine pitch screws (not shown) to align their respective components.*

fit into the base along the same line to build a nominal datum in the system. Each mount was screwed into the baseplate with three screws with a raised patch around the mounting through hole to have a more well defined contact point, rather than two mating flat surfaces. This raised patch technique was also used on the fiber coupling mounts. During alignment, these well defined patches can be shimmed to adjust the mount about the Y- and Z-axes and shift the optic in the X-direction. Figure 6.20 shows these features on the mounts.

6.4.2 Vacuum Vessel & Shielding

A shielded environment was created for the 1st Measurement System by covering the interferometer with 4 cm thick insulation foam. This created an approximately 50:1 reduction between the temperature outside of the box and the temperature within the box over the duration of the measurements. However, the two interferometer signals still showed fluctuations at 12 minute to 15 minute intervals which was consistent with the temperature controller in the laboratory. In addition, although the interferometer was shielded, the box still had several heat sources inside, including a pressure sensor and photodetectors. In the 2nd Measurement Setup, the goal was to reduce the temperature fluctuations by a factor of ten and remove heat sources from the surrounding environment. This was done by adding more shielding and moving the setup to a better measurement environment.

The interferometer and source were moved from the laboratory at TU Delft to an ISO Class 6 cleanroom facility jointly operated by TU Delft and TNO Science & Industry. In this new facility, the temperature fluctuations in the laboratory environment were less than

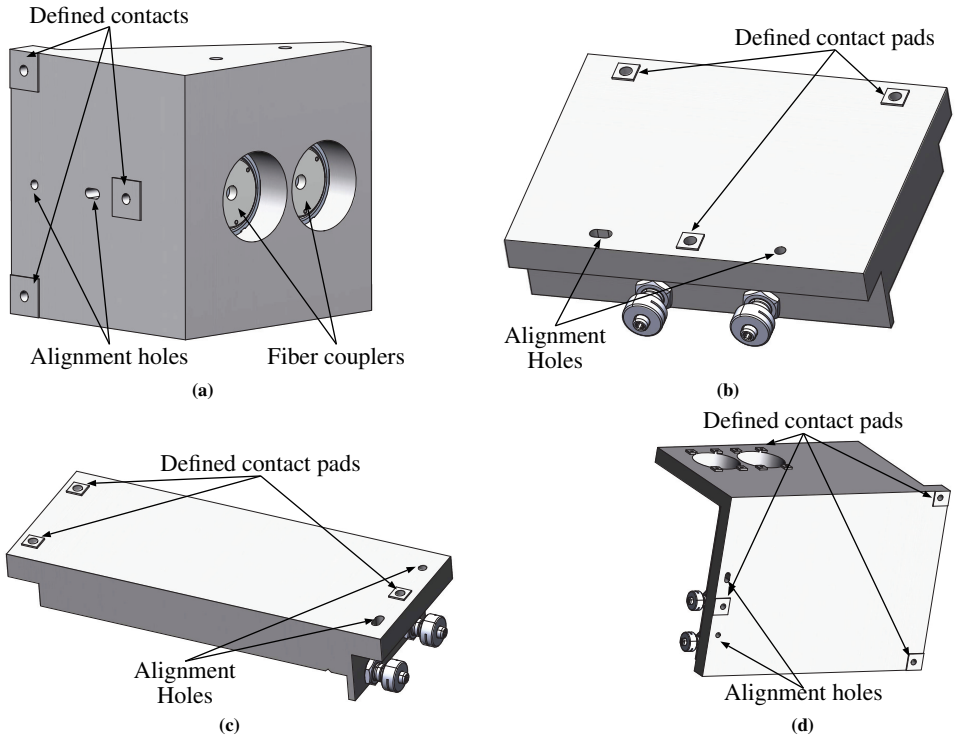

Figure 6.20: *Bottom view of the (a) input fiber coupling mount, (b) initial beamsplitter mount, (c) left PBS optic mount, and (d) right PBS optic mount. Each mount has a raised patch around the mounting holes to establish a well defined contact point with the baseplate. Each mount also has a 3 mm slip fit dowel hole and a 3.1 mm wide slot to provide initial alignment with respect to the common baseplate.*

1 K and the interferometer was placed in a large vacuum vessel previously used for space instrumentation experiments.

The vacuum vessel also allows for several changes to the system from the first generation. The source and interferometer were decoupled using fibers fed into the vessel. This removed one heat source near the original system. Also, the pressure sensor was mounted on the vessel, which eliminated another heat source due to its electronics. The interferometer was fiber fed and the interference beams were launched into fibers, which eliminated photodetector heat sources. The remaining potential heat source in the vacuum vessel were the temperature probes which supply minimal heat load and absorption of the laser in the optics which should also be minimal.

The area of non-overlapping air path is of the most concern for temperature fluctuations because this will cause spatially and temporally shifting refractive index changes. The largest non-overlapping air path in the interferometer is in the area where the sample and vacuum tube are mounted. This was shielded with an aluminum plate to help maintain a uniform temperature profile in the surrounding area. Figure 6.21a shows the aluminum shield around the air path difference. Also, the shield was designed to limit the gaps for air currents to flow into the air path. A second aluminum isolation cover was placed around the whole system to also make a uniform temperature profile across the interferometer and limit

gradient effects, as shown in Figure 6.21b. Then, the interferometer with cover was placed in the vacuum vessel which contained a passive vibration isolation table for frequencies greater than 400 Hz. The whole vacuum vessel was then placed on a separate passive vibration, air damped system which reduced resonances at frequencies greater than 1 Hz. The vacuum vessel and lab bench with equipment is shown in Figure 6.21c.

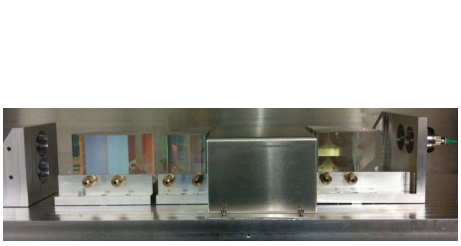

(a)

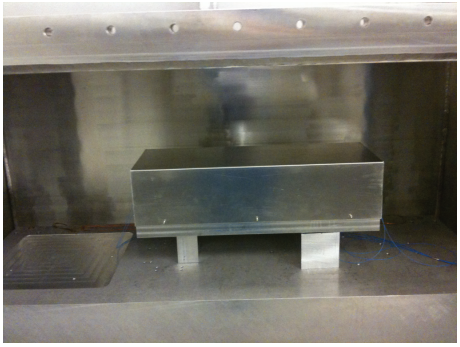

(b)

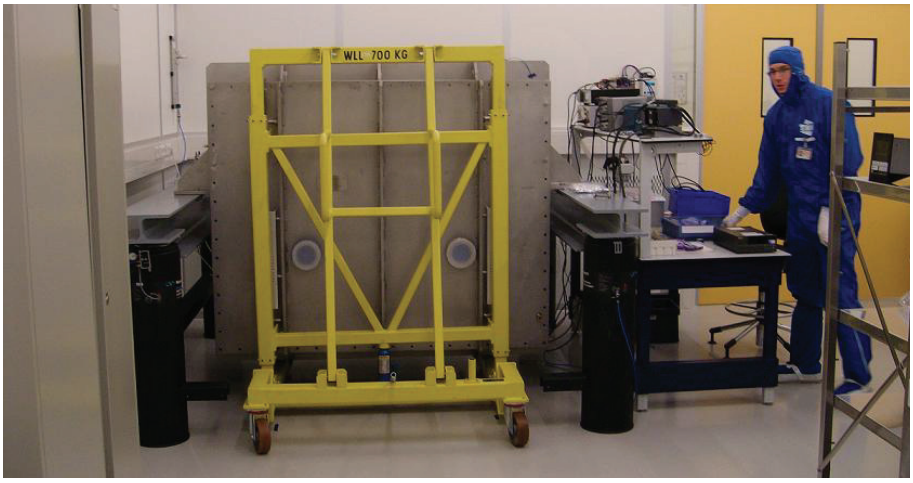

(c)

Figure 6.21: *(a) Local aluminum shield directly blocking air currents around the non-overlapping air paths. (b) Large aluminum shield around the complete optical system for further isolation. All mounts and shield were made of aluminum to maintain minimal thermal gradients and provide a uniform air temperature surrounding the optical system. The aluminum shield is approximately 600 mm wide. (c) Photo of the vacuum vessel, jack for removing the door, and peripheral equipment setup in the lab.*

6.4.3 Laser System & Fiber Alignment

For the 2nd Measurement Setup, the laser system from the 1st Measurement Setup was improved by tuning the three-mode laser stabilization controller and removing thermal mass, as described in Chapter 5. Also, the laser stabilization benefited from a better

controlled environment with enough air flow to transfer heat away from the laser system.

After stabilizing the laser, the beam was split equally and passed through two acousto-optic modulators, driven at 19.99 MHz and 20.00 MHz, respectively. The alignment of the acousto-optic modulators was optimized by measuring the power of the 1st order beam. The acousto-optic modulators were driven by two function generators which did not provide enough power to obtain a high efficiency. Prior to the acousto-optic modulator, each beam had greater than 500 μW of available power, but after diffracting, the maximum power achieved was about 250 μW per beam.

The two 1st order diffracted beams from the two acousto-optic modulators were then launched into polarization maintaining fibers connected to a vacuum feedthrough using commercial 5-DOF fiber couplers. Half wave plates were placed before the fiber couplers to adjust the polarization angle to align them with the polarization axis of the polarization maintaining fiber. The alignment was adjusted using two methods while measuring the power output of the other end of the fiber. The coupling alignment was adjusted by the three displacement DOFs and the two rotational DOFs (tip and tilt). Better alignment provided a higher output power at the end of the fiber.

The roll axis, or polarization axis, was aligned by thermally stressing the fiber and placing a fixed polarizer before the power meter on the fiber output. The core of polarization maintaining fiber is pre-stressed with two slightly differing refractive indices. If the polarization axis of the beam is aligned to one axis, the axis defined by the polarizer axis before the power meter, then stressing the fiber should induce no optical power degradation. If the polarization axis of the beam is not aligned, then the fiber behaves like a half wave plate and the output angle is dependent on applied stress. When this occurs and the fiber is stressed, the output power drops significantly. Thus, the polarization axis is aligned by minimizing the power drop while stressing the fiber.

Aligning the coupler and the polarization axis is an iterative process because rotating the half wave plate to adjust the polarization could influence launching alignment and vice versa. After meticulous alignment, the power output of both beams was greater than 190 μW, which is an efficiency of approximately 80%.

After launching the light into the fibers, the lower output beam was collimated using the same 5-DOF commercial coupler, with the desire to obtain a near infinite wavefront radius. This was done using the setup shown in Figure 6.22. A beamsplitter was placed before the input fiber coupler. The light was then launched into the fiber and collimated at the output to a nominally flat wavefront. A mirror was mounted to the right PBS optic mount where the beam was aligned to reflect back down the fiber. The output beam power was then measured and used as feedback for the alignment. The highest power is obtained when either the wavefront radius is near infinity and the pointing is normal to the mirror or when the focal point of the coupler is coincident and normal at the mirror surface. To distinguish the difference between the two, the nominal beam diameter was checked along its length between the output coupler and the mirror to ensure a constant diameter rather than a converging spot size.

The second output beam (top beam) was aligned to the lower beam using the the main interference surface in the left PBS optic. After establishing a nominal alignment, fine tuning alignment was done by placing an aperture after the optic, which was in line with

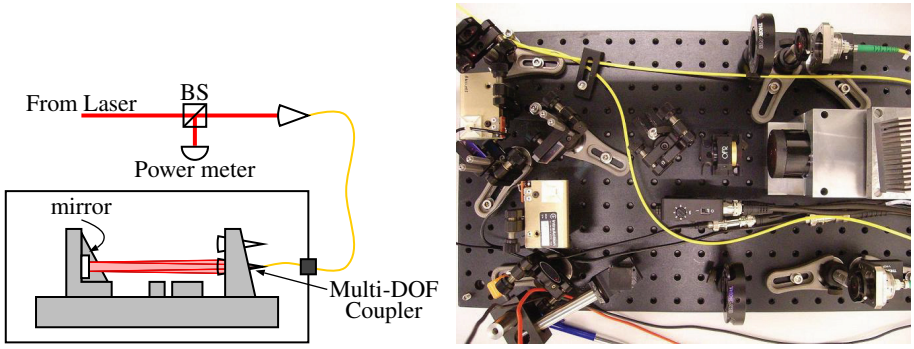

Figure 6.22: *(a) Schematic of the fiber collimation alignment proceedure. The multi-DOF coupler changes the lens location in the X-, Y-, and Z-directions as well as tip and tilt relative to the end of the fiber. (b) Photo of the laser stabilization system, heterodyning components, and fiber couplers. The initially fiber coupled beam from the source was launching into the optical setup and targeted to a mirror. The fiber collimator was adjusted to align the beam to reflect off the mirror and back down the same fiber where it was optimized by the measured power.*

the bottom beam. The top beam was then aligned to ensure it overlapped with the bottom beam after interfering. This established a position alignment. The angular alignment was performed by adjusting the tip and tilt while looking at the spot overlap at a far distance away (across the room), while still maintaining the same spatial location in the aperture. This established a position alignment in two rotational directions and two lateral directions. The third rotational direction (polarization) was established from the fiber coupler and polarization maintaining fiber. The beam focus was also checked to ensure a constant diameter throughout the beam length rather than a converging or diverging beam. As with the initial fiber input alignment, this was an iterative process because each alignment was not mutually exclusive.

6.4.4 Practical Implementation

After relocating the setup and peripheral equipment to TNO Science & Industry, the interferometer was placed in the vacuum vessel. After the laser setup was built, the fiber coupling was performed, followed by the collimation and interferometer alignment. The system was measured in a double deadpath configuration to compare with the previous double deadpath measurements of the 1st Measurement Setup. The two interference beams were coupled into polarization maintaining fiber and detected using photodetectors outside of the vessel. A schematic of the laser system and optical setup is shown in Figure 6.23.

The phase was measured using a custom two-channel lock-in amplifier programed in Simulink which ran on a dSPACE system, as shown in Figure 6.24. The reference signal was generated by mixing the two acousto-optic modulator driver signals to generate a reference signal at 10 kHz. This was then acquired by dSPACE at 75 kHz. The reference signal was then band-pass filtered and sent to a phase locked loop. The output of the phase locked loop was sent to two voltage controlled oscillators with a 90° phase offset, which generated matched sine and cosine signals, R_c and R_s, respectively. Four multipliers were

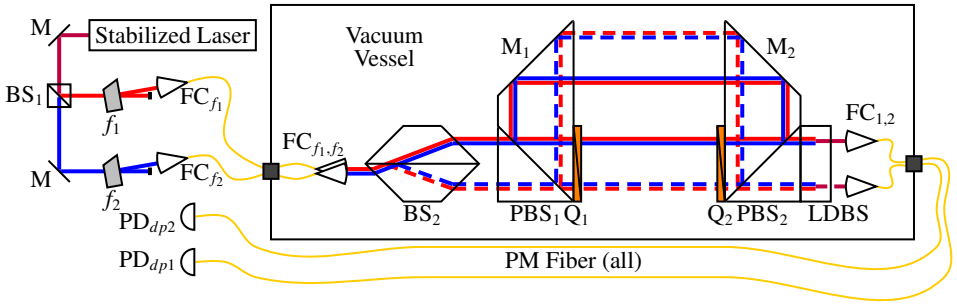

Figure 6.23: *Schematic of the interferometer and laser source for the 2nd Measurement System. The custom three-mode stabilized laser from Chapter 5 was split equally and upshifted by two acousto-optic modulators driven at slightly different frequencies. After the two beams were launched into fibers, they were collimated and aligned into the custom three component optics. The interference beams were then collected by two more fibers and the light was sent to two fiber-coupled photodetectors for further signal processing.*

used in conjunction with the two measurement signals, which were also filtered at the same bandpass filter cutoff frequencies, and the four outputs were sent to four low pass filters at 20 Hz. The phase was then calculated using two arctangent functions, maintaining sign consistency with the quadrant location, and then the phase was unwrapped, converted to nanometers, and displayed on screen.

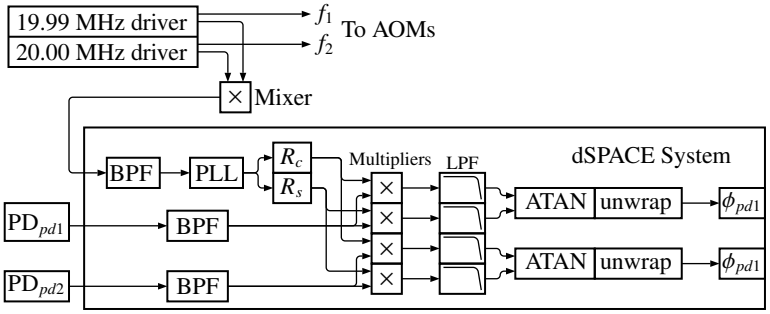

Figure 6.24: *Block diagram of the electronics and data processing for the 2nd Measurement System. The acousto-optic modulators were driven by two function generators. A synchronized output from each function generator was mixed and sent to a custom lock-in amplifier built in dSPACE. The two interference signals from PD$_{dp1}$ and PD$_{dp2}$ were multiplied with in-phase and quadrature components of the function generator reference signals, generating two phase values.*

The phase was acquired using a separate computer and a multi-channel National Instruments data acquisition card [144]. Since the resolution of the card was only 12-bit with a finite range, this normally provides a range against resolution problem for the measurement. This was alleviated by taking the unwrapped phase (-π to π) and dividing it by π, which created an output signal of -10 V to 10 V in dSPACE. This was then sent to the analog output channel where it was acquired by the NI 6025E card using the Matlab Data Acquisition Toolbox. The wrapped phase (scaled -10 to 10) was converted to phase by dividing by ten, multiplying by π, and the wrapped phase was unwrapped. The phase was then converted to nanometers and used to determine the length change of the interferometer.

6.4.5 Measurements

The double deadpath interferometer was measured to establish a baseline noise level and drift in the interferometer. Figure 6.25 shows the measured length change of the two interferometers for two separate measurements. The first measurement (M1) showed about 20 μm of length change over 21.5 hours. The first three hours show typical thermal soakout drift behavior. The second measurement (M2) showed less overall length change from the interferometers, only 10 μm over 15 hours.

Since both measurements and both interferometers were in double deadpath configurations, the difference between the two deadpath measurement signals (S1 and S2) was taken to determine the drift during the measurement. The measurements showed 30 nm pk-pk drift in M1 and 35 nm pk-pk drift in M2, as shown in Figure 6.25b.

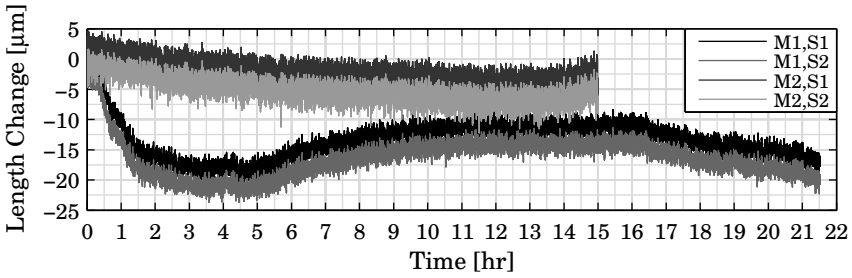

(a)

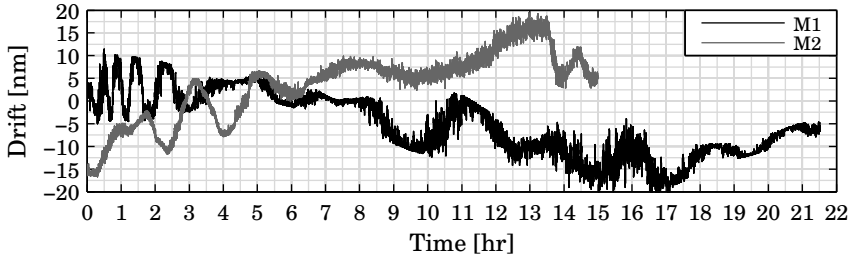

(b)

Figure 6.25: *(a) Two measurements (M1 and M2) of the measured double deadpath length change of both interferometers (S1 and S2). The length change and noise level of each individual interferometer was much higher than anticipated. (b) Drift between the two deadpath interferometers for both measurements. The drift showed a significant reduction from the individual interferometer measurements but was still much higher than previous measurements.*

Several distinct observations were made from the individual interferometer measurements and the measured drift. The overall length change from the individual interferometers was very high compared to previous measurements (about 20 times higher). Also, the short term noise level, 3 μm, was also much higher. The overall length change, however, showed the characteristic profile of a slow thermal system. Also, even though the length change was high and the noise was very high (about 60 times higher), the difference between the

interferometers produced a high common mode rejection.

The high noise and high overall length change was caused by the input fibers. In this system, the reference signal was taken from the function generators driving the acousto-optic modulators. However, after launching into the fiber, the frequency output on the other end of the fiber in the system changes with applied stress or temperature which produces a Doppler shift inside the fiber. Thus, the frequency output of each fiber is continuously changing from outside temperature changes and applied stresses such as vibration. This was not anticipated in the initial design of the system, thus there was limited space to correct this effect by placing an optical reference in the vacuum vessel.

Ideally, four signals should have been measured in this system: the two main interference signals, the electrical reference, and an optical reference in the vacuum vessel. By splitting a portion and interfering the two input beams, the length change induced from the fiber would be decoupled from the measurement provided the phase locked loop maintained consistent locking in the dSPACE system. Also, the phase difference between the electrical reference and optical reference could be used to estimate the applied stress on the fiber by measuring the phase changes. However, due to space limitations, this could not be performed with this current setup.

The measured drift values were also higher than expected because the original measurements had a noise level of approximately 7 nm pk-pk and about 1 nm drift over 10 hours. These measurements showed considerably higher drift in an environment that was more shielded with better, more stable alignment and higher quality optics. One likely cause of this is the limited common mode noise rejection obtainable from the system, even though both interferometers see the same source beams. The drift is decoupled 100 times from the measured length change of the individual interferometers. This decoupling ratio was similar in previous experiments.

The drift data was analyzed using the same two techniques described in the 1st Measurement System: the Allan deviation and the single sided Fourier amplitude spectrum amplitude, as shown in Figure 6.26. The Allan deviations showed a 4 nm single standard deviation value over the full integration time with no characteristic dip and upswing. Instead, the Allan deviation appears to continuously trend upward, which confirms the time domain results showing drift.

The Fourier analysis showed $1/f$ noise behavior at frequencies lower than 0.1 Hz. This appears to be driven by interferometer drift and refractive index fluctuations and is slightly higher than in the 1st Measurement System results.

6.4.6 Periodic Nonlinearity

During measurements with the 2nd Measurement System, periodic nonlinearity was observed in the measured signals. Figure 6.27 shows two screen shots of the dSPACE readout screen. The top plot (green) shows the difference between the two deadpath interferometers (drift) and the bottom plot shows the wrapped fringes of the length change of the two interferometers (red and blue). When the length change for the two interferometers is fairly rapid, the wrapped fringes display a sawtooth-type form. During those rapid length change periods, the stability signal shows a sinusoidal-like behavior with a pk-pk value of 0.4 nm with a period matching the same period of the sawtooth wrapped fringes. This is a clear

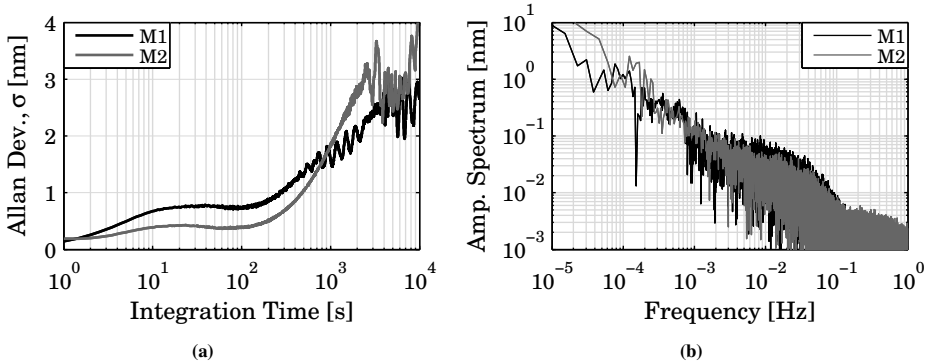

Figure 6.26: *Allan deviation (a) and single sided amplitude spectrum (b) of the measured drift from Figure 6.25b. The Allan deviation was about 20 times worse than the previous measurements and shows continuous drift. The single sided amplitude spectrum showed distinct 1/f noise characteristics. (The power spectral densities and cumulative amplitude spectra are shown in Figure G.3.)*

indication of periodic nonlinearity in the measurement.

This was mimicked by holding the input fibers which caused an artificial length change in S1 and S2 spanning several fringes, while the drift exhibited a sinusoidal behavior. This was caused by frequency mixing between the two axes in the polarization maintaining fiber. Moreover, the value of the periodic nonlinearity changed depending on the amount of stress applied. This was a clear indication that the periodic nonlinearity amplitude was time dependent and stress dependent but was not repeatable for similar applied stresses. For instance, after holding a heat source near the fiber, one periodic nonlinearity was observed. However, after removing the heat source, waiting for thermal equilibrium, and then reapplying the same heat source near the fiber, the periodic nonlinearity amplitude and length change rate was not consistent. Thus, the periodic nonlinearity observed had a temporal amplitude fluctuation, which is difficult to remove from the measurement using signal processing techniques.

Knarren [145] showed modeling the polarization maintaining fiber as a linear birefringent retarder is an effective way to describe the polarization degradation in the fiber. Also, typical polarization maintaining fiber has an extinction ratio around 100:1, which essentially causes 10% frequency mixing in the fibers. The panda fibers used in this research were specified with an extinction ratio of better than 100:1, which should result in a periodic error amplitude between 4 nm and 10 nm. In this setup, one of the first components encountered by the beams is a high extinction ratio polarizing beamsplitter (greater than 1000:1). This polarizing beamsplitter blocks much of the unwanted mode but some mixing still remains within the main mode. Additionally, there is a still a small leakage portion transmitted by the polarizing beamsplitter, which contributes to the 0.3 nm periodic nonlinearity amplitude seen in this research.

6.4.7 2nd Measurement System Summary & Conclusions

For the 2nd Measurement System, the optical system was moved to a more stable environment and placed into a vacuum vessel which could be used to shield the interferometer and

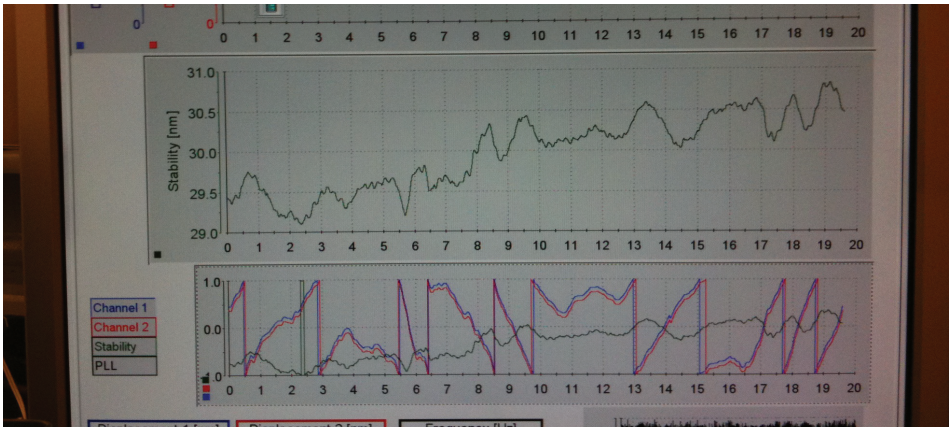

(a)

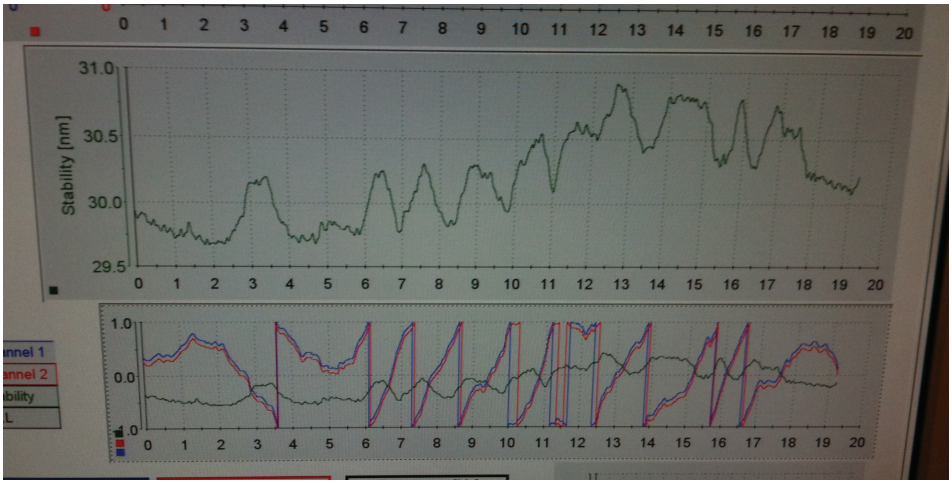

(b)

Figure 6.27: *Photos of the dSPACE display screen showning wrapped fringes (bottom plots) and the difference between S1 and S2 (top plot). When the displacement as seen by the wrapped fringes is a sawtooth waveform, the measured displacement is fairly linear. The difference had sinusoidal behavior with the same sawtooth period which is an indication of drift.*

ultimately perform experiments in vacuum (although this specific system was not measured in vacuum). Vacuum compatible, custom optics and mounts were also used to eliminate the multitude of optics and separate mounts from the 1st Measurement System. The laser system was placed outside of the vessel and split into two different beams with slightly different frequencies after up-shifting with two acousto-optic modulators. After launching into fiber, the two beams were aligned in the interferometer and two interference signals were generated and launched out of the vessel via two more fibers. The signals were then detected and the phase was measured using a custom two-channel lock-in amplifier relative to the difference between the acousto-optic modulator drive frequencies.

The individual interferometer signals S1 and S2 showed length changes greater than 10 μm in two double deadpath measurements, M1 and M2, which lasted 21.5 and 15 hours,

respectively. The measured drift (difference between S1 and S2 for a given measurement) was about 30 nm to 35 nm, which was higher than anticipated. The noise level over short timespans increased from 50 nm in the 1st Measurement System to near 3 μm in these measurements.

The increased noise and overall length change of S1 and S2 was attributed to not having an optical reference in the vacuum vessel. Thermal and mechanical stress on the input fibers created an artificial length change that was measured by the system. This length change was not due to drift but to the Doppler shifts in the fibers.

While stressing the fibers and inducing artificial length changes into the system, first order periodic nonlinearity was observed. The periodic nonlinearity amplitude was time varying and was not repeatable over several experiments. The periodic nonlinearity was from frequency mixing in the fiber and stress-induced changes to the polarization state in the fiber.

Another practical observation was made when closing the 700 kg door of the vacuum vessel. The added weight and impact forces when aligning the mounting holes of the door caused tip and tilt of the whole vacuum vessel on its air vibration isolation. The tip and tilt of the vacuum vessel in conjunction with the optics resting on the three small spheres created a difficult situation[4] when sealing the vessel while maintaining alignment. Fortunately, the five point kinematic mounts were sufficiently stable that realigning a displaced optic did not require additional fiber coupling adjustments or a complete system realignment. This did, however, force an additional iterative process where the fringe contrast was observed while placing the vacuum vessel door. If the fringe contrast dropped too low, the door was removed and the optics were realigned.

6.5 3rd Measurement System

The three key points addressed from the 2nd Measurement System in the 3rd Measurement System were the lack of an optical reference inside the vacuum vessel, the time varying periodic nonlinearity from the fibers, and not placing the optics on rolling elements. This was accomplished by reverting back to commercial optic mounts and adapting them to use the custom optics. The stabilized laser signal was directly fed into the vacuum vessel and the acousto-optic modulators were placed in the vessel. By placing the acousto-optic modulators in the vacuum vessel, the periodic nonlinearity from the fiber was eliminated. Also, since the system was completely free space, from the acousto-optic modulators to the main interfering surface, an optical reference was not needed. Lastly, the optics were placed on three separate tip-tilt mounts and clamped. While this eliminates the kinematic mount, it alleviates the issue of misalignment while mounting the door.

6.5.1 Practical Implementation

A schematic and photos of the optical system are shown in Figure 6.28. A Glan-Thompson polarizer was used after the input fiber coupler (FC_i) to block unwanted polarization states

[4]Pegs were placed in the optic mounts to ensure the optics could not roll off a mount and damage the optic. However, placing the door on the vacuum vessel while maintaining alignment was an arduous task to say the least. This was a clear lesson where additional constraints were necessary for the optic mounts.

with a high extinction ratio (10^5 is typical for a Glan-Thompson polarizer). After blocking unwanted polarization states, a half wave plate was used to reorient the polarization state such that it transmitted through PBS_1. The input beam was then split vertically using a beamsplitter and mirror to create a lateral displacement beamsplitter ($LDBS_1$). The bottom beam (red) was up-shifted in an acousto-optic modulator driven at 20 MHz (f_1). Then, two mirrors were used to align the beam into the interferometer. The top beam (blue) was up-shifted in an acousto-optic modulator driven at 19.99 MHz (f_2). It also was aligned via two mirrors into the interferometer.

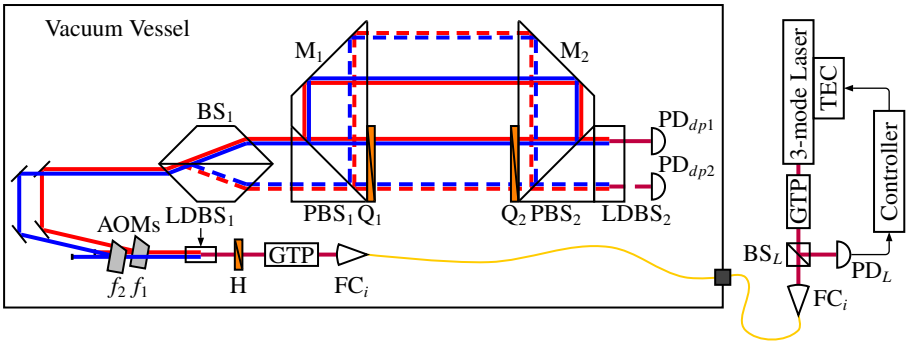

(a)

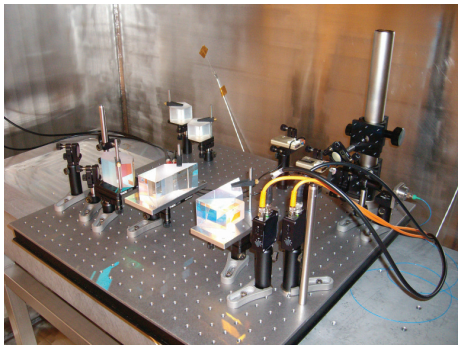

(b)

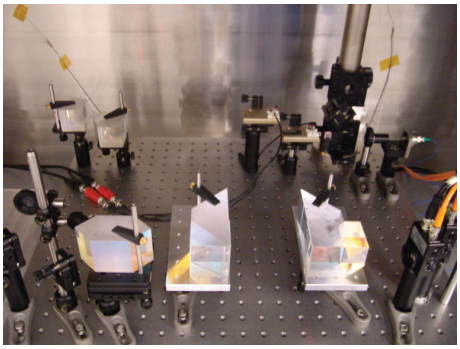

(c)

Figure 6.28: *(a) Optical schematic of the 3rd Measurement System. The stabilized laser was directly launched into a fiber and sent into the vacuum vessel. The polarization of the beam was cleaned using a Glan-Thompson polarizer prior to splitting into two beams and passing through two acousto-optic modulators. The two beams were then directed into the interferometer. The data acquisition system was the same from Figure 6.24. (b) and (c) Two photos of the system showing the acousto-optic modulators added in the vacuum vessel.*

Two photodetectors, PD_{dp1} and PD_{dp2}, were placed in the vacuum vessel to measure the two deadpath interferometer signals, S1 and S2. The data acquisition from Figure 6.24 was used to measure the phase. Also, the wrapped fringes were acquired with the NI data acquisition card using Matlab as previously described.

6.5.2 Initial Short Measurement

An initial short term measurement of the double deadpath interferometer showed the noise level and length change of the individual interferometers was much less than the 2nd Measurement System. As shown in Figure 6.29, the two interferometers, S1 and S2, changed less than 50 nm and the relative drift over 45 minutes was about 500 pm pk-pk.

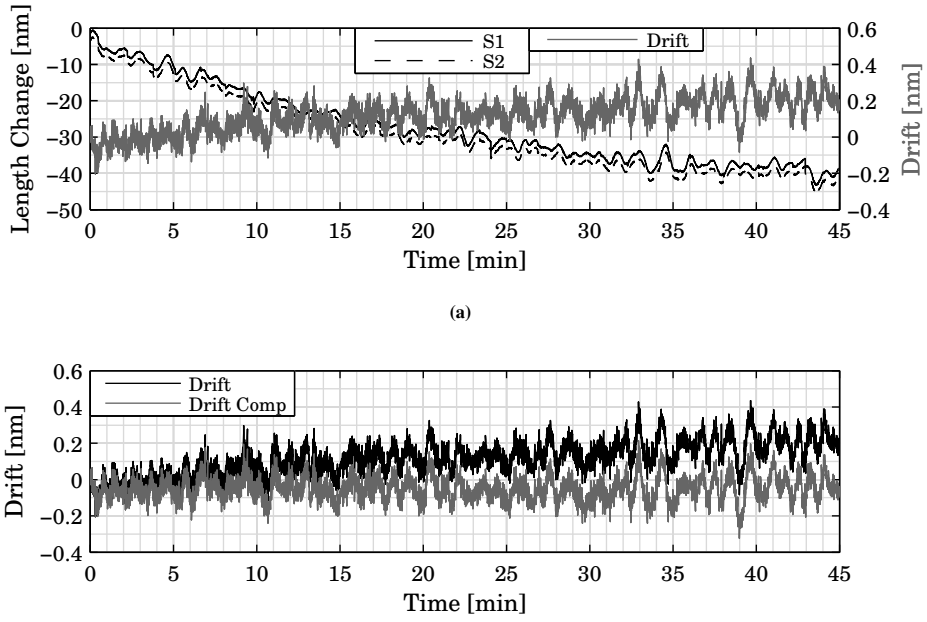

Figure 6.29: *(a) Initial measurement from the 3rd Measurement System with the custom optics and commercial mounts. The length change and noise level from the individual interferometers was significantly reduced from previous measurements. (b) Difference between the two interferometer signals (drift) and difference after removing a strong correlation to the interferometer length change using a linear least squares fit. The correlation to the interferometer length change suggests a cosine error in the measurement.*

The S1 and S2 length change appeared to be inversely proportional to drift. The correlation coefficient between each individual interferometer and the drift was -0.705 and -0.710, respectively. When S1, S2, and the drift change with a similar form, this suggests there is a cosine error between the two interferometers due to imperfect initial alignment. This would occur if BS_1 from Figure 6.28a is misaligned. The solid beams from BS_1 will transmit parallel to the input, with the manufacturing wedge angle, because the beamsplitter in the transmission axis behaves like a plane plate. The reflected beams, however, reflect at a different angle based on the initial alignment BS_1. If BS_1 is not aligned perfectly, the optical path length of the dashed beams is slightly longer than the solid beams. As the interferometer fluctuates due to temperature, the fluctuation rate is slightly different per interferometer from this cosine error.

This effect was corrected by applying a linear least squares fit between the difference (drift) and S2. S2 was chosen because it was designated as the 'reference' signal and is used consistently for all of the measurements in this and subsequent sections. To perform the least squares fit, the matrix $\mathbf{Q}$ is

$$\mathbf{Q} = [\mathbf{P}_1\ \mathbf{P}_2\ \ldots\ \mathbf{P}_i\ \mathbf{1}], \tag{6.27}$$

where $\mathbf{P}_1$ through $\mathbf{P}_i$ are column vectors (of the same length) containing the parameters to which the data correlates, and $\mathbf{1}$ is a vector (of the same length as $\mathbf{P}_1$) that contains only ones to correct for an offset. The matrix $\mathbf{A}$ is a n by 1 matrix containing the fitting coefficients and offset for the n columns in $\mathbf{Q}$. This is determined by

$$\mathbf{A} = \left(\mathbf{Q}^\top \mathbf{Q}\right)^{-1} \mathbf{Q}^\top \Delta\mathbf{S}, \tag{6.28}$$

where $\Delta\mathbf{S}$ is the difference between $\mathbf{S}_1$ and $\mathbf{S}_2$. The compensated drift is then

$$\Delta\mathbf{S}_c = \Delta\mathbf{S} - (A_1\mathbf{P}_1 + A_2\mathbf{P}_2 + \ldots + A_{n-1}\mathbf{P}_i + A_n) \tag{6.29}$$

In this instance, $\mathbf{Q} = [\mathbf{S}_2\mathbf{1}]$ and Figure 6.29b shows ΔS and ΔS_c. The short term noise levels of both the drift and the compensated drift are still at similar levels, suggesting this noise level is not due to the cosine error, as is expected. This means this noise is likely due to another effect such as direct pressure fluctuations or refractive index.

From Figure 6.30a, the drift Allan deviation had two dips dropping to 20 pm, one at three seconds and the other at 150 seconds, before the typical upswing. The first dip is most likely due to short term noise averaging, while the second dip is the drift in the system. When the cosine error was compensated, the first dip in the Allan deviation remained the same and the Allan deviation continued to decrease where the second dip occurred. Overall both the corrected and uncorrected Allan deviations were an order of magnitude lower than the 1$^{\text{st}}$ Measurement System.

The single sided Fourier amplitude spectrum, shown in Figure 6.30b, showed the $1/f$ ramp start at approximately 0.03 Hz with amplitudes of a few picometers at higher frequencies. The slight uptick between 0.01 Hz and 0.02 Hz is likely refractive index fluctuations in the system, caused by air currents generated by the thermal sources in the vessel. The cosine error compensation reduced the low frequency amplitudes by half.

After the initial measurement was performed, the results from the 1$^{\text{st}}$ Measurement System were confirmed, at least for relatively short timespans. Also, the changes to the setup from the 2$^{\text{nd}}$ Measurement System clearly had an impact on the measurements. The overall drift was less, but more importantly, the individual interferometer length change was almost two orders of magnitude less and the noise was significantly lower. The short term drift noise was a few nanometers in the 1$^{\text{st}}$ Measurement Systems, whereas the noise dropped to approximately 100 pm in this test. These are clear indicators that the fiber did cause false length changes and instability in the previous system.

Also, these measurements showed a strong correlation to the individual deadpath measurements. This suggested there was a cosine error between the two interferometers which was corrected using a linear least squares approximation.

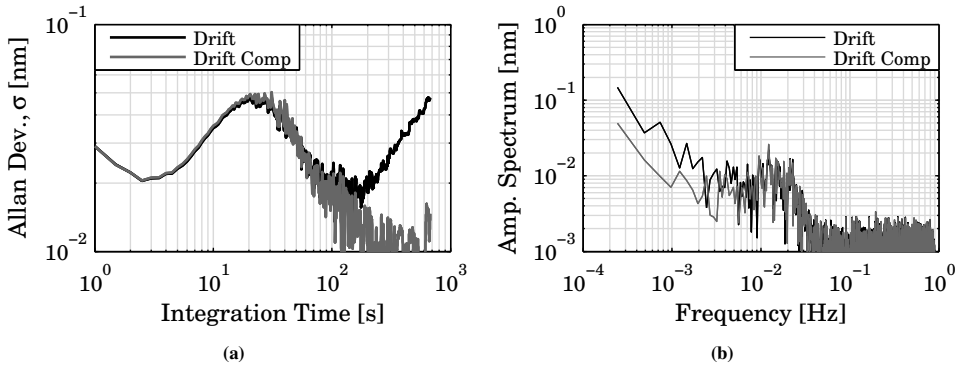

Figure 6.30: *Allan deviation (a) and single sided amplitude spectrum (b) of the drift and compensated drift from the initial measurement from the 3rd Measurement System. The drift showed a considerable reduction in the Allan deviation and amplitude spectrum in the 10^{-2} to 10^{-1} Hz regime from previous measurements. The compensated drift showed a further reduction, specifically in the long integration time and low frequency regimes, as expected.*

6.5.3 Daily Measurements

Two longer measurements were performed with this measurement system as shown in Figure 6.31. In both measurements, M1 and M2, the length change of each interferometer, S1 and S2, showed a strong correlation to each other. The length change of the first measurement, M1, was fairly linear for 2.1 µm over 15.5 hours. The second measurement, M2, showed sinusoidal drift with a range of 900 nm over 24 hours.

The drift in M1 was about 25 nm and had a 0.976 correlation coefficient with both M1,S1 and M1,S2. After removing the correlation using a linear least squares fit, the corrected drift was better than 10 nm pk-pk. The drift in M2 was also approximately 25 nm but had a slightly lower correlation coefficient of 0.90 with both M2,S1 and M2,S2. After removing the correlation, the corrected drift was also better than 10 nm pk-pk.

In both measurements, the short term drift noise level had bands where it was low and other bands where it was more than ten times higher. At the time, the cause of this was unknown. In the 4th Measurement System, this effect also occurred and the source was noise in the data acquisition from analog to digital conversion saturation. In these measurements, now that the source is known, the probable cause is thermal expansion changing the alignment. When the alignment changed, the fringe contrast was increased and the voltage input into the dSPACE system was outside ±10 V.

The data from Figure 6.31b was analyzed using the Allan deviation and a single sided Fourier amplitude spectrum, as shown in Figure 6.32. The drift Allan deviations for M1 and M2 were were below 1 nm until the characteristic upswing after 20 min. After applying the cosine correlation correction, the Allan deviations dropped significantly for longer integration times. The corrected M1's upswing is not as strong as it is prior to the correction. The corrected M2 shows a similar trend to M2 until 200 seconds before dipping further and the drifting. The short term limit to the Allan deviation is presumably the noise caused by saturating the analog to digital converters. The long term limit is likely the consistency of the cosine correction. The single sided Fourier amplitude analysis showed similar to trends

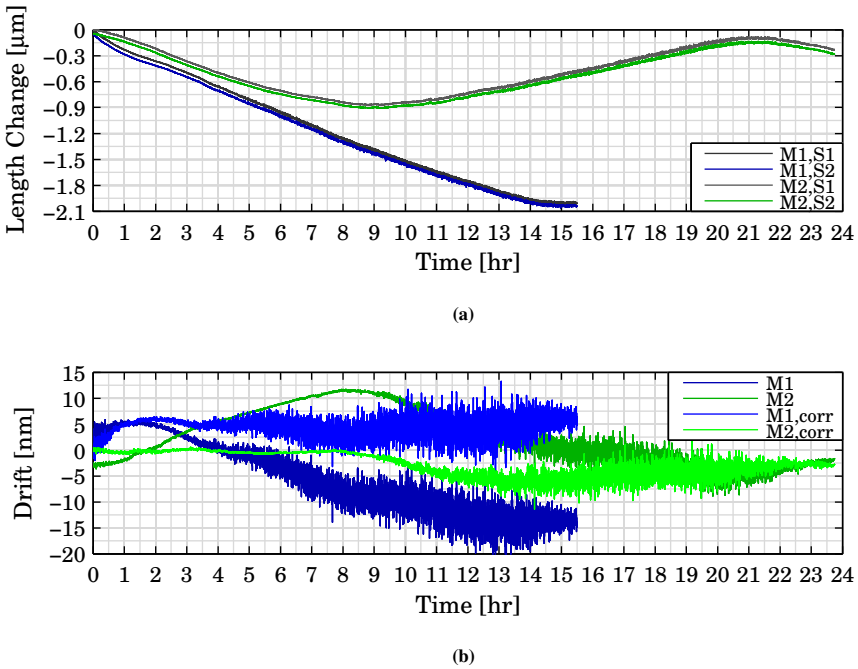

Figure 6.31: *(a) Two measurements (M1 and M2) of the individual interferometer drift (S1 and S2) using the 3rd Measurement System. Placing the acousto-optic modulators in the vacuum vessel largely removed the artificial length change caused by fiber elongation. (b) Measured drift of each interferometer and measured drift after compensating for the cosine error. These drift measurements had bands of high noise which was caused by voltage saturation in the dSPACE (discovered later).*

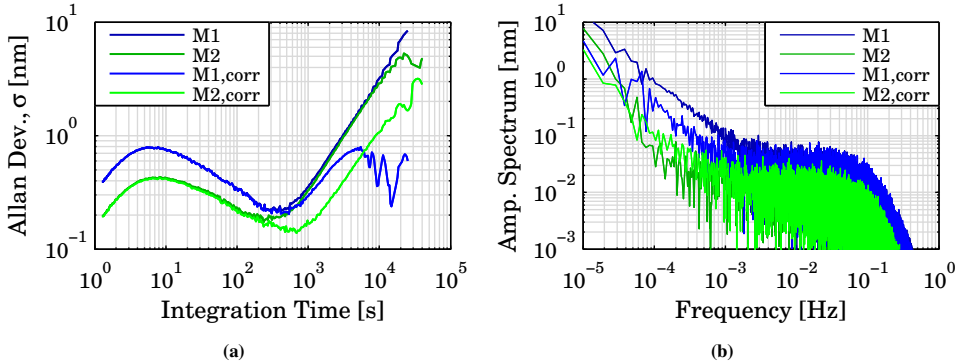

Figure 6.32: *Allan deviation (a) and single sided amplitude spectrum (b) of the two drift measurements and the two compensated drift measurements. The Allan deviation was reduced ∼5 times from the 1st Measurement System. The Fourier analysis showed minimal components in the high frequency regime. The middel frequency regime is still dominated by refractive index fluctuations. The low frequency regime suggests long term drift but was reduced after removed the cosine effect.*

in previous measurements. The drift showed high common-mode rejection at frequencies higher than 0.1 Hz. At frequencies lower than 0.1 Hz, the noise is dominated by spatial and time varying refractive index fluctuations which are uncommon between measurement and reference arms in the interferometer. This effect can only be reduced by either measuring the refractive index with the internal refractometer if possible or correcting the measurements using the Edlén equation. However, since these effects are localized variations, reducing this effect for measurements in air will be limited. The low frequency amplitude is dominated by thermal expansion effects due to daily temperature cycles.

6.5.4 Long Term Measurement

A long term measurement was performed over 100 hours which would allow for four daily cycles to be viewed. Figure 6.33a shows the measured length change of the two interferometer signals, S1 and S2, during the measurement. The measurement started on a Thursday morning, as evidenced by the 1 µm length change over the first 24 hours, followed by another daily thermal cycle on Friday up to 50 hours. Over the weekend, the next two smaller bumps, the maximum length change was much lower than the previous two days presumably because the thermal fluctuations in the laboratory were minimal. The last upswing in the data is due to thermal effects starting Monday morning.

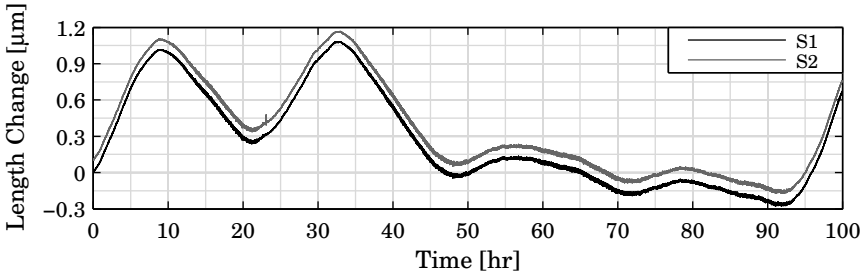

(a)

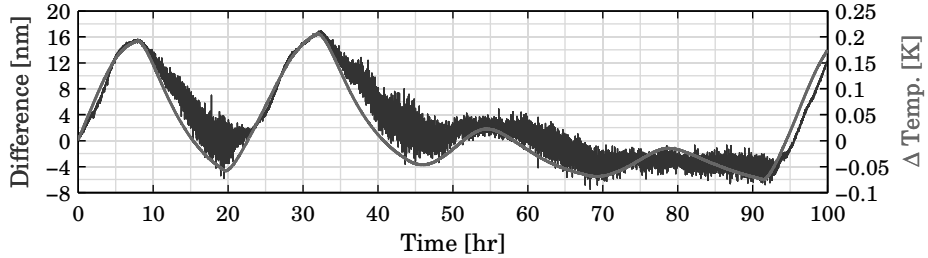

(b)

Figure 6.33: *(a) Long term measurement of the individual interferometers using the 3rd Measurement System. The results clearly show a daily cycle. The last two cycles were lower because the measurement started on a Thursday and those days landed on the weekend. (b) Drift between the two interferometer signals and the temperature of the system. The temperature was clearly a driver of the measured length changes.*

The difference between S1 and S2 was less than 22 nm pk-pk, over 100 hours, as shown in Figure 6.33b. Figure 6.33b also shows the temperature fluctuations with a clear and direct correlation to the length change of S1 and S2, and the drift.

Similar to the previous measurements, there were periods where the noise level was much higher than other periods. This was due to saturation in the dSPACE analog to digital converters but was only discovered in later measurements.

The drift data, which was correlated to S1 and S2 with a coefficient of 0.95 and temperature with a coefficient of 0.94, was corrected for both fluctuations using a least squares approximation. Both S2 and the temperature were used because they had a correlation coefficient of 0.85 with respect to each other. The drop in correlation coefficient between temperature and S2 is probably due to a thermal lag. Thus, the drift may have two effects, one directly related to cosine error and one related to thermal gradients in the system. The corrected drift data and the original drift data is shown in Figure 6.34.

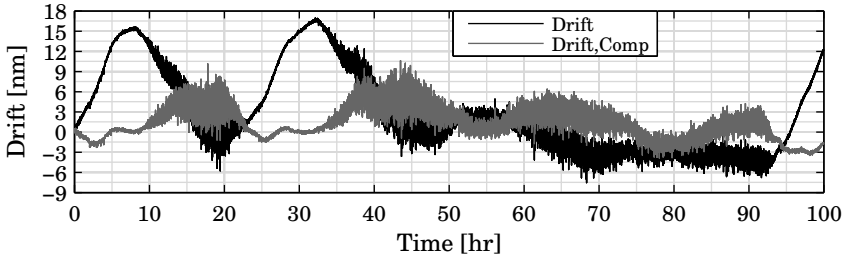

Figure 6.34: *Original drift results and compensated drift results for the long term measurement. The measurements were corrected using a linear least squares approximation assuming correlations due to temperature (thermal expansion) and the individual interferometer length change (cosine). The high noise bands are due to voltage saturation in the dSPACE system. The higher order effects are likely caused by a lag between the measured temperature and the effect on the system which would cause a temporal shift.*

The 22 nm pk-pk dropped to 9 nm pk-pk after correcting for cosine and thermal effects. Additionally, if the saturation had not occurred, the correlation correction may have been more accurate and a better correction of the drift data will improve results. Assuming the high noise areas actually had the noise level without the saturation in the dSPACE system, the pk-pk error would be halved to approximately 4.5 nm

The Allan deviation results, shown in Figure 6.35a, showed a similar short term deviation to the daily measurements with an initial upswing due to the dSPACE saturation error, followed by a downswing to the low drift regime and then then overall drift on a final upswing. After compensating for thermal and cosine effects, the Allan deviation was approximately ten times better, although the large upswing still signifies drift.

The single sided Fourier amplitude spectrum, Figure 6.35b, showed similar results to the previous measurement, with high mechanical coupling in the higher frequencies, refractive index effects in the middle frequencies, and daily cycles in the lower frequencies. There was no difference between the drift amplitude spectrum and the corrected drift amplitude spectrum except in the low frequency area where the daily cycles were canceled for the

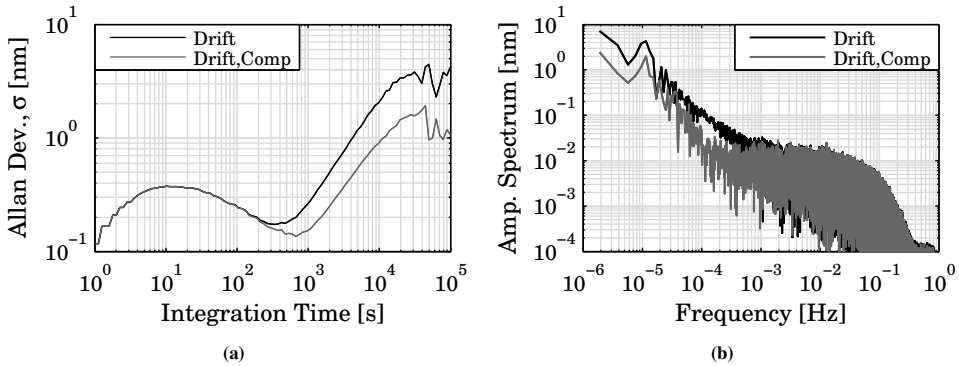

Figure 6.35: *Allan deviation (a) and single sided amplitude spectrum (b) for the long term drift and corrected drift measurements. The corrected drift showed a reduction by a factor of two from the original drift measurement. In the Fourier analysis, the results are nominally the same except the the low frequency amplitudes are lower at approximately 10^{-5} Hz which is the daily cycling in the data. (The power spectral density and cumulative amplitude spectrum is shown in Figure G.4.)*

corrected drift. This can be seen at frequencies lower than 3×10^{-4} Hz.

6.5.5 3rd Measurement System Summary & Conclusions

The fiber induced errors such as false length change and periodic nonlinearity were corrected in the 3rd Measurement System by fiber feeding a single stabilized laser beam and performing the splitting inside the vacuum vessel. This added heat sources into the system but the thermal power input remained constant and the system could reach a thermal equilibrium after a soakout period (~10 hours in this case). The custom optics still provided a simpler interferometer alignment and the noise level was much lower than the measurements with commercial optics. Also, the added stress by placing the optics on a flat surface and applying a vertical force to hold the optic in place had little effect in these measurements. However, for these measurements to be improved, then this should be assessed in more detail.

The initial measurement showed a significant improvement from the previous systems in both the dual interferometer length change, the drift, and the noise level. The dual interferometer length change and the drift showed a strong correlation, which suggested a cosine error from the alignment of the initial beamsplitter. Two longer measurements showed similar effects although the measured drift had periods where the data was affected by the dSPACE saturation.

The long term measurement showed the interferometers and drift had a clear correlation to daily thermal cycling. Since the drift can be affected by a cosine error and by thermal gradients in the optics, the drift was corrected for both effects using a least squares approximation. After correcting, the corrected drift showed periods with significant noise and a higher order effect which is assumed to be thermal lag between the temperature change and the effect on the interferometer. A phase mismatch between these two will create a higher order error in the difference.

Currently, for short measurements below one hour, the drift from the instrument is in the sub-nanometer range. For longer measurements, the thermal influence is much more critical and limits the interferometer drift to a few nanometers.

6.6 4th Measurement System

The previous measurements showed a little improvement over the original results in the 1st Measurement System. The noise level was reduced and optical alignment was easier with the custom optics. For this next measurement system, many small practical adjustments were made to the system and a manufacturing defect in the custom optics was corrected. The lateral displacement beamsplitter on the right PBS optic had a dual coating at the main interference surface. This dual coating created a double reflection at the beamsplitting surface meaning surface fringes appeared in the output beam even when only one beam was used as the input. This created a lateral sensitivity to the fringe contrast which could degrade the interference signal and cause error.

This was corrected by removing the defective component and using commercial lateral displacement beamsplitters as the main interfering surface. Also, another commercial lateral displacement beamsplitter was used to generate an optical reference signal.

Some of the practical improvements to the system included mounting a pressure sensor on the vessel, wiring vacuum feedthrough connectors for the electrical signals to pass between, and realigning the entire interferometer. This allowed for a fully pressure sealed environment in the chamber with the aim of reducing the refractive index fluctuations.

6.6.1 Practical Implementation

The optical setup schematic and two photos are shown in Figure 6.36. The laser source remained the same from previous measurements. After the two acousto-optic modulators, a beamsplitter was used to split 15% of the input beams, which were combined using a lateral displacement beamsplitter to generate an optical reference signal. This was used instead of an electrical reference signal as used in the previous setups. The electrical reference gave a cleaner signal but did not account for refractive index variations in the air or thermal effects in the acousto-optic modulators which may have caused phase shifts. These effects could have contributed to a false length change similar to when each individual acousto-optic modulator signal was fiber fed, although not to the same magnitude.

The last lateral displacement beamsplitter in the interferometer, mounted to PBS_2, was removed and two commercial lateral displacement beamsplitters were used instead as interfering elements. A separate optical mount was used to hold the commercial lateral displacement beamsplitters in place. This will contribute some instability because they are not directly mounted on the right PBS optic. However, this did provide a temporary solution to the manufacturing defect while that part was being manufactured again.

The data acquisition system, shown in Figure 6.37 was slightly modified from the previous version, removing the mixed function generator signals. This reduced some of the artificial noise on the reference signal from the mixer. However, the overall noise remained the same because the optical signal has slight phase shifts from the electrical signal due to thermal and refractive index effects. Additionally, the three photodetector signals were

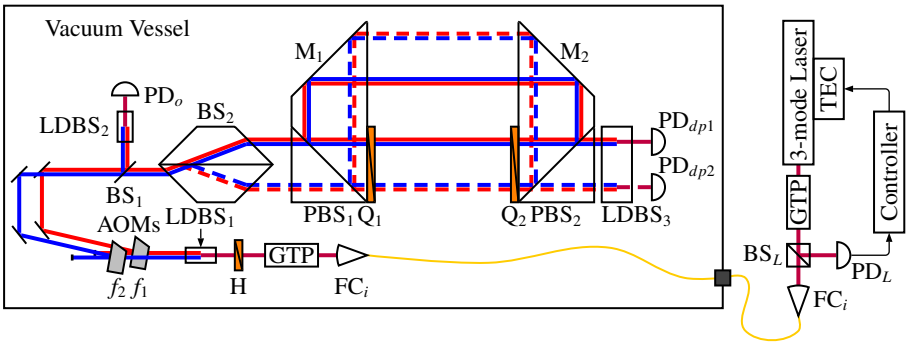

(a)

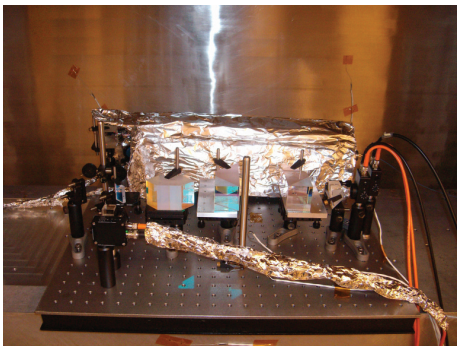

(b)

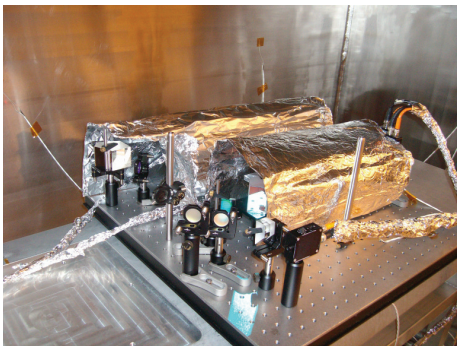

(c)

Figure 6.36: *Schematic of the optical layout for the 4th Measurement System. The source remained the same from the previous system. An optical reference was added, measured by PD_o to account for phase shifts in the signal between the acousto-optic modulator drive and the actual optical output. Also, commercial lateral displacement beamsplitters were used to interfere the measurement and reference arms of the two interferometers. (b) Photo of the setup after sheilding the input section. (c) Photo of the setup after shielding the air paths in the interferometer.*

passed through a pre-filter and amplifier to remove the DC-level component and generate AC voltages of ±9 V.

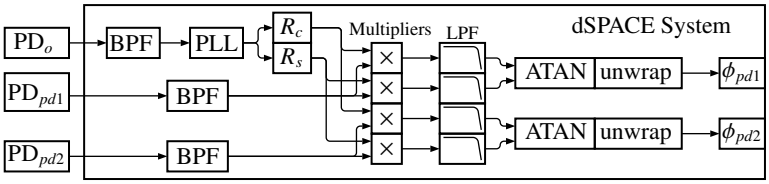

Figure 6.37: *Schematic of the lock-in amplifier for the 4th Measurement System. The electric reference from the two function generators was replaced by an optical reference generated from the two frequency up-shifted beams after the acousto-optic modulators.*

In the previous measurements, there were sections where the noise level was low enough to see the bit noise in the NI data acquisition card. The dSPACE system, however, did have a sufficiently low enough noise level to observe smaller fluctuations than what was observable by the NI system due to range against resolution limitations. This issues was alleviated by

setting up another channel in the dSPACE and NI systems for sending a super fringe signal. As shown in Figure 6.38, the difference between the two unwrapped phase signals from the two interferometers was calculated. This provided a signal with the measured drift between the two interferometers.

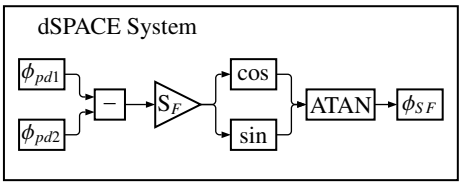

Figure 6.38: *Schematic of the added super fringe phase resolution enhancement.*

The difference was then multiplied by a known constant S_F, 200 to 600 in these measurements, and then the sine and cosine of the signal was calculated. This generates in-phase and quadrature signals of the drift which have a period equal to S_F times the original lock-in in-phase and quadrature rates. Another arctangent function was then used to calculate the phase of the super fringe signal and then a gain was applied to scale it from -10 V to +10 V for the dSPACE output. When the data was collected in Matlab using the NI data acquisition card, the wrapped fringes of $\pm\pi$ were equal to λ/S_F. Figure 6.39 shows a schematic of the signals sent to the NI data acquisition from dSPACE.

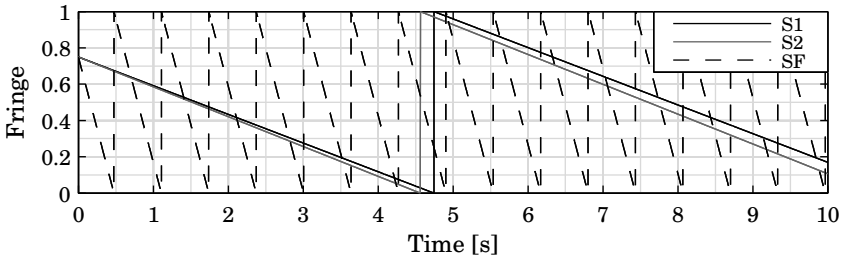

Figure 6.39: *Simulation of 1 μm and 1.04 μm displacements from the two interferometers. The difference is calculated and then mulitplied by 250, prior to being phase wrapped. This allows for a resolution enhancement of 250 times, while the wrapped range is reduced 250 times. SF is the super fringe signal.*

An example of this analysis is shown here. The length change of the interferometers (S1 and S2) over 10 seconds are 1 μm and 1.04 μm, which is a drift between the two interferometers of 40 nm. This corresponds to changes of 1.58 fringes and 1.643 fringes for S1 and S2, respectively. The difference between S1 and S2 is only 0.063 fringes. However, if the super fringe technique is used, the difference becomes 15.802 fringes. Since the NI data acquisition system can resolve 12 bits over a 20 V range, the smallest possible resolution without the super fringe technique is (0.154 nm)/N with a maximum displacement before phase wrapping of λ/N, where N is the interferometer resolution. Using the super fringe technique, the smalled resolution is (0.154 nm)/($S_F N$) and the range is reduced to $\lambda/(S_F N)$. There are some practical limitations with the noise level and phase

unwrapping but the following measurements all used S_F values of 250 or higher.

6.6.2 Atmospheric Measurements

After aligning the system and generating interference signals in the same double deadpath configuration, the vacuum vessel was pressure sealed. Additionally, a slight over pressure was generated using compressed nitrogren. This was done to ensure the vacuum vessel was truly pressure sealed. The over pressure was not released from the vacuum vessel because a large pressure jump in the measured data would indicate the pressure sealing of the vessel was not successful.

Common-Mode Rejection

The 4th Measurement System had a much lower noise level and vibrations were much more distinguishable than with the previous measurement systems because the tank was pressure sealed. The vacuum vessel resting on the air vibration isolation had a natural frequency near 1 Hz. This mode was excited by pushing on the vacuum vessel and results in a deformation of the mounting breadboard and a length change in the two interferometers, shown in Figure 6.40a. The difference (drift) between the two signals, confirms a better than 40 dB reduction in vibration amplitude. Additionally, the residual drift still had a profile similar to the excitation amplitude due to the cosine error. After taking this into account and correcting the measurement, the reduction was better than 330:1. This explains why the measured drift and corrected drift values at higher frequencies, greater than 10 Hz, show minimal contribution to the overall error.

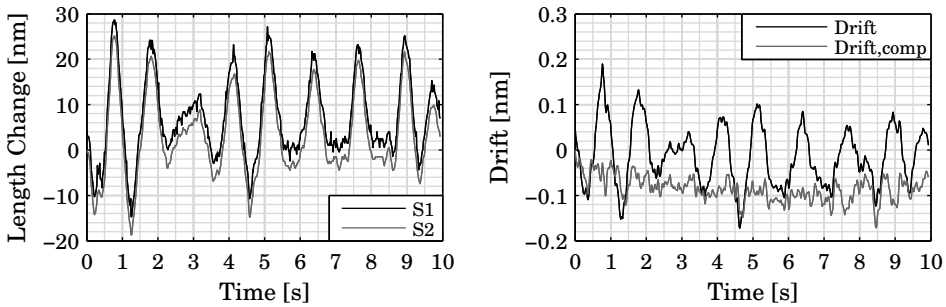

Figure 6.40: *Measured length change (a) and drift and compensated drift (b) for the 4th Measurement System after oscillating the vacuum vessel on its air vibration isolation at its natural frequency. The interferometer has a mechanical decoupling better than 115:1 on the direct difference (drift). After correcting for the cosine error, the reduction is better than 330:1.*

Initial Measurement

Figure 6.41 shows the measured deadpath drift from the two interferometers and the drift between the two interferometers. Additionally, the temperature of the air near

the interferometer and the optical breadboard where the components were mounted was measured. Also, the pressure was monitored during this measurement to ensure the vessel remained pressure-sealed.

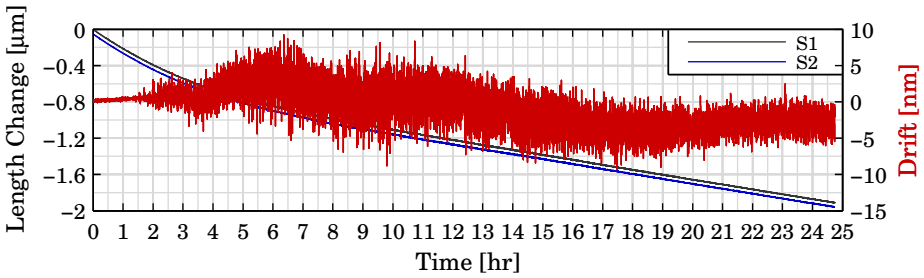

(a)

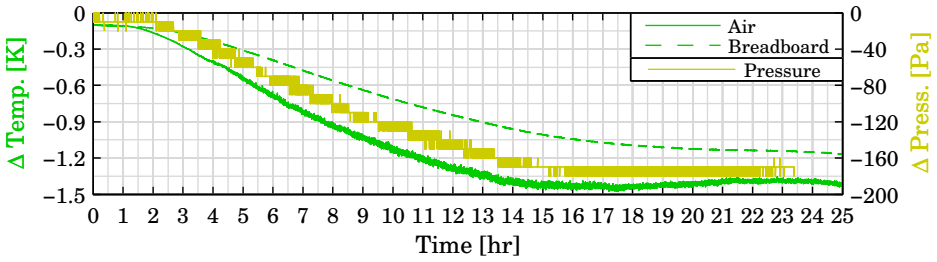

(b)

Figure 6.41: *(a) Measured length change from the two interferometers, S1 and S2, and difference (drift) using the 4th Measurement System. (b) Air and optical breadboard temperature change and pressure change during the day. The slight pressure drop not indicative of a loss of over pressure. The measured length change from S1 and S2 did not closely follow the temperature fluctuations.*

The measured drift over the first 1.5 hours was minimal until the system showed significant fluctuations and noise. When this measurement was stopped the following day, the noise level was apparent on the dSPACE readout screen. The interference signals were checked using an oscilloscope and the signal values were greater than ±13 V. The gain in the preamplifier was reduced to ±7.5 V and the noise was immediately eliminated on the dSPACE readout. This led to the assumption that the previous noise spikes were also driven by a similar phenomena.

Another observation was the individual interferometer signals did not have a strong correlation to the temperature. Also, the temperature change over 1 day was more than 1.5 K in the tank, and greater than 2.5 K outside the tank, which was much higher than anticipated. Upon further inquiry, the laboratory temperature regulation was not working properly and was undergoing repairs. The tank was pressure sealed and only had minimal fluctuations over the full day. The pressure change appears similar to the temperature change which would be expected as per the ideal gas law. However, due to some compressibiliy in the air and some heat-induced air currents from heat sources, this relationship is not perfect. Also,

the pressure resolution (10 Pa), limits a potential pressure correlation to the data without heavy filtering, which will add considerable delay.

The saturation in the dSPACE system was corrected by ensuring only ±5 V was sent to the system from the initial signal. This allowed for a doubling of the signal strength without reaching the saturation voltage threshold.

Sealed Vessel Measurement In Air

The double deadpath interferometer was measured again, as shown in Figure 6.42. In this measurement, S1 and S2 did not closely follow the 0.3 K thermal fluctuations. However, the drift between S1 and S2 did have a strong correlation.

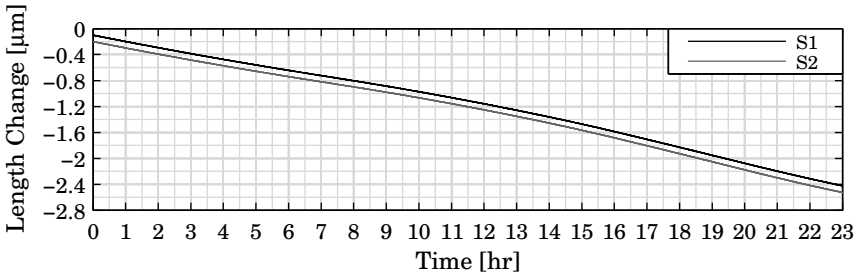

(a)

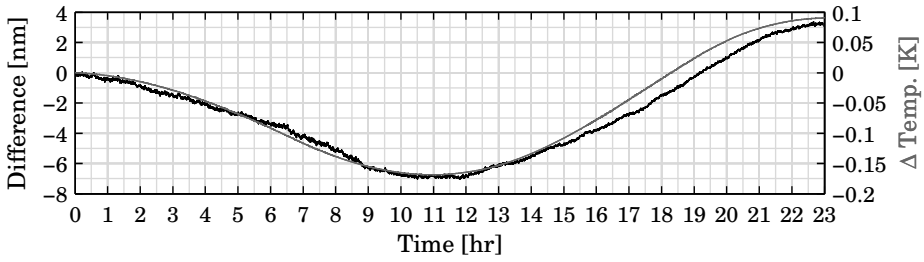

(b)

Figure 6.42: *(a) Length change of the two interferometers after correcting the over saturation issue with dSPACE. (b) Drift between the two interferometers and the corresponding temperature measurement of the air. (c) Corrected drift after compensating for the thermal fluctuations and the cosine error. The pk-pk corrected drift is better than 1.6 nm and the noise level is significantly reduced from previous measurements because the refractive index fluctuations are lower in the pressure sealed environment.*

As shown in Figure 6.42b, the temperature change is closely tracked by the drift until it slowly diverges towards the end of the measurement. Also, the drift noise level is consistent throughout the measurement, which means the dSPACE was not saturated. The correlation to temperature and the slight divergence between the two towards the end is an indication that the interferometer has a thermal dependence and there is still a cosine error between the two measurement signals. The reasoning behind the suspected cosine error is because

the length changes for S1 and S2 are in a nominally constant direction and the difference between the thermal changes and the drift appears to be growing at a constant rate.

The drift data was corrected for both thermal fluctuations and individual interferometer changes using a linear least squares fit. After correcting the drift for thermal and cosine effects, the corrected drift was better than 1.6 nm pk-pk over a 23 hour measurement, as shown in Figure 6.43. Also, the noise level is much lower than in previous measurements, which could be from the pressure sealed environment which limited refractive index changes.

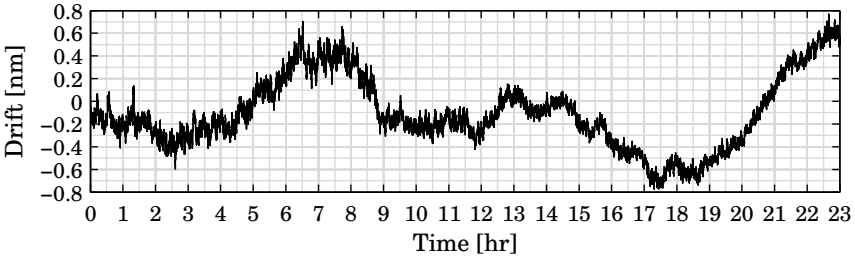

Figure 6.43: *Corrected drift after compensating for the thermal fluctuations and the cosine error. The pk-pk corrected drift is better than 1.6 nm and the noise level is significantly reduced from previous measurements because the refractive index fluctuations are lower in a pressure sealed environment.*

Figure 6.44 shows the corrected drift results in terms of the Allan deviation and single sided amplitude spectrum. In each analysis, the values were generally an order of magnitude lower or more than previous measurements over a similar timespan. The Allan deviation starts out at less than 5 pm before drifting slowly up to 50 pm over 20 min, which seems to be the most stable region for this interferometer. After that, the Allan deviation increases to 300 pm over about 3 hour time spans, before leveling off. The correlation correction for the temperature and cosine effects significantly reduce the Allan deviation upswing at long integration times.

The Fourier analysis showed a large improvement in the middle frequency range from 0.001 Hz to 0.1 Hz which is caused by sealing the vacuum vessel and limiting pressure fluctuations. The amplitudes above 10 pm all come from frequencies below 0.001 Hz.

6.6.3 Vacuum Measurement

After measuring in a sealed environment, the system was assessed in a vacuum environment at ~3 mbar (300 Pa) for 170 hours. The measurement was started on a Friday morning and the first 10 hours were removed because of vibrations from pumping and because the turbulance from the rapid changes in refractive index caused numerous phase jumps in the 'super-fringe' data. Figure 6.45 shows the length change of the two interferometers, S1 and S2, and the differences (drift) and the fitted correlation to temperature and cosine effects.

As with the previous measurements, the thermal fluctuations outside the vacuum vessel were unacceptable (±2°C pk-pk), which translated to greater than ±0.5°C pk-pk in the

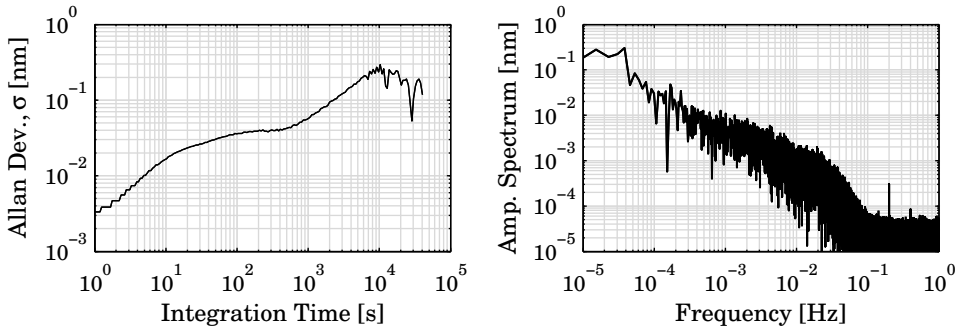

(a) (b)

Figure 6.44: *Allan deviation (a) and single sided amplitude spectrum (b) of the corrected drift measurements. The Allan deviation was significantly lower from previous measurements with a lower noise level even at short integration times. Also, no upswing was present, signifying little drift. The single sided amplitude spectrum was an order of magnitude lower than previous measurements. This indicates the saturation issue is fixed and the thermal and cosine corrections lead to lower measured drift. (The power spectral density and cumulative amplitude spectrum is shown in Figure G.5a.)*

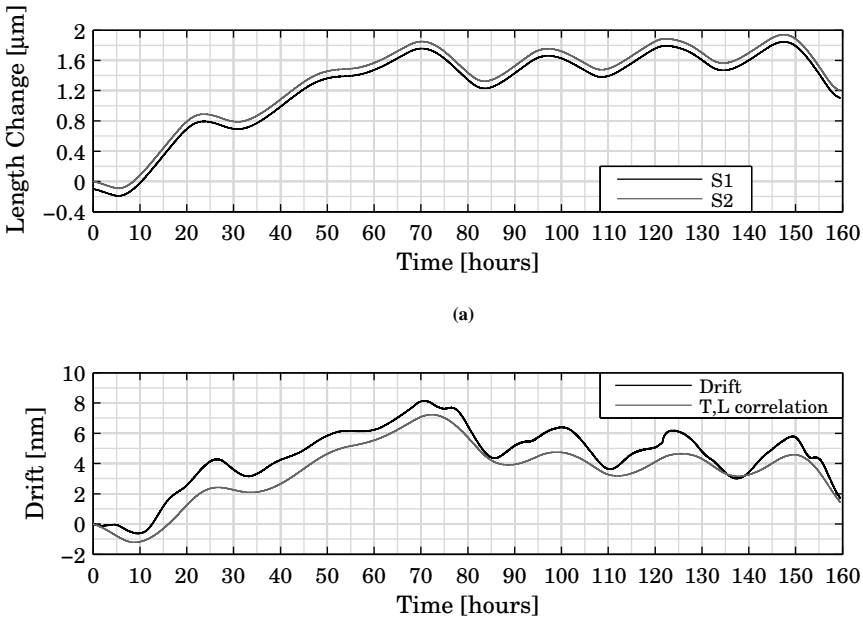

(a)

(b)

Figure 6.45: *(a) Measured length change of the two interferometers in a vacuum environment over 160 hours. The two signals are offset for clarity. (b) Difference between S1 and S2 (drift) and the corresponding correlation after correcting for thermal effects and the cosine error. The correlation does not perfectly follow the drift due to differing thermal time constants and the temperature was measured at non-ideal locations.*

vacuum vessel near the interferometer. Also, although the temperature probes were measuring in non-ideal locations, they remained in the same spots for this measurement to maintain consistency. Thus, the temperature correlation was not as exact as the previous measurement in the sealed air environment. Each interferometer showed deviations around 2 μm and the difference was under 10 nm pk-pk, which was similar to previous measurements. After correlating temperature and cosine effects, the fitted parameters showed significant gaps, likely due to differing thermal time constants. The drift after removing the temperature and cosine correlation is shown in Figure 6.46.

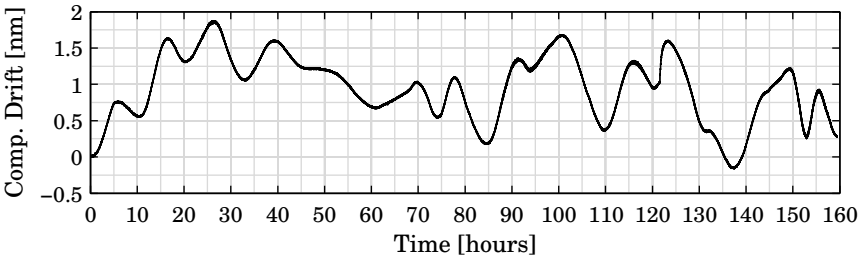

Figure 6.46: *Measured drift after compensating for the thermal effects and cosine error. The daily thermal cycle effect is reduced but the frequency was increased to a 10 hour cycle because of improper fitting. Overall, the compensated drift was better than 2 nm pk-pk over 160 hours.*

After removing the thermal and cosine effects, the compensated drift was better than 2 nm pk-pk over 160 hours with the added higher frequency drift due to an improper correlation. In the uncompensated data, there is clearly a daily cycle, whereas the compensated data had a decrease in the daily cycle amplitude but the drift over a 10 hour cycle increased.

The Allan deviation, shown in Figure 6.47, at 1 second was 3 pm and decreased to near 1 pm after integrating for 15 seconds. The Allan deviation then showed a steady increase to 300 pm after integrating for 4×10^4 seconds (~10 hours). After that peak, the Allan deviation then decreases to almost 100 pm. Thus, the improper correlation between temperature and cosine effects caused an increase in the Allan deviation over 10 hours but the long term effects are near 100 pm (1σ).

The single sided amplitude spectrum showed the $1/f$ starting point shift to near 10^{-2}, which is almost ten times better than the measurements in air. Also, the only slight peak occurs near 3×10^{-5} Hz, which corresponds to the 10 hour effects from inaccurate fitting.

6.6.4 4th Measurement System Summary & Conclusions

Four significant changes were made to the system between the 3rd and 4th Measurement Systems. The defective lateral displacement beamsplitter on the right PBS optic was removed and is currently in the process of being manufactured again. In the meantime, two commercial lateral displacement beamsplitters were used to continue measurements with the system. The electrical reference was switched to an optical reference to account for refractive index fluctuations and errors in the acousto-optic modulators. Additionally, the

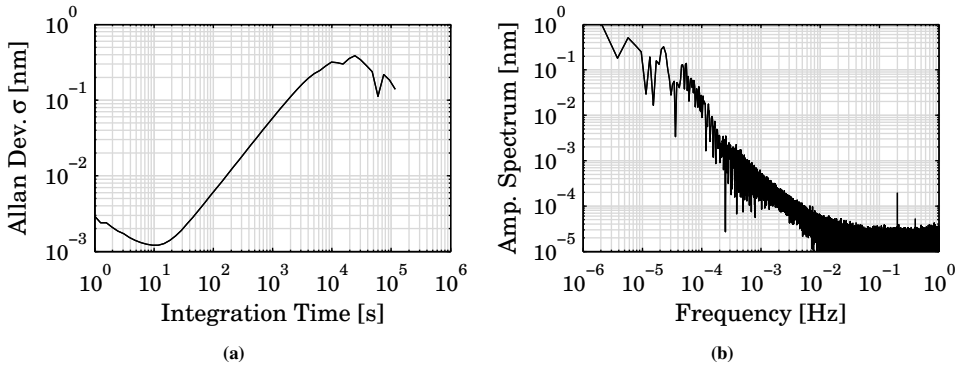

Figure 6.47: *Allan deviation (a) and single sided amplitude spectrum (b) for the compensated drift measurement in vacuum. The peak in the Allan deviation is from the improper temperature and cosine correlation, which manifests as a 10 hour cyclic error. The amplitude spectrum shows a significant decrease from previous measurements in the 10^{-4} Hz to 10^{-1} Hz range because the refractive index has little effect in a light vacuum environment. (The power spectral density and cumulative amplitude spectrum is shown in Figure G.5b.)*

vacuum vessel was sealed and an over pressure was applied to verify if the vessel remained sealed during the measurements, which it did. Lastly, a super fringing data manipulation was devised and implemented to reduce the range but increase the drift resolution. The only limitation to the super fringing method is the short term noise level of the signal and its affect on phase unwrapping. In these experiments, a super fringe constant of 250 was used without any problems. Also, the system was assessed in a light vacuum environment to contrast the differences between that and a sealed environment.

The initial measurements revealed the cause of the increased noise bands in the drift measurements which was due to voltage saturation in the dSPACE system. This was corrected and another measurement was made over 1 day. The drift between the two interferometers had a strong correlation to thermal changes in the system and a slight correlation to interferometer length change. After correcting for both thermal changes and the cosine effect, the corrected drift had a pk-pk error of 1.6 nm over 1 day. The Allan deviation and Fourier analysis showed an improvement of at least an order of magnitude from previous measurements. While the refractive index effects were not completely eliminated, they were significantly reduced.

The measurement in vacuum (3 mbar) showed a significant drop in refractive index effects, particularly in the 10^{-4} Hz to 10^{-1} Hz regime. The vacuum measurements did not have a perfect temperature and cosine correlation because the temperature was measured in the wrong spots. However, this was done to ensure consistency between this and previous measurements. Overall, the compensated drift was better than 2 nm over 160 hours.

6.7 Comparisons & Conclusions

Aside from switching to a medium vacuum environment, which is difficult to implement because the optic mounts are not vacuum compatible, the biggest gain to be made in the

system is by controlling the temperature at least an order of magnitude better than to which it is currently controlled. Also, more thermal shielding and buffering between the laboratory and the vacuum vessel with futher improve the measurements. While a better thermal environment and more thermal shielding will globally improve measurements, changing the optic mounts to a more dedicated and kinematic system will also improve the stability of specific components. Currently, modular commercial mounts were used as a practical means to obtain measurements. In the 2nd Measurement System, new mechanical mounts were designed and built but were not successfully implemented due to other unforeseen effects. However, adapting those custom mounts should be viewed as the logical 'next step'.

Several measurement setups did show decent results. The 1st Measurement System had two good initial measurements, one measuring the double deadpath (MS1 DP) and one measuring the 30 mm steel gauge block (MS1 GB). The 3rd Measurement System had a marginally successful long term measurement (MS3), although it had increased noise bands due to saturation in the dSPACE system. Lastly, two long term measurements with the 4th Measurement System showed the additional benefit of being in a pressure sealed environment in air (MS4 Air) and finally a light vacuum environment (MS4 Vac). The Allan deviations for these five measurements are shown in Figure 6.48.

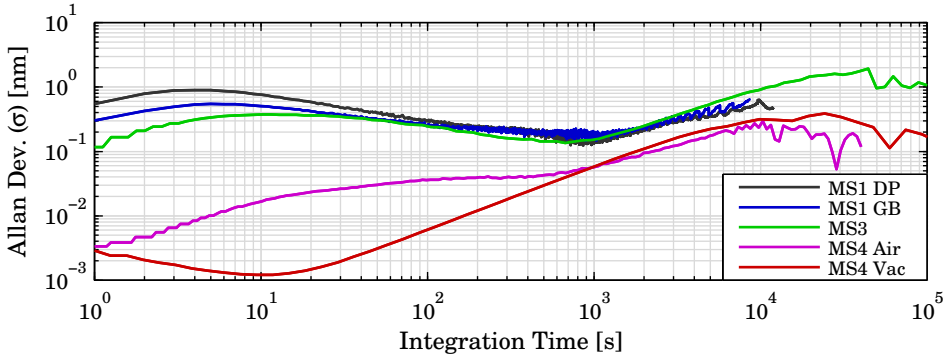

Figure 6.48: *Comparison of the Allan deviation from five different measurements using three different measurement systems. The measurements in air in an unsealed environment (MS1 DP, DS1 GB, & MS3) showed essentially the same trend, whereas the sealed measurement in air (MS4 Air) and the vacuum measurement (MS4 Vac) showed a large decrease at short integration times. In the long term, this interferometer is limited to ~300 pm (1σ) likely from temperature and cosine effects.*

The first three measurements (MS1 DP, MS1 GB, and MS3) all show a similar trend with the only differences in the short integration times, which are likely due to varying levels of shielding and alignment. After pressure sealing the vacuum vessel, the short term (less than 10^3 seconds) Allan deviation drops significantly because the refractive index fluctuations were minimized. The pressure sealed environment also showed a decrease of nearly an order of magnitude to 300 pm over the long term. The vacuum measurement showed a further reduction in the Allan deviation for below 10^3 seconds, although the long term stability is still limited to approximately 300 pm (1σ).

The difference between the sealed environment and the vacuum environment is also apparent in the single sided amplitude spectrum, showed in Figure 6.49. Here, there is a significant amplitude decrease between 10^{-4} Hz and 10^{-1} Hz.

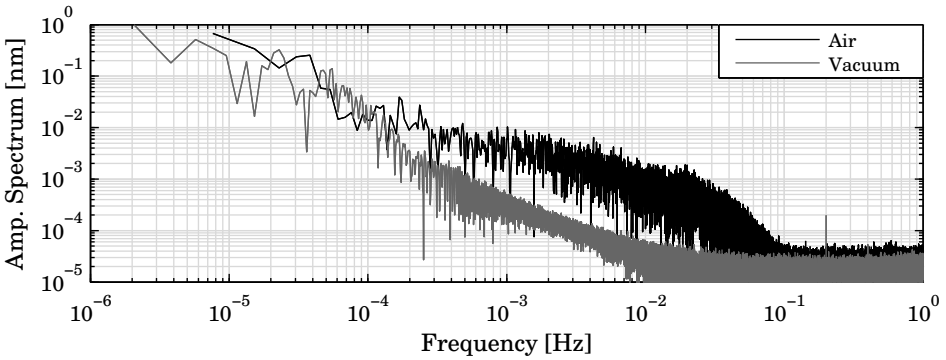

Figure 6.49: *Single sided amplitude spectrum comparison between the pressure sealed environment measurements in air versus the light vacuum environment. The low and high frequency regions are largely unaffected by the vacuum environment but the middle frequency regime shows more than an order of magnitude difference in the amplitude from the refractive index fluctuations.*

Chapter 7

Conclusions

The main goal of the research in this thesis was to design, build, and characterize an instrument for material stability testing. Interferometry was chosen as the measurement method because an instrument could be designed largely independent of the sample size and it did not require a grounded measurement target, compared to other measurement methods such as capacitive sensing. A double side interferometer was chosen as the configuration because it removed a large measurement uncertainty source by not measuring with respect to a reference plate and the measurement is directly traceable to the meter.

One unique aspect of this research differentiating it from comparable research was the focus on the capability to measure stability events. Most measurement systems of this type typically obtain a low noise level by averaging many data points. However, averaging can filter out stability events which would make them show up as slow thermal drift. Since stability events are a characteristic sought in this research, a high level of averaging was unsuitable for reducing noise. Instead, a sample model centered around the thermal bandwidth was developed.

Using a simplified thermomechanical model, the maximum thermal bandwidth for typical materials used in precision applications was estimated. For 50 mm long, gauge block sized samples, aluminum 7075-T6 and silicon carbide had the highest bandwidth, approximately 0.5 Hz. For smaller samples, the thermal band should increase because the thermal capacitance is reduced and the heat path is smaller. Thus, any thermal effects should show up in the 1 Hz or lower regime.

For stability events to be present in the data, they would most likely appear at frequencies higher than the thermal bandwidth. Otherwise, they would likely be a slower thermal expansion driven effect. Therefore, the target measurement bandwidth was chosen to be 25 Hz or higher.

A detailed uncertainty analysis was performed assuming a balanced interferometer with no contribution to the measurement uncertainty. The uncertainty analysis identified two large uncertainty contributors, the laser frequency stability and the refractive index fluctuations. In addition to those error sources, periodic nonlinearities were also identified as a large error contributor and must be addressed in the interferometer design. Lastly, since temperature fluctuations in the system have a finite controllable band and error contribution,

that error combined with the material thermal expansion was another large uncertainty contributor.

The previously stated thermomechanical model was developed as a method to overcome the length change measurement uncertainty when identifying stability events. While the length change uncertainty sets a boundary to which the length change can be estimated, it does not limit identifying stability events. Based on the thermomechanical model, the maximum length change rate due to thermal expansion should occur at a rate defined by the material properties and sample geometry. If the measured length change occurs at rates faster than this and the interferometer is capable of detecting these events, then the interferometer can make some assessment of the material stability even though the length change measurement uncertainty would normally prohibit this.

Research in three specific areas, periodic nonlinearity reduction, refractive index correction, and laser frequency stabilization, was needed prior to applying this principle. Once those error sources were reduced below their target level and a suitable interferometer configuration was investigated which demonstrated minimal drift, then applying the thermomechanical model can be used to identify stability events.

The following four sections summarize the findings from the main research topics investigated during this work. Following that, some future work and recommendations for future system generations is outlined.

7.1 Periodic Nonlinearity Reduction

In Chapter 3, research on reducing and eliminating periodic errors was presented. Periodic errors are caused by frequency mixing, imperfect polarization optics, and stray reflections. In most displacement interferometry systems, these are typically 1 nm to 5 nm. In dedicated, high-end displacement interferometers, the periodic error can be as low as 0.3 nm, as demonstrated during this research. However, special alignment techniques and expensive optics are needed to accomplish this. Additionally, no periodic error is desired as this is particularly problematic for feed forward control systems, where the periodic error is magnified.

For stability measurements, the feed forward error does not cause a problem, however, it still leads to a measurement error. The measured displacement in stability measurements is slow and nonlinear which also presents a problem when correcting periodic errors.

Because the starting phase value of the measurement is unknown, predicting the starting point on the periodic nonlinearity curve is difficult. Also, since the measured drift is likely to be much less than one fringe, the periodic error effect can be difficult to assess and correct. Assuming the drift is less than 20 nm, which is expected from measurements in a highly controlled environment and stable interferometer, the maximum periodic error contribution is approximatley 30% of the nominal pk-pk periodic error over one fringe. For typical periodic error values of 1 nm to 5 nm, this means a potential uncertainty contribution of 300 pm to 1.5 nm.

Several algorithms were presented which either measured periodic errors or measured and compenstated periodic errors. These algorithms were generally designed for systems which have either a linear or predictable motion, thus, they were tested for their suitability

for use in stability measurements. The only algorithm which showed some promise for correcting periodic errors was the continuous elliptical compensation. However, this algorithm requires at least one fringe of nominally linear motion to properly correct errors. Therefore, either a scanning method is needed for inducing a known fringe displacement or another alternative should be used instead.

A common theme of interferometers which demonstrate minimal or no periodic error is they typically have spatially separated beams which limits the amount of frequency mixing and relaxes the tolerances on polarization components. Then, by aligning to minimize detected stray reflections, the periodic error can be significantly reduced or eliminated.

While not specifically tailored to stability measurements, research was performed on interferometer configurations which showed no appreciable periodic nonlinearity to the noise level of 50 pm. These interferometers, called Joo-type interferometers, were designed for a series of configurations and a variety of implementations. Two difference configurations, one with a retroreflector target and another with a plane mirror target, were built, tested, and characterized. A generalized Joo-type interferometer was also presented, suitable for scalable systems which may require multiple measurement axes.

In terms of stability measurements, this research demonstrated that spatially separating the input beams in a heterodyne interferometer is more effective at reducing periodic errors than any algorithm-based solution. Thus, the interferometer for stability measurements should have spatially separated input beams to reduce periodic errors.

7.2 Refractive Index Correction

Correcting for refractive index fluctuations is the most difficult error source to overcome in this research. A target measurement bandwidth of 25+ Hz creates a strong contrast compared to accurate temperature and pressure measurements which have bandwidths around 0.1 Hz because of their integration time for noise reduction. Thus, for effective characterization and correction, another measurement method was sought which would allow for measurements at the same interferometer measurement bandwidth.

Fabry-Pérot interferometers are commonly used as refractometers where one arm passes through an open cavity and the other passes through a vacuum cavity. By balancing the Fabry-Pérot cavities and making them out of thermally stable materials, the refractive index can be measured effectively. However, errors will still persist when the Fabry-Pérot cavity is not dimensionally stable. Plus, this system will have a different measurement correlation to refractive index than in the interferometer because two drastically different measurement principles are used.

To minimize the cavity stability effect, five different Fabry-Pérot cavity designs were presented. Two cavities has a doubling of the free spectral range and one cavity quadrupled the free spectral range. By doubling or quadrupling the free spectral range, the cavity length can be shorter by that amount, making it less susceptible to length changes.

The most promising of the three alternative designs is the folded Fabry-Pérot. In this system, the FSR is doubled when compared to traditional etalons. When used for displacement measurements and sensor calibration, this interferometer is well suited because the moving element is insensitive to tip and tilt and neither the input nor output

beams must be transmitted through this component. The estimated finesse is only slightly less than the transmission cavity which means the locking stability should not be affected. This system should use a hollow retroreflector to minimize polarization effects and to increase the mirror efficiency.

Fabry-Pérot interferometry was also tested experimentally for refractive index tracking and wavelength correcting interferometry. In both cases, a transmission Fabry-Pérot cavity was used. The refractive index tracking was measured to be within 4.9×10^{-8} which is nearly the limit achievable with Edlén equations. In the wavelength correcting experiments, the difference between the equation based methods and the wavelength corrected DMI was approximately 2 nm over a 100 nm range.

While this method could be used to correct for refractive index fluctuations, it requires a stable cavity made of thermally stable materials. Additionally, the Fabry-Pérot mirrors must be highly efficient and must be mounted in a thermally neutral plane. This increases the complexity of the cavity design and more optical components are needed to utilize this system in conjunction with a sample measuring interferometer. Since this type of system employs a completely different measurement principle to measure and correct the refractive index, an alternative method should be used to correct the refractive index fluctuations.

An alternative method presented in this work is to develop a dual interferometer. One interferometer measures the sample fluctuations and the other measures refractive index fluctuations. If the refractive index fluctuations are nominally uniform throughout the interferometer, then this configuration could be suitable for measuring refractive index fluctuations. A detailed uncertainty analysis was presented and the two largest uncertainty contributors are the phase measurement itself and the temperature change uncertainty.

The design chosen in this research is a dual interferometer because the measurement and reference beams from both interferometers would pass through the same components, adding more balance into the system. Additionally, the sample measurement and refractive index measurement would both be performed with heterodyne interferometry. Building a dual system with additional channels for measurements which have the same measurement principles is easier to achieve than two completely different measurement principles. This system also has the potential for wavelength correcting inteferometry, where source frequency is changed to cancel the refractive index fluctuations.

7.3 Laser Frequency Stabilization

In this research, the technology for laser frequency stabilization was not the limiting factor but rather the practical aspects of implementing a stabilized laser with enough power suitable to obtain a detectable interference signal. Iodine stabilized lasers have more than enough frequency stability for this research but their output power is much lower than even conventional displacement interferometry laser sources. Tunable lasers locked to a stabilized femtosecond laser and cesium atomic clock also have a very high frequency stability but are still research tools themselves. Additionally, both systems have a high cost which was unattractive for this research.

Conventional displacement interferometry systems typically have a two frequency output with coaxial, orthogonally polarized beams. Splitting these beams into two separate

components will result in some frequency mixing which was not desired. A two-mode intensity balanced laser system could be used for as a source but its power output is still relatively low because it does not use a central cavity mode which typically has a higher output power.

Instead, a three-mode stabilized laser was researched during the course of this work. The three-mode laser uses the central mode of the laser as the main beam supplied to the interferometer and, in this case, had over 2 mW of usable power. An intrinsic mixed mode signal arising from third order harmonics was used to stabilize the laser.

The mixed mode signal at nominally 300 kHz was detected, filtered, amplified, and converted to a square wave. Then, a microcontroller was used as a pulse counter and PID controller. The PID output was sent to a current amplifier and then a Peltier cooler which changed the temperature of the laser tube. By changing the tube temperature, and thus, length, the absolute frequency of the central mode was stabilized.

This novel laser system had a fractional frequency stability of 5×10^{-10} compared to an iodine stabilized laser. After moving the laser system to a temperature controlled environment, removing some thermal mass, shielding the system, and tuning the controller, an estimated short term stability of 2×10^{-11} was achieved.

In practical applications, a heterodyne frequency was generated using an acousto-optic modulator driven at 20 MHz or two acousto-optic modulators at 20 MHz and 19.99 MHz. The resulting heterodyne frequencies at 20 MHz and 10 kHz were both sufficiently far from the 300 kHz mixed mode signal which had no effect on the measurements.

7.4 Interferometer & System Design

Several interferometer generations were designed, built, and tested during this research. The Preliminary Optical Concept of a double sided interferometer showed two important criteria that must be considered when designing an interferometer. First, the optical power at the detector is crucial for obtaining clear interference signals. Second, anti-reflection coatings are needed on all air-glass transition surfaces to reduce the power loss in the interferometer. This preliminary concept was refined into a more robust interferometer configuration and several optical path length differences were corrected. This interferometer was described in detail and contained an internal phase refractometer for correcting refractive index fluctuations. Also, modeling of this interferometer estimated a stability of 90 pm.

The 1st Measurement system was the first demonstrator of the Main Optical System concept. A higher powered, novel laser source and optics with anti-reflection coatings were used, which showed clear interference signals directly from the detector. Measurements were performed in a double deadpath configuration (no sample or vacuum tube present) and with a 30 mm gauge block. After correcting for thermal expansion, refractive index changes, frequency fluctuations, and pressure changes, the measured drift of the gauge block was comparable to the double deadpath measurement.

The Allan deviation for these measurements showed sub-nanometer performance up to integration times of 10^4 seconds. The low point in the Allan deviations appeared at an integration time of 10^3 seconds. Aside from expected but higher than wanted environmental fluctuations, the limiting noise source was the optics and mounts. Each optic was mounted

separately using commercial tip-tilt stages which are known to drift and vibrate at slightly different rates. This contributed to short term noise band of 50 nm in the individual interferometer measurements.

Since vibrations on this order of magnitude were not originally considered, the measured length change equations were reexamined in the presence of common vibrations to ensure the sample measurements, the deadpath measurements, and the refractometer measurements would all see the vibrations cancel. Based on the theory, the common vibrations should completely cancel although there are still additional coupling variables that may affect the measurements at the picometer range. Also, the difference between vacuum tube length and sample length was considered and confirms that a linear correction on the refractometer phase measurement signal is needed to fully compensate the difference. This correction is suitable for up to a ten times difference between sample length and vacuum tube length and 100 nm vibration induced length changes.

For the 2nd Measurement System, custom optics and mounts were manufactured by TNO to provide a more stable and less stressful mount condition for the optics. The optics consisted of three components: an initial beamsplitter, a left PBS optic, and a right PBS optic. These new optics and mounts were used in a different laboratory jointly operated by TU Delft and TNO. The system was placed inside a vacuum vessel and was fiber fed in and out of the vessel to remove heat sources from the system. The heterodyne frequency generation was done outside of the vacuum vessel and each of the spatially separated beams was launched into its own PM fiber and sent to the interferometer.

Preliminary measurements showed the fibers caused large false frequency changes which were due to differences between the two fibers' stress and expansion. While the individual interferometer signals saw large length changes, the drift between the two interferometers was in the tens of nanometers. The false length changes and high noise level (several micrometers) could have been corrected by placing an optical reference prior to the interferometer but after the fiber connection into the vessel. However, periodic nonlinearity ranging between 0.2 nm and 0.5 nm was discovered in the measured drift data. This was also caused by the fibers but would not have been corrected by placing an optical reference in the vacuum vessel.

Because the fibers were the source of the main issues with the 2nd Measurement System, the next system eliminated separate input fibers. Instead, a single fiber carrying the stabilized laser signal was sent to the vacuum vessel and the optical heterodyning was performed inside the vessel using the two acousto-optic modulators. Also, the optic mounts where switched back to commercial alternatives because the custom mounts were not compatible with the changed source.

The initial measurements with the 3rd Measurement System showed considerable improvement over the previous two systems. The overall interferometer fluctuations were less than 50 nm per hour and the drift was better than 0.3 nm per hour. This initial measurement was also the first indication of a cosine error in the measurement. The individual interferometers and the drift had similar profiles. After applying a linear least squares fit for the cosine error, the drift was about 60 pm for the 45 minute measurement.

Subsequent measurements showed more measured length change and drift in the system then in the initial measurements. Also, these measurements had periods of very high noise

and the source of the noise was unknown at the time. Later, it was discovered that the noise was from voltage saturation in the dSPACE system. The probable cause is the length change in the interferometer caused the fringe contrast to increase, which then exceeded the voltage in the dSPACE input.

One long term measurement of 100 hours showed four clear cycles due to daily temperature fluctuations. This measurement also suffered from the same voltage saturation problems of the previous measurement. The drift clearly showed correlation to temperature fluctuations and it was corrected for cosine effects and thermal fluctuations. The corrected drift was better than 9 nm pk-pk and would have been less if the voltage did not saturate the dSPACE system. Some higher order effects were also seen in the corrected data which is likely due to a phase lag between the temperature measurement and its effect on the interferometer.

An optical reference signal was added for the 4th Measurement System, replacing the electrical reference signal. Also, a manufacturing defect with the right PBS optic was corrected by removing the lateral displacement beamsplitter portion and using commercial components in its place. Also, the resolution was enhanced at the expense of the range by using a super fringe technique. The difference between the two interferometers was calculated in dSPACE and then multiplied by a constant and re-wrapped into wrapped fringes. Then, the wrapped fringes are acquired by the main data acquisition system, unwrapped, and then divided by the super fringe constant. This allows for a variable measurement resolution depending on the noise level observed. Using a super fringe constant of 250, which was case for the 4th Measurement System, the smallest resolvable length is 0.6 pm (theoretically).

These measurements were performed in a pressure sealed environment, rather than just as with shielding the interferometer in previous experiments. After the initial measurement, the voltage saturation was discovered and corrected. Another measurement was made with a 10 nm pk-pk drift which had a strong correlation to the temperature change. Also, a smaller cosine effect was visible in the data. After correcting for temperature and cosine effects, the resulting corrected drift was better than 1.4 nm pk-pk over 23 hours. The Allan deviation, single sided amplitude spectrum, amplitude spectral density, and cumulative amplitude spectrum were all an order of magnitude better than previous measurements. Also, because the interferometer was in a pressure sealed environment, the refractive index fluctuations were less than in previous measurements. The peak in the Allan deviation was at 0.4 nm (1σ). This interferometer was also tested for mechanical coupling which showed the drift was decoupled from the individual interferometer length change by 115 times. After accounting for cosine effects, the decoupling was better than 330 times. A measurement in vacuum over 160 hours showed the double deadpath interferometer drift was less than 2 nm pk-pk after correcting for thermal cycles and the cosine error. The Allan deviation showed a minimum of near 1 pm at an integration time of 10 seconds and a maximum of 0.3 nm (1σ) at 10^3 seconds.

7.5 Conclusions for Stability Testing

The drift measurements using this interferometer showed little influence from mechanical effects on the interferometer, especially when the cosine error was corrected. The next

largest effect was due to spatial and temporal refractive index fluctuations in beam paths in air. This effect typically occurred at frequencies lower than 0.1 Hz. The effect of the vacuum tube for in-process refractive index correction was not assessed due to budgetary limitations. Aside from improving the temperature and pressure stability of the surrounding environment, implementing a refractometer is the only way to reduce refractive index influences on measurements in air.

Improving the temperature and pressure stability will also improve measurements. Some measurements were subjected to 1 K to 2 K temperature changes, which were much higher than anticipated. In the original uncertainty estimate, the maximum temperature change was assumed to be 10 mK. These measurements had fluctuations up to 200 times worse. Also, more investigation is needed to determine the thermal correlation to the drift, which should be near zero. Instead, there was a 90+% correlation in most measurements. One possible source is thermal gradients in the large optics.

Thermal gradients in the optics explain both a thermal dependency and the cosine error. The location where the temperature is being measured still has some lag between when the increase is measured and when the beam in the optic is affected by the increase. However, each interferometer lag may differ depending on the location of the heat source. Thus, the drift between the two interferometers will change in a profile similar to the thermal changes in the system. Because there is a lag in the system, there will also be a difference in the rate of expansion, which means there will be a cosine effect on the measurement. Reducing the outside thermal fluctuations and shielding the interferometer are the only effective ways to limit this.

The refractive index fluctuations occurred in the 10^{-3} Hz to 10^{-1} Hz frequency regime and the mechanical influence was in the 10^{-1} Hz and higher regime. It is unclear at this time what specifically affects the measurement in the lower frequency regime, 10^{-3} Hz and lower. While thermal effects have some influence, daily temperature cycles for instance, this does not explain all of the drift. Another source is the mechanical mounts shifting in the low frequency regime, possibly driven by thermal effects as well. Modifying the custom mounts to accommodate the heterodyne frequency generating part and the optical reference should improve the mechanical stability. Also, shielding the heat from the acousto-optic modulators from the remaining optical components should improve the system. More specific improvements to the system are discussed in the following section.

Another limiting external factor in this research was due to facility issues and delays with the custom optics. This reduced the time available for performing stability testing. Additionally, issues with power in the laboratory, air supply to the optical benches, computer crashes, and scheduling time for the optical bench with other ongoing research projects all reduced the time allocated for measuring and, in some case, data was lost on potentially successful measurements. Additionally, since this is a research tool, individual experiments showing one day of data sometimes took many days or even weeks to make changes from previous measurements and perform a successful measurement. This also limited the amount of measurements that were performed.

Currently, the interferometer is still being modified and double deadpath measurements are still being performed. More research is needed to definitively say whether this interferometer can be used for material stability assessments. If the thermal and cosine effects scale linearly, then achieving a 10 mK stability in the surrounding environment

should produce results in the 10 pm to 20 pm range. Then, the vacuum tube should be implemented and another series of characterization tests should be performed. If those are successful, then samples and the thermomechanical model can be investigated in more detail. This may include a more rigorous three dimensional model of the sample, rather than the simplified one dimensional model presented in this research.

At this time, this research and interferometer shows inconclusive results as a tool for determining material stability.

7.6 Recommendations & Future Work

Several steps should be taken to improve the interferometer and obtain better results. Once these step are taken, the possibility of using this system for stability measurements can be re-evaluated. The two largest improvements to the system to obtain better measurements are to improve the temperature stability to 10 mK and to perform measurements in a vacuum environment. There are practical limitations to achieving both of these that will be addressed in the following section.

7.6.1 Periodic Nonlinearity

Spatially separating the two heterodyne beams prior to fiber coupling into the vacuum vessel caused many problems, including periodic nonlinearity. One way to still fiber couple the system using this technique, which places the heat sources far away from the interferometer, is to add high extinction ratio polarizers after launching the light into the system. This polarization cleanup can block much of the unwanted mixed states. This should be tested using a periodic error free interferometer, such as the Joo-type interferometers which showed no significant periodic nonlinearity in a comparable free-space version. The sensitivity to thermal effects and mechanical stresses should also be assessed. Also, an optical reference should be placed after the polarization cleanup in the system to eliminate the frequency shift in the fibers.

If periodic errors are still present in the system, then a modulation should be added to one input beam which would cause a known linear length change in the data. Then, a periodic error correction algorithm can be used to further reduce the periodic errors. The continuous elliptical compensation algorithm, discussed in Appendix D showed the most promise for eliminating periodic nonlinearity. This algorithm is time consuming and computationally expensive to perform but this can be performed post-process and offline.

7.6.2 Refractive Index Correction

The internal refractometer using the vacuum tube was not used due to budgetary limitations. Two vacuum tubes were purchased but did not meet the required specifications. The input and output beams must be highly parallel, thus, this vacuum tube should not have wedged windows. Using wedged windows makes the alignment much more critical than with plane parallel windows.

Alternatively, a Fabry-Pérot based refractometer can be used to measure the refractive index changes. The mirrors mounted to the fixed cavity should be thermally neutral

with respect to the low expansion cavity. This will reduce the refractive index change measurement uncertainty. An electro-optic modulator and either an acousto-optic modulator or faster laser controller (see next section) will be needed to implement this. The eletro-optic modulator can be used for scanning the Fabry-Pérot cavity and provide the looking signal for the Pount-Drever-Hall method while the acousto-optic modulator or laser can be used in feedback to change the frequency to remain locked to the laser.

One issue that may arise from using the acousto-optic modulator is the pointing stability will change as a function of frequency. This may limit the stability in the Fabry-Pérot cavity. However, if the laser is used, as carried out during this research for wavelength tracking and wavelength correcting, then this technique should be fairly robust.

7.6.3 Laser Stabilization

Replacing the TEC-based actuator with a non-thermal method of controlling the cavity length would remove the unwanted thermal effects in the system and increase the locking point stability. A possible solution is to use a sealed cavity laser with anti-reflectance coatings on one side of the laser tube and an externally located, piezo controlled laser mirror. A piezo-controlled mirror would increase bandwidth and remove most heat generation but alignment and the overall system concept need to be considered.

A long-term assessment is still needed to verify the frequency stability compared to a metrology laser system. Additionally, the intrinsic mixed mode may depend on the temperature and pressure of the plasma tube. Changes in temperature and pressure may cause density changes in the HeNe mixture, which may affect the mixed mode signal. By stabilizing the system without using a thermal actuator, potentially more stability can be gained from the system because the cavity length and tube temperature can then be controlled independently.

7.6.4 Interferometer & System Design

The interferometer, and in particular the optic mounts, should have several improvements made to increase the likelihood of obtaining better results. First, the periodic nonlinearity from the fibers should be investigated. If the periodic nonlinearity can be eliminated by having polarization cleanup after collimating the light in the vacuum vessel, then the custom mounts should be modified to allow for an optical reference. If the periodic nonlinearity cannot be eliminated, then the mounts should be modified to accommodate the acousto-optic modulators. The acousto-optic modulator should also be shielded to mitigate heat transfer into the interferometer. The mounts should also be modified, in general, for an optical reference. This provided a much cleaner reference signal rather than the electrical reference.

The lateral displacement beamsplitter on the right PBS optic should be manufactured and mounted back on the optic. The optic mounts should also have a soft vertical spring added to apply a mounting force on the optics. While this adds unwanted stress, the practical limitations of mounting the vacuum vessel door outweigh the added stress.

For measurements in air, the vacuum vessel does not appear to provide any additional benefit except for pressure sealing the environment. The thermal transfer into the tank

was about a 3:1 reduction. When the 4 cm insulation foam was used in the preliminary measurement system, the reduction was greater than 50:1. If measurements in vacuum are not necessary, then a double thick insulation foam box should provide much more stability than the vacuum vessel. This, in combination with characterizing the refractive index changes using the vacuum tube, is the most viable way to improve the measurement and reduce the noise level and uncertainty.

Appendix A

Abbreviations

1D	one dimensional
18-8 SS	standard grade stainless steel
Al_2O_3	alumina
Al7075-T6	aluminum, aircraft grade
AC	a signal oscillating at a nominally know frequency
AOM	acousto-optic modulator
AR	anti-reflection
ASD	amplitude spectra density
APD	avalanche photodiode
BC	birefringent crystal
BK7	Borosilicate glass, Schott
BPF	band-pass filter
bs	beam sampler
BS	beamsplitter
CAS	cumulative amplitude spectrum
CCD	charge-coupled device
CMM	coordinate measuring machine
CO_2	carbon dioxide
CTE	coefficient of thermal expansion
DC	signal with a nominal offset, no fluctuations
DMI	displacement measuring interferometer
DOF	degree of freedom
DWS	differential wavefront sensor
ECDL	external cavity diode laser
EOM	electro-optic modulator
EUV	extreme ultra-violet
$f_{1,2}$	frequency
f_s	split frequency
fs	femtosecond
FP	Fabry-Pérot
FPGA	field programmable gate array
FSR	free spectral range

FWHM	full-width half-maximum
GUM	Guide to the Expression of Uncertainty in Measurement
H	half wave plate
HeNe	Helium-Neon
HPF	high pass filter
HV	high voltage
I	in-phase signal, from lock-in amplifier
ISO	International Organization for Standardization
LB	lower bound
LDBS	lateral displacement beamsplitter
LPF	low-pass filter
M	mirror
NI	National Instruments
NIST	National Institute for Standards and Technology, US Metrology Laboratory
Nd:VYO_4	Neodimium Doped Yttrium Vanadate
Nd:YAG	Neodimium Doped Yttrium Aluminum Garnet
OI	optical isolator
OSA	optical spectrum analyzer
P	polarizer
PBS	polarizing beamsplitter
PCB	printed circuit board
PD	photodiode or photodetector
PDH	Pound-Drever-Hall
PH	pin hole
PID	proportional-integral-derivative
pk-pk	peak-to-peak
PLL	phase-locked loop
PM	polarization maintaining (fiber)
PMI	plane mirror interferometer
PP	penta prism
ppm	parts per million
PZT	lead zirconate titanate, typically an actuator or sensor
Q	quarter wave plate, typically for figures
QWP	quarter wave plate, typically for descriptions
Q	quadrature signal, from lock-in amplifier
RAP	right angle prism
RC	resistance-capacitance [circuit]
R_c	reference cosine signal
RF	radio frequency
R_s	reference sine signal
RR	retroreflector, also called a corner cube
RSS	root-sum-square
SiC	silicon carbide
SNR	signal to noise ratio
TEC	thermo-electric cooler (or peltier)
Ti:S	titanium doped sapphire
UB	upper bound

ULE	Ultra Low Expansion material
UV	ultra violet
VCO	voltage-controlled oscillator

Appendix B

Maxwell's Equations

When a point charge, q [C], is placed in an electric field, $\mathbf{E}$ [N·C^{-1} or V·m^{-1}], the force, $\mathbf{F}_E$, due to the electric field on the charge is

$$\mathbf{F}_E = q\mathbf{E}. \tag{B.1}$$

If a point charge is moving, the force, $\mathbf{F}_M$, experienced is proportional to the velocity, $\mathbf{v}$, of the motion by

$$\mathbf{F}_M = q\mathbf{v} \times \mathbf{B}, \tag{B.2}$$

where $\mathbf{B}$ is the magnetic field [T or N·A^{-1}·m^{-1}] where the motion occurs. When both fields are simultaneously acting on the same charge, the total force, $\mathbf{F}$, on the charge is

$$\mathbf{F} = \mathbf{F}_E + \mathbf{F}_M = q\left(\mathbf{E} + \mathbf{v} \times \mathbf{B}\right). \tag{B.3}$$

B.1 Faraday's Induction Law

One of many contributions to electromagnetic theory by Faraday is that a magnetic flux, Φ_M, in the presence of a closed conducting loop, C, generates a current along the loop. The magnetic flux [T·m^{-2} or N·A^{-1}·m^{-3}], a scalar quantity, is the strength of a magnetic field for a given surface area S

$$\Phi_M = \iint \mathbf{B} \cdot d\mathbf{S}. \tag{B.4}$$

A time varying change in magnetic flux creates a proportional electromotive force, emf, given by

$$emf = -\frac{d\Phi_M}{dt}. \tag{B.5}$$

Similarly, an electromotive force in a closed conducting loop exists only as a result of an electric field, resulting in

$$emf = \oint_C \mathbf{E} \cdot d\mathbf{l}, \tag{B.6}$$

where l is integrated along closed loop C. When the conducting loop remains constant and is completely enveloped by the magnetic field, the conditions for the Faraday Induction Law

are true. In other words, solving and rearranging Equations B.4 and B.5 with Equation B.6 yields

$$\oint_C \mathbf{E} \cdot d\mathbf{l} = -\iint_A \frac{\partial \mathbf{B}}{\partial t} \cdot d\mathbf{S}, \tag{B.7}$$

which states that a point charge in a time varying magnetic field experiences a force or a stationary point charge in a changing magnetic field experiences a force. Because the charge experiences a force, it must be in the presence of an electric field, even in the absence of a current source. As a result, a change in magnetic field has an accompanying electric field.

B.2 Gauss's Law: Electricity

For a charge completely enclosed within a closed area A, the electric field intensity flux Φ_E [$\mathrm{N{\cdot}C^{-1}{\cdot}m^{-2}}$ or $\mathrm{V{\cdot}m^{-3}}$] is

$$\Phi_E = \oiint_A \mathbf{E} \cdot d\mathbf{S}, \tag{B.8}$$

wher the vector $d\mathbf{S}$ is the outward normal vector of the area. The double contour integral denotes a closed surface. If there is a continuous charge distribution density, ρ, throughout the volume, V, enclosed by, A, then using Coulomb's Law it can be shown that

$$\oiint_A \mathbf{E} \cdot d\mathbf{S} = \frac{1}{\epsilon} \iiint_V \rho dV, \tag{B.9}$$

which is Gauss's Law for electricity. The constant ϵ is the electric permittivity of the medium

$$\epsilon = \epsilon_r \epsilon_o, \tag{B.10}$$

where ϵ_r is the dielectric constant or relative electric permittivity to a vacuum and ϵ_o is the electric permittivity in a vacuum which is derived to be $8.8542{\times}10^{-12}$ $\mathrm{C^2{\cdot}\,N^{-1}{\cdot}m^{-2}}$.

B.3 Gauss's Law: Magnetism

The complement to Equation B.9 is Gauss's Law for magnetism. However, because there are no magnetic monopoles (sinks or sources), the net magnetic flux across an enclosed surface is always zero. Thus, Gauss's Law for magnetism is

$$\oiint_A \mathbf{B} \cdot d\mathbf{S} = 0. \tag{B.11}$$

B.4 Ampere's Circuital Law

The last main equation to describe electromagnetism is Ampere's Circuital Law. It states that on a closed conducting loop, l, the total magnetic field surrounding the loop is proportional to the current, i, carried in the loop

$$\oint_C \mathbf{B} \cdot d\mathbf{l} \propto \sum i. \tag{B.12}$$

The summation of currents around the loop occurs if there is more than one closed conducting loop. The proportionality in Equation B.12 is through the permeability of the medium, μ. For a perfect vacuum, the permeability, μ_o, also called the permeability of free space, is defined as $4\pi \times 10^{-7}$ N·s^2·C^{-2}. Similar to the permittivity of a medium, the permeability of a medium is

$$\mu = \mu_r \mu_o, \tag{B.13}$$

where μ_r is the relative permeability. The general solution is found using Equation B.13 and assuming the current in Equation B.12 is non-uniform, yielding

$$\oint_C \mathbf{B} \cdot d\mathbf{l} = \mu \iint_A \mathbf{J} \cdot d\mathbf{S}, \tag{B.14}$$

where $\mathbf{J}$ is the current density (per unit area) and $d\mathbf{S}$ is the incremental normal vector of the surface. Although this is true for a closed loop, this equation breaks down when a capacitor is charged, for example. In this case, the current through the capacitor is zero, resulting in no magnetic field. However, in practice, there is a magnetic field between the capacitor plates. The electric field, E, on a capacitor plate is

$$E = \frac{Q}{\epsilon A} \tag{B.15}$$

where Q is the charge and A is the plate area. Rearranging and taking the time derivative yields

$$\epsilon \frac{\partial E}{\partial t} = \frac{i}{A} \tag{B.16}$$

which was contributed by Maxwell. This led to the definition of the current density vector, $\mathbf{J}$,

$$\mathbf{J} \equiv \epsilon \frac{\partial \mathbf{E}}{\partial t} \tag{B.17}$$

describing a time change in an electric field. As a result, Ampere's Circuital Law was then restated to

$$\oint_C \mathbf{B} \cdot d\mathbf{l} = \mu \iint_A \left(\epsilon \frac{\partial \mathbf{E}}{\partial t} + \mathbf{J} \right) \cdot d\mathbf{S} \tag{B.18}$$

which is similar to Faraday's Induction Law, but showing that a time varying electric field has a associated magnetic field. This occurs even in the absence of a current in the loop.

B.5 Integral Form

The simplest form of Maxwell's Equations is when the charge density distribution, ρ, and the current density vector, $\mathbf{J}$ are zero. Thus, the four basic equations in integral form are

$$\oint_C \mathbf{E} \cdot d\mathbf{l} = -\iint_A \frac{\partial \mathbf{B}}{\partial t} \cdot d\mathbf{S}, \tag{B.19}$$

$$\oint_C \mathbf{B} \cdot d\mathbf{l} = \mu\epsilon \iint_A \frac{\partial \mathbf{E}}{\partial t} \cdot d\mathbf{S}, \tag{B.20}$$

$$\oint\!\!\oint_A \mathbf{E} \cdot d\mathbf{S} = 0, \quad \text{and} \tag{B.21}$$

$$\oint\!\!\oint_A \mathbf{B} \cdot d\mathbf{S} = 0. \tag{B.22}$$

B.6 Differential Form

To transfer Maxwell's equations to a vector or differential form form, Gauss's Divergence Theorem and Stoke's Theorem are used. The Gauss Divergence Theorem,

$$\oiint_A \mathbf{F} \cdot d\mathbf{S} = \iiint_V \nabla \cdot \mathbf{F} dV, \tag{B.23}$$

states that a net change in energy across a surface boundary enclosing a specific volume is a result of a change in energy density within the area. Stoke's Theorem,

$$\oint_C \mathbf{F} \cdot d\mathbf{l} = \iint_A \nabla \times \mathbf{F} \cdot d\mathbf{S}, \tag{B.24}$$

states that the line integral of a vector field of a bounded surface is equal to the surface integral curl of the vector field. The gradient, divergence, and curl of a vector are needed to finish the derivation of Maxwell's equations in differential form. For a vector, $\mathbf{F}(x, y, z)$, the gradient, divergence, and curl are

$$\text{grad}\,(\mathbf{F}) \equiv \nabla \mathbf{F} = \frac{\partial \mathbf{F}}{\partial x}\vec{i} + \frac{\partial \mathbf{F}}{\partial y}\vec{j} + \frac{\partial \mathbf{F}}{\partial z}\vec{k}, \tag{B.25}$$

$$\text{div}\,(\mathbf{F}) \equiv \nabla \cdot \mathbf{F} = \frac{\partial \mathbf{F}_x}{\partial x} + \frac{\partial \mathbf{F}_y}{\partial y} + \frac{\partial \mathbf{F}_z}{\partial z}, \quad \text{and} \tag{B.26}$$

$$\text{curl}\,(\mathbf{F}) \equiv \nabla \times \mathbf{F} = \begin{bmatrix} \vec{i} & \vec{j} & \vec{k} \\ \frac{\partial}{\partial x} & \frac{\partial}{\partial y} & \frac{\partial}{\partial z} \\ \mathbf{F}_x & \mathbf{F}_y & \mathbf{F}_z \end{bmatrix}. \tag{B.27}$$

When Stoke's Theorem (Equation B.24) is applied to the Faraday Induction Law (Equation B.7)

$$\oint_C \mathbf{E} \cdot d\mathbf{l} = \iint_A \nabla \times \mathbf{E} \cdot d\mathbf{S} = -\iint_A \frac{\partial \mathbf{B}}{\partial t} \cdot d\mathbf{S}, \tag{B.28}$$

the curl of the electric field and the time-varying magnetic field are integrated over the same area. It follows that

$$\nabla \times \mathbf{E} = -\frac{\partial \mathbf{B}}{\partial t}. \tag{B.29}$$

Applying Stoke's Theorem in a similar fashion to Ampere's Circuital Law (Equation B.18) yields

$$\nabla \times \mathbf{B} = \mu\left(\epsilon\frac{\partial \mathbf{E}}{\partial t} + \mathbf{J}\right). \tag{B.30}$$

Applying Gauss's Divergence Theorem (Equation B.23) to his Law for electricity (Equation B.9) results in

$$\oiint_A \mathbf{E} \cdot d\mathbf{S} = \iiint_V \nabla \cdot \mathbf{E} dV = \frac{1}{\epsilon}\iiint_V \rho dV, \tag{B.31}$$

and similarly for his Law for magnetism (Equation B.11)

$$\oiint_A \mathbf{B} \cdot d\mathbf{S} = \iiint_V \nabla \cdot \mathbf{B} dV = 0. \tag{B.32}$$

As with integrating over the same area with Stoke's Theorem, the integration of Equations B.31 and B.32 over the same in volume results in

$$\nabla \cdot \mathbf{E} = \frac{\rho}{\epsilon} \quad \text{and} \tag{B.33}$$

$$\nabla \cdot \mathbf{B} = 0. \tag{B.34}$$

Once again, if the current and charge distribution densities are both zero, then Maxwell's Equations in differential form are

$$\nabla \times \mathbf{E} = -\frac{\partial \mathbf{B}}{\partial t}, \tag{B.35}$$

$$\nabla \times \mathbf{B} = \mu\epsilon \frac{\partial \mathbf{E}}{\partial t}, \tag{B.36}$$

$$\nabla \cdot \mathbf{E} = 0 \quad \text{and} \tag{B.37}$$

$$\nabla \cdot \mathbf{B} = 0. \tag{B.38}$$

Appendix C

Material Property Tables

The following tables were used in Chapter 2 for the thermomechanical sample model.

Table C.1: *Alumina (99.5%) material properties used for phase uncertainty and thermomechanical model.*

Property	Symbol	Nominal Value	Uncertainty
CTE	α	8.4 $\mu m \cdot m^{-1} \cdot K^{-1}$	84 $nm \cdot m^{-1} \cdot K^{-1}$
Elastic Modulus	E	375 GPa	3.8 GPa
Poisson's Ratio	ν	0.22	0.02
Thermal Conductivity	k	35 $W \cdot m^{-1} \cdot K^{-1}$	-
Thermal Resistance	R_{th}	0.043 $K \cdot W^{-1}$	-
Specific Heat	C_p	880 $J \cdot kg^{-1} \cdot K^{-1}$	-
Density	ρ	3890 $kg \cdot m^{-3}$	-
Thermal Capacitance	C_{th}	46.21 $J \cdot K^{-1}$	-
Thermal Time Constant	τ	1.99 s	
Thermal Bandwidth	f_T	0.08 Hz	
Expansion Rate	$\dot{z}_{CTE}$	1.0 $nm \cdot s^{-1}$	

Table C.2: *Aluminum 7075-T6 material properties used for phase uncertainty and thermomechanical model.*

Property	Symbol	Nominal Value	Uncertainty
CTE	α	23.5 $\mu m \cdot m^{-1} \cdot K^{-1}$	235 $nm \cdot m^{-1} \cdot K^{-1}$
Elastic Modulus	E	72 GPa	0.7 GPa
Poisson's Ratio	ν	0.33	0.03
Thermal Conductivity	k	130 $W \cdot m^{-1} \cdot K^{-1}$	-
Thermal Resistance	R_{th}	0.011 $K \cdot W^{-1}$	-
Specific Heat	C_p	960 $J \cdot kg^{-1} \cdot K^{-1}$	-
Density	ρ	2730 $kg \cdot m^{-3}$	-
Thermal Capacitance	C_{th}	35.38 $J \cdot K^{-1}$	-
Thermal Time Constant	τ	0.389 s	
Thermal Bandwidth	f_T	0.41 Hz	
Expansion Rate	$\dot{z}_{CTE}$	15.1 $nm \cdot s^{-1}$	

Table C.3: *BK7 material properties used for phase uncertainty and thermomechanical model.*

Property	Symbol	Nominal Value	Uncertainty
CTE	α	4.5 $\mu m \cdot m^{-1} \cdot K^{-1}$	45 $nm \cdot m^{-1} \cdot K^{-1}$
Elastic Modulus	E	65 GPa	0.7 GPa
Poisson's Ratio	ν	0.19	0.02
Thermal Conductivity	k	1 $W \cdot m^{-1} \cdot K^{-1}$	-
Thermal Resistance	R_{th}	1.5 $K \cdot W^{-1}$	-
Specific Heat	C_p	800 $J \cdot kg^{-1} \cdot K^{-1}$	-
Density	ρ	2350 $kg \cdot m^{-3}$	-
Thermal Capacitance	C_{th}	25.38 $J \cdot K^{-1}$	-
Thermal Time Constant	τ	38.1 s	
Thermal Bandwidth	f_T	0.004 Hz	
Expansion Rate	$\dot{z}_{CTE}$	0.03 $nm \cdot s^{-1}$	

Table C.4: *Fused Silica material properties used for phase uncertainty and thermomechanical model.*

Property	Symbol	Nominal Value	Uncertainty
CTE	α	0.55 $\mu m \cdot m^{-1} \cdot K^{-1}$	6 $nm \cdot m^{-1} \cdot K^{-1}$
Elastic Modulus	E	70 GPa	0.7 GPa
Poisson's Ratio	ν	0.17	0.02
Thermal Conductivity	k	1.38 $W \cdot m^{-1} \cdot K^{-1}$	-
Thermal Resistance	R_{th}	1.09 $K \cdot W^{-1}$	-
Specific Heat	C_p	740 $J \cdot kg^{-1} \cdot K^{-1}$	-
Density	ρ	2200 $kg \cdot m^{-3}$	-
Thermal Capacitance	C_{th}	21.98 $J \cdot K^{-1}$	-
Thermal Time Constant	τ	30.3 s	
Thermal Bandwidth	f_T	0.005 Hz	
Expansion Rate	$\dot{z}_{CTE}$	0.006 $nm \cdot s^{-1}$	

Table C.5: *Invar material properties used for phase uncertainty and thermomechanical model.*

Property	Symbol	Nominal Value	Uncertainty
CTE	α	1.05 $\mu m \cdot m^{-1} \cdot K^{-1}$	10 $nm \cdot m^{-1} \cdot K^{-1}$
Elastic Modulus	E	140 GPa	1.4 GPa
Poisson's Ratio	ν	0.21	0.02
Thermal Conductivity	k	22.5 $W \cdot m^{-1} \cdot K^{-1}$	-
Thermal Resistance	R_{th}	0.067 $K \cdot W^{-1}$	-
Specific Heat	C_p	487 $J \cdot kg^{-1} \cdot K^{-1}$	-
Density	ρ	8000 $kg \cdot m^{-3}$	-
Thermal Capacitance	C_{th}	52.6 $J \cdot K^{-1}$	-
Thermal Time Constant	τ	3.16 s	
Thermal Bandwidth	f_T	0.05 Hz	
Expansion Rate	$\dot{z}_{CTE}$	0.075 $nm \cdot s^{-1}$	

Table C.6: *Silicon Carbide material properties used for phase uncertainty and thermomechanical model.*

Property	Symbol	Nominal Value	Uncertainty
CTE	α	4.4 $\mu m \cdot m^{-1} \cdot K^{-1}$	45 $nm \cdot m^{-1} \cdot K^{-1}$
Elastic Modulus	E	410 GPa	4.1 GPa
Poisson's Ratio	ν	0.21	0.02
Thermal Conductivity	k	150 $W \cdot m^{-1} \cdot K^{-1}$	-
Thermal Resistance	R_{th}	0.01 $K \cdot W^{-1}$	-
Specific Heat	C_p	800 $J \cdot kg^{-1} \cdot K^{-1}$	-
Density	ρ	3150 $kg \cdot m^{-3}$	-
Thermal Capacitance	C_{th}	34.02 $J \cdot K^{-1}$	-
Thermal Time Constant	τ	0.34 s	
Thermal Bandwidth	f_T	0.47 Hz	
Expansion Rate	$\dot{z}_{CTE}$	3.2 $nm \cdot s^{-1}$	

Table C.7: *18-8 Stainless Steel material properties used for phase uncertainty and thermomechanical model.*

Property	Symbol	Nominal Value	Uncertainty
CTE	α	16.6 $\mu m \cdot m^{-1} \cdot K^{-1}$	166 $nm \cdot m^{-1} \cdot K^{-1}$
Elastic Modulus	E	193 GPa	1.9 GPa
Poisson's Ratio	ν	0.305	0.03
Thermal Conductivity	k	16.3 $W \cdot m^{-1} \cdot K^{-1}$	-
Thermal Resistance	R_{th}	0.092 $K \cdot W^{-1}$	-
Specific Heat	C_p	500 $J \cdot kg^{-1} \cdot K^{-1}$	-
Density	ρ	7890 $kg \cdot m^{-3}$	-
Thermal Capacitance	C_{th}	53.26 $J \cdot K^{-1}$	-
Thermal Time Constant	τ	4.90 s	
Thermal Bandwidth	f_T	0.032 Hz	
Expansion Rate	$\dot{z}_{CTE}$	0.85 $nm \cdot s^{-1}$	

Table C.8: *Titanium (Grade 5) material properties used for phase uncertainty and thermomechanical model.*

Property	Symbol	Nominal Value	Uncertainty
CTE	α	9 $\mu m \cdot m^{-1} \cdot K^{-1}$	90 $nm \cdot m^{-1} \cdot K^{-1}$
Elastic Modulus	E	110 GPa	1.1 GPa
Poisson's Ratio	ν	0.34	0.03
Thermal Conductivity	k	7.2 $W \cdot m^{-1} \cdot K^{-1}$	-
Thermal Resistance	R_{th}	0.21 $K \cdot W^{-1}$	-
Specific Heat	C_p	565 $J \cdot kg^{-1} \cdot K^{-1}$	-
Density	ρ	4420 $kg \cdot m^{-3}$	-
Thermal Capacitance	C_{th}	33.71 $J \cdot K^{-1}$	-
Thermal Time Constant	τ	7.08 s	
Thermal Bandwidth	f_T	0.022 Hz	
Expansion Rate	$\dot{z}_{CTE}$	0.32 $nm \cdot s^{-1}$	

Table C.9: *Zerodur® material properties used for phase uncertainty and thermomechanical model.*

Property	Symbol	Nominal Value	Uncertainty
CTE	α	0.07 $\mu m \cdot m^{-1} \cdot K^{-1}$	10 $nm \cdot m^{-1} \cdot K^{-1}$
Elastic Modulus	E	90 GPa	0.9 GPa
Poisson's Ratio	ν	0.24	0.03
Thermal Conductivity	k	1.46 $W \cdot m^{-1} \cdot K^{-1}$	-
Thermal Resistance	R_{th}	1.03 $K \cdot W^{-1}$	-
Specific Heat	C_p	800 $J \cdot kg^{-1} \cdot K^{-1}$	-
Density	ρ	2530 $kg \cdot m^{-3}$	-
Thermal Capacitance	C_{th}	27.32 $J \cdot K^{-1}$	-
Thermal Time Constant	τ	28.1 s	
Thermal Bandwidth	f_T	0.006 Hz	
Expansion Rate	$\dot{z}_{CTE}$	0.0004 $nm \cdot s^{-1}$	

Appendix D

Periodic Error Modeling

As discussed previously in Chapter 3, two types of periodic error algorithms are typically employed in displacement interferometry applications. The first type of algorithm is a periodic error measurement algorithm and the second type is a algorithm that measures and corrections period error. While many of these algorithms have been described in literature, there is very little cross comparison between algorithms. This research was performed to establish a baseline cross comparison between algorithms. Two example data sets, one with constant velocity and one with constant acceleration are used to characterize the effectiveness of each algorithm. Following that, the two correction algorithms are applied to a practical situation simulating the overlap errors in a lithography system due to periodic error.

D.1 Example Dataset Generation

Two different data sets have been generated to demonstrate the effectiveness of each algorithm. One dataset assumes a constant velocity of 13 $\mu m \cdot s^{-1}$, which is a constant Doppler frequency shift of 41.3 Hz. The other dataset assumes a constant acceleration of 20 $\mu m \cdot s^{-2}$. In both cases, a single pass interferometer was assumed. The heterodyne frequency was 1 kHz and the phase change from displacement was simulated over 1 second with 9600 data points, which is divisible by 320, specifically needed by one compensation algorithm to work properly. A lock-in amplifier based measurement technique, shown in Figure D.1, was used to simulate quadrature signals, and ultimately, obtain the phase.

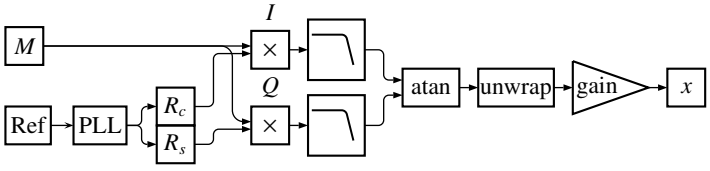

Figure D.1: *Schematic of the lock-in amplifier used to generate the simulated signals. Instead of a signal reference signal (Ref) and phase locked loop as used in normal systems, digital sine and cosine signals were generated as the two reference signals.*

The split frequency, velocity, and acceleration values were chosen to simplify the computation time rather than performing the simulations using a megahertz level split frequency and higher velocities. Also, since this is theoretical research, the phase locked loop is not necessary for generating the matched sine and cosine pairs. The two digital reference signals created

$$R_c = \cos(2\pi f_s t) \quad \text{and} \tag{D.1}$$

$$R_s = \sin(2\pi f_s t), \tag{D.2}$$

where f_s is the heterodyne frequency. The measurement signal with periodic errors was

$$M = \Gamma_0 \cos(2\pi f_s t + \phi_x) + \Gamma_1 \cos(2\pi f_s t) + \Gamma_2 \cos(2\pi f_s t - \phi_x) \tag{D.3}$$

where

$$\phi_x = \frac{2\pi x N}{\lambda} \tag{D.4}$$

and Γ_0 is the nominal signal amplitude, Γ_1 is the first order periodic error coefficient, Γ_2 is the second order periodic error coefficient, x is the displacement, N is the optical resolution (2), and λ is the laser wavelength (632.8 nm) [35]. For these data sets, Γ_0, Γ_1 and Γ_2 were 1, 0.026, and 0.019, respectively. Essentially, the reference sine and cosine signals are individually multiplied with the measurement signal, creating two mixed signals. The high frequency component of each signal is filter with the same two pole, low pass Butterworth filter with a cutoff frequency of 200 Hz. Finally, the phase is determined by unwrapping an arctangent function performed on the two signals. Figure D.2 shows the two generated data sets after dropping the first 1600 data points due to the initial filter effects and removing DC offsets.

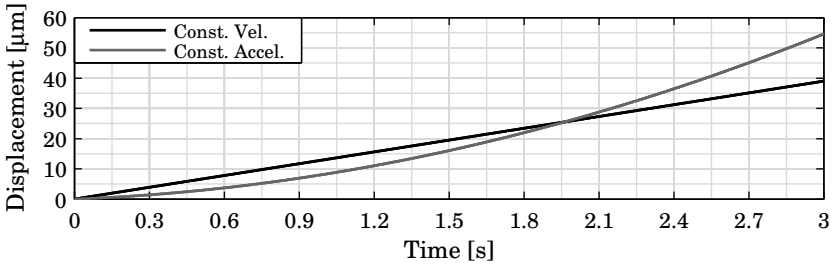

Figure D.2: *Simulated displacement of the two sample data sets. The one dataset assumes a constant velocity of 13 $\mu m \cdot s^{-1}$ and the other assumes a constant acceleration of 20 $\mu m \cdot s^{-2}$. These data sets have an initial section removed due to initial filter effects.*

D.2 Periodic Error Measurement Algorithms

There are two typical algorithms used to measure the presence of periodic errors: a single sided Fourier amplitude spectrum and a Fourier peak separation. In these two algorithms, the periodic error value is measured but cannot be corrected. To correct periodic errors, three

typical algorithms are: the Lissajous fit, the Continuous Elliptical Compensation, and the Chu-Ray algorithm. The Lissajous Fit can correct for periodic errors but does not explicitly measure the periodic error value. Thus, the single sided Fourier amplitude spectrum is needed in conjunction with this algorithm to fully measure and correct periodic errors. The Continuous Elliptical Compensation is based on a Lissajous fitting technique, however, it has addition components making it suitable for continuous correction and updating in real-time. The third algorithm, the Chu-Ray, is an algorithm that can measure and correct for periodic errors and is designed to be implemented in real-time.

In the following sections, each of theses algorithms is briefly described and are implemented on the two previously described example data sets. Following those sections, a brief summary and comparison between algorithms is discussed.

D.2.1 Single Sided Fourier Amplitude Spectrum

The single sided Fourier amplitude spectrum is arguably the simplest method to measure periodic errors if the measured phase is supposed to be linear. Once the unwrapped phase is measured, the measured displacement, x, can be determined by Equation D.4. A best-fit, low-order polynominal fit, x_{fit} is then determined using a least squares approximation. Then, the residual error, x_e, is determined by taking the difference between the measured data and the polynominal fit. Since this algorithm assumes a constant sampling time and a linear displacement, the linear fit can be used to determine the fringe passing frequency, f_f. First, the estimated displacement in fringes[1] is determined by

$$\mathrm{f} = \frac{N x_{fit}}{\lambda}, \tag{D.5}$$

which is essentially taking the fitted displacement and dividing by the fringe spacing (λ/N). The fringe passing frequency[2] is then calculated by

$$f_\mathrm{f} = \left| \frac{n}{\sum_{i=2}^{n} (\mathrm{f}_i - \mathrm{f}_{i-1})} \right|, \tag{D.6}$$

where n is the number data points in x_{fit}. For the constant velocity sample dataset, f_f is 121.7 points per fringe. A single sided Fourier analysis is then applied to the residual error, x_e, where the time domain data is transferred to the frequency domain. The frequency values from the single sided Fourier analysis must be appropriately scaled using f_f.

D.2.2 Fourier Peak Separation

Another periodic nonlinearity measurement technique uses peak separation in the Fourier domain to measure the first and second order periodic nonlinearity [35]. Similar to the single sided Fourier analysis, the Fourier peak separation is intended for situations where the velocity is constant. From Equation D.3, measured interference signal contains three different frequency components $(f_s + f_d)$, (f_s), and $(f_s - f_d)$, where f_s is the nominal

[1] A fringe in this analysis is defined as the normalized displacement causing a 2π phase change in the measured signal. As the phase changes from 0 to 2π, the displacement in fringes is 0 to 1.

[2] The units of fringe passing frequency is points per fringe of displacement. This is akin to frequency but rather than based on time, this is based on length.

heterodyne frequency and f_d is the measured frequency shift due the Doppler frequency. When the Doppler frequency is constant from a constant velocity motion, the amplitudes of the three peaks in the frequency domain are used to determine the amount of periodic nonlinearity.

From Vivek and Patterson [35], the maximum phase error from the first order periodic nonlinearity occurs when

$$\phi_{e,1} \approx \frac{\Gamma_1}{\Gamma_0} \sin(\Delta\phi_x). \tag{D.7}$$

Likewise, the maximum second order periodic nonlinearity occurs when

$$\phi_{e,2} \approx \frac{\Gamma_2}{\Gamma_0} \sin(2\Delta\phi_x). \tag{D.8}$$

In both cases, it is assumed the first and second order periodic error amplitudes are much smaller than the nominal signal amplitude ($\Gamma_0 \gg \Gamma_1, \Gamma_2$). The total first and second order periodic nonlinearity values can then be determined by

$$L_{e,1} = \text{range}\left(\frac{\phi_{e,1}\lambda}{4\pi N}\right) \quad \text{and} \tag{D.9}$$

$$L_{e,2} = \text{range}\left(\frac{\phi_{e,2}\lambda}{4\pi N}\right), \quad \text{where} \tag{D.10}$$

$$\text{range}(\text{A}) = \max(\text{A}) - \min(\text{A}). \tag{D.11}$$

Figure D.3 shows the peak separation for the constant velocity dataset which has calculated periodic errors of 2.0 nm and 1.1 nm, first and second order, respectively. This differs slightly from single sided amplitude spectrum results (1.9 nm and 0.9 nm, respectively).

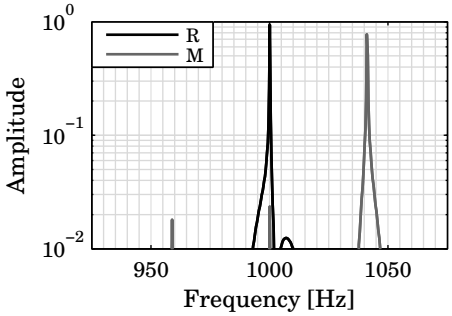

Figure D.3: *Peak separation in the frequency domain from the original measurement signal (M) and one of the reference signals (R_c). The measurement signal splits into three different peak, which (left to right) are the main measurement signal, first order error, and second order error. The magnitude of peaks is then used to determine the periodic error amplitude.*

D.2.3 Lissajous Compensation

Lissajous compensation involves fitting an ellipse to the quadrature outputs of a lock-in amplifier and using those fitted parameters to correct the data post-process. As

shown shortly, this process is computationally difficult but could be suitable for stability measurements because only measurement, not control is necessary. This means the corrected data does not need to be generated in real-time.

From Figure D.1, the measurement signal is multiplied by a sine and a cosine signal with the same frequency in the lock-in amplifier. After the two multipliers, the two signals are

$$I = \cos(2\pi f_s t)\left[\Gamma_0 \cos(2\pi f_s t + \phi_x) + \Gamma_1 \cos(2\pi f_s t) + \Gamma_2 \cos(2\pi f_s t - \phi_x)\right] \quad \text{and} \tag{D.12}$$

$$Q = \sin(2\pi f_s t)\left[\Gamma_0 \cos(2\pi f_s t + \phi_x) + \Gamma_1 \cos(2\pi f_s t) + \Gamma_2 \cos(2\pi f_s t - \phi_x)\right]. \tag{D.13}$$

These signals are then low pass filtered, which simplify to

$$I = \frac{1+\Gamma_2}{2}\cos(\phi_x) + \frac{\Gamma_1}{2} \quad \text{and} \tag{D.14}$$

$$Q = -\frac{1-\Gamma_2}{2}\sin(\phi_x), \tag{D.15}$$

where Γ_1 and Γ_2 are the first and second order periodic error coefficients [36]. When no periodic errors are present, plotting I versus Q results in a circle, as shown in Figure D.4a. However, when periodic errors are present, the plot of I versus Q results in a tilted ellipse, also shown in Figure D.4a. The general form of Equations D.14 and D.15, including errors from the lock-in amplifier technique are

$$I_g = a\cos(\phi_x + \varphi) + I_o \quad \text{and} \tag{D.16}$$

$$Q_g = b\sin(\phi_x) + Q_o, \tag{D.17}$$

where a, b, φ, I_o, and Q_o are all fitted parameters. These parameters are shown in Figure D.4b in conjunction with the tilted ellipse.

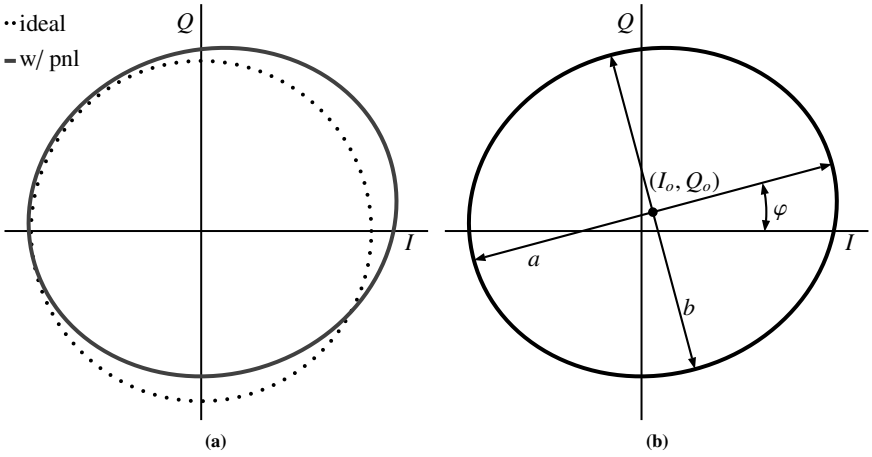

Figure D.4: *(a) Residual error for the original and Lissajous compensated linear dataset after detrending. (b) Frequency domain analysis of (a) where the Lissajous shows no second order periodic error and the first order periodic error is half the amplitude.*

One way to solve for these parameters is to employ a least squares approximation to a generalized ellipse in conic form. Once those parameters are determined from the least

squares fit, the parameters from Equations D.16 and D.17 can be determined. The fitting process involves many computation steps and transformations. Table D.1 shows the fitted parameters for the two data sets from Equations D.16 and D.17. Although the input periodic

Table D.1: *Lissajous fit parameters for the two data sets.*

Parameter	Linear Dataset	Nonlinear Dataset
a	0.347	0.452
b	0.341	0.453
φ [rad]	0.033	0.057
I_o	0.011	-0.013
Q_o	0.0065	-0.030

error amplitudes, Γ_1 and Γ_2 are the same for both data sets, the filtering and delay changes cause errors between the respective fitting parameters. Once the Lissajous fit parameters are determined, compensated phase from Eom, *et al.* [36] is

$$\phi_c = \arctan\left(\frac{\cos(\varphi)}{\sin(\varphi) + \frac{b(I-I_o)}{a(Q-Q_o)}}\right), \tag{D.18}$$

D.2.4 Continuous Elliptical Compensation

The continuous elliptical compensation technique is an extension of the Lissajous compensation technique. This algorithm, also by Eom, *et al.* [40], is designed to use an occasional Lissajous fit on the data to continuously corrects for periodic error. This technique has several advantages because it can be used to update data in real time and the algorithm can adjust to changing periodic error. However, this technique still uses the same time consuming Lissajous fitting technique to determine the periodic error coefficients.

The principle of the algorithm is the same as with the Lissajous fit. The quadrature signals obtained from the lock-in amplifier are modified using fitted parameters to correct for periodic errors. One of the quadrature signals is corrected using a multiplier determined after obtaining the initial Lissajous fit paramters (a, b, and φ). The multiplier constant, V, is calculated by

$$V = \frac{10a}{b}\sin(\varphi) + 5. \tag{D.19}$$

Once the multiplier constant is determined, one of the quadrature signals, I, can be corrected by

$$I_c = \frac{b\Big((0.1V - 0.5)\,Q + I\Big)}{a\cos(\varphi)}, \tag{D.20}$$

where I_c is the corrected quadrature signal and I and Q are the original quadrature signals. The corrected length, L_c, is then determined by

$$L_c = \frac{\lambda}{2\pi N}\arctan\left(\frac{I_c}{Q}\right). \tag{D.21}$$

where the corrected length, L_c, is then calculated by $\frac{\lambda\phi_c}{2\pi N}$. In these calculations, the fitting and compensation algorithm was implemented in Matlab. The first 320 data points of I and Q were used to determine the fitting parameters and the multiplier constant V and the compensated quadrature signal I_c. The phase was then calculated using I_c and Q. The algorithm then proceeds to the next set of 320 data points, where a new V is determined, along with a new compensated quadrature signal I_c. This proceeds until the data set is complete, where a matrix of phase data is used to determine the compensated length. The phase is then unwrapped and multiplied by a constant to determine the compensated length.

As with the original Lissajous compensation, the continuous elliptical compensation needs an additional measurement algorithm to determine the periodic errors. Once again the single sided Fourier amplitude spectrum is used on L_c to determine the periodic errors.

D.2.5 Chu-Ray Algorithm

The Chu-Ray algorithm [41] is designed to correct for periodic errors in real-time using simple look-up tables and shift registers which can be implemented using a field programmable gate array (FPGA). The algorithm is not explained in detail here, however, the reader is directed authors' original papers [41, 62].

In summary, over relatively short displacements (several fringes) for relatively smooth displacements, the length change can be described by

$$\Delta L = Ax^2 + Bx + C + \alpha_1 \cos(2\pi\phi_x) + \beta_1 \sin(2\pi\phi_x) + \alpha_2 \cos(4\pi\phi_x) + \beta_2 \sin(4\pi\phi_x), \quad \text{(D.22)}$$

where x is the measured displacement from the phase, A, B, and C are polynomal coefficients for the overall motion profile, ϕ_x is the measured phase, $\alpha_{1,2}$ are the amplitude coefficients for the first and second order cosine fit, and $\beta_{1,2}$ are the amplitude coefficients for the first and second order sine fit. Since Equation D.22 has seven unknown parameters that must be determined, this is cumbersome to solve in real-time. However, Equation D.22 can be simplified into two separate equations, each with the same form with only five terms; three terms for the gross displacement and two terms for the periodic error compensation. Then, the algorithm can be simplified to operate in real-time.

The algorithm takes the first 320 data points and compensates for the first order periodic error. During the next 320 data points, the original 320 data points are further compensated for the second order periodic error, while the current 320 data points are corrected for the first order periodic error. Thus, there is a lag of 640 data points before the algorithm is compensating for both first and second order periodic errors. Additionally, the displacement during the 320 data points must be greater than one fringe, otherwise, the previous compensation values are used and the current ones are discarded.

D.2.6 Simulation Results

Figure D.5a shows the residual error as a function of fitted fringes for the original constant velocity data set and the residual error after compensating using the Lissajous fit, continuous elliptical compensation, and the Chu-Ray algorithm. The residual error from the original displacement is 4.5 nm pk-pk, resulting from 1.9 nm first order error and 0.9 nm second order error. This is closely matched to the periodic error determined by the Fourier peak analysis, showing 2.0 nm and 1.1 nm, respectively.

The residual error after performing the Lissajous fit showed the the first order error decreased to 0.9 nm and the second order error was largely eliminated, as showing in Figure D.5a. The Chu-Ray algorithm and the continuous elliptical compensation both showed significant improvement over the original residual error. The Chu-Ray algorithm shows the two steps needed for full compensation, whereas the continuous elliptical compensation showed a low amplitude, high frequency error which can be reduces with a models low pass filter.

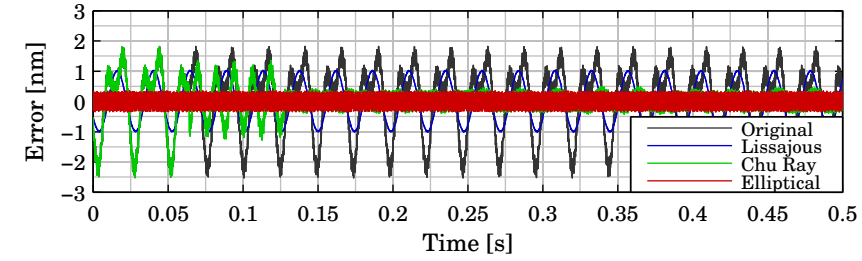

(a)

(b)

Figure D.5: *(a) Residual error after removing the best fit linear line from the original, Lissajous fitted, continuous elliptical compensation, and Chu-Ray algorithm data. The periodic error is significantly reduced for the Chu-Ray and Elliptical compensation algorithms. (b) Single sided Fourier amplitude spectrum of the residual error in (a). The continuous elliptical compensation amplitude is well below the 10 pm amplitude limit of the plot.*

The single sided amplitude spectrum showed a significant reduction in periodic nonlinearity from the original data set. The peaks using the Chu-Ray algorithm are less well defined and have less amplitude. The peaks in the continuous elliptical compensation were significantly lower and are below the 10 pm threshold in Figure D.6.

When the motion is nonlinear, as is in the constant acceleration data sets, the residual error shows some slight differences from the linear example. The residual error for the original constant acceleration data set and after compensating with the three algorithms is shown in Figure D.6. The original data set shows the same periodic nonlinearity as in the linear example. The Lissajous fit shows a slight reduction in amplitude at low frequencies but the amplitude increases to higher amplitudes as the velocity increases. Also, there is an overall waviness or low-frequency component which is not in the original signal. This

is due to an imperfect fit because of the near zero velocity at the start of the simulation. The Chu-Ray algorithm and continuous elliptical compensation show similar trends to their previous linear example.

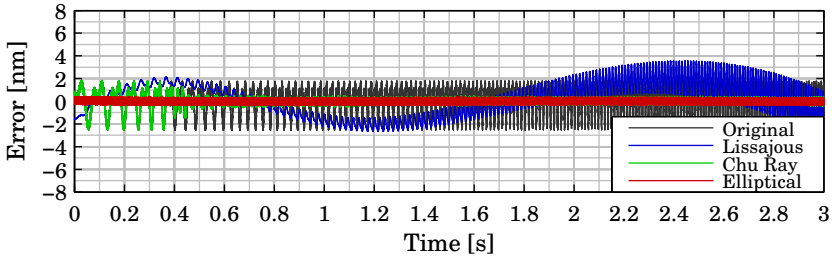

Figure D.6: *Residual error after removing the best fit, second order polynomial from the original constant acceleration data set and after correcting using the Lissajous fit, the continuous elliptical compensation, and the Chu-Ray algorithm.*

D.2.7 Simulations for High Speed Stages

In lithography systems, the image overlay error between the mask and the wafer is a critical parameter to reduce. Reducing the overlay error between subsequent layers in a chip means smaller linewidths can be achieved and more functions can be placed with a higher density. In this research, the effect of periodic nonlinearity in interferometers and the overall optical design on the overlay error used for feedback on the wafer stages was investigated and estimated. Two different measure-and-correct algorithms were simulated for characterizing and compensating the periodic nonlinearity under estimated operating conditions. Also, interferometer design parameters such as heterodyne split frequency and sampling frequency are considered.

The simulation parameters were estimated from a lithography tool projecting a 26 mm wide slit and scanning a distance of 33 mm at a constant speed of 600 mm/s and a maximum stage acceleration of 35 m/s^2. At this velocity and acceleration, the wafer stage has a position and velocity profile similar to the profile shown in Figure D.7, where two consecutive dies scans are shown. In these simulations, a four pass Michelson plane mirror interferometer is used to measure the displacement. A schematic of the interferometer and electronics is shown in Figure D.8. The measurement and reference signals are sent to a digital lock-in amplifier to measure the phase. Both signals are band-pass filtered to remove aliasing and DC intensity fluctuations. Matching sine and cosine signals are generated from the reference signal using a phase locked loop. Two multipliers are used, mixing a sine and a cosine reference signal with the measured signal. Low pass filters remove the high frequency components, generating quadrature signals (X,Y) for the continuous elliptical fit [40]. The quadrature signals are also sent to an arctangent function, which computes the phase (ϕ) after unwrapping. This is then used for the Chu-Ray compensation algorithm [41].

From Figure D.9, it is clear there are several unwanted signals in the measurement bandwidth as a function of stage velocity. If the split frequency is too low, the doppler shift

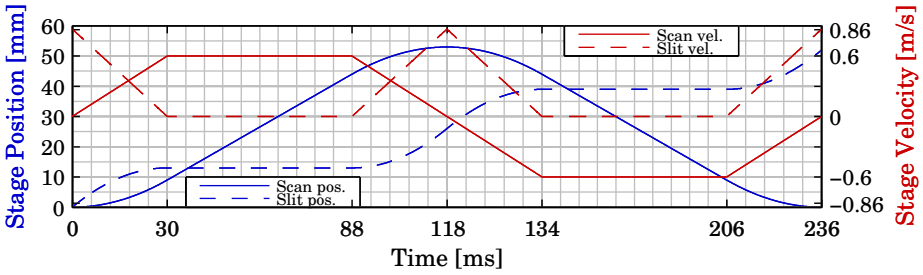

Figure D.7: *Profiles for the stage position (blue) and velocity (red) in the scanning and slit directions while scanning two consecutive dies. The slit direction is held at a constant position while the wafer is scanned.*

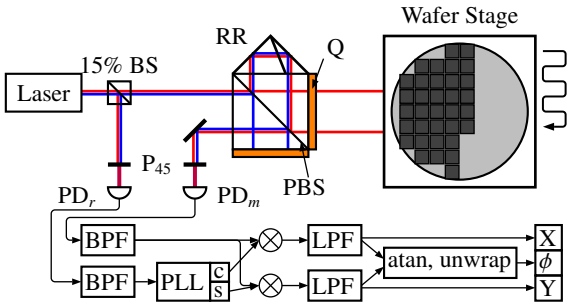

Figure D.8: *Schematic of a plane mirror interferometer measuring the wafer stage scanning motion axis (not to scale). An individual die is illuminated and then the stage shifts in the orthogonal direction, while reversing the scan direction. The signals are then sent to a digital lock-in amplifier and controller.*

induced frequency change will pass through zero frequency, causing a direction ambiguity. Additionally, when a negative doppler shift occurs, there can be multiple harmonics in the measurement bandwidth. Also, there is first and second order periodic nonlinear where the former occurs at the split frequency (f_s) and the latter is mirrored from the main frequency shift with respect to the split frequency.

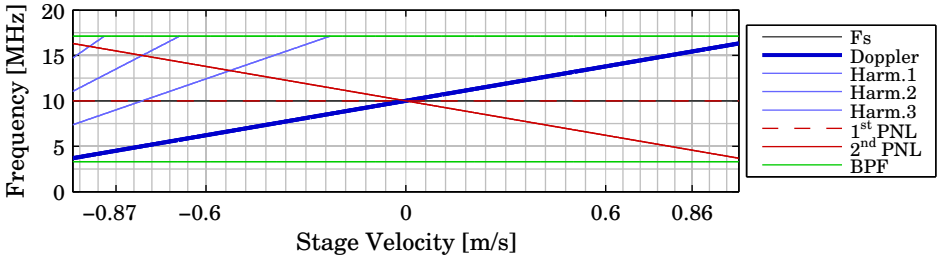

Figure D.9: *Signals in the measurement bandwidth as a function of velocity for a 10 MHz heterodyne frequency. The main measurement signal sweeps from approximately 4 MHz to 16 MHz with several harmonics and 1st and 2nd order periodic components in the measurement bandwidth.*

When determining the optical system specifications, there are several user controlled variables. The laser split frequency (f_s) can be chosen to shift the overall measurement bandwidth. The bandpass filter should be selected to limit aliasing and slow amplitude fluctuations while also accommodating the measurement frequency range. A higher sampling frequency (F_s) can be chosen with the tradeoff of less resolution (typically). The laser power can be increased to reduce noise at the detector. The periodic nonlinearity from frequency mixing should be reduced to also limit errors.

The source of periodic nonlinearity has been widely investigate and alignment techniques have been proposed for limiting periodic nonlinearity. In these simulations, the periodic errors were modeled as described by Wu [146]. Additionally, there are several algorithms for either measurement or measurement-and-correction of periodic nonlinearity. Assessing periodic nonlinearity and the interplay between other error sources and optical design parameters is important in displacement interferometry. Additionally, this investigation is simulated situations which mimic the practical application. This is particular to the controller design because the phasemeter updates at a much higher rate than the controller. A typical phasemeter must update at megahertz rates while a controller will typically run at 20 kHz with a mechanical bandwidth limit of 300 Hz. Thus, it is important to see how this downsampling will affect the measurement for the controller.

There are three main algorithms used in this investigation. The first algorithm is only used for characterizing the nonlinearity amplitude when the motion is linear. After detrending the main displacement, a single sided Fourier amplitude spectrum is calculated on the residual error. If the frequency axis is appropriately scaled for displacement (or fringes), the single sided amplitude spectrum can be used to detect the amplitude of periodic errors, either those fundamental to the interferometer or those due to stage motions. The second algorithm used is a continuous elliptical compensation algorithm by Eom, *et al.* [40], which is based on their Lissajous fitting algorithm [36]. The last algorithm used in this work is the Chu-Ray algorithm for first and second order periodic non-linearity correction [41].

Simulation Results

Simulations were performed assuming different heterodyne frequencies, different sampling rates, and varying levels of periodic nonlinearity. The complete profile from the start of the acceleration in the scan direction to half way through the scan. This was chosen because the rapid acceleration in the scan direction and deceleration in the slit direction combined with the periodic errors may affect the overall alignment. The alignment error is this paper is deviation from the ideal path assuming no periodic errors. The alignment error was determined by simulating a nominal displacement profile and also the simulated values after correcting with the two algorithms. The simulated measurements were then downsampled to 20 kHz where the offset, noise level (standard deviation), and error range was calculated.

20 MHz Split Frequency

Displacement interferometers often have a heterodyne frequency of 20 MHz because it is a high enough frequency to account for, a high stage velocity in both directions. The sampling frequency was 130 MHz, which was 5× the highest doppler frequency shift. Because the stage speed is high and the controller bandwidth is low in comparison, the direct periodic errors in the scan direction are not seen. However, there was a consistently increasing

offset as a function of periodic error amplitude, as shown in Figure D.10. The uncorrected measurements also showed significant noise and a high range of errors, although these were at frequencies much higher than the mechanical bandwidth of 300 Hz and can be reduced with proper filtering. The results are similar for the slit direction where there was little noise added from the algorithms but an increasing offset as a function of periodic error amplitude. The offset error in the slit direction was approximately half the offset error in the scan direction. In both directions, the periodic error correction algorithms reduced the noise and range of the error but did not reduce offset error. In the high periodic nonlinearity case, the correction algorithms increased this error in the slit direction.

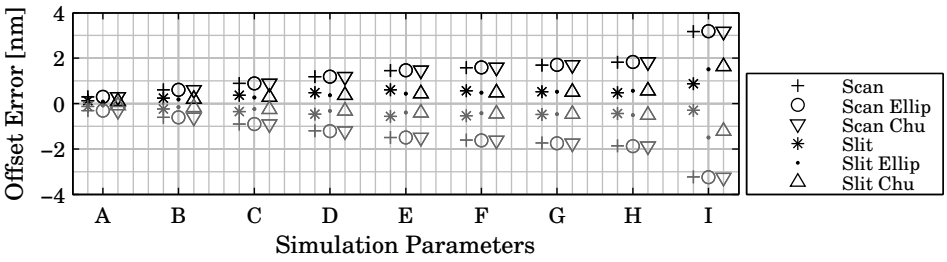

Figure D.10: *Offset error from the ideal path during illumination for the scan and slit directions assuming a 20 MHz heterodyne frequency with a 130 MHz sampling frequency. The simulations were nominally the same between positive doppler shifting (black) and negative doppler shifting (grey). In each case, the two periodic error algorithms did not compensate this offset and made the error worse for higher periodic error amplitudes.(Amplitude [nm], 1st(2nd); A, 0.25(0.1); B, 0.5(0.18); C, 0.75(0.27); D, (0.35); E, 1.25(0.45); F, 1.25(0.55); G, 1.25(0.63); H, 1.25(.73); I 2.5(1.12))*

10 MHz Split Frequency

Since the doppler frequency shift is at most 7 MHz, it is possible to use a 10 MHz heterodyne frequency without passing through zero frequency. Also, because the highest measured frequency is around 17 MHz, the requirements for the sampling frequency can be reduce 80 MHz while still having 5 points per cycle at the highest frequencies.

The same simulations for a 20 MHz heterodyne frequency were performed assuming a 10 MHz heterodyne frequency and an 80 MHz sampling rate. These results, shown in Figure D.11a, had a similar trend for the scan direction compared to the 20 MHz results. However, in the slit direction, the results has a different trend where the periodic error correction algorithms increased the offset error.

The slower split frequency also allowed for a higher sampling frequency than in the 20 MHz case. The same simulations were repeated, but this time with a sampling frequency of 112 MHz, as shown in Figure D.11b. The effect of the higher sampling frequency is quite clear in the slit direction. The uncorrected results showed a significant offset, while the corrected results show a similar trend to the previous 10 MHz case. Also, the magnitude of the offset error is slightly more with a higher sampling frequency.

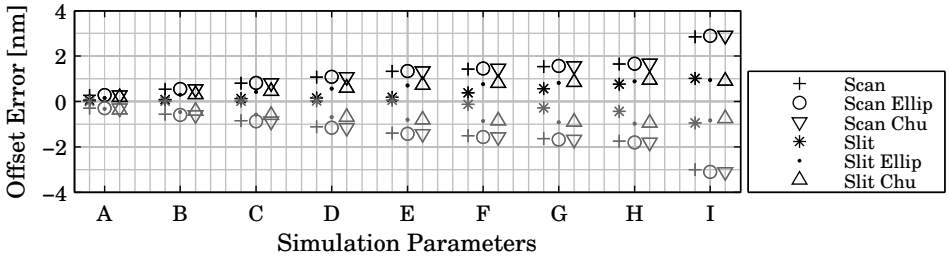

(a)

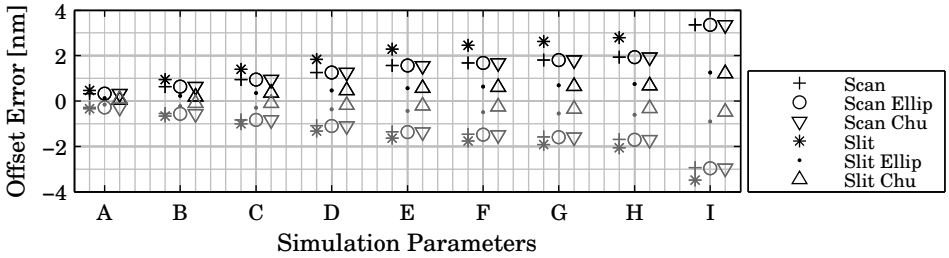

(b)

Figure D.11: *(a) Offset error from the ideal path during illumination for the scan and slit directions assuming a 10 MHz heterodyne frequency and an 80 MHz sampling rate. In the slit direction, the periodic error correction algorithms increase the offset error. (b) Offset error from the ideal path during illumination for the scan and slit directions assuming a 10 MHz heterodyne frequency and an 112 MHz sampling rate. The increased sampling frequency increased the offset error, although the periodic nonlinearity correction algorithms reduce this effect. (Amplitude [nm], 1st(2nd); A ,0.25(0.1); B, 0.5(0.18); C, 0.75(0.27); D, (0.35); E, 1.25(0.45); F, 1.25(0.55); G, 1.25(0.63); H, 1.25(.73); I 2.5(1.12))*

Preliminary Conclusions

These simulations show there is a coupled effect between the offset error and the amount of periodic nonlinearity in the measurement system. This offset error increase with increased periodic nonlinearity and will ultimately contribute uncertainty to the overlay error in the lithography tool. The difference in heterodyne frequency in the system had little effect on this offset error but the sensitivity to sampling frequency effects suggest this could an aliased or spurious signal in the desired measurement band. In these simulations, this was accounted for, thus it is not quite clear what causes this effect. In each of the simulations, both periodic nonlinearity algorithms reduced the pk-pk error and the noise level when compared to uncorrected measurements. The Chu-Ray algorithm had pk-pk errors and noise levels that were approximately twice the values obtained after correcting using the continuous elliptical fit. In most cases, the pk-pk error was less than 0.5 nm and the noise level was approximately 0.1 nm, typically the resolution of a commercial phasemeter.

D.3 Algorithm Summary

These simulations show two distinct results which are undesirable for stability measurements. The first result is the measured displacement should be linear or close to linear for the these algorithms to properly measure or compensate. This is especially for the continuous elliptical compensation, which showed the largest reduction in the periodic error. When the displacement was linear, the periodic error was near zero after using this compensation technique. However, when the displacement was nonlinear, the periodic error was not zero, although it was still better than using the Lissajous compensation. In dimensional stability measurements, the measured displacement is assumed to be nonlinear which reduce the effectiveness of algorithm-based periodic error compensation.

The second distinct result from these simulations is the total displacement during a measurement or compensation period should be greater than one fringe (or more), to properly measure or compensate periodic errors. If there is less than one fringe of displacement, the measurement algorithms have difficulty measuring the periodic error because the sampling frequency is less than the displacement frequency. This is because these algorithms use a Fourier domain analysis which a full fringe of displacement is needed to measure a complete cycle.

In the case of the Lissajous fit, and its extension, the Continuous Elliptical Compensation, a small displacement means the fitted ellipse can show up as a hyperbole or a parabola, which is not enclosed and limits the feasibility of the algorithms. The Chu-Ray algorithm needs at least a complete cycle (at least one fringe) to properly determining the correction parameters.

From this analysis, it is clear that removing periodic errors already present in stability measurements is difficult and prone to errors and improper correction. Thus, an interferometer designed for stability measurements should be designed to have no source mixing and no mixed polarization states to significantly reduce the chance for periodic errors. Another consideration is to implement a constant velocity scan greater than one fringe, which will then allow for a compensation technique to be implemented. This, however, may introduce an instability because a modulating component is needed and it may create an imbalance in the system. The following sections detail interferometer designs which are specifically designed to mitigate source mixing and periodic errors. From these examples, several interferometer design adaptions will be considered for a stability measuring interferometer.

Appendix E

Fabry-Pérot Interferometry

A Fabry-Pérot cavity consists of two highly reflecting surfaces, typically one flat and one concave mirror, which helps create multiple interferences. The input light passes through the first mirror and reflects off the second mirror and travels back to the first mirror. When the hits the first mirror, a portion is transmitted but the majority is reflected. The reflected portion passes back through the cavity and reflects off the second mirror again. This is repeated until the light finally exits the cavity.

If a continuous laser source is used, then light will be added to the cavity continuously and multiple interferences occur prior to exiting. If the cavity length matches the frequency of the input light, then the multiple interferences create constructive interference. Conversely, if the cavity length does not match the frequency of the light, destructive interference occurs.

The multiple passes in a Fabry-Pérot cavity make it highly sensitive to laser frequency changes, refractive index changes, and cavity length changes. A standard Fabry interferometer configuration uses a tunable laser to lock to the Fabry-Pérot resonance peak and the frequency shift is measured when one cavity mirror is moved [96–99]. From this, the displacement can be calculated using the nominal cavity length and the calibrated optical frequency. In principle, a tunable laser source and a stabilized optical frequency standard are necessary to measure the frequency shifts in Fabry-Pérot interferometry.

An external cavity diode laser (ECDL) with 635 nm wavelength is an attractive, tunable source due to its wide tunable range (10 nm) and its narrow linewidth. The frequency shift can be measured with an iodine stabilized He-Ne laser up to a few tens of gigahertz, which is dependent on the bandwidth of the photodetector used. Thus, the displacement can be measured continuously without any fly back states in the range of a few micrometers [98]. Alternatively, if the cavity is dimensionally stable, refractive index changes can be measured using the same technique. However, using an ECDL is a costly solution and standard HeNe laser tube is more attractive because of its low cost and high reliability.

The major drawback from using HeNe lasers is that the tunable range of the HeNe laser is rather narrow, only approximately 1.5 GHz. In this case, the free spectral range of the Fabry-Pérot cavity should be narrower than the gain bandwidth of the HeNe laser [97]. However, this leads to using long cavities because of the narrow bandwidth, which are undesirable

because they decrease the stability of the system caused by mechanical vibrations, laser frequency instabilities, and refractive index changes [98].

If a Fabry-Pérot based system is used for refractive index measurements, it must have a stable reference cavity. This is an issue for this research because a major assumption of this work is all components will have some dimensional instability over time. Therefore, a smaller cavity is more desirable because thermal effects are reduced. However, a longer cavity is more desirable because the increased sensitivity for the Fabry-Pérot interferometer.

The following sections detail several Fabry-Pérot interferometer configurations including several novel designs to reduce the physical cavity length but increase the effective cavity length. There are two standard Fabry-Pérot interferometers, one based on a reflecting cavity and the other based on a transmitting cavity. The transmitting cavity design was presented in Chapter 4. Thus, only the reflecting cavity is presented here. Then, a folded configuration and a quarter wave plate based configuration are discussed. Finally, a combination system, the folded, QWP-based Fabry-Pérot interferometer is shown.

E.1 Reflectance Fabry-Pérot Interferometer

A schematic of the traditional reflectance Fabry-Pérot interferometer is shown in Figure E.1. In this interferometer, a HeNe laser tube is locked to the resonance peak of the Fabry-Pérot cavity. The beam from the HeNe laser passes through an optical isolator to ensure back reflecting beams do not destabilize the laser. Then a portion, usually 4%, is split from the HeNe laser using a beam sampler (bs). The beam is then phase modulated using an electro-optic modulator, which is used for the PDH locking technique [102]. After passing through a 50% beamsplitter, the beam enters the Fabry-Pérot cavity of length, L, consisting of two mirrors, M_1 and M_2, with reflectances R_1 and R_2, respectively. The measurement beam passes back through M_1, where it reflects off the beamsplitter and is detected with a photodiode.

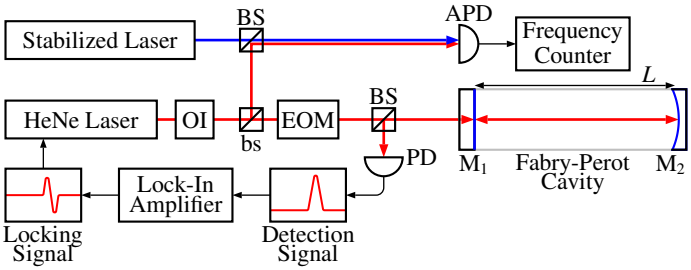

Figure E.1: *Optical configuration of a reflectance Fabry-Pérot interferometer. The output beam from the cavity exits the same place where it entered.*

The portion split from the beam sampler travels to another 50% beamsplitter where it interferes with a frequency stabilized laser and is detected with an avalanche photodiode. When the resonance peak is detected with the photodiode, a lock-in amplifier can be used to determine the derivative of the peak using the electro-optic modulator's phase modulation. This creates a servo signal to control the HeNe laser to stabilize the laser frequency relative

to the cavity length. Once the peak is locked, the cavity length change and the refractive index change in the cavity is transferred to laser frequency modulations which are detected by the frequency change detected by avalanche photodiode.

The signal exiting the Fabry-Pérot cavity is

$$(FP_R) = t_1^2 r_2 \mathrm{e}^{2ikL} + t_1^2 r_1 r_2^2 \mathrm{e}^{4ikL} + t_1^2 r_1^2 r_2^3 \mathrm{e}^{6ikL} + t_1^2 r_1^3 r_2^4 \mathrm{e}^{8ikL} + \cdots \tag{E.1}$$

$$= t_1^2 \mathrm{e}^{2ikL} \sum_{p=0}^{\infty} r_1^p r_2^{p+1} \mathrm{e}^{2pikL}, \tag{E.2}$$

where t_1 is the electric field transmission coefficient for M_1, $r_{1,2}$ are the electric field reflectance coefficients for M_1 and M_2, respectively, k is the wavenumber ($\lambda/2\pi\eta$), L is the cavity length and p is the cavity pass number. Equation E.2 is a geometric series of the form

$$y = a + ax + ax^2 + ax^3 + \cdots \tag{E.3}$$

$$= \sum_{p=0}^{\infty} ax^p, \tag{E.4}$$

whose sum converges to a solution, providing x is less than one. The sum of Equation E.4 is

$$y_\Sigma = \frac{a}{1-x}. \tag{E.5}$$

Applying Equation E.5 to Equation E.2 yields

$$(FP_R)_\Sigma = \frac{t_1^2 r_2 \mathrm{e}^{2ikL}}{1 - r_1 r_2 \mathrm{e}^{2ikL}}. \tag{E.6}$$

The total intensity of the light exiting the reflecting Fabry-Pérot, $I_{FP,R}$ is $(FP_R)_\Sigma^* (FP_R)_\Sigma$. Thus, the gain can be simplified to

$$\frac{I_{FP,R}}{I_i} = \frac{T_1^2 R_2}{(1 + R_1 R_2) - 2\sqrt{R_1 R_2}\cos(2kL)}, \tag{E.7}$$

where I_i is the input intensity, T_1 is the intensity transmission coefficient for M_1 and $R_{1,2}$ are the intensity reflectance coefficients for for M_1 and M_2, respectively. Figure E.2 shows the cavity gain as a function of cavity displacement, where R_1 is 99%, T_1 is (1-R_1), and R_2 is 100%. This is assumed to be the ideal case. For the complete system, shown in Figure E.1, there are more components which affect the measured intensity from the reflecting Fabry-Pérot. The intensity of the complete reflecting Fabry-Pérot detected by the photodiode is

$$I_{sys,R} = T_{OI} T_{bs} T_{EOM} T_{BS} R_{BS} \left(R_1 + I_{FP,R}\right) I_i, \tag{E.8}$$

where R_1 is reflective intensity coefficient of M_1, T_{OI} is the optical isolator intensity transmission coefficient, T_{bs} is the beam sampler intensity transmission coefficient, T_{EOM} is the electro-optic modulator intensity transmission coefficient, and T_{BS}, R_{BS} are the beamsplitter transmission and reflectance intensity coefficients. If an ideal case is assumed, then T_{OI} is 90%, T_{bs} is 96%, T_{EOM} is 90%, T_{BS} is 50%, and R_{BS} is 50%. Figure E.2 also shows the system gain as a function of cavity displacement, where R_1 is 1-T_1.

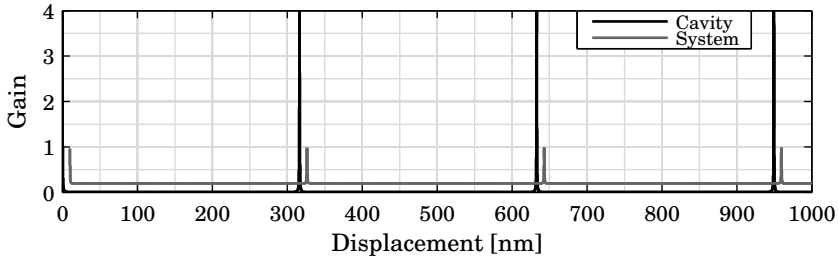

Figure E.2: *Ideal gain of the reflectance Fabry-Pérot cavity and system as a function of cavity displacement. The system includes modest losses in components before and after the Fabry-Pérot Cavity. The system plot is offset in the X-axis for clarity. The system has a DC offset from a high power back beam.*

The reflecting Fabry-Pérot cavity has an ideal gain near four when the cavity displaces $\lambda/2$. However, when the full system is considered, the range drops to near one, where 75% of the drop occurs from passing through the 50%beamsplitter twice. The remaining 5% drop is from the other optical elements. In addition to the drop in peak height, the DC offset is increased. This is from the input beam reflectance off M_1.

Another important aspect to consider in Fabry-Pérot interferometry is the stringent requirements on reflectance and transmission coefficients for components. Figure E.2 assumed the reflectivity of M_1 was 99% and M_2 was 100%, which is considered ideal. However, as the reflectance decreases, the Fabry-Pérot gain drops dramatically. This is shown in Figure E.3 where R_1 is the value listed and R_2 is 100%.

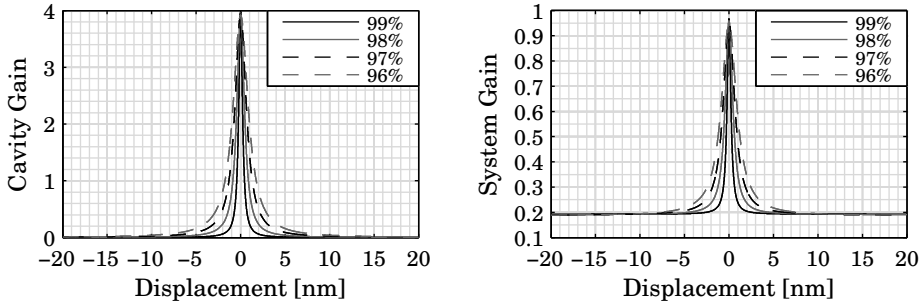

(a) **(b)**

Figure E.3: *Close-up of a single resonance peak of the (a) cavity and (b) system in the reflectance Fabry-Pérot interferometer. These values are from a numerical simulation where M_1 has the value listed and M_2 has 100% reflectance.*

The largest contributor to the overall system deficiency is the losses in the 50% beamsplitter. Because the measurement signal passes through it twice, there is a 75% drop in intensity at minimum. This will be further decreased because beamsplitters usually have an efficiency around 45%, which drops the efficiency another 5% to 20%. There are two ways to mitigate this problem. The first method is to assume the input beam is vertically

polarized and the 50% beamsplitter is replaced by a polarizing beamsplitter. By placing a quarter wave plate between the polarizing beam splitter and the Fabry-Pérot cavity, the measurement beam travels back to the polarizing beam splitter with a horizontal polarization state. This is due to passing through the quarter wave plate twice, once on the way to the cavity and once on the way back from the cavity.

This configuration improves the overall efficiency, but there is still an issue with the beam initially reflected from M_1. This back reflected beam also benefits from the increased efficiency, which adds a high DC offset into the measurement. Detectors in Fabry-Pérot interferometers usually have a very high gain to increase the Q (gain factor). Since both the offset and the measurement signal get amplified by the same amount, the Q is not enhanced by an increased detector gain. Thus, a transmission Fabry-Pérot interferometer is typically used instead.

E.2 QWP Fabry-Pérot Interferometer

A schematic of the QWP Fabry-Pérot interferometer is shown in Figure E.4. In this system the light passing through the electro-optic modulator is assumed to be vertically polarized, which in this case means it will pass through the polarizing beamsplitter. The cavity consists of a quarter wave plate with a highly reflective coating on one surface and a mirror, spaced L distance apart.

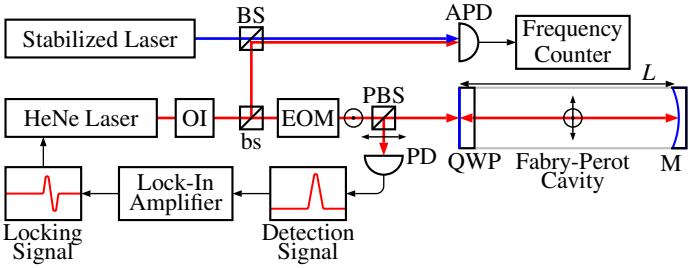

Figure E.4: *Optical configuration of a Fabry-Pérot interferometer using a QWP with a mirror coating to create multiple polarization states. Since a polarizing beamsplitter is used, only horizontally polarized beams are detected, which means the beams must travel the Fabry-Pérot cavity twice befor being detected.*

The back beam incident on the mirror-coated quarter wave plate has the same polarization state as its input, thus, it passes back through the polarizing beamsplitter and does not get detected. The first cavity pass rotates the polarization state 90° because the beam passes through the quarter wave plate twice. When a portion transmits through the quarter wave plate, it reflects off the polarizing beamsplitter and gets detected. The second pass rotates the polarization state another 90°, which means the transmitted portion passes through the polarizing beamsplitter and does not get detected. This polarization rotation means the cavity appear to have a length of $2L$, thus the output beam phase changes with $4kL$.

The mathematical representation of the QWP Fabry-Pérot cavity is

$$(\mathbf{FP}_Q) = q_r\mathbf{M} + q_t^2 r \mathrm{e}^{2ikL}\mathbf{Q}_\perp \sum_{p=0}^{\infty} r^{2p} q_r^{2p} \mathrm{e}^{4ikLp} + q_t^2 r^2 q_r \mathrm{e}^{4ikL}\mathbf{Q}_\parallel \sum_{p=0}^{\infty} r^{2p} q_r^{2p} \mathrm{e}^{4ikLp+\pi}, \quad \text{(E.9)}$$

where

$$\mathbf{M} = \begin{bmatrix} 1 & 0 \\ 0 & -1 \end{bmatrix},$$

$$\mathbf{Q}_\perp = \sum_{p=0}^{\infty} q_{abs}^{4p+2} \begin{bmatrix} \cos^2\gamma + \mathrm{e}^{i(4p+2)\left(\pi/2+\gamma_q\right)}\sin^2\gamma & \left(1-\mathrm{e}^{i(4p+2)\left(\pi/2+\gamma_q\right)}\right)\cos\gamma\sin\gamma \\ \left(1-\mathrm{e}^{i(4p+2)\left(\pi/2+\gamma_q\right)}\right)\cos\gamma\sin\gamma & \sin^2\gamma + \mathrm{e}^{i(4p+2)\left(\pi/2+\gamma_q\right)}\cos^2\gamma \end{bmatrix},$$

$$\mathbf{Q}_\parallel = \sum_{p=0}^{\infty} q_{abs}^{4p+4} \begin{bmatrix} \cos^2\gamma + \mathrm{e}^{i(4p+4)\left(\pi/2+\gamma_q\right)}\sin^2\gamma & \left(1-\mathrm{e}^{i(4p+4)\left(\pi/2+\gamma_q\right)}\right)\cos\gamma\sin\gamma \\ \left(1-\mathrm{e}^{i(4p+4)\left(\pi/2+\gamma_q\right)}\right)\cos\gamma\sin\gamma & \sin^2\gamma + \mathrm{e}^{i(4p+4)\left(\pi/2+\gamma_q\right)}\cos^2\gamma \end{bmatrix},$$

$q_{r,t}$ are the electric field reflectance and transmission coefficients of the quarter wave plate, r is the electric field reflectance of the mirror, γ is the quarter wave plate rotation about the azimuthal angle, γ_q is the quarter wave plate phase error, and q_{abs} is one minus the power loss in the quarter wave plate. The matrix $(\mathbf{FP}_Q)$ is a 2×2 matrix which is the Jones matrix representation of the Fabry-Pérot cavity. The total detected electric field in Jones matrix form is

$$\mathbf{E}_o = T_{OI}T_{bs}T_{EOM}\,(\mathbf{PBS}_r)\,(\mathbf{FP}_Q)\,(\mathbf{PBS}_t)\,\mathbf{E}_i, \quad \text{(E.10)}$$

where $(\mathbf{PBS}_{r,t})$ are the reflectance and transmission Jones matrices for the polarizing beamsplitter and $\mathbf{E}_i$ is a 2×1 input electric field Jones matrix. The total detected irradiance is determined by pre-multiplying the output electric field vector by its Hermitian adjoint (transposed conjugate)

$$I = \mathbf{E}_o^\dagger \mathbf{E}_o = \begin{bmatrix} \mathbf{E}_{o,\parallel}^* & \mathbf{E}_{o,\perp}^* \end{bmatrix} \begin{bmatrix} \mathbf{E}_{o,\parallel} \\ \mathbf{E}_{o,\perp} \end{bmatrix} \quad \text{(E.11)}$$

The transmission and reflectance matrices for the polarizing beamsplitter are

$$\mathbf{PBS}_t = \begin{bmatrix} \alpha_{1,\parallel} & 0 \\ 0 & \alpha_{2,\parallel} \end{bmatrix} \quad \text{and} \quad \text{(E.12)}$$

$$\mathbf{PBS}_r = \begin{bmatrix} \alpha_{2,\perp} & 0 \\ 0 & \alpha_{1,\perp} \end{bmatrix}, \quad \text{(E.13)}$$

respectively, where $\alpha_{1,\parallel}$ and $\alpha_{2,\parallel}$ is the transmission coefficients for the vertical and horizontal polarization states and $\alpha_{1,\perp}$ and $\alpha_{2,\perp}$ are the reflectance coefficients for the horizontal and vertical polarization states.

The ideal scenario is when $\alpha_{1,\parallel} = \alpha_{1,\perp} = q_{abs} = 1$, $\alpha_{2,\parallel} = \alpha_{2,\perp} = \gamma_q = 0$, $\gamma = {}^{pi}/_{2}$, and q_{abs} is $(1 - 0.25\%)$. The the quarter wave plate absorption coefficient is from an assumed anti-reflection coating on the surface. When this occurs, Equation E.10 simplifies to

$$\mathbf{E}_o = T_{OI}T_{bs}T_{EOM} \begin{bmatrix} 0 & 0 \\ 0 & 1 \end{bmatrix} \begin{bmatrix} 0 & \frac{q_t^2 r q_{abs}^2 \mathrm{e}^{2ikL}}{1-r^2 q_r^2 q_{abs}^2 \mathrm{e}^{4ikL}} \\ \frac{q_t^2 r q_{abs}^2 \mathrm{e}^{2ikL}}{1-r^2 q_r^2 q_{abs}^2 \mathrm{e}^{4ikL}} & 0 \end{bmatrix} \begin{bmatrix} 1 & 0 \\ 0 & 0 \end{bmatrix} \begin{bmatrix} 1 \\ 0 \end{bmatrix} \mathbf{E}_i. \quad \text{(E.14)}$$

Thus, in the ideal case, the total Fabry-Pérot cavity and systems gains are

$$\frac{I_{FP,Q}}{I_i} = \frac{Q_t^2 R Q_{abs}^2}{1 + R^2 Q_r^2 Q_{abs}^2 - 2RQ_r Q_{abs} \cos(4kL)} \quad \text{and} \tag{E.15}$$

$$\frac{I_{FP,Q}}{I_i} = \frac{T_{OI} T_{bs} T_{EOM} Q_t^2 R Q_{abs}^2}{1 + R^2 Q_r^2 Q_{abs}^2 - 2RQ_r Q_{abs} \cos(4kL)}, \tag{E.16}$$

respectively. The best-case scenario is when R is 100%, Q_r is 99%, and Q_{abs} is 99.75%, which is considered the highest transmission possible with a properly designed anti-reflection coating. Figure E.5 shows the cavity and system gains as a function of cavity length change.

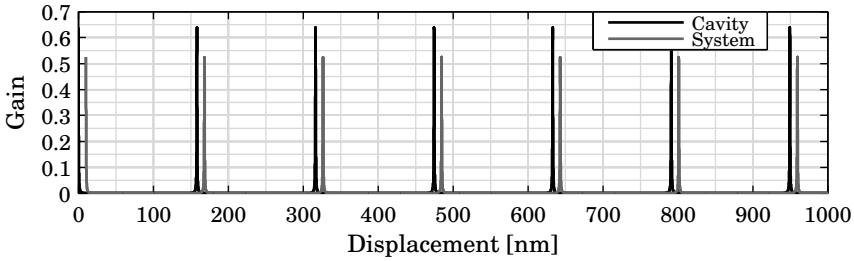

Figure E.5: *Ideal gain of the QWP Fabry-Pérot cavity and system as a function of cavity displacement. The system includes modest losses in components before the Fabry-Pérot cavity. The system plot is offset in the X-axis for clarity. This cavity has twice as many peak per displacement as the reflectance and transmission Fabry-Pérot interferometers.*

Because of the added losses in the quarter wave plate, the peak intensity for both the cavity and system is less than in the transmission Fabry-Pérot. However, the quarter wave plate effectively doubles the cavity length, which means the resonance peaks occur twice as often as in the transmission Fabry-Pérot.

As with the transmission and reflectance Fabry-Pérot interferometers, the mirror coating efficiency has an effect on the linewidth and peak intensity value, as shown in Figure E.6. In these simulations, the quarter wave plate mirror coating has the value listed while the mirror has a 100% reflectance. Contrary to the transmission Fabry-Pérot system, the mirror coating efficiency increase the linewidth and increases the peak intensity, although the ratio remains the same.

However, both the cavity gain and system gain are unaffected by the back beam from the initial reflection off the quarter wave plate mirror. This is because its polarization state is the same as the input polarization state, which transmits back through the polarizing beamsplitter and is eventually blocked by the optical isolator. In the practical case, there is a slight influence from the back beam because the transmission and reflectance matrices are

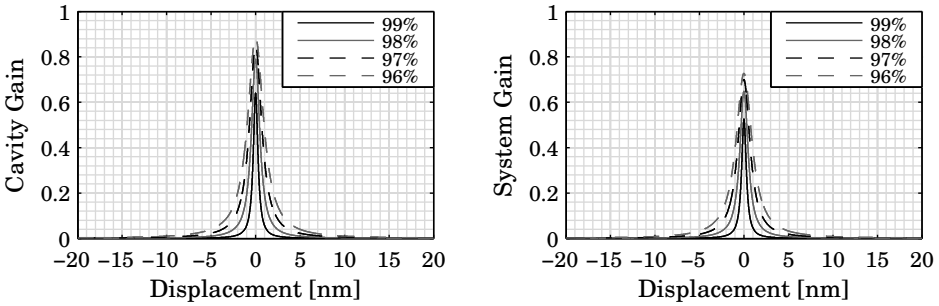

Figure E.6: *Close-up of a single resonance peak of the (a) cavity and (b) system in the QWP Fabry-Pérot interferometer assuming ideal polarization effects. These values are from a numerical simulation where the mirror on the quarter wave plate and opposite cavity mirror both had the reflection value labeled in the figure.*

typically

$$\mathbf{PBS}_t = \begin{bmatrix} 0.98 & 0 \\ 0 & 0.02 \end{bmatrix} \quad \text{and} \tag{E.17}$$

$$\mathbf{PBS}_r = \begin{bmatrix} 0.04 & 0 \\ 0 & 0.96 \end{bmatrix}. \tag{E.18}$$

Thus, when a vertically aligned beam is used as the input, approximately 4% of the back beam is detected which is a slight offset and should have minimal effect on the overall system stability. The imperfect polarizing beamsplitter also affects the Fabry-Pérot gain, as shown in Figure E.7.

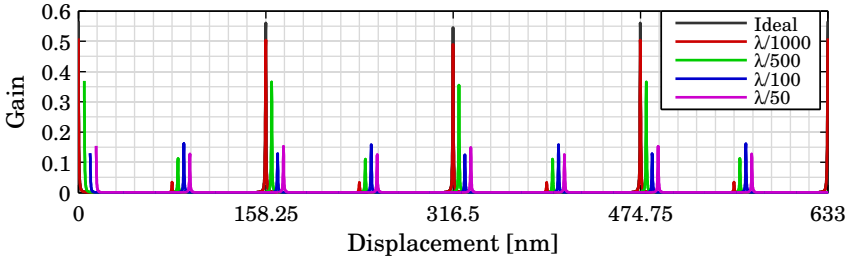

Figure E.7: *Cavity gain for the QWP Fabry-Pérot interferometer assuming non-perfect phase retardence in the quarter wave plate. Because of the polarization switching, additional peaks with π phase difference appear. Also, the peak intensity for the desired peaks drops dramitically as a function of phase error.*

Figure E.7 also shows the effects of an imperfect quarter wave plate. In the ideal case, the quarter wave plate creates a perfect 45° retardation. Thus, the total Fabry-Pérot output alternates between vertically and horizontally polarized beams. Then, because the measurement beam passes through a polarizing beamsplitter, the vertical beam is

transmitted and not detected whereas the horizontal beam is reflected to a detector. Figure E.8 shows the output intensity as a function of the number of passes in the Fabry-Pérot. This estimate is for an ideal QWP Fabry-Pérot with reflectances of 99% and 100% for Q_r and R, respectively, and a transmission of 99.75% for Q_{abs}.

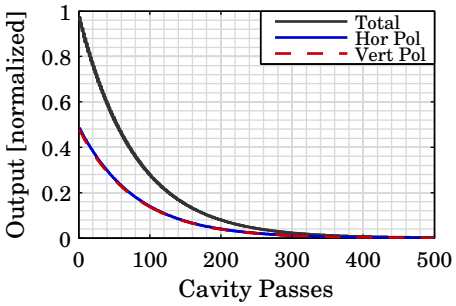

Figure E.8: *Comparison between both polarization state outputs and their sum as a function of cavity passes for an ideal case. The of the 500 passes, only 250 are detected because those are the horizontal polarization state.*

Because of the losses in Q_r and Q_{abs}, a new input beam takes approximately 500 passes to completely decay in Fabry-Pérot. If the quarter wave plate is perfect, the total output is half of the ideal output because 50% is lost due to the polarization exchange. If the quarter wave plate is not perfect, the output polarization state from the Fabry-Pérot becomes elliptical. The creates an error because the odd passes in the Fabry-Pérot are 180° out of phase from the even passes due to the polarization rotation. Figure E.9 shows the effect of quarter wave plate phase error as the power output decays. The phase errors of $\lambda/1000$ and $\lambda/500$ are minimal which means the detected signal contains mostly components from $Q_\perp$ and only has a small portion from $Q_\parallel$. As the phase error increases to $\lambda/100$ and $\lambda/50$, the detected signal has increased components from $Q_\parallel$.

The shape of the curves in Figure E.9 appear to be Bessel functions of the 1st kind for J_α for α integer orders of 0 and 2 for the horizontal and vertical polarization states, respectively. Rather than solve this analytically, the rotated quarter wave plate Jones matrix was determined numerically, assuming steady state was reached after 500 passes. Table E.1 shows the estimated quarter wave plate Jones matrices for each of the four different phases errors. These values were used in Equation E.9 to determine the Fabry-Pérot gain as a function of displacement shown in Figure E.7.

As the phase error in the quarter wave plate increases, a peak appears at π intervals with respect to the main peak. This is because passing through a quarter wave plate twice introduces a 180° phase shift (π in radians). When the quarter wave plate is error free, the only the first series in Equation E.9 must be considered. However, as the error increases, both series must be considered for the complete answer.

The reflectance, transmission, and quarter wave plate Fabry-Pérot interferometer configurations all suffer from the same drawback. Both mirrors must be aligned in both rotational directions to ensure proper cavity stability. In fixed cavity situations (refractometers, for instance), this means four rotational directions must be pre-aligned and mounted in a stable

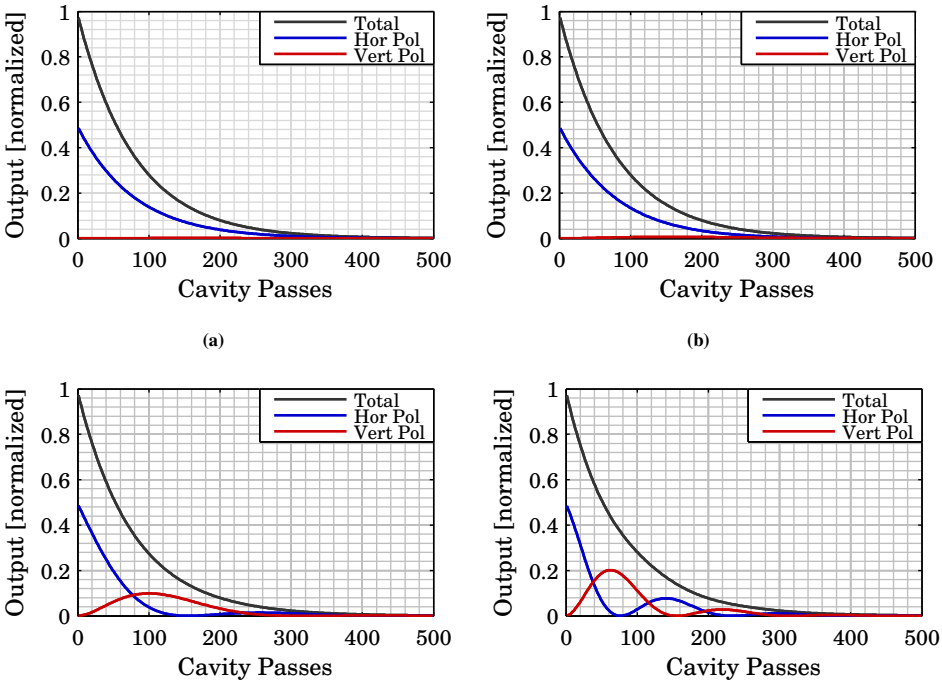

Figure E.9: *Detected signal by polarization state and sum as a function of cavity passes for various quarter wave plate phase error values. When phase error is small, $\lambda/1000$ in (a) and $\lambda/500$ in (b), most of the detected signal is the desired horizontal polarization state. As the phase error increases to $\lambda/100$ in (c) and $\lambda/50$ in (d), both polarization states are detected. This causes the additional peaks in Figure E.7.*

Table E.1: *Steady state Jones matrices for the two polarization states as a function of quarter wave plate phase error. When the phase error is small, the matrix is near the ideal case. As the error increases, the polarization state becomes highly mixed.*

	$\mathbf{Q}_\perp$	$\mathbf{Q}_\parallel$
$\lambda/1000$	$\begin{bmatrix} 0.08-0.23i & 0.92+0.23i \\ 0.92+0.23i & 0.08-0.23i \end{bmatrix}$	$\begin{bmatrix} 0.92+0.23i & 0.08-0.23i \\ 0.08-0.23i & 0.92+0.23i \end{bmatrix}$
$\lambda/500$	$\begin{bmatrix} 0.28-0.36i & 0.73+0.35i \\ 0.73+0.35i & 0.28-0.36i \end{bmatrix}$	$\begin{bmatrix} 0.72+0.35i & 0.27-0.35i \\ 0.27-0.35i & 0.72+0.35i \end{bmatrix}$
$\lambda/100$	$\begin{bmatrix} 0.53-0.09i & 0.47+0.09i \\ 0.47+0.09i & 0.53-0.09i \end{bmatrix}$	$\begin{bmatrix} 0.47+0.09i & 0.53-0.09i \\ 0.53-0.09i & 0.47+0.09i \end{bmatrix}$
$\lambda/50$	$\begin{bmatrix} 0.48-0.02i & 0.52+0.02i \\ 0.52+0.02i & 0.48-0.02i \end{bmatrix}$	$\begin{bmatrix} 0.52+0.02i & 0.48-0.01i \\ 0.48-0.01i & 0.52+0.02i \end{bmatrix}$

configuration. In moving cavity situations (linear calibration systems, for instance), the

alignment must remain stable during the motion of one mirror in addition to the stable pre-alignment. This adds stringent requirements to minimize the straightness error of the moving mirror stage.

E.3 Folded Fabry-Pérot Interferometer

One method to mitigate the mirror tilt sensitivity is to use a retroreflector. Using a retroreflector has five distinct advantages. The first advantage is the input mirror angular alignment is the only critical alignment. The second advantage is there is no back beam because it can be in a transmission mode. The third advantage is the moving element is rotationally insensitive, making initial alignment easier. The fourth advantage is a sensor can be placed on the moving element without worrying about interfering with a transmission beam. The fifth advantage is the free spectral range is double the free spectral range of the reflectance and transmission Fabry-Pérot interferometers and has the same free spetral range as the QWP Fabry-Pérot. A schematic of a folded Fabry-Pérot interferometer is shown in Figure E.10.

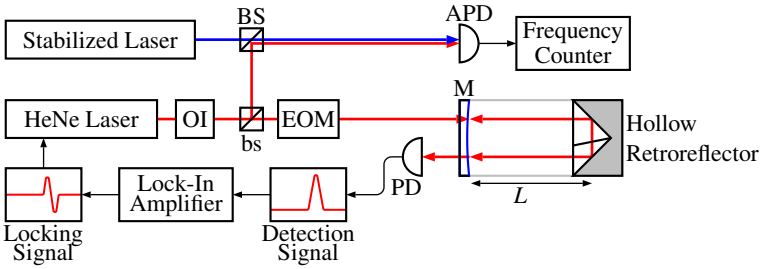

Figure E.10: *Optical configuration of a folded Fabry-Pérot interferometer using a retroreflector to effectively lengthen the cavity.*

This Fabry-Pérot interferomter has many of the same components as with the transmission Fabry-Pérot interferometer. After passing through the electro-optic modulator, the beam travels to the Fabry-Pérot cavity which is comprised of a mirror and a hollow retroreflector[1]. A portion of the beam is transmitted into the cavity, where it reflectors off the hollow retroreflector and is displaced. It passes back to the initial mirror where a portion is transmitted and detected. The remaining portion gets reflected where it travels to the retroreflector again and then back to the input mirror. Most of the beam reflects again where it reflects of the retroreflector for a third time and then passes back to the mirror after being displaced. Here, another portion is transmitted and detected.

The detected signal can be represented mathematically by

$$\left(FP_f\right) = t^2 \mathrm{e}^{2ikL} \sum_{p=0}^{\infty} (rr)^{2p}\, r^{2p} \mathrm{e}^{4pikL}, \tag{E.19}$$

[1]Standard retroreflectors have added glass paths which will increase the absorption and polarization effects per cavity pass in the Fabry-Pérot. A hollow retroreflector is better suited towards this application because these effects can be minimized by eliminating the added glass path, glass-to-air transitions, and has less polarization errors[147]. Additionally, a hollow retroreflector typically has a flat back instead of the usual three-faceted back, thus it is easier for mounting components.

where t and r are the mirror electric field transmission and reflection coefficients and (rr) is the hollow retroreflector electric field reflection coefficient. The sum of this series is

$$\left(FP_f\right)_\Sigma = \frac{t^2 \mathrm{e}^{2ikL}}{1-(rr)^2 r^2 \mathrm{e}^{4ikL}}. \tag{E.20}$$

Similar to the reflectance and transmission Fabry-Pérot interferometers, the folded Fabry-Pérot cavity and system gains are

$$\frac{I_{FP,f}}{I_i} = \frac{T^2}{\left(1+(RR)^2 R^2\right) - 2(RR)R\cos(4kL)} \quad \text{and} \tag{E.21}$$

$$\frac{I_{sys,f}}{I_i} = \frac{T^2 T_{OI} T_{bs} T_{EOM}}{\left(1+(RR)^2 R^2\right) - 2(RR)R\cos(4kL)}, \tag{E.22}$$

where the uppercase variables are the intensity coefficients instead of electric field coefficients. Both the cavity gain and system gain are shown in Figure E.11 as a function of cavity length change.

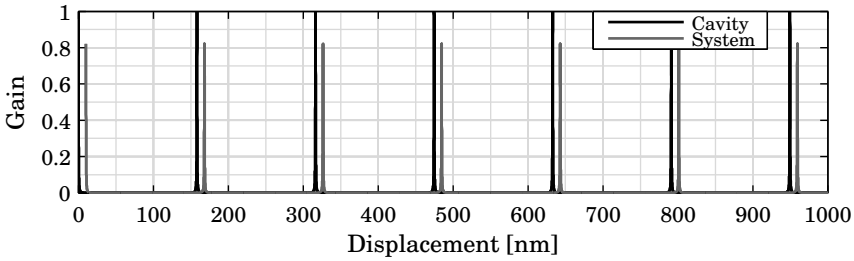

Figure E.11: *Ideal gain of the folded Fabry-Pérot cavity and system as a function of cavity displacement. This cavity has twice the number of peaks as the reflectance and transmission cavities. The system includes modest losses in components before the Fabry-Pérot cavity. The system plot is offset in the X-axis for clarity.*

As with the QWP Fabry-Pérot interferometer, the folded Fabry-Pérot interferometer has four peaks per wavelength traveled which increases the free spectral range. Additionally, peak gains are near 1 and 0.82 for the cavity and system when the retroreflector is assumed lossless. As with the transmission Fabry-Pérot interferometer, the linewidth increases when the output mirror efficiency decreases, as shown in Figure E.12. In these calculations, the retroreflector is assumed to have a reflectance of 100%.

The folded and QWP Fabry-Pérot interferometers both have double the free spectral range of the reflectance and transmission Fabry-Pérot interferometers. However, the folded and quarter wave plate configurations can be used simultaneously to further increase the free spectral range and combine advantages of both systems.

E.4 QWP-Folded Fabry-Pérot Interferometer

The QWP Fabry-Pérot interferometer only needs one access port because the input and measurement beams travel the same path. This makes initial alignment simpler, eliminates

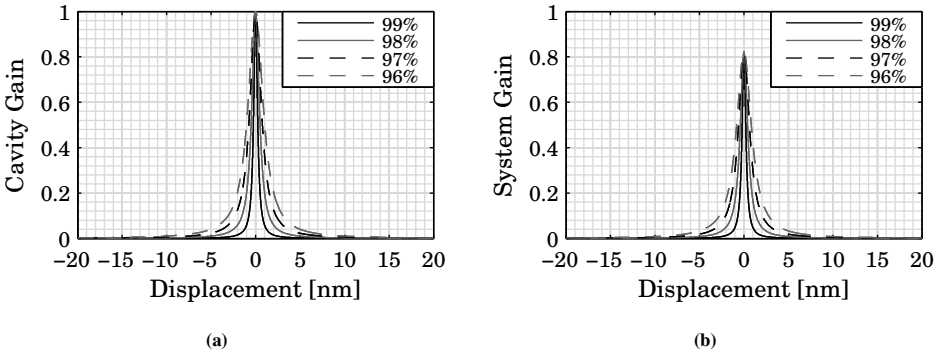

Figure E.12: *Close-up of a single resonance peak of the (a) cavity and (b) system in the folded Fabry-Pérot interferometer. These values are from a numerical simulation where the mirror and retroreflector both have the reflection value labeled in the figure. Because the light reflects off two "lossy" surfaces per pass, the peak intensity drops rapidly.*

the back beam, and doubles the free spectral range. If a hollow retroreflector is added to this system, as shown in Figure E.13, the system can also benefit from an additional free spectral range doubling and tilt insensitivity for the moving component

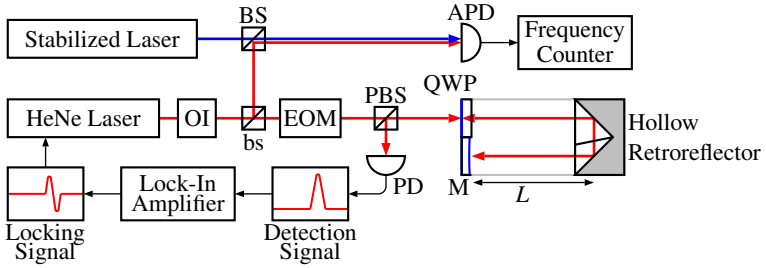

Figure E.13: *Optical configuration of a folded Fabry-Pérot interferometer using a quarter wave plate with a mirror coating to create multiple polarization states and length doubling using a retroreflector. Since a polarizing beamsplitter is used, only horizontally polarized beams are detected, which means the beams must travel the Fabry-Pérot cavity four times befor being detected.*

One again, if the input beam is assumed to be vertically polarized and passes through the polarizing beamsplitter, it then travels to the Fabry-Pérot cavity comprising a quarter wave plate with a mirror coating, a hollow retroreflector, and another mirror. The beam reflects off the retroreflector and is displaced before traveling to the mirror. It then reflects off the mirror where it reflects off the retroreflector again and is displaced again. This time, when it passes through the quarter wave plate a second time, the polarization state is rotated 90° where a portion will be transmitted and detected. Then, every second pass in the Fabry-Pérot cavity will result in a beam with a horizontal polarization state, which will be detected.

Rather than define a complete generalized solution, this mathematical representation of the cavity assumes a perfect polarizing beamsplitter, a perfect quarter wave plate with perfect alignment and a mirror and retroreflector with 100% reflectivity and no polarization

effects. While this is an overly simplified assumption, it will allow for a common comparison (ideal cavities) between the five different Fabry-Pérot configurations. This simplifies the mathematical expression for the QWP-folded Fabry-Pérot cavity to

$$\left(FP_{Qf}\right) = q_t^2 (rr)^2 \, r q_{abs}^2 \mathrm{e}^{4ikL} \sum_{p=0}^{\infty} (rr)^{4p} \, r^{2p} q_{abs}^{4p} q_r^{2p} \mathrm{e}^{8pikL}, \tag{E.23}$$

whose sum is

$$\left(FP_{Qf}\right)_{\Sigma} = \frac{q_t^2 (rr)^2 \, r q_{abs}^2 \mathrm{e}^{4ikL}}{1 - (rr)^4 \, r^2 q_{abs}^4 q_r^2 \mathrm{e}^{8ikL}}. \tag{E.24}$$

Using Equation E.24 and the aforementioned assumptions, the cavity gain is

$$\frac{I_{FP,Qf}}{I_i} = \frac{Q_t^2 (RR)^2 \, R Q_{abs}^2}{\left(1 + (RR)^4 \, R^2 Q_{abs}^4 Q_r^2\right) - 2 (RR)^2 \, R Q_{abs}^2 Q_r \cos(8kL)}, \tag{E.25}$$

which is shown in Figure E.14.

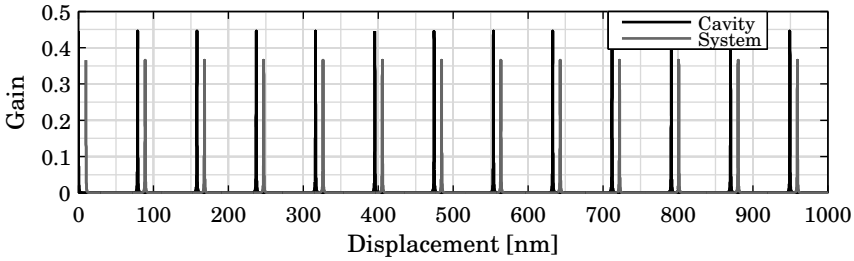

Figure E.14: *Ideal gain of the QWP-folded Fabry-Pérot cavity and system as a function of cavity displacement. This cavity has four times the number of peaks as the reflectance and transmission cavities. The system includes modest losses in components before the Fabry-Pérot cavity. The system plot is offset in the X-axis for clarity.*

E.5 Fabry-Pérot Cavity Comparison

Several different metrics are typically used to compare differences between Fabry-Pérot cavities. These are the free spectral range (FSR, $\delta\nu$), the full-width half-maximum (FWHM, $\delta\lambda$), and the finesse ($\mathcal{F}$). The FSR is an important parameter for tracking and locking a laser to a fixed cavity because the FSR must be less than the gain bandwidth of the laser. For instance, most HeNe lasers have a gain bandwidth around 1.5 GHz. Thus, the FSR of a Fabry-Pérot cavity to stabilize this HeNe laser must be less than 1.5 GHz to ensure the laser peak is always visible. The FWHM determines the peak linewidth and from the combination of FSR and FWHM, the finesse can be determined, which is essentially the sharpness of the peak. If a peak has a high finesse, then the locking stability is more efficient because slight changes in laser frequency or cavity length cause a large signal change. If the finesse is low, then the locking sensitivity is also low.

Figure E.15 shows a comparison of the ideal peak intensity for each of the five cavity types. Clearly, the reflectance cavity has the highest peak. The transmission and QWP cavities appear to have a broader peak with a wider linewidth. The folded and QWP-folded appear to have the same aspect ratio as the reflectance peak but their peak intensity is much lower but their linewidth is also smaller.

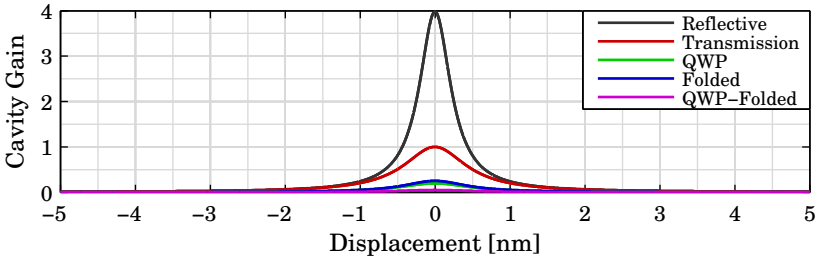

Figure E.15: *Comparison of a single resonance peak for each of the five Fabry-Pérot cavities for the ideal case. This shows clear distinctions between the line width and the peak gain.*

This is contrasted by the peak intensity of the complete systems, which is shown in Figure E.16. In this comparison, the common initial components such as optical isolators, etc. are assumed to all have the same loss between Fabry-Pérot cavities. Because the reflectance Fabry-Pérot interferometer includes passing through a 50% beamsplitter twice, the power is dropped by 75%, plus the losses in the other components. Thus, the reflective, transmission, and folded systems all have a peak gain above 0.5, although the transmission system has a much wider linewidth. The QWP and QWP-folded systems have a lower peak intensity, which is due to the additional losses in the quarter wave plate anti-reflection coating (assumed 0.25%).

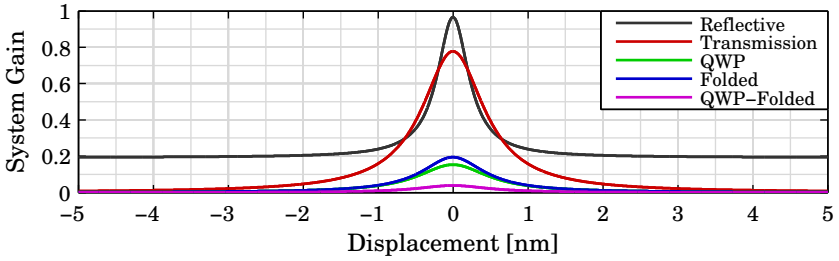

Figure E.16: *Comparison of a single resonance peak for each of the five Fabry-Pérot systems. This shows clear distinctions between the line width and the peak gain.*

In this comparison, two different cavity lengths, L, will be assumed. The length L has been shown in each of the five optical layouts for the Fabry-Pérot interferometers. The cavity lengths assumed will be 50 mm and 150 mm. The FSR in the frequency domain is

$$\delta\nu = \frac{c}{ML}, \tag{E.26}$$

where c is the speed of light, M is the optical resolution of the Fabry-Pérot cavity, and L is the cavity length shown in the optical layout. For the reflectance and transmission Fabry-Pérot cavities, the optical resolution is two. For the QWP and folded systems, the optical resolution is four. The QWP-folded cavity has the highest optical resolution, eight, of the cavities shown. Table E.2 summarizes the FSR for the two cavity lengths. When the cavity is short (50 mm), the FSR of the reflectance and transmission cavities is insufficient to continuously stabilize the laser. The folded and QWP cavities are only marginally stable and depend on the HeNe mixture in the supply laser because the gain bandwidth depends on the mixture. When the cavity is larger, however, all configurations presented in this work can be used for locking the HeNe laser.

Table E.2: *Calculated free spectral range for two different cavity lengths for each of the five cavity types.*

L	$(FP)_R$	$(FP)_T$	$(FP)_Q$	$(FP)_f$	$(FP)_{Qf}$
50 mm	3000	3000	1500	1500	750
150 mm	1000	1000	500	500	250

In this research, however, the desired Fabry-Pérot use is not for displacement or laser frequency measurements, but rather for refractive index measuring, tracking, or correcting. If the cavity is assumed fixed, and the supply laser is locked to the resonance peak, then refractive index changes in the cavity can be measured. If the cavity is not perfectly fixed or stable even though it is assumed stable, then cavity instability will show up as a refractive index change, which is undesirable. Ideally, the cavity will be a compact, monolithic structure, which is insensitive to thermal variations in the environment. In practice, the cavity will consist of mirror, supports, mounts, and adjustment mechanisms to fine-tune the alignment. Thus, a smaller cavity is more desirable because the environmental factors are minimized.

The FWHM was determined numerically for the ideal Fabry-Pérot cavities and system, from Figures E.15 and E.16. The FWHM is the width of the peak at the half of the maximum peak value ($\delta\lambda$). After determining $\delta\lambda$, the linewidth in the frequency domain is determined by

$$\delta\nu_\lambda = \frac{\delta\lambda\delta\nu}{\lambda}. \tag{E.27}$$

Once the linewidth is determined, the finesse is found by

$$\mathcal{F} = \frac{\delta\nu}{\delta\nu_\lambda}. \tag{E.28}$$

The linewidths of the five Fabry-Pérot interferometers and their finesse are shown in Table E.3. The linewidth is not affected by the gain in the cavity and nor is it dependent on cavity length. This means the linewidth is the same for both the ideal Fabry-Pérot cavity and the ideal Fabry-Pérot system. Since the maximum value and FWHM are scaled by the same amount, the net difference is zero. The linewidth is not dependent on cavity length because the FSR scales with the cavity length by a counter balancing amount, thus this net effect is also zero.

Since the FSR, however, is dependent on the cavity length, the cavity finesse, which determines the locking stability, does vary between Fabry-Pérot cavity types. Based on this

Table E.3: *Linewidth at full-width half-maximum in megahertz and calculated finesse for each of the five Fabry-Pérot cavities. All surfaces which transmit light are assumed to transmit 0.5% and reflect 99.5%. Any surface which does not transmit light is assumed to have a reflectance of 100%. This is estimated as the ideal case.*

L	$(FP)_R$	$(FP)_T$	$(FP)_Q$	$(FP)_f$	$(FP)_{Qf}$
50 mm	1.20	2.39	0.90	0.60	0.30
150 mm	0.40	0.80	0.20	0.20	0.10
Finesse ($\mathcal{F}$)	2510	1254	1674	2510	2510

analysis, the transmission Fabry-Pérot cavity has the lowest finesse of the five shown. The QWP cavity was marginally better, whereas the reflectance and folded cavities were twice as good. The QWP-folded cavity had the height calculated ideal finesse.

These results do not take into account the inefficiencies in the optical components and it does not account for the back-beam which may saturate the detector. Additionally, the main difference between the transmission and folded Fabry-Pérot cavities and the others is these two interferometers must deal with two mirror surfaces with a reflectance less than 100%. In the other cases, all mirror surfaces are assumed perfect, except the main transmission mirror, which is common in all cases. Table E.4 shows the calculated finesse, assuming all mirror surfaces have the same reflectance coefficient.

Table E.4: *Calculated cavity finesse as a function of mirror efficiency. These values assume all relevant mirrors and reflecting surface have the reflectance efficiency listed, except for the ideal case which was described in Table E.3.*

Reflectance	$(FP)_R$	$(FP)_T$	$(FP)_Q$	$(FP)_f$	$(FP)_{Qf}$
Ideal	2510	1254	1674	2510	2510
99.5%	1257	1254	1003	1254	1003
99%	631.6	625.4	555.9	625.4	555.9
98.5%	425.3	415.7	384.0	415.7	383.9
98%	323.6	311.1	292.9	311.0	292.7
97.5%	263.9	248.2	236.5	248.1	236.3

As the mirror coatings decrease in efficiency, there is a drastic decrease in the finesse, which is expected. However, the dropoff for the transmission Fabry-Pérot is not quite as step as the other four interferometers.

E.6 Summary & Conclusions

Fabry-Pérot interferometry uses multi-beam interference to detect the resonance peak in an optical cavity. When all beams are in phase, the constructive interference occurs, greatly increasing the DC output of the system. Fabry-Pérot interferometers typically have one of three main applications. The first is to stabilize a laser frequency, by locking to a resonance peak in a fixed cavity. The second is to use the Fabry-Pérot cavity displacement to calibrate a sensor. A tunable laser is typically locked to the resonance peak. If the laser remains locked, the tunable laser frequency change is proportional to the cavity length change. The third typical application is to have a tunable laser track a resonance peak in a fixed Fabry-

Pérot cavity. If the cavity is stable, then refractive index changes will be tracked by the tunable laser locked to the resonance peak.

Based on this analysis of these five Fabry-Pérot cavities, the reflectance, folded, and QWP-folded cavity all have the highest ideal finesse, and the QWP-folded cavity has the smallest free spectral range. The net effect is a smaller cavity can be used with the same effect as a larger cavity, to achieve the same free spectral range, linewidth, and finesse. In applications where the cavity stability is critical, the smaller cavities will lead to a higher overall stability because their dimensional change due to environment effects is decreased.

The added bonus of a smaller cavity might be mitigated due to the added alignment components or other special considerations needed in the cavity design for the QWP, folded, and QWP-folded cavities. Additionally, as the mirror efficiency decreases, the dropoff for the transmission Fabry-Pérot cavity is not as steep and it does not have to deal with a high power back-beam. Also, it does not have many components other than two mirrors and their accompanying support structure. Thus, this Fabry-Pérot configuration is well suited for Fabry-Pérot refractometry applications.

Appendix F

Preliminary Optical System

The first generation interferometer configuration comprised a similar layout to the interferometer shown in Figure 6.1. The reference input beam was moved to enter the interferometer on the same side as the measurement input beam, removing the large optical path imbalance between the reference and measurement beam arms for each interfeormeter. The last imbalance to fix was the difference between the sample measurement arm and the refractometer measurement arm. A beamsplitter was needed where the output beams each had the same path length in the glass.

One method to solve this was to use a normal cube beamsplitter at 45° as shown in Figure F.1. This was adapted from researchers at EADS/Astrium and the University of Konstanz in Germany which successfully employed this technique in their adapted Wu-type interferometer [72, 74]. From Snell's Law, the refracted beam passes through at an angle

$$\theta_r = \arcsin\left(\frac{\eta_a \sin(\theta_i)}{\eta_g}\right), \tag{F.1}$$

where $\theta_{i,r}$ are the incident and refracted beams, respectively, and $\eta_{a,g}$ are the air and glass refractive index values, respectively. For most optical glasses, θ_r is typically between 22° and 29°. The beam incident to the splitting surface is not a 45°, which means an uneven splitting ratio will occur when using cube beamsplitters without a special coating to account for this. When a normal 50% beamsplitter is used, the output splitting ratio is approximately 70%/30%.

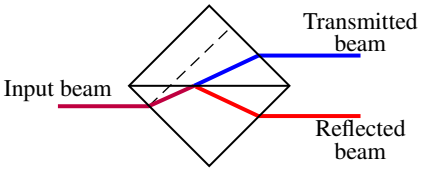

Figure F.1: *Schematic of the rotated beamsplitter. The input and transmitted beams are parallel. The parallelism of the output reflected beam depends on the alignment of the beamsplitter*

F.1 Interferometer Concept

This concept was adapted for this research to devise the interferometer shown in Figure F.2. The interferometer uses a source which has two linearly polarized input beams with frequencies of f_1 and $f_1 + \delta f$ whos initial polarization state allows them to pass through PBS_1. Both beams pass through a 50% beamsplitter turned 45°, resulting in four beams, RM, SR, RR, and SM (top to bottom Figure F.2). The RM and RR beams are the *refractometer-measurement* arm and *refractometer-reference* arm, respectively and interfere to create the refractometer signal. The SR and SM beams are the *sample-reference* arm and *sample-measurement* arm, respectively, and interfere to create the sample measurement signal. The SR and RR beams follow the same path. First they pass through PBS_1, Q_1

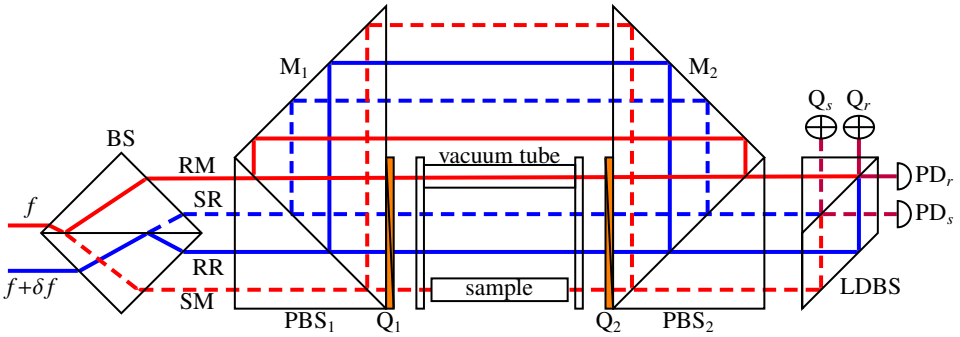

Figure F.2: *Optical schematic of the 1st generation interferometer. This is a dual interferometer with one interferometer measuring refractive index changes and the other measures sample fluctuations. (RM, refractometer-measurement arm; SR, sample-reference arm; RR, refractometer-refrerence arm; SM, sample-measurement arm)*

and Q_2, where the polarization state changes 90°. Both quarter wave plates are oriented to produce a half wave plate when passing through both from the same direction. They then reflect off PBS_2, M_2, M_1, and PBS_1. They pass through Q_1, Q_2, and PBS_2 where they then are combined at the lateral displacement beamsplitter. The RM beam also follows the same exact path except it passes through a vacuum tube twice between the two quarter wave plates.

The SM beam passes through PBS_1 and Q_1 where it reflects off one side of the sample. It passes through Q_1 again and then reflects off PBS_1, M_1, M_2, and PBS_2. It then passes through Q_2, reflects off the other side of the sample, passes through Q_2 again, as well as PBS_2. It then travels through the lateral displacement beamsplitter where it interferes with the SR beam. Ideally, to compensate for the windows of the vacuum tube, the windows are extended through the three other beams.

In this interferometer, the sample signal measures sample length changes, plus refractive index changes and interferometer perturbations. The refractometer signal measures refractive index changes and interferometer perturbations. However, this interferometer largely compensates for interferometer component motions because the motions are largely common to both the sample measurement and refractometer measurement. Additionally, the nonpolarizing beamsplitter used as an interference element creates two equal beams for each measurement. Thus, the difference between the two photodetector signals (PD_s,

PD_r) measures the sample length change while correcting for refractive index effects and, if desired, quadrant detectors (Q_s,Q_r) can measure the sample tilt versus interferometer tilt if needed.

Large, fast displacements should not occur from material stability-induced motion and thus, the measurement environment should be very stable. One main assumption for this interferometer to work effectively is the air refractive index is uniform throughout all beam paths. The added vacuum tube allows the refractometer signal to follow the localized refractive index changes in the system, in a directly correlated wavelength tracker.This eliminates the uncertainty from measuring the refractive index with a separate refractometer (i.e. typical Fabry-Pérot configuration) and determining its cross correlation to the refractive index in this interferometer. Additionally, if the refractive index is uniform throughout the beam paths, the limiting uncertainty in the modified Edlén formula can be overcome because an equation-based correction is not needed [28–30]. This was discussed in more detail in Section 4.3.

The polarization states throughout the interferometer is shown in Figure F.3 to further clarify the beam path evolution. Each beam passes through and reflects off a surface the same number of times and at the same polarization state except for the SM beam because it reflects off the sample. This causes a slight discrepancy in the phase change from reflectance stacking. Because some polarization effects or phase jumps may occur at a reflecting surface, a difference in order can cause an error if the polarization effect or phase jump is large. The net electric field at each detector can be described as

$$\mathbf{E}_s \propto \mathbf{J}_{sys,sm}\mathbf{E}_{sm} + \mathbf{J}_{sys,sr}\mathbf{E}_{sr} \tag{F.2}$$

$$\mathbf{E}_r \propto \mathbf{J}_{sys,rr}\mathbf{E}_{rr} + \mathbf{J}_{sys,rm}\mathbf{E}_{rm} \tag{F.3}$$

where $\mathbf{E}_s$ and $\mathbf{E}_r$ are the net sample and refractometer electric fields, $\mathbf{J}_{sys,i}$ is the Jones matrix representing the system for the i^{th} beam path, and $\mathbf{E}_i$ is the initial electric field for the i^{th} beam. Because this interferometer is largely balanced, the Jones matrices for the SR, RR, and RM beams are identical. The Jones matrix for the SM beam is different from the other three but if there is no source mixing between $\mathbf{E}_f$ and $\mathbf{E}_{f+\delta f}$, then the chance for mixed polarization states and periodic nonlinearity in minimal. Additionally, all important reflection angles are at either 45° or 90°, which minimizes phase change errors and polarization rotation.

There is one instance where a leakage bean can affect the measurement and cause a mixed state, potentially leading to periodic nonlinearity. When the RM, SR, and RR beams pass reflect off PBS2, some leakage component will pass through from improper splitting and alignment. When the beams travel around a second time and then pass through PBS_2, they may overlap with the first pass leakage component. This effect can be minimized by proper alignment techniques. Both PBS_1 and PBS_2 can be slightly tilted which will create an offset between the desired and leakage beams. An iris can then be used to optically isolate the desired beam prior to detecting.

F.2 Source and Data Acquisition

For this interferometer generation, a commercial heterodyne laser [109] with a 20 MHz split frequency was used as the source. The two polarization states were split using a polarizing

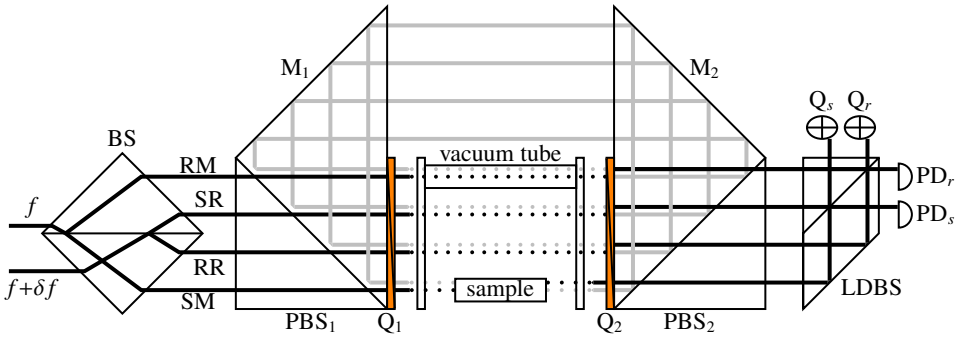

Figure F.3: *Schematic of the 1st generation interferometer showing the polarization state evolution in the interferometer.*

beamsplitter and one state passed through a half wave plate to rotate its polarization state by 90°. Two mirrors were then used to align and steer the beams into the interferometer. After passing through the interferometer, the two signals were detected using commercial photodetectors. The nominal 20 MHz signal was too fast to acquire and generate a phase measurement equipment readily available. Thus, the 20 MHz signal was mixed with a common, 19.975 MHz signal, which results in a signal with 25 kHz and 39.975 MHz components.

The high frequency signals were rejected using a low pass butterworth filter with a cutoff frequency at 30 kHz and the resulting signal was then amplified. Finally, the phase was measured using a lock-in amplifier [106] with a time constant of 300 ms and an output signal between ±1.8 V. A 12-bit data acquisition system [144] was used to collect the signal. Because the data acquisition system was 12 bits over a 20 V range, the minimum phase resolution was approximately 0.5°, corresponding to 0.44 nm. This was enhanced by applying a 14 dB gain prior to acquiring the signal, which means 18 V of the possible 20 V range was used. This increased the resolution to 0.1°, corresponding to a theoretical displacement resolution of 0.09 nm. The phase was measured with a 20 kHz sampling rate every 20 ms (50 Hz) and averaged into a single data point (400 point averaging). Because of lag in the data acquisition computer and loop timing, the effective sampling frequency was 34 Hz.

F.3 Preliminary Measurements

A baseline measurement was desired to estimate whether this interferometer configuration had the potential to measure material stability effectively. Previous research by Ren, *et at.* showed a thin film sample could be used as an effective reference material because the optical path length difference caused by the sample in a balanced interferometer is negligible [148]. Additionally, the thermal expansion of the sample is also negligible because the nominal length is so short. Using a thin film sample, the desired interferometer stability was 20 nm or better. If the initial measurements showed drift at this level or below, then this interferometer configuration was deemed suitable for further development.

The interferometer including the source used in the tests is shown in Figure F.4. This system also used the data acquisition system described in the previous section. The sample measured was an 86 nm thin film of silver coated on a 1 mm thick glass slide. The silver

sample's thermal expansion effects are negligible (approximately 4 pm) and the refractive index effects induced should be no more than the spatially separated effects. A vacuum tube was not included in these measurements because the optical path difference was only 86 nm and the 1 mm glass slide extends through all four beams. The spacing between the two polarizing beamsplitters and the sample was kept minimal (around 4 mm), which limits the room for air flow. Lastly, temperature and pressure were not explicitly monitored nor controlled. From previous experiments, the laboratory temperature fluctuates approximately ±1°C per 12 min to 15 min.

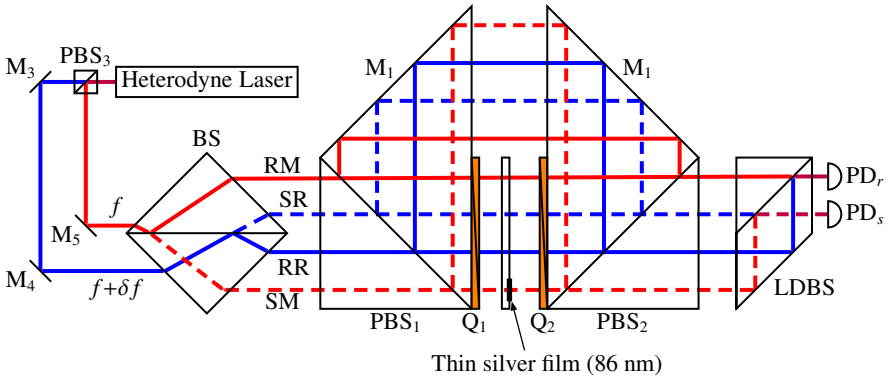

Figure F.4: *Optical schematic for testing the 86 nm thin film sample. The laser source was a standard two frequency, orthogonally polarized axial source split into two spatially separated beams.*

The refractometer signal in this interferometer is the deadpath signal, which should have no phase changes in an ideal measurement situation. Some distinct observations were made during the course of aligning and setting up this interferometer. The most profound observation was the lack of optical power at the detector. Using a 2 GHz oscilloscope, the interference signals were not directly visible. This is most likely from the losses in the optical components. The initial beamsplitter had a very low splitting efficiency. Additionally, none of the optics had anti-reflection coatings, which meant every glass-air transition was a loss of approximately 4% power.

After frequency mixing, filtering, and amplifying, the two 25 kHz interference signals were clearly visible on the oscilloscope. The measured data was logged in 30 min intervals (44 min including lag). An error in the Matlab code used to measure the data caused the measurement to stop after 66 data sets were taken. Also, there was a long delay in between the end of one dataset and the start of the next data set and each starting time and displacement value was reset to zero. This meant is was difficult to piece together the data in one continuous measurement.

However, analyzing the data as 66 separate measurements of the thin film sample was possible. Figure F.5 shows each of the 66 measurements for the 44 minute intervals. The results show the measured length change was within 60 nm with the majority of the values in an 8 nm spread around zero. These measurements show two distinct attributes: the observable linear drift was minimal and the noise level was approximately the same between all measurements. This is a clear indication that this interferometer produces repeatable

measurements with minimal drift. A linear fit was taken of each of the 66 measurements to

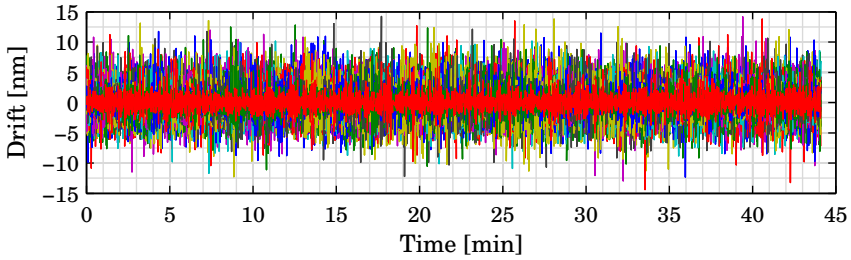

Figure F.5: *Measured length change of the thin film sample for 66 measurements. The ±2σ noise band is approximately 8 nm for each of the measurements. No appreciable linear drift was detected.*

determine the linear drift. Figure F.6 shows the drift rate in pm·hr^{-1} on the left axis for each of these measurements. The mean linear drift rate was 0.4 pm·hr^{-1} with a standard deviation value of 16.5 pm·hr^{-1} when comparing the drift from all 66 measurements. The spread in these drift rates indicate some measurement dependency on the surrounding environment and optical setup. However, these measured values are much lower than anticipated. The

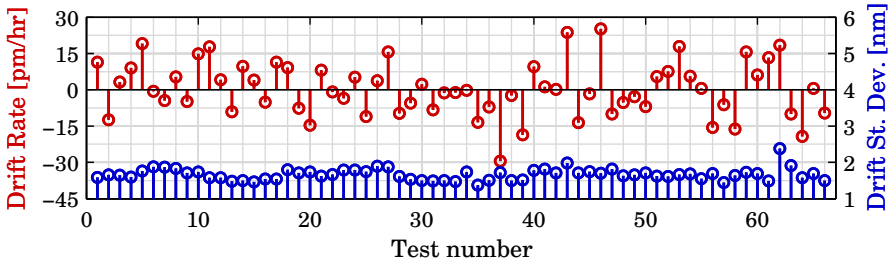

Figure F.6: *Linear drift rate and noise rms for each of the 66 measurements. The measurements showed no appreciable linear drift but the relatively high noise level prohibits a definitive assessment.*

noise level in the system was much higher than anticipated. The mean measured length change was 1.9 nm rms, and the maximum of the 66 measurements was 2.8 nm rms and the minimum was 1.5 nm rms, which is shown in Figure F.6 on the right axis. This noise level is approximately two orders of magnitude higher than the estimated drift rate which suggests a true value for drift cannot be determined with noise levels this high. The high noise level is a combination of a low signal to noise ratio at the detector and perturbations from the surrounding environment.

The long term drift was assessed after correcting the data acquisition system to properly log measurements without resetting to zero after each interval. The same 86 nm thin film sample was measured using the identical signal conditioning system for measurement periods of 9.3 hours and 12.7 hours. The results from these measurements are shown in Figure F.7 with the ±2σ bands shown in the dashed lines. The linear drift from the 12.7 hr

measurement was -14.4 pm and from the 9.3 hr measurement, it was 4 pm. This is an average drift rate of 1.1 pm·hr^{-1} for the 12.7 hr measurement and 0.4 pm·hr^{-1} for the 9.3 hr measurement. Both of these measurements showed a length change of 1.6 nm rms. As with

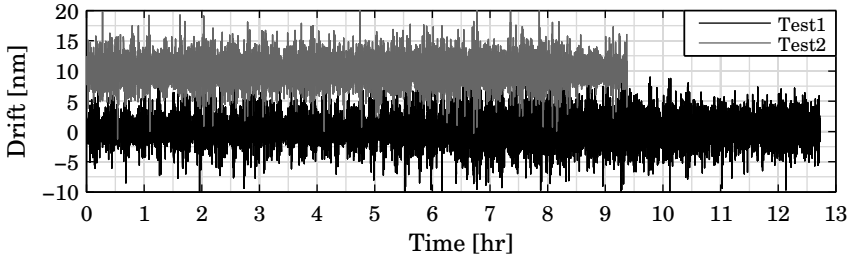

Figure F.7: *Two long term measurements of the thin film sample. Both measurements showed a minimal drift rate.*

the short term repeatability experiments, the measured linear drift rate was much less than the observed noise. Both of these drift rates are in agreement with drift rate results from the short term measurements. However, the exact drift rate is difficult to determine due to the relatively high amounts of noise.

There are three main sources of measurement noise: noise from the laser source, noise from the electronics and data acquisition, and environmental fluctuations. Noise from the laser source and electronics was measured by placing a 45° polarizer directly in front of the laser source. The beam was then split using a 50% beam splitter and detected using the same two detectors from the experiments. The phase difference between the two signals was processed and measured using the same electronics and characteristics as in the experiments. Figure F.8 shows the measured phase noise from the laser head. These results show the laser, signal processing, and data acquisition contribute approximately 0.6 nm (±2σ) in the thin film experiments.

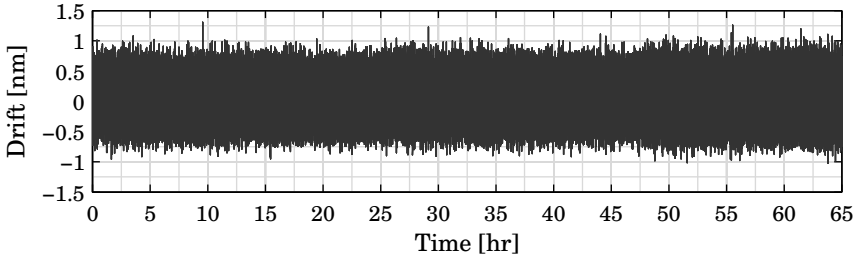

Figure F.8: *Long term phase noise of the laser source, detection, and data acquisition system. While no linear drift is measured, this combination of source to data acquisition has a much higher noise level than anticipated.*

The Allan variance from the laser and electronics noise and the two long term measurements is shown in Figure F.9. The variance show similar trends with the laser and

electronics noise at a consistent order of magnitude lower until approximately 300 seconds of averaging. After this time, it is unclear whether the long term measurements start to converge with the laser and electronics. These measurements do not show the characteristic upswing that occurs in typical Allan variance figures [149]. This suggests that this interferometer is stable for long term measurements.

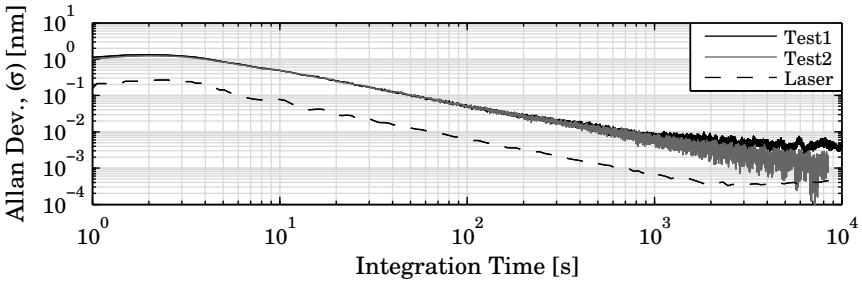

Figure F.9: *Allan variance of the two long term drift measurements of the thin film sample compared to the laser phase noise. This did not show the typical characteristic up-swing with long integration times signifying this system has minimal drift.*

The phase noise from the lock-in amplifier was assessed by using a function generator and a BNC splitter to send the same signal to the measurement and reference inputs in the lock-in amplifier. This gives an indication of whether the laser phase noise is from the frequency/intensity stability of the laser head itself or the phase detectors and data acquisition. The measured results showed a phase noise of approximately 0.2 nm ($\pm 2\sigma$), which is three times lower than the measured laser phase noise.

One parameter that was not taken into consideration when measuring the laser phase noise was the optical power at the detector. The optics used in these measurements were not anti-reflection coated, which means approximately 4% of the light was lost at each of the approximately 28 glass-air transitions and 10% at each of the three mirror surfaces. Assuming 300 μW of power from the source, that leaves about 15 μW of power assuming all beamsplitters were perfect. Additionally, a portion of the beam was lost due to using a pin photodiode. When the laser phase noise was directly measured, the measured signal was clearly visible on an oscilloscope. However, in the thin film experiments, the signal was buried in noise due to the low optical power (approximately 1 μW to 3 μW) at the detector. The signal could only be seen on the oscilloscope after frequency mixing, low pass filtering, and then amplifying by 60 dB. This lack of power contributes to a low signal to noise ratio, which must be addressed.

The tilting effect on the sample was not addressed in this version. It is possible that the observed displacements could be attributed to rotational motions of the thin film sample. Based on optical modeling, the sample tip and tilt sensitivity is approximately 11 pm·μrad^{-1} and 13 pm·μrad^{-1}, respectively. The effects of tip and tilt should be negligible compared to the observed noise level.

The temperature in the laboratory has been measured previously with ±1°C changes every 12 min to 15 min. The refractive index changes are largely common between both measurement and reference signals and the sample creates only an additional 86 nm of

optical path difference, which can be considered negligible for these experiments. What is not clear based on this information is the effect of thermal gradients and localized refractive index changes in the glass. Because the temperature variations can be large, and rapid, this can cause significant changes of the glass refractive index, which will be translated to phase noise at the detector. These issues will be evaluated indepth when improvements to the system are performed.

F.4 1st Generation Summary & Conclusions

This single pass interferometer was designed, built, and tested for both short term and long term drift using a 86 nm thin film silver sample. The thin film sample was chosen because it reduces the effect from refractive index and laser frequency changes, while still having the same beam paths in the system as with a sample. In a non-controlled, but shielded environment, the mean short term and long term linear drift estimates were approximately 1 pm·hr^{-1}, which was much lower than anticipated.

The short term measurements showed a fairly repeatable trend with an rms drift rate of 16.5 pm·hr^{-1}, which is about 33 times higher than the mean drift rate. This shows some influence from the surrounding environment and dependence on optical mount stability.

Although the estimated linear drift values were higher from the short term measurements than the long term measurements, the noise level prohibits a proper estimate of the actual value. Even with the measured noise level, typically, most measurements will exhibit some noticeable drift. Because these measurements did not exhibit any appreciable amount of drift, it can be inferred this interferometer configuration is highly insensitive to its own stability. Another factor that skews the long term drift to appear better is that it may be temperature induced drift. If this is the case, the temperature fluctuations will cause positive and negative length changes to be measured, which averages out over time.

The high noise yet low drift behavior could also be from a spurious signal in the data acquisition system. Because the optical power of the heterodyne signal at 20 MHz was very low, a stray signal in the electronics at either 20 MHz or at 25 kHz could easily cause the wrong signal to be measured. This was check separately for each of the peripheral components in the data acquisition and none was found. Also, the data showed consistent measurements taken over a period of about 2 weeks, which is another reason to suspect a spurious signal was not being measured.

The next generation interferometer for this research must address several issues. The two largest issues are the noise in the detection and data acquisition system, and the lack of optical power at the detector. Optics with anti-reflection coatings and a higher powered laser source can help reduce both issues. Another issue to address is the beam separation. In the current system, the spacing between the beams was 5 mm. In practice, it is difficult to place a sample without clipping another beam. Additionally, the vacuum cell will need space for the beam to pass though while having walls sufficiently thick to support the vacuum.

Appendix G

Power Spectral Density Plots

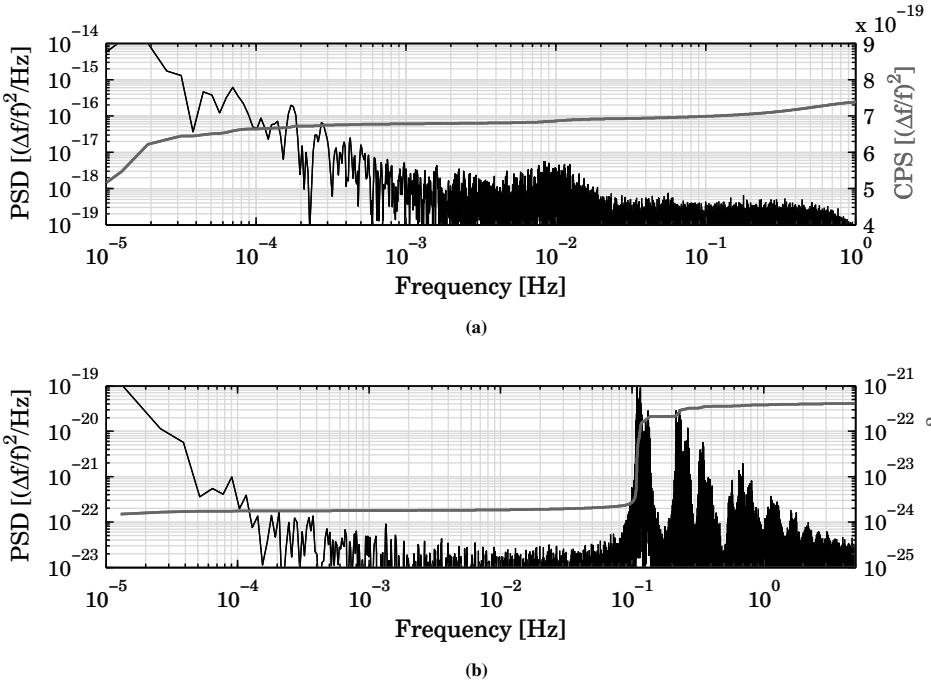

Figure G.1: *Fractional frequency stability power spectral density and cumulative power spectrum of the 3-mode laser using the first controller specifications (a) and the second controller after making improvements and removing thermal mass.*

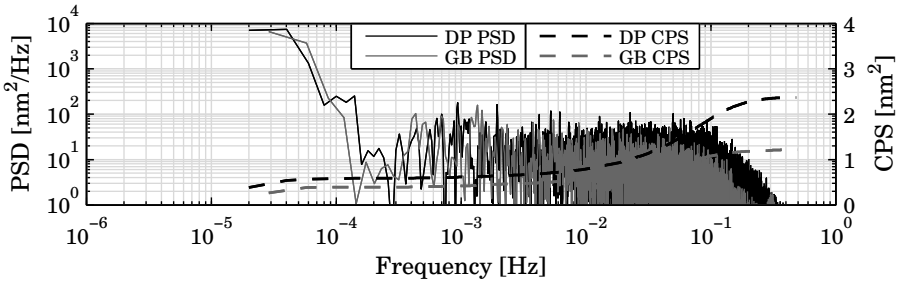

Figure G.2: *Power spectral density and cumulative power spectrum of the double deadpath (DP) and 30 mm gauge block (GB) measurements from the 1st Measurement System.*

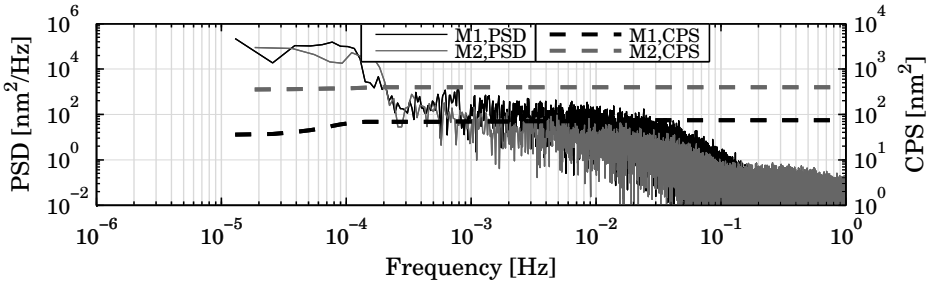

Figure G.3: *Power spectral density and cumulative power spectrum of the two deadpath measurements from the 2nd Measurement System.*

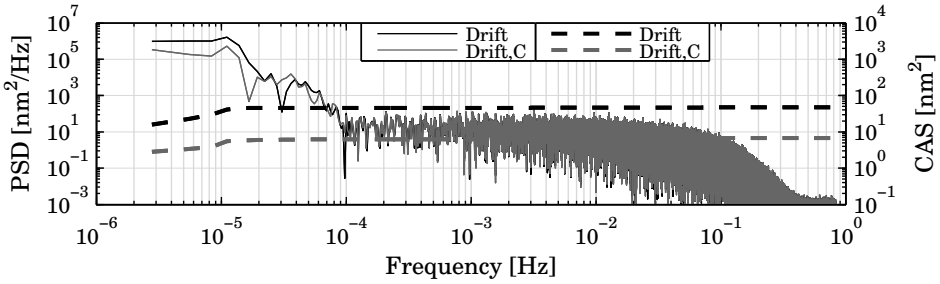

Figure G.4: *Power spectral density and cumulative power spectrum of the long term deadpath measurement from the 3rd Measurement System.*

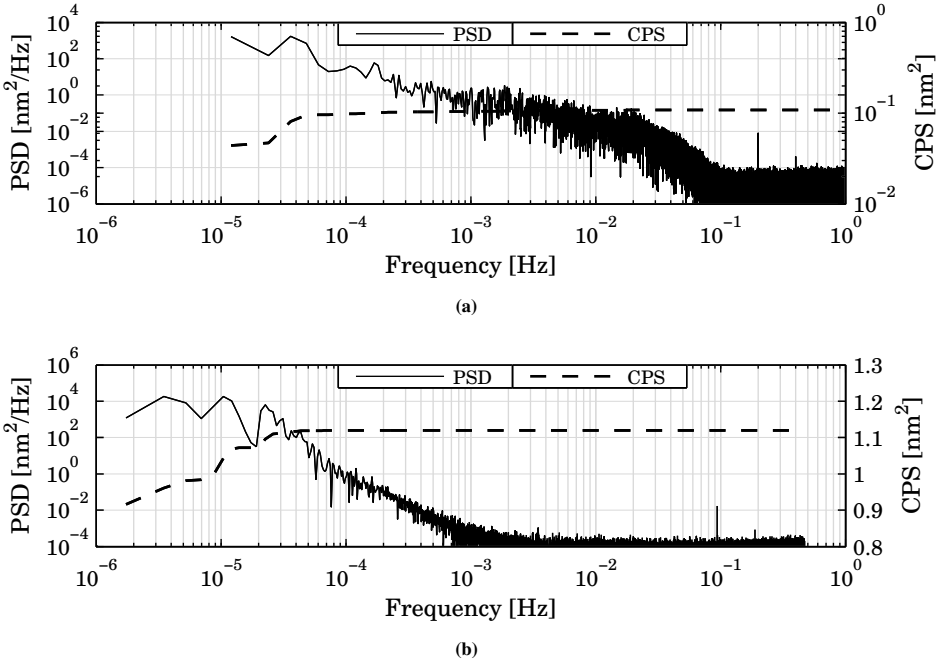

Figure G.5: *Power spectral density and cumulative power spectrum of the long term deadpath measurements from the 4th Measurement System in air (a) and vacuum (b).*

References

[1] Smartt RN, Ciddor PE, Leistner AJ, Seckold JA, Long-term stability of optical surfaces. *Optical Engineering* 2002;**41**:2688–2691.

[2] Schmidtlin EG, Shaklan SB, Carlson AE, Novel wide-field-of-view laser retroreflector for the space interferometry mission. *In: Astronomical Interferometry, Reasenberg RD and Unwin SC, eds, Proceedings of the SPIE* 1998;**3350**(1):81–88.

[3] Ressel S, Gohlke M, Rauen D, Schuldt T, Kronast W, Mescheder U, Johann U, Weise D, Braxmaier C, Ultrastable assembly and integration technology for ground- and space-based optical systems. *Applied Optics* 2010;**49**(22):4296–4303.

[4] Doiron TD, Beers JS, The gauge block handbook. *Technical report*, 2005.

[5] Medicus KM, Chaney M, John E Brodziak J, Davies A, Interferometric measurement of phase change on reflection. *Applied Optics* 2007;**46**(11):2027–2035.

[6] Seugling RM, LeBrun T, Smith ST, Howard LP, A six-degree-of-freedom precision motion stage. *Review of Scientific Instruments* 2002;**73**(6):2462–2468.

[7] Angel R, Kang T, Cuerden B, Active thermal figure control for large, lightweight honeycomb mirrors in vacuum and space. *In: proceedings of Coronagraph Workshop 2006, Pasadena, CA, USA* 2006;**1**:321–324.

[8] Woody SC, Smith ST, Damping of a thin-walled honeycomb structure using energy absorbing foam. *Journal of Sound and Vibration* 2006;**291**(1-2):491–502.

[9] Berthold JW, Jacobs SF, Norton MA, Dimensional stability of fused silica, invar, and several ultra-low thermal expansion materials. *Metrologia* 1977;**13**(1):9–16.

[10] Kuriyama Y, Yokoyama Y, Ishii Y, Ishikawa J, Makino H, Development of a new interferometric measurement system for determining the main characteristics of gauge blocks. *CIRP Annals - Manufacturing Technology* 2006;**55**(1):563–566.

[11] Schödel R, Ultra-high accuracy thermal expansion measurements with ptb's precision interferometer. *Measurement Science and Technology* 2008;**19**(8):084003 (11pp).

[12] International Standard ISO 3650: Geometrical Product Specifications (GPS)–Length standards–Gauge Blocks. International Organization for Standardization, 2nd edition. 1998.

[13] International Standard ISO 1: Geometrical Product Specifications (GPS)–Standard reference temperature for geometrical product specification and verification. International Organization for Standardization, 2nd edition. 2002.

[14] International Standard ISO 15530: Geometrical Product Specifications (GPS)–Coordinate measuring machines (CMM): Technique for determining the uncertainty of measurement. International Organization for Standardization. 2004.

[15] ASME B89.4.1: Methods for Performance Evaluation of Coordinate Measuring Machines. ASME International. 1997.

[16] Thompson A, Taylor BN, Guide for the Use of the International System of Units (SI). *Technical Report Special Publication 811*, NIST, 2008.

[17] Giacomo P, News from the BIPM. *Metrologia* 1984;**20**(1):25–30.

[18] Quinn TJ, *Mise en Pratique* of the Definition of the Metre (1992). *Metrologia* 1994; **30**(5):523–541.

[19] Guide to the expression of uncertainty in measurement, first edition, International Organization for Standardization (Geneva, Switzerland). 2008.

[20] Taylor BN, Kuyatt CE, Guidelines for evaluating and expressing the uncertainty of nist measurement results. *Technical Report Technical Note 1297*, NIST, 1994.

[21] Winters M, Model 100 Iodine-Stabilized HeNe Laser. Winters Electro-Optics, Inc, 7227 Mt. Sherman Rd. Longmont, CO 80503 USA, 1995.

[22] Bennett SJ, An absolute interferometric dilatometer. *Journal of Physics E: Scientific Instruments* 1977;**10**(5):525–530.

[23] Okaji M, Imai H, A practical measurement system for the accurate determination of linear thermal expansion coefficients. *Journal of Physics E: Scientific Instruments* 1984;**17**(8):669–673.

[24] Birch KP, An automatic absolute interferometric dilatometer. *Journal of Physics E: Scientific Instruments* 1987;**20**(11):1387.

[25] Wolff EG, Savedra RC, Precision interferometric dilatometer. *Review of Scientific Instruments* 1985;**56**(7):1313–1319.

[26] Suska J, Tschirnich J, An interferometric device for precise thermal expansion measurements on bar-shaped materials. *Measurement Science and Technology* 1999; **10**(5):N55.

[27] Ren D, Lawton KM, Miller JA, A double-pass interferometer for measurement of dimensional changes. *Measurement Science and Technology* 2008;**19**(2):025303 (4pp).

[28] Edlén B, The refractive index of air. *Metrologia* 1966;**2**(2):71–80.

[29] Birch KP, Downs MJ, An updated edlen equation for the refractive index of air. *Metrologia* 1993;**30**:155–162.

[30] Birch KP, Downs MJ, Correction to the updated edlen equation for the refractive index of air. *Metrologia* 1994;**31**(4):315–316.

[31] Estler WT, High-accuracy displacement interferometry in air. *Applied Optics* 1985; **24**(6):808–815.

[32] Hou W, Wilkening G, Investigation and compensation of the nonlinearity of heterodyne interferometers. *Precision Engineering* 1992;**14**(2):91–98.

[33] De Freitas JM, Player MA, Polarization effects in heterodyne interferometry. *Journal of Modern Optics* 1995;**42**(9):1875–1899.

[34] Stone JA, Howard LP, A simple technique for observing periodic nonlinearities in michelson interferometers. *Precision Engineering* 1998;**22**(4):220–232.

[35] Badami VG, Patterson SR, A frequency domain method for the measurement of nonlinearity in heterodyne interferometry. *Precision Engineering* 2000;**24**(1):41–49.

[36] Eom T, Choi T, Lee K, Choi H, Lee S, A simple method for the compensation of the nonlinearity in the heterodyne interferometer. *Measurement Science and Technology* 2002;**13**(2):222–225.

[37] Schmitz TL, Beckwith JF, An investigation of two unexplored periodic error sources in differential-path interferometry. *Precision Engineering* 2003;**27**(3):311–322.

[38] Schmitz TL, III LH, Chu D, Kalem L, Bench-top setup for validation of real time, digital periodic error correction. *Precision Engineering* 2006;**30**(3):306–313.

[39] Schmitz TL, Kim HS, Monte carlo evaluation of periodic error uncertainty. *Precision Engineering* 2007;**31**(3):251–259.

[40] Eom TB, Kim JA, Kang CS, Park BC, Kim JW, A simple phase-encoding electronics for reducing the nonlinearity error of a heterodyne interferometer. *Measurement Science and Technology* 2008;**19**(7):075302 (6pp).

[41] Schmitz TL, Chu DC, Kim HS, First and second order periodic error measurement for non-constant velocity motions. *Precision Engineering* 2009;**33**(4):353–361.

[42] Kim HS, Schmitz TL, Periodic error calculation from spectrum analyzer data. *Precision Engineering* 2010;**34**(2):218–230.

[43] Agilent Technologies, Inc., 5301 Stevens Creek Blvd, Santa Clara, CA 95051 USA, Agilent 5517D Laser Head.

[44] Zygo Corporation, Laurel Brook Road Middlefield, CT 06455 USA, Zygo 7714 Laser Head.

[45] Born M, Wolf E, Principles of Optics: Electromagnetic Theory of Propagation, Interference and Diffraction of Light. 7th edition, Cambridge University Press, 1999.

[46] Hecht E, Optics. 4th edition, Addison Wesley, 2002.

[47] Pedrotti FL, Pedrotti LS, Introduction to Optics. 2nd edition, Prentice Hall, 1993.

[48] Kreyszig E, Advanced Engineering Mathematics. 8th edition, John Wiley & Sons, Inc., 1999.

[49] Demarest FC, High-resolution, high-speed, low data age uncertainty, heterodyne displacement measuring interferometer electronics. *Measurement Science and Technology* 1998;**9**(7):1024–1030.

[50] About lock-in amplifiers. *White paper*, Stanford Research Systems, 1290-D Reamwood Avenue Sunnyvale, CA 94089, 2010.

[51] Horowitz P, Hill W, The Art of Electronics. 2nd edition, Cambridge University Press, 1989.

[52] Oka K, Tsukada M, Ohtsuka Y, Real-time phase demodulator for optical heterodyne detection processes. *Measurement Science and Technology* 1991;**2**(2):106–110.

[53] Oldham NM, Kramar JA, Hetrick PS, Teague EC, Electronic limitations in phase meters for heterodyne interferometry. *Precision Engineering* 1993;**15**(3):173–179.

[54] Holmes ML, Analysis and design of a long range scanning stage. Ph.D. thesis, University of North Carolina at Charlotte, 1998.

[55] Pollack SE, Analytic and interferometric techniques for the laser interferometer space antenna. Ph.D. thesis, University of Colorado, 2005.

[56] Shaddock D, Ware B, Halverson PG, Spero RE, Klipstein B, Overview of the lisa phasemeter. In: AIP Conf. Proc., volume 873, AIP, Greenbelt, Maryland (USA), 654–660.

[57] Bönsch G, Potulski E, Measurement of the refractive index of air and comparison with modified Edlén's formulae. *Metrologia* 1998;**35**(2):133–139.

[58] Bobroff N, Recent advances in displacement measuring interferometry. *Measurement Science and Technology* 1993;**4**(9):907–926.

[59] Quenelle RC, Nonlinearity in interferometer measurements. *Hewlett Packard J* 1983; **34**:10.

[60] Cosijns SJAG, Haitjema H, Schellekens PHJ, Modeling and verifying non-linearities in heterodyne displacement interferometry. *Precision Engineering* 2002;**26**(4):448–455.

[61] Haitjema H, Cosijns SJAG, Roset NJJ, Jansen MJ, Improving a commercially available heterodyne laser interferometer to sub-nm uncertainty. *In: Recent Developments in Traceable Dimensional Measurements, Decker JE and Brown N, eds, Proceedings of the SPIE* 2003;**5190**(2):347–354.

[62] Chu D, Ray A, Nonlinearity measurement and correction of metrology data from an interferometer system. *In: Proceedings of the 4th euspen international conference, 30 May–3 June, Glasgow, UK* 2004;:301–304.

[63] Tanaka M, Yamagami T, Nakayama K, Linear interpolation of periodic error in a heterodyne laser interferometer at subnanometer levels [dimension measurement]. *IEEE Transactions on Instrumentation and Measurement* 1989;**38**(2):552–554.

[64] Wu C, Lawall J, Deslattes RD, Heterodyne interferometer with subatomic periodic nonlinearity. *Applied Optics* 1999;**38**(19):4089–4094.

[65] Lawall J, Kessler E, Michelson interferometry with 10 pm accuracy. *Review of Scientific Instruments* 2000;**71**(7):2669–2676.

[66] Schmitz T, Beckwith J, Acousto-optic displacement-measuring interferometer: a new heterodyne interferometer with angstrom-level periodic error. *Journal of Modern Optics* 2002;**49**(13):2105–2114.

[67] Joo KN, Ellis JD, Spronck JW, van Kan PJM, Munnig Schmidt RH, Simple heterodyne laser interferometer with subnanometer periodic errors. *Optics Letters* 2009;**34**(3):386–388.

[68] Joo KN, Ellis JD, Buice ES, Spronck JW, Munnig Schmidt RH, High resolution heterodyne interferometer without detectable periodic nonlinearity. *Optics Express* 2010;**18**(2):1159–1165.

[69] Schmitz TL, Chu D, Houck III L, First-order periodic error correction: validation for constant and non-constant velocities with variable error magnitudes. *Measurement Science and Technology* 2006;**17**(12):3195.

[70] Ellis JD, Baas M, Spronck JW, Errors in measurement and compensation algorithms for periodic nonlinearity correction. *In: proceedings of the 25th ASPE annual meeting, 31 Oct-5 Nov, Atlanta, GA, USA* 2010;.

[71] Machado JC, Heinrich T, Schuldt T, Gohlke M, Lucarelli S, Weise D, Johann U, Peters A, Braxmaier C, Picometer resolution interferometric characterization of the dimensional stability of zero CTE CFRP. *In: Advanced Optical and Mechanical Technologies in Telescopes and Instrumentation, Atad-Ettedgui E and Lemke D, eds, Proceedings of the SPIE* 2008;**7018**(1):70183D.

[72] Schuldt T, Gohlke M, Weise D, Peters A, Johann U, Braxmaier C, A compact high-sensitivity heterodyne interferometer for industrial metrology. *In: Optical Sensors 2008, Berghmans F, Mignani AG, Cutolo A, Meyrueis PP, Pearsall TP, eds, Proceedings of the SPIE* 2008;**7003**(1):70030Y.

[73] Cordero J, Heinrich T, Schuldt T, Gohlke M, Lucarelli S, Weise D, Johann U, Braxmaier C, Interferometry based high-precision dilatometry for dimensional characterization of highly stable materials. *Measurement Science and Technology* 2009;**20**(9):095301.

[74] Schuldt T, Gohlke M, Weise D, Johann U, Peters A, Braxmaier C, Picometer and nanoradian optical heterodyne interferometry for translation and tilt metrology of the LISA gravitational reference sensor. *Classical and Quantum Gravity* 2009; **26**(8):085008.

[75] Müller H, wey Chiow S, Long Q, Vo C, Chu S, Active sub-Rayleigh alignment of parallel or antiparallel laser beams. *Optics Letters* 2005;**30**(24):3323–3325.

[76] Hahn I, Weilert M, Wang X, Goullioud R, A heterodyne interferometer for angle metrology. *Review of Scientific Instruments* 2010;**81**(4):045103.

[77] Lawall J, Pedulla JM, Coq YL, Ultrastable laser array at 633 nm for real-time dimensional metrology. *Review of Scientific Instruments* 2001;**72**(7):2879–2888.

[78] Joo KN, Ellis JD, Spronck JW, van Kan PJ, Munnig Schmidt RH, Simple heterodyne laser interferometer without periodic errors. *In: Proceedings of the 9th International Symposium on Measurement Technology and Intelligent Instruments, 29 Jun - 2 July, St Petersburg, Russia* 2009;.

[79] Joo KN, Ellis JD, Spronck JW, Munnig Schmidt RH, A novel heterodyne displacement interferometer with no detectable periodic nonlinearity and optical resolution doubling. *In: Proceedings of the 10th euspen International Conference, 31 May - 3 Jun, Delft, The Netherlands* 2010;.

[80] Thorlabs, Inc., 435 Route 206 North, Newton, NJ 07860 USA, 3-Axis NanoMax, part no. MAX311/M.

[81] Stanford Research Systems, Inc., 1290-D Reamwood Avenue, Sunnyvale, CA 94089 USA, SRS830 Digital Lock-In Amplifier.

[82] Agilent Technologies, Inc., 5301 Stevens Creek Blvd, Santa Clara, CA 95051 USA, Agilent Plane Mirror Interferometer, E1826G.

[83] Hou W, Zhao X, Drift of nonlinearity in the heterodyne interferometer. *Precision Engineering* 1994;**16**(1):25–35.

[84] Ciddor PE, Refractive index of air: new equations for the visible and near infrared. *Applied Optics* 1996;**35**(9):1566–1573.

[85] Schellekens P, Spronck J, van de Pasch E, van der Wolf A, Design and results of a new interference refractometer based on a commercially available laserinterferometer. *CIRP Annals - Manufacturing Technology* 1986;**35**(1):387–391.

[86] Schellekens P, Wilkening G, Reinboth F, Downs MJ, Birch KP, Spronck J, Measurements of the refractive index of air using interference refractometers. *Metrologia* 1986;**22**(4):279–287.

[87] Renkens M, Schellekens P, An accurate interference refractometer based on a permanent vacuum chamber - development and results. *CIRP Annals - Manufacturing Technology* 1993;**42**(1):581–583.

[88] Terrien J, An air refractometer for interference length metrology. *Metrologia* 1965; **1**(3):80–83.

[89] Agilent Technologies, Inc., 5301 Stevens Creek Blvd, Santa Clara, CA 95051 USA, Agilent 10717A Wavelength Tracker. 2002.

[90] Fox RW, Washburn BR, Newbury NR, Hollberg L, Wavelength references for interferometry in air. *Applied Optics* 2005;**44**(36):7793–7801.

[91] Ishige M, Aketagawa M, Quoc TB, Hoshino Y, Measurement of air-refractive-index fluctuation from frequency change using a phase modulation homodyne interferometer and an external cavity laser diode. *Measurement Science and Technology* 2009;**20**(8):084019.

[92] Quoc TB, Ishige M, Ohkubo Y, Aketagawa M, Measurement of air-refractive-index fluctuation from laser frequency shift with uncertainty of order 10^{-9}. *Measurement Science and Technology* 2009;**20**(12):125302.

[93] Ishida A, Two-wavelength displacement-measuring interferometer using second-harmonic light to eliminate air-turbulence-induced errors. *Japanese Journal of Applied Physics* 1989;**28**(Part 2, No. 3):L473–L475.

[94] Meiners-Hagen K, Abou-Zeid A, Refractive index determination in length measurement by two-colour interferometry. *Measurement Science and Technology* 2008;**19**(8):084004 (5pp).

[95] Korpelainen V, Lassila A, Acoustic method for determination of the effective temperature and refractive index of air in accurate length interferometry. *Optical Engineering* 2004;**43**(10):2400–2409.

[96] Wetzels S, Schellekens P, Development of a traceable laser-based displacement calibration system with nanometer accuracy. *CIRP Annals - Manufacturing Technology* 1997;**46**(1):481–484.

[97] Haitjema H, Schellekens PHJ, Wetzels SFCL, Calibration of displacement sensors up to 300 μm with nanometre accuracy and direct traceability to a primary standard of length. *Metrologia* 2000;**37**(1):25–33.

[98] Howard L, Stone J, Fu J, Real-time displacement measurements with a fabry-perot cavity and a diode laser. *Precision Engineering* 2001;**25**(4):321–335.

[99] Cosijns S, Haitjema H, Schellekens P, Traceable calibration of non-linearities in laser interferometers. *In: proceedings of the ASPE Summer Topical: Precision Interferometric Metrology, 20–22 July, Middletown, CT* 2005;.

[100] Eickhoff ML, Hall JL, Real-time precision refractometry: new approaches. *Applied Optics* 1997;**36**(6):1223–1234.

[101] Topçu S, Alayli Y, Wallerand JP, Juncar P, Heterodyne refractometer and air wavelength reference at 633 nm. *Eur Phys J Appl Phys* 2003;**24**(1):85–90.

[102] Drever RWP, Hall JL, Kowalski FV, Hough J, Ford GM, Munley AJ, Ward H, Laser phase and frequency stabilization using an optical resonator. *Applied Physics B: Lasers and Optics* 1983;**31**:97–105.

[103] Yariv A, Quantum Electronics. 3rd edition, New York: Wiley, 1988.

[104] JDS Uniphase Corporation, 430 N. McCarthy Blvd., Milpitas, CA 95035 USA, JDSU Helium Neon Laser Tube model 1008.

[105] Thorlabs, Inc., 435 Route 206 North, Newton, NJ 07860 USA, Electo-optic modulator, part no. EO-PM-NR-C1.

[106] AMETEK Advanced Measurement Technology, Inc., 801 South Illinois Avenue, Oak Ridge, TN 37831-2011 USA, Model 5210 Lock-in Amplifier.

[107] Newport Corporation, 1791 Deere Avenue, Irvine, CA 92606 USA, Spectra Physics Laser Model 117A.

[108] Sommargren GE, Apparatus to transform a single frequency, linearly polarized laser beam into a beam with two, orthogonally polarized frequencies. 1987.

[109] Zygo Corporation, Laurel Brook Road Middlefield, CT 06455 USA, Zygo 7702 Laser Head.

[110] Hanes GR, Dahlstrom CE, Iodine hyperfine structure observed in saturated absorption at 633 nm. *Applied Physics Letters* 1969;**14**(11):362–364.

[111] Wallard AJ, The reproducibility of 633-nm lasers stabilized by $^{127}I_2$. *IEEE Transactions on Instrumentation and Measurement* 1974;**23**(4):532–535.

[112] Jennings DA, Pollack CR, Peterson FR, Drullinger RE, Evenson KM, Wells JS, Hall JL, Layer HP, Direct frequency measurement of the i_2-stabilized He-Ne 473-THz (633-nm) laser. *Optics Letters* 1983;**8**:136–138.

[113] Lazar J, Číp O, Jedlička P, Tunable extended-cavity diode laser stabilized on iodine at λ = 633 nm. *Appl Opt* 2000;**39**(18):3085–3088.

[114] Lazar J, Číp O, Electronics for he-ne-i_2 stabilized laser with digital control. *Review of Scientific Instruments* 1997;**68**(10):3660–3665.

[115] Mäkinen J, Ståhlberg B, Long-term frequency stability and temperature response of a poliarzation-stabilized he-ne laser. *Measurement* 1998;**24**(3):179–185.

[116] Madej AA, Bernard JE, Robertsson L, Ma LS, Zucco M, Windeler RS, Long-term absolute frequency measurements of 633 nm iodine-stabilized laser standards at nrc and demonstration of high reproducibility of such devices in international frequency measurements. *Metrologia* 2004;**41**(3):152–160.

[117] Mungall AG, Bailey R, Daams H, Morris D, A re-evaluation of the nrc long cesium beam frequency standard. *Metrologia* 1968;**4**(4):165–168.

[118] Wynands R, Weyers S, Atomic fountain clocks. *Metrologia* 2005;**42**(3):S64–S79.

[119] Oskay WH, Diddams SA, Donley EA, Fortier TM, Heavner TP, Hollberg L, Itano WM, Jefferts SR, Delaney MJ, Kim K, Levi F, Parker TE, Bergquist JC, Single-atom optical clock with high accuracy. *Phys Rev Lett* 2006;**97**(2):020801.

[120] Diddams SA, Jones DJ, Ye J, Cundiff ST, Hall JL, Ranka JK, Windeler RS, Holzwarth R, Udem T, Hänsch TW, Direct link between microwave and optical frequencies with a 300 THz femtosecond laser comb. *Phys Rev Lett* 2000;**84**(22):5102–5105.

[121] Holzwarth R, Udem T, Hänsch TW, Knight JC, Wadsworth WJ, Russell PSJ, Optical frequency synthesizer for precision spectroscopy. *Phys Rev Lett* 2000;**85**(11):2264–2267.

[122] Cundiff ST, Ye J, Hall JL, Optical frequency synthesis based on mode-locked lasers. *Review of Scientific Instruments* 2001;**72**(10):3749–3771.

[123] Jones RJ, Diels JC, Stabilization of femtosecond lasers for optical frequency metrology and direct optical to radio frequency synthesis. *Phys Rev Lett* 2001; **86**(15):3288–3291.

[124] Udem T, Holzwarth R, Hänsch TW, Optical frequency metrology. *Nature* 2002; **416**:233–237.

[125] Ye J, Schnatz H, Hollberg L, Optical frequency combs: from frequency metrology to optical phase control. *IEEE Journal of Selected Topics in Quantum Electronics* 2003; **9**(4):1041–1058.

[126] Cundiff ST, Ye J, Colloquium: Femtosecond optical frequency combs. *Rev Mod Phys* 2003;**75**(1):325–342.

[127] Kim YJ, Jin J, Kim Y, Hyun S, Kim SW, A wide-range optical frequency generator based on the frequency comb of a femtosecond laser. *Opt Express* 2008;**16**(1):258–264.

[128] Baer T, Kowalski FV, Hall JL, Frequency stabilization of a 0.633-μm He-Ne longitudinal Zeeman laser. *Applied Optics* 1980;**19**:3173–3177.

[129] Balhorn R, Kunzmann H, Lebowsky F, Frequency stabilization of internal-mirror helium-neon lasers. *Applied Optics* 1972;**11**(4):742–744.

[130] Sommargren G, A new laser measurement system for precision metrology. *Precision Engineering* 1987;**9**(4):179–184.

[131] Suh HS, Yoon TH, Chung MS, Choi OS, Frequency and power stabilization of a three longitudinal mode he-ne laser using secondary beat frequency. *Applied Physics Letters* 1993;**63**(15):2027–2029.

[132] Yokoyama S, Araki T, Suzuki N, Intermode beat stabilized laser with frequency pulling. *Applied Optics* 1994;**33**:358–363.

[133] Yeom JY, Yoon TH, Three-longitudinal-mode he-ne laser frequency stabilized at 633 nm by thermal phase locking of the secondary beat frequency. *Applied Optics* 2005; **44**(2):266–270.

[134] Ellis JD, Joo KN, Buice ES, Spronck JW, Munnig Schmidt RH, Magnetic field effects on the secondary beat frequency profile for three mode HeNe laser stabilization. *In: proceedings of the 24th ASPE annual meeting, 4-9 Oct, Monterey, CA USA* 2009;.

[135] Lamb WE, Theory of an optical maser. *Phys Rev* 1964;**134**:A1429–A1450.

[136] Sayers MD, Allen L, Amplitude, competition, self-locking, beat frequency, and time dependent in a threemode gas laser. *Phys Rev A* 1970;**1**:1730–1746.

[137] Dekker H, Theory of self-locking phenomena in the pressure broadened three-mode he-ne laser. *Appl Phys* 1974;**4**:257–263.

[138] Yokoyama T, Araki T, Yokoyama S, Suzuki N, A subnanometre heterodyne interferometric system with improved phase sensitivity using a three-longitudinal-mode he-ne laser. *Measurement Science and Technology* 2001;**12**(2):157–162.

[139] White AD, Pressure- and current-dependent shifts in the center frequency of the Doppler-broadened ($2p_4$–$3s_2$) 6328-Å ^{20}Ne transition. *Applied Physics Letters* 1967; **10**(1):24–26.

[140] Bloom AL, Wright DL, Pressure shifts in a stabilized single wavelength helium-neon laser. *Appl Opt* 1966;**5**(10):1528–1532.

[141] Thorlabs, Inc., 435 Route 206 North, Newton, NJ 07860 USA, Fiber Coupler, part no. PAF-X-5-B.

[142] Lambda Research Optics, Inc., 1695 West MacArthur Blvd., Costa Mesa, CA 92626 USA, Laser Line Polarizing Beamsplitter Cube, part no. PB-50.8B-633.

[143] Lambda Research Optics, Inc., 1695 West MacArthur Blvd., Costa Mesa, CA 92626 USA, 2.0in Dia unmounted Cemented QWP (633 coated) , part no. WP-50.8CQ-0-4-633.

[144] National Instruments Corporation, 11500 N Mopac Expwy, Austin, TX 78759-3504 USA, Model 6025E data acquisition card.

[145] Knarren BAWH, Application of optical fibres in precision heterodyne laser interferometry. Ph.D. thesis, Eindhoven University of Technology, 2003.

[146] Wu C, Periodic nonlinearity resulting from ghost reflections in heterodyne interferometry. *Optics Communications* 2003;**215**(1-3):17–23.

[147] Kalibjian R, Stokes polarization vector and mueller matrix for a corner-cube reflector. *Optics Communications* 2004;**240**(1-3):39–68.

[148] Ren D, Optical measurements of dimensional instability. Ph.D. thesis, University of North Carolina at Charlotte, 2006.

[149] Rutman J, Characterization of phase and frequency instabilities in precision frequency sources: Fifteen years of progress. *Proceedings of the IEEE* 1978; **66**(9):1048–1075.

Index

Summary

The main goal of the research in this thesis was to design, build, and characterize an instrument for material stability testing. Interferometry was chosen as the measurement method because an instrument could be designed largely independent of the sample size and it did not require a grounded measurement target, compared to other measurement methods such as capacitive sensing. A double side interferometer was chosen as the configuration because it removed a large measurement uncertainty source by not measuring with respect to a reference plate and the measurement is directly traceable to the meter.

One goal for this instrument is to be capable of measuring stability events, which are estimated to occur at higher frequencies than the thermal bandwidth of the sample. Measuring these stability events may give insight into the fundamental stability of a material. Based on this hypothesis, a thermomechanical model was developed to determine the maximum thermal bandwidth for typical materials used in precision systems. For 50 mm long, gauge block sized samples, aluminum 7075-T6 and silicon carbide had the highest bandwidth, approximately 0.5 Hz. For smaller samples, the thermal band should increase because the thermal capacitance is reduced and the heat path is smaller. Thus, any thermal effects should show up in the 1 Hz or lower regime. To observe and measure stability events, the instrument must be capable of measuring at a higher bandwidth than 1 Hz, thus, the target measurement bandwidth for this system is 25 Hz or higher.

For short term measurements, less than one hour, the target measurement uncertainty for a 50 mm sample is 10 pm (k=2) in both air and vacuum. For longer measurements, up to four weeks, the target measurement uncertainty for a a 50 mm sample is 100 pm (k=2). Research in three specific areas, periodic nonlinearity reduction, refractive index correction, and laser frequency stabilization, was needed to build an instrument with a high resolution and a low measurement uncertainty.

Periodic nonlinearity, caused by frequency mixing, imperfect polarization optics, and stray reflections, can typically cause nanometer level errors in displacement interferometry measurements. Because the starting phase value is unknown in displacement interferometry and the measured length change is likely to be less than one fringe, the periodic nonlinearity is difficult to assess and correct. For typical periodic error values of 1 nm to 5 nm, this means a potential uncertainty contribution of 300 pm to 1.5 nm. Thus, the stability measuring interferometer was designed to have a spatially separated source which does not contribute frequency mixing. By having no overlap among beams in the interferometer prior to the main interfering element, the periodic nonlinearity can be avoided.

Correcting for refractive index fluctuations is the most difficult error source to overcome

in this research. A target measurement bandwidth of 25+ Hz creates a strong contrast compared to accurate temperature and pressure measurements which have bandwidths around 0.1 Hz because of their integration time for noise reduction. Thus, for effective characterization and correction, another measurement method was sought which would allow for measurements at the same interferometer measurement bandwidth. One such measurement method is to use wavelength correcting interferometry where the laser source is locked to the resonance peak of a Fabry-Pérot cavity with a fixed length. Using this technique, it is possible to correct refractive index fluctuations at a bandwidth much higher than using environmental parameter measurements and with a lower measurement uncertainty than the empirical equation-based methods typically employed. Using this technique requires a laser with a fast actuator and a stable Fabry-Pérot cavity, two items which were not available during this research.

An alternative method presented in this thesis is a dual interferometer. One interferometer measures the sample fluctuations and the other measures refractive index fluctuations. The refractive index fluctuations are measured by having a balanced interferometer with the only optical path length difference caused by the reference arm passing through a vacuum tube while the measurement arm does not. If the refractive index fluctuations are nominally uniform throughout the interferometer, then this configuration could be suitable for measuring refractive index fluctuations. A detailed uncertainty analysis was presented and the two largest uncertainty contributors are the phase measurement itself and the temperature change uncertainty.

In this thesis, the technology for laser frequency stabilization was not the limiting factor but rather the practical aspects of implementing a stabilized laser with enough power suitable to obtain a detectable interference signal while accounting for a complex optical system and the possibility of fiber coupling losses. Iodine stabilized lasers have more than enough frequency stability for this research but their output power is much lower than even conventional displacement interferometry laser sources. Tunable lasers locked to a stabilized femtosecond laser and cesium atomic clock also have a very high frequency stability but are still research tools themselves. Additionally, both systems have a high cost which was unattractive for this research.

A three-mode stabilized laser was researched during the course of this work. The three-mode laser uses the central mode of the HeNe laser as the main beam supplied to the interferometer and, in this case, had over 2 mW of usable power. An intrinsic mixed mode signal arising from third order harmonics was used to stabilize the laser. The mixed mode signal at nominally 300 kHz was detected, filtered, amplified, and converted to a square wave. Then, a microcontroller was used as a pulse counter and PID controller. The PID output was sent to a current amplifier and then a Peltier cooler which changed the temperature of the laser tube. By changing the tube temperature, and thus, length, the absolute frequency of the central mode was stabilized. The second generation system had an estimated short term stability of 2×10^{-11}. The intrinsic mixed mode signal had a relative sensitivity of 593 $^{\text{Hz}}/_{\text{Hz}}$ to the absolute frequency.

Several different interferometry system generations are presented, centered around a double-sided, balanced design with an internal refractometer for wavelength tracking. This design was chosen because it is directly scalable based on the sample size and it can be comprised of only a few optical components if manufactured appropriately.

Initial measurements were performed in a double deadpath configuration (no sample or vacuum tube present) and with a 30 mm gauge block. After correcting for thermal expansion, refractive index changes, frequency fluctuations, and pressure changes, the measured drift of the gauge block was comparable to the double deadpath measurement. The Allan deviation for these measurements showed sub-nanometer performance up to integration times of 10^4 seconds. The low point in the Allan deviations appeared at an integration time of 10^3 seconds. Aside from expected but higher than wanted environmental fluctuations, the limiting noise source was the optics and mounts. Each optic was mounted separately using commercial tip-tilt stages which are known to drift and vibrate at slightly different rates. This contributed to short term noise band of 50 nm in the individual interferometer measurements.

After two other system iterations were made, the fourth iteration resulted in significant short term improvements due to pressure sealing. In the pressure sealed environment, a double deadpath measurement was made with a 10 nm pk-pk drift which had a strong correlation to the temperature change. Also, a smaller cosine effect was visible in the data. After correcting for temperature and cosine effects, the resulting corrected drift was better than 1.4 nm pk-pk over 23 hours. The Allan deviation, single sided amplitude spectrum, amplitude spectral density, and cumulative amplitude spectrum were all an order of magnitude better than previous measurements. Also, because the interferometer was in a pressure sealed environment, the refractive index fluctuations were less than in previous measurements. The peak in the Allan deviation was at 0.4 nm (1σ). This interferometer was also tested for mechanical coupling which showed the drift was decoupled from the individual interferometer length change by 115 times. After accounting for cosine effects, the decoupling was better than 330 times. A measurement in vacuum over 160 hours showed the double deadpath interferometer drift was less than 2 nm pk-pk after correcting for thermal cycles and the cosine error. The Allan deviation showed a minimum of near 1 pm at an integration time of 10 seconds and a maximum of 0.3 nm (1σ) at 10^3 seconds.

Currently, the interferometer is still being modified and double deadpath measurements are still being performed. More research is needed to definitively say whether this interferometer can be used for material stability assessments. If the thermal and cosine effects scale linearly, then achieving a 10 mK stability in the surrounding environment should produce results in the 10 pm to 20 pm range. Then, the vacuum tube should be implemented and another series of characterization tests should be performed. If those are successful, then samples and the thermomechanical model can be investigated in more detail. This may include a more rigorous three dimensional model of the sample, rather than the simplified one dimensional model presented in this research. At this time, this research and interferometer shows inconclusive results as a tool for determining material stability.

Samenvatting

Het hoofddoel van het in dit proefschrift beschreven onderzoek was het ontwerpen, bouwen en karakteriseren van een instrument voor het meten van materiaal stabiliteit. Als meetmethode is interferometrie gekozen, omdat dan een instrument ontworpen kan worden dat grotendeels onafhankelijk is van de afmetingen van het te meten object en bovendien hoeft het object niet geaard te zijn, zoals bij capacitieve meting. Een dubbelzijdige interferometer is gekozen vanwege de directe traceerbaarheid naar de meter als lengtestandaard en omdat door niet te meten ten opzichte van een referentieplaat een grote bron van meetonzekerheid verdwijnt.

Één doel van dit instrument is om stabiliteitsgebeurtenissen te kunnen meten, waarvan verwacht wordt dat ze een hogere frequentie hebben dan de thermische bandbreedte van het meetobject. Het meten van deze stabiliteitsgebeurtenissen kan inzicht geven in de fundamentele stabiliteit van materialen. Op basis van deze hypothese is een thermisch model ontwikkeld om de maximale thermische bandbreedte te bepalen voor materialen die toegepast worden in precisie systemen. Voor 50 mm lange, op eindmaten gelijkende meetobjecten hebben aluminium 7075-T6 en siliciumcarbide de hoogste bandbreedte, ongeveer 0,5 Hz. Voor kleinere objecten zou de thermische bandbreedte toe moeten nemen, omdat de thermische capaciteit afneemt en het thermisch pad kleiner is. Daarom wordt ingeschat dat thermische effecten optreden bij 1 Hz of lagere frequenties. Om zulke stabiliteit gebeurtenissen waar te nemen moet het instrument met meer dan 1 Hz bandbreedte meten, en daarom is de beoogde meetbandbreedte voor dit systeem 25 Hz of hoger.

Voor korte termijn metingen, korter dan een uur, is de beoogde meetonzekerheid voor een 50 mm object 10 pm (k=2); zowel in lucht als in vacum. Voor langere termijn metingen, tot en met vier weken, is de beoogde meetonzekerheid voor een 50 mm object 100 pm (k=2). Om een instrument te bouwen met een hoge resolutie en een lage onzekerheid was nader onderzoek nodig in drie specifieke interferometrische aandachtsgebieden: periodieke niet-lineariteit, brekingsindex correctie en laser frequentie stabilisatie.

Periodieke niet-lineariteit, veroorzaakt door frequentie menging in de laserbundels, onperfecte polarisatie optiek en ongewenste reflecties, kan bij verplaatsings interferometrie meetfouten veroorzaken in het nanometer gebied. Aangezien de aanvangswaarde van de interferentie fase onbekend is bij verplaatsings interferometrie en de lengteverandering waarschijnlijk minder is dan een fractie van de laser golflengte, is de periodieke niet-lineariteit moeilijk te bepalen en te corrigeren. Voor typische periodieke fouten van 1 nm tot 5 nm betekent dit een bijdrage in de meetonzekerheid van 300 pm tot 1,5 nm. Debelangrijkste meetfout ontstaat door periodieke niet-lineariteit ten gevolge van frequentie

menging. De interferometer voor stabiliteitsmeting is speciaal ontworpen met ruimtelijk gescheiden laserbundels om zodoende frequentie menging te vermijden.

In dit onderzoek blijken de meetfouten veroorzaakt door de benodigde correcties voor brekingsindex variaties blijken het moeilijkst. Nauwkeurige temperatuur en druk metingen met een bandbreedte rond de 0,1 Hz vraagt om integratie tijd voor onderdrukking van ruis en dit contrasteert sterk met een nagestreefde meetbandbreedte van 25+ Hz .Daarom is voor effectieve karakterisatie en correctie een andere meetmethode gezocht die meet met dezelfde bandbreedte als de interferometer. Een voorbeeld van een dergelijke meetmethode is het gebruik van golflengte gecorregeerde interferometrie waarbij de laserbron gekoppeld wordt aan een resonantie piek van een Fabry-Pérot holte met een vaste lengte. Met deze techniek is het mogelijk om te corrigeren voor brekingsindex variaties met een veel hogere bandbreedte dan bij metingen van omgevingsparameters en tevens met een lagere meetonzekerheid dan de op empirische vergelijkingen gebaseerde methode die vaak wordt toegepast. Deze techniek vereist echter een snelle actuator en een stabiele Fabry-Prot holte die beiden niet beschikbaar waren voor dit onderzoek.

Een alternatieve methode die in dit proefschrift wordt gepresenteerd is een dubbele interferometer. De eerste interferometer meet de variaties van het object en de andere meet de brekingsindex variaties. De variaties van de brekingsindex worden gemeten door een gebalanceerde interferometer met slechts één verschil in de optische weglengten veroorzaakt doordat de referentie arm een vacumbuis bevat en de meet arm niet. Wanneer de brekingsindex variaties uniform zijn door de gehele interferometer, dan kan deze configuratie geschikt zijn om de brekingsindex variaties te meten. Een gedetailleerde onzekerheids analyse wordt gepresenteerd en de twee grootste onzekerheids bijdrage komen van de fasemeting van de interferentie en de meting van de temperatuursverandering.

In dit proefschrift was de technologie voor frequentie stabilisatie niet de beperkende factor, maar meer de praktische implementatie van een laserbron met voldoende vermogen om een detecteerbaar interferentie signaal te verkrijgen, rekening houdend met het complexe optische systeem en de mogelijke verliezen in de fiberkoppelingen. Jodium gestabiliseerde lasers hebben voldoende frequentie stabiliteit voor dit onderzoek, maar hun uitgangsvermogen is zelfs veel lager dan van normale voor verplaatsing interferometrie gebruikte laserbronnen. Instelbare lasers gekoppeld aan een gestabiliseerde femto-seconde laser en een cesium atoomklok hebben ook een heel hoge frequentie stabiliteit, maar zijn zelf nog altijd onderzoeksgereedschap. Bovendien zijn beide systemen duur en dat was onaantrekkelijk voor dit onderzoek.

Een drie-mode gestabiliseerde HeNe laser is onderzocht tijdens dit project. De drie-mode laser maakt gebruik van de centrale mode van de HeNe laser als hoofdbundel voor de interferometer en had, in dit geval, meer dan 2 mW nuttig vermogen. Een intrinsiek mixed-mode signaal veroorzaakt door derde orde harmonischen werd gebruikt om de drie-mode laser te stabiliseren. Het mixed-mode signaal van nominaal 300 kHz werd gedetecteerd, gefilterd, versterkt en omgezet naar een blokgolf. Daarna is een microcontroller gebruikt als pulsenteller en PID regelaar. Het uitgangssignaal van de PID regelaar werd naar een stroomversterker gestuurd om met een Peltier element de temperatuur van de laserbuis te regelen. Door de temperatuur van de buis aan te passen, en dus de lengte van de buis, werd uiteindelijk de absolute frequentie van de centrale mode gestabiliseerd. De tweede gerealiseerde versie had een geschatte korte termijn stabiliteit van 2×10^{-11} en het intrinsiek

mixed-mode signaal had een relatieve gevoeligheid van 593 Hz/Hz ten opzicht van de absolute frequentie.

Verschillende generaties interferometer systemen worden gepresenteerd, gebaseerd op een dubbelzijdig, gebalanceerd ontwerp met een interne refractometer voor het volgen van de golflengtevariaties. Dit ontwerp is gekozen, omdat het direct schaalbaar is met de grootte van de meetobjecten en omdat het slechts enkele op specificatie gefabriceerde optische componenten bevat.

De eerste metingen betroffen een dubbele symmetrische configuratie (zonder sample en vacumbuis) en met een 30 mm eindmaat. Na correctie voor thermische uitzetting, verandering van de brekingsindex, frequentie variaties en drukveranderingen, was de gemeten drift van de eindmaat vergelijkbaar met de dubbele symmetrische meting. Bij integratie tijden tot 10^4 seconden blijven de gemeten Allan-afwijkingen, bepaald uit de Allan-variantie, beperkt tot sub-nanometer niveau. Het minimum in de Allan-afwijkingen lag bij een integratie tijd van 10^3 seconden. Afgezien van verwachte, maar hoger dan gewenste, fluctuaties in de omgevings omstandigheden, bleken de optiek en de montage ervan de beperkende ruisbronnen. Elk optisch element was apart gemonteerd met commerciële tip-tilt tafels waarvan bekend is dat deze driften en trillen. Dit veroorzaakte een korte termijn ruisband van 50 nm in de individuele interferometer metingen.

Na twee verdere systeem iteraties resulteerde de vierde iteratie in significante korte termijn verbeteringen door het beperken van drukvariaties. In een tegen drukvariaties afgesloten omgeving werd een dubbele symmetrische meting uitgevoerd met 10 nm top-top drift welke sterk gecorreleerd was aan de temperatuursveranderingen. Daarbij was ook een kleinere cosinus fout zichtbaar in de meetdata. Na correctie voor temperatuur en cosinus effecten was de resulterende gecorrigeerde drift beter dan 1,4 nm top-top over 23 uur. De Allan-afwijking, het enkelzijdige amplitude spectrum, de amplitude spectrale dichtheid en het cumulatieve amplitude spectrum waren allemaal een orde grootte beter dan bij vorige metingen. Verder waren de brekingsindex variaties kleiner, omdat de interferometer zich in een afgesloten omgeving bevond. De piek in de Allen-afwijking lag bij 0,4 nm (1σ). Deze interferometer is ook getoetst op mechanische koppeling, de drift is ontkoppeld met een factor 115 van de verandering van de individuele interferometerlengte. Na het meewegen van cosinus effecten was de ontkoppeling beter dan een factor 330. Een meting in vacum over 160 uur vertoonde een drift van de dubbele symmetrische interferometer van minder dan 2 nm top-top; dit is na correctie voor thermische cycli en de cosinus fout. De Allan-afwijking vertoonde een minimum van bijna 1 pm bij een integratie tijd van 10 seconden en een maximum van 300 pm (1σ) bij 1000 seconden.

Op dit moment wordt de interferometer nog altijd gemodificeerd en dubbele symmetrie metingen worden nog steeds uitgevoerd. Meer onderzoek is nodig voordat definitief geconcludeerd kan worden dat deze interferometer geschikt is voor het meten van materiaal stabiliteit. Als de thermische en cosinus fouten lineair schalen dan kunnen resultaten in het 10 pm tot 20 pm bereik gehaald worden mits de omgeving binnen 10 mK gestabiliseerd wordt. Tevens zou de vacumbuis ingebouwd moeten worden voor een nieuwe serie karakterisatie metingen waarmee, bij geslaagde metingen, de meetobjecten en de thermische modellen in meer detail onderzocht kunnen worden. Dit kan een uitgebreider driedimensionaal model zijn van het te meten object in plaats van het vereenvoudigde eendimensionale model zoals gepresenteerd in dit onderzoek. De tot nu toe verkregen

meetresultaten uit dit onderzoek en deze interferometer geven nog geen uitsluitsel over de bruikbaarheid van dit concept als gereedschap voor materiaal stabiliteitsonderzoek .

Related Work

The follow publications all related to the work performed in during this thesis.

Journal Publications

Joo K, **Ellis JD**, Spronck JW, Munnig Schmidt RH. Real-time wavelength corrected heterodyne laser interferometry, *Precision Engineering* 2010; (in press)

Ellis JD, Joo K, Buice ES, Spronck JW. Frequency stabilized three mode HeNe laser using nonlinear optical phenomena, *Optics Express* 2010; **18**(2): pp. 1373–1379 [www]

Joo K, **Ellis JD**, Buice ES, Spronck JW, Munnig Schmidt RH. High resolution heterodyne interferometer without detectable periodic nonlinearity, *Optics Express* 2010; **18**(2): pp. 1159–1165 [www]

Joo K, **Ellis JD**, Spronck JW, Munnig Schmidt RH. Design of a folded, multi-pass Fabry-Perot interferometer using a He-Ne laser for displacement metrology (Technical Design Note), *Measurement Science & Technology* 2009; **20**(10): 107001 (5pp) [www]

Ellis JD, Joo K, Spronck JW, Munnig Schmidt RH. Balanced interferometric system for stability measurements, *Applied Optics* 2009; **48**(9): pp. 1733–1740 [www]

Joo K, **Ellis JD**, Spronck JW, van Kan PJM, Munnig Schmidt RH. A simple heterodyne laser interferometer with sub-nm periodic errors, *Optics Letters* 2009; **34**(3): pp. 386–388 [www]

Conference Proceedings

Ellis JD, Baas M, Spronck JW. Errors in measurement and compensation algorithms for periodic nonlinearity correction, *In: Proceedings of the 25th ASPE Annual Meeting, 31 Oct - 5 Nov 2010, Atlanta, GA*

Voigt D, **Ellis JD**, Verlaan A, Spronck JW, Bergmans R, Munnig Schmidt RH. Towards traceable metrology for material stability characterization , *In: Proceedings of the NanoScale 2010, 27 - 29 Oct 2010, Brno, Czech Republic*

Verlaan A, **Ellis JD**, Voigt D, Spronck JW, Munnig Schmidt RH. Interferometric system for pm-level stability characterization , *In: Proceedings of the ISCO 2010, 4 - 8 Oct 2010, Rhodes Island, Greece*

Joo K, **Ellis JD**, Buice ES, Spronck JW, Munnig Schmidt RH. A novel heterodyne

displacement interferometer with no detectable periodic nonlinearity and optical resolution doubling, *In: Proceedings of the 10th euspen International Conference, 31 May - 3 Jun 2010, Delft, The Netherlands*

Ellis JD, Joo K, Buice ES, Spronck JW, Munnig Schmidt RH. Frequency stabilization and heterodyne system via the mixed mode in three mode HeNe lasers , *In: Proceedings of the 10th euspen International Conference, 31 May - 3 Jun 2010, Delft, The Netherlands*

Ellis JD, Joo K, Buice ES, Spronck JW, Munnig Schmidt RH. Magnetic field effects on the secondary beat frequency profile for three mode HeNe laser stabilization, *In: Proceedings of the 24th ASPE Annual Meeting, 4-9 Oct 2009, Monterey, CA* [www]

Ellis JD*, Joo K, Spronck JW, Munnig Schmidt RH. Double-sided interferometer with low drift for stability testing, *In: Proceedings of the 9th International Symposium on Measurement Technology and Intelligent Instruments, 29 Jun - 2 July 2009, St. Petersburg, Russia*

Joo K*, **Ellis JD**, Spronck JW, van Kan PJM, Munnig Schmidt RH. Simple heterodyne laser interferometer without periodic errors, *In: Proceedings of the 9th International Symposium on Measurement Technology and Intelligent Instruments, 29 Jun - 2 July 2009, St. Petersburg, Russia*

Joo K, **Ellis JD**, Spronck JW, Munnig Schmidt RH. Wavelength corrected, non-polarizing heterodyne laser interferometry in air, *In: Proceedings of the 9th euspen International Conference, 2-5 Jun 2009, San Sebastian, Spain*

Ellis JD*, Joo K, Verlaan A, Spronck JW, Munnig Schmidt RH. Uncertainty considerations for interferometric stability testing, *In: Proceedings of the 23rd ASPE Annual Meeting, 19-23 Oct 2008, Portland, OR* [www]

Buice ES, **Ellis JD**, Langen HH, Munnig Schmidt RH. Importance of metrology in micromachines, *In: Proceedings of the 6th International Workshop on Microfactories, 14-19 Oct 2008, Chicago, IL*

Ellis JD, Hatzigeorgopoulos JH, Spronck JW, Munnig Schmidt RH. Optically balanced, multi-pass displacement interferometry for picometer stability testing, *In: Proceedings of the 22nd ASPE Annual Meeting, 14-19 Oct 2007, Dallas, TX* [www] *denotes oral speaker, [www] is the link to the journal article/conference website

Acknowledgments

In any Ph.D. project, there are always a few people who are instrumental to the success of the Ph.D. student and the project. In my case, I was fortunate to have a brilliant colleague, Dr. Ki-Nam Joo, to work with for much of my stint at TU Delft. Ki-Nam, I am very grateful for your mentoring and friendship, and I thank you for the many discussions, disagreements, successes, and failures that we shared. I would gladly work with you again in the future.

I appreciate the efforts by my two supervisors, Prof. Robert Munnig Schmidt and Ir. Jo Spronck. Rob, Jo, each day I understand more and more the non-trivial task of supervising someone like me. While we shared ups and downs, overall they were the result of each of us trying to progress forward, yet inadvertently stumbling over each other along the way. I learned many things from both of you during my stay at TU Delft and my experiences in Delft and the Netherlands will last a lifetime. Thank you for your supervision and support for all of these years.

I would like to thank my colleagues in the IOP project, Ad Verlaan, Dr. Dirk Voigt, Dr. Dario Lo Cascio, Dr. Robert Bergmans, Joep Pijnenburg, and Dr. Paul van Kan, and the Dutch IOP for funding this research. Also, I would to thank the IOP User Committee for many fruitful discussions. Specifically, I appreciate the advice and guidance from Dr. Han Haitjema and Dr. Suzanne Cosijns. Also, I would like to thank my thesis committee members, Dr. Voigt, Prof. Leach, Prof. Regtien, Prof. Schellekens, Prof. Urbach, and Prof. van Eijk, for their meticulous review of my thesis.

I would like to thank my friends and colleagues at TU Delft, Freidjof, Warner, Jan, Marianne, Jasper, Jeroen, Pablo, Rudolf, Michiel, Maarten, Ivan, Walter, Chris, Patrice, Dick, and anyone else I might have left off, for their comments on my research and for putting up with my antics. I would particularly like to thank Dr. Eric Buice and Dr. Sander Paalvast. Eric, thanks for our brainstorming sessions (on clear whiteboards), our many travels in Europe and abroad, and your dedication in the lab. Sander, thanks for your advice about the Dutch university system (and also barbequeing at TU Delft), your translation skills, and your assistance in the cleanroom.

I would be remiss if I left off my previous advisors at UNC Charlotte, Prof. Stuart Smith, Prof. Robert Hocken, and Dr. Shane Woody, for their instrumental support at the beginning of this journey. Also, I appreciate the guidance and advice of Prof. Michiel Kreutzer, Dr. Matthew Davies, Dr. Angela Davies, and Dr. Brigid Mullany on everything it takes to make it in academia.

Kate, I would not have made it this far without your love and support. Throughout the good times and the more difficult ones, you have been there for me whenever I needed

someone the most. Also, your proofreading isn't too shabby. Julia, although you are too young to know it, your arrival during the final stages of this work gave me a single minded purpose to get it done because I have more important things in my life. To my family and friends back in the US, thanks for your love and encouragement over the years.

And thanks to Sara, for coming into my life like a butterfly flapping its wings 1000 miles away...

Biography

Jonathan Ellis was born on March 12, 1982 in Hackensack, New Jersery in the United States of America. After growing up in Cranford, NJ, he moved to Charlotte, North Carolina where he pursued a Bachelor of Science in mechanical engineering at the University of North Carolina at Charlotte. As an undergraduate, he got his first taste of precision engineering while working with Prof. Stuart Smith and Dr. Shane Woody, and he was hooked. Jon received his BS in mechanical engineering in May 2005 and worked for a summer at InsituTec Incorporated (Charlotte, NC) before starting his MSc research in the Center for Precision Metrology at UNC Charlotte. Jon finished his Master's work under Prof. Stuart Smith and Prof. Robert Hocken's direction in January 2007 on "Reducing frame stiffness dependency in nanoindentation" and graduated in May 2007.

In February 2007, Jon hopped across the pond and begain his Ph.D. work, ultimately resulting in this thesis, at the Delft University of Technology in the Netherlands under the supervison of Prof. Robert Munnig Schmidt and Ir. Jo Spronck. The focus of his research was optical metrology techniques and building interferometry systems for characterizing material stability. The instrument built during his thesis work is currently housed at the VSL Dutch Metrology Institute where further research is ongoing. To date, Jon has co-authored seven journal papers and fourteen conference proceedings and is co-inventor on three patents.